Synthesis and characterization of layered transition metal trihalides MCl_3 (M = Ru, Mo, Ti, Cr) and CrX_3 (X = Cl, Br, I)

Von der Fakultät für Umwelt und Naturwissenschaften der Brandenburgischen Technischen Universität Cottbus-Senftenberg zur Erlangung des akademischen Grades eines Doktors der Naturwissenschaften (Dr. rer. nat.)

genehmigte Dissertation

vorgelegt von

M. Sc.

Martin Grönke

aus Altdöbern

Gutachter:	Prof. Dr. Peer Schmidt	(BTU Cottbus-Senftenberg)
Gutachter:	Prof. Dr. Bernd Büchner	(Leibniz-IFW Dresden)
Tag der mündlichen Prüfung:		09.10.2020

DOI: 10.26127/BTUOpen-5282

Danksagung

Eine Doktorarbeit stellt in den meisten Fällen nie ausschließlich die Leistung einer einzelnen Person über einen längeren Zeitraum dar, sondern ist vielmehr das Resultat einer Vielzahl von wissenschaftlichen Beiträgen eines Kollektivs. Auch diese Dissertation basiert auf der Basis der Zusammenarbeit als Schlüssel zum Erfolg.

Auf diesem Weg haben mich einige Personen begleitet, denen ich auf diese Weise danken möchte. Zunächst bedanke ich mich bei Prof. Dr. Bernd Büchner, für die Betreuung seitens des IFW Dresden und die Möglichkeit grundlegende, wissenschaftliche Fragestellungen über einen mehrjährigen Zeitraum bearbeiten und dabei eine Vielzahl an Analytik nutzen zu können. Ich bedanke mich außerordentlich bei Prof. Dr. Peer Schmidt für die Betreuung seitens der BTU Cottbus-Senftenberg und die zahlreichen Treffen zur Erörterung der Phasenbeziehungen MX_3 und zu Modellierungen mittels TRAGMIN. Meine tiefste Dankbarkeit gebührt unser Gruppenleiterin Dr. Silke Hampel für die Betreuung, das entgegengebrachte Vertrauen und die mentale Unterstützung während der gesamten Promotionszeit. Ihre Tür stand jederzeit offen und Sie nahm sich jederzeit meiner wissenschaftlichen sowie sonstigen Fragen und Probleme an.

Grundsätzlich ist die Promotionszeit nicht ausschließlich mit Erfolgserlebnissen verbunden und die Aneignung eines gewissen Maßes an Frustrationstoleranz nicht von Nachteil. Dass mir meine Promotionszeit jedoch letztendlich positiv in Erinnerung bleiben wird liegt vor allem an der außerordentlich positiven Zusammenarbeit mit Kollegen aus unserer Arbeitsgruppe “Functional crystals on the nanoscale”. Ich danke auf diesem Wege Dr. Christian Nowka für die Einführung in die Welt des Gasphasentransportes und unsere gemeinsam entdeckte Leidenschaft für einen Fußballklub. Weiterhin danke ich ausdrücklich PD Dr. Martin Valldor für die Unterstützung beim Schreiben wissenschaftlicher Publikationen, der magnetische und röntgenographische Untersuchungen, tolle Konferenzbesuche und Diskussionen über das Leben. Das der Spaß im Büroalltag in der C1E.01 nicht zu kurz kam verdanke ich außerdem Salvatore Carrocci, Mohamed A. A. M., Samuel Froeschke und Xenophon Zotos. Ich danke Dr. Maik Scholz für die kollegiale Zimmeraufteilung während der externen Doktorandenseminare und Dr. Victoria Eckert für Messungen am Transmissionselektronenmikroskop. Mein Dank gebührt ebenso allen weiteren Kollegen der

Arbeitsgruppe, allen voran unserem Techniker Robert Heider sowie Felix Hansen, Katrin Wruck und Felix Kaiser für inspirierende Kaffeerunden.

Außerordentlich danke ich meinen Studenten Danny Pohflepp, Nadine Bronkalla, Benjamin Buschbeck und Martha Fechner, die ich während der Erstellung ihrer jeweiligen Graduierungsarbeiten betreuen durfte. Ich denke, ihr konntet nicht nur von mir, sondern auch ich von euch lernen. Weiterhin danke ich Franziska Pfeifer und Lukas Kurzweg für die Unterstützung im Labor.

Ich danke auf diesem Wege Dr. Axel Lubk und Dr. Daniel Wolf für die tolle Zusammenarbeit und atomare Visualisierung von zahlreichen Nanoschichten mittels hochauflösender Transmissionselektronenmikroskopie. Ich danke weiterhin Dr. Steffen Oswald für Messungen am XPS-Spektrometer, Frau Barbara Eichler für Untersuchungen am Rasterkraftmikroskop und Dr. Qi Hao sowie Frau Sandra Schiemenz für Messungen am Mikro-RAMAN. Dr. Thomas George Woodcock danke ich für SEM-Untersuchungen mit einer Vakuumtransferkammer. Des Weiteren gebührt mein Dank Dr. Franziska Hammerath für NMR Messungen, Gesine Kreutzer für weitere TEM- und WDX-Messungen und Hilfestellungen sowie den beiden Marcos (M. Naumann und M. Rosenkranz) für Untersuchungen am IR Spektrometer.

Zudem danke ich Prof. Dr. Stefan Kaskel und Ubed S.F. Arrozi für die Zusammenarbeit bei der Untersuchung von Titan(III)-chlorid Mikroschichten. Jeder gute Morgen beginnt mit einem freundlichen Lächeln. Auf diesem Wege gebührt mein Dank Frau Made am Empfang des IFW Eingangstores. Frau Kerstin Höllerer und Frau Katja Schmiedel aus dem Sekretariat danke ich für die schnelle Bearbeitung meiner Anfragen.

Ein letzter großer Dank gebührt natürlich meinen Eltern, die es mir letztendlich ermöglicht haben, eine fast zehnjährige Ausbildung an mein Abitur anzuschließen. Mein letzter Dank gebührt meiner Freundin Tanja und ihrer Katze Happy, die mich die meiste Zeit während der Promotion ausgehalten haben und immer für mich da waren.

Acknowledgement

To earn a PhD is in most cases not related to the achievements of a single person only, but more often a result of contributions of a scientific collective. Likewise, the collaboration is the main key to success for the outcome of this dissertation.

During the years I was cooperating with many people which I would like to thank. First of all, I thank Prof. Dr. Bernd Büchner for the supervision related to the IFW Dresden. He gave me the chance to work on basic scientific questions over many years and get access to a myriad of analytics. I exceedingly thank Prof. Dr. Peer Schmidt for the supervision related to the BTU Cottbus-Senftenberg and numerous appointments and discussions to the phase relations of MX_3 compounds and simulations by TRAGMIN. My deepest gratitude refers to Dr. Silke Hampel for the supervision, the shown confidence and the mental support during the whole PhD.

In principle the time of being a PhD student is not shaped by permanent success and the acquisition of a bit of frustration tolerance a significant benefit. As I recall it, anyhow my time as a PhD student will be kept in good memory, mainly because of a hugely positive collaboration in our team “Functional crystals on the nanoscale”. In this way I thank Dr. Christian Nowka for the introduction into the topic and our together discovered passion for a soccer club. Besides I exceedingly thank PD Dr. Martin Valldor for the support at writing scientific papers, magnetic and X-ray investigations and discussions about life in general. Thanks to Salvatore Carrocci, Mohamed A. A. M., Samuel Froeschke and Xenophon Zotos that the fun in everyday office life was not neglected in C1E.01. I thank Dr. Maik Scholz for the cooperative room segmentation during the external PhD seminars. Further I thank Dr. Victoria Eckert for TEM measurements, Robert Heider for X-ray investigations as well as Felix Hansen, Katrin Wruck and Felix Kaiser for inspiring rounds of coffee.

I greatly thank my students Danny Pohflepp, Nadine Bronkalla, Benjamin Buschbeck and Martha Fechner, which I supervised during their graduation works, since I could learn a lot of things from you, too. Furthermore I thank Franziska Pfeifer and Lukas Kurzweg for the support in the lab.

I thank Dr. Axel Lubk and Dr. Daniel Wolf for the great cooperation inside the IFW and nice TEM high-resolution measurements of nanosheets. Besides, I thank Dr. Daniel Oswald for

XPS-, Barbara Eichler for AFM- and Dr. Qi Hao for micro-RAMAN measurements. Furthermore I thank Dr. Thomas George Woodcock for SEM measurements by using a vacuum transfer chamber, Dr. Franziska Hammerath for NMR measurements, Gesine Kreutzer for WDX and TEM measurements and assisting with SEM and EDX. I thank both Marcos (M. Naumann and M. Rosenkranz) for IR measurements.

Besides I thank Prof. Stefan Kaskel and Ubed S.F. Arrozi for the nice cooperation related to the $TiCl_3$ project. Every morning starts with a smile. Related to this, I thank Mrs. Made at the entrance of the IFW. Further I thank Mrs. Höllerer and Mrs. Schmiedel for fast processing of my requirements in the office.

Finally many thanks to my parents who enabled me to proceed with a decennial education after finishing school. My last thank is addressed to my girlfriend Tanja and her cat Happy who endured and were always there for me during the PhD years.

Kurzfassung

Die Untersuchung von neuartigen Struktur-Eigenschaftsbeziehungen durch Miniaturisierung bis hin zu Monolagen steht für viele Übergangsmetalltrihalogenide MX_3 noch aus. Zudem ist die Herstellung der für diese Untersuchungen notwendigen zweidimensionalen Schichten, die gleichzeitig hochkristallin und dünn sind, eine experimentelle Herausforderung.

Diese Dissertation beschreibt die rationale Syntheseplanung und die daraus abgeleitete gezielte Darstellung von dünnen MX_3 Nanoschichten (≤ 100 nm) auf geeigneten Substraten mittels chemischem Gasphasentransport (chemical vapor transport, CVT) sowie deren umfassende Charakterisierung mittels komplementärer analytischer Methoden. Das Wachstum von Nanoschichten auf einem Substrat mittels CVT zeichnet sich durch niedrige Zeitskalen, einen geringen Materialverbrauch bei gleichzeitig hoher Qualität der abgeschiedenen Kristalle aus. Für die Bestimmung der optimalen Wachstumsbedingungen wurde der CVT Prozess aller untersuchen Verbindungen zunächst unter Anwendung der Calphad-Methode (Programmpaket TRAGMIN) modelliert. Dadurch konnten die jeweiligen transportwirksamen Gasspezies und die temperaturabhängigen, dominierenden Transportgleichgewichte bestimmt und die Synthesebedingungen optimiert werden.

Basierend auf diesen Simulationsergebnissen wurden einkristalline Schichten von Verbindungen MCl_3 (M = Ru, Mo, Ti, Cr) und CrX_3 (X = Cl, Br, I) in Temperaturbereichen zwischen 573-1023 K auf YSZ- (Yttrium stabilisiertes Zirkondioxid) oder Saphir-Substraten abgeschieden. Im Anschluss wurden die CVT Parameter (Transportzeit, Temperaturen oder Einwaage) zur gezielten Abscheidung von entweder Bulk-Material oder Nanoschichten optimiert. Es wurden sowohl Mikroschichten mit Schichtendicken um 4 µm ($TiCl_3$), um 20 nm dünne Nanoschichten ($RuCl_3$, $CrCl_3$ und CrI_3) als auch ultradünne Schichten um 3 nm ($MoCl_3$ und $CrBr_3$) erhalten. Ein weiteres Highlight der Arbeit ist die erfolgreiche Isolierung von $RuCl_3$ und $CrCl_3$ Monolagen mittels nachgeschalteter Delamination.

Die Morphologie und Dimensionen der Schichten wurden mittels optischer- und Elektronenmikroskopie bestimmt. Durch Röntgenspektroskopie und Beugungsmethoden konnte die gewünschte Zusammensetzung (M:X = 1:3) sowie eine hohe Kristallinität und Phasenreinheit der Bulk-Materialien und dünnen Schichten bestätigt werden. Es wurde weiterhin aufgezeigt, dass sich Restmengen von kontaminierendem Sauerstoff nicht in das Kristallgitter einlagern (Oxidation), unabhängig von der Dicke der Materialien.

Dünne MX_3 Schichten unterschieden sich durch eine Verschiebung von Photonen-Energie zu höheren ($RuCl_3$, $MoCl_3$, $CrBr_3$) oder niedrigeren Werten ($CrCl_3$) im Vergleich zum

Bulk-Material. Die magnetischen Eigenschaften von $CrCl_3$ Mikroschichten zeigten ausschließlich ferromagnetische Ordnungszustände, im Gegensatz zu anti-ferromagnetischem Bulk-$CrCl_3$. NMR Messungen von $CrCl_3$ Mikroschichten konnten Spannungen im System nachweisen, die möglicherweise aus einem großen Gitterfehlanpassungsparameter (zwischen MX_3 Schichten und dem Substrat) resultieren.

Die katalytischen Eigenschaften von $TiCl_3$ Mikroschichten wurden anhand von Polymerisationsreaktionen von Ethylen bestimmt. Für die Mikroschichten wurde ein Anstieg der Aktivität von 16 %, im Vergleich zum Bulk-Material, beobachtet. Nachfolgende Delaminierung der Schichten, bis hin zu noch dünneren Nanoschichten, resultierte in einer weiteren Aktivitätssteigerung auf 24 % durch ein vergrößertes Oberfläche-zu-Volumen Verhältnis der $TiCl_3$ Partikel.

Ein Großteil der in dieser Dissertation aufgezeigten Ergebnisse wurde bereits in wissenschaftlichen Fachjournalen publiziert (siehe List of contributions). In den jeweiligen Kapiteln wird stets darauf hingewiesen.

Abstract

The investigation of novel structure-to-property relations of many transition metal trihalides MX_3 by downscaling to promising monolayer is still pending. However, the production of two-dimensional MX_3 sheets that are both high crystalline and thin is an experimental challenge.

This thesis is focused on the rational synthesis planning and the derived targeted preparation of thin MX_3 nanosheets (≤ 100 nm) on suitable substrates by chemical vapor transport (CVT) as well as their characterization by complementary analytical methods. CVT of nanosheets directly on substrates benefits of low timescales, less material consumption and only few structural distortions. For the determination of optimal growth conditions, the CVT processes of investigated compounds were initially simulated by using the Calphad method (program package TRAGMIN). Thus, the occurring transport efficient gas species and temperature dependent, dominating vapor transport equilibria were calculated to optimize the growth process in a direct and straightforward way.

Based on prior simulation results single crystalline sheets of MCl_3 (M = Ru, Mo, Ti, Cr) and CrX_3 (X = I, Br, Cl) were successfully prepared at temperatures between 573 – 1023 K on YSZ (yttrium stabilized zirconia) or sapphire substrates. The adjustable CVT parameters (transport duration, temperatures or weighed starting material) were optimized with respect to the targeted synthesis of either bulk or nanosheets at substrates. Microsheets with thicknesses of less than 4 µm (α-$TiCl_3$) and about 20 nm thin nanosheets (α-$RuCl_3$, $CrCl_3$ and CrI_3) down to ultrathin flakes (≈ 3 nm, α-$MoCl_3$ and $CrBr_3$) were obtained by CVT. As a highlight, monolayers of α-$RuCl_3$ and $CrCl_3$ were isolated successfully by means of a subsequent delamination.

The MX_3 sheets morphology and dimension was described by optical and electron microscopy, highlighting their two-dimensional nature. By several X-ray spectroscopy and diffraction techniques the desired composition (M:X = 1:3), high crystallinity and phase-purity of thick and thin MX_3 platelets was confirmed subsequently. Further it was emphasized that oxygen impurities do not affect the crystals structure, independent from their thickness. With respect to MX_3 nanosheets a slight increase (α-$RuCl_3$, α-$MoCl_3$ and $CrBr_3$) or decrease ($CrCl_3$) in phonon energies was observed in comparison to their bulk counterparts.

The magnetic properties of $CrCl_3$ micro- and nanosheets were determined to be solely ferromagnetic and thus different than those of the bulk samples. By further NMR measurements of $CrCl_3$ nanosheets we obtained a frequency shift to higher values that could be affected by tension of thin deposited structures, originating from the substrate surface.

Finally, the structure-to-property relations were investigated at a first example. The catalytic properties of α-$TiCl_3$ microsheets were investigated by gas-phase polymerization of ethylene. By downscaling the catalysts thickness by CVT, we obtained an activity improvement of 16 % in comparison to bulk α-$TiCl_3$. Further subsequent delamination down to nanosheets led to an even enhanced catalytic activity up to 24 %, highly probable due to an enlarged surface-to-volume ratio.

The majority of demonstrated results related to this thesis are part of already published scientific papers (see List of contributions), which is declared at appropriate positions.

List of contributions

The majority of demonstrated results related to this thesis are part of previously published and licensed scientific papers. The suitable affiliations to these papers are declared at appropriate positions in the running text. This list of contributions summarizes the scientific contributions of the author from the period of February 2016 – December 2019.

Contributions in scientific journals

V. **Martin Grönke**, Benjamin Buschbeck, Peer Schmidt, Martin Valldor, Steffen Oswald, Qi Hao, Axel Lubk, Daniel Wolf, Udo Steiner, Bernd Büchner and Silke Hampel, *Chromium Trihalides CrX_3 (X = Cl, Br, I): Direct Deposition of Micro- and Nanosheets on Substrates by Chemical Vapor Transport,* ***Advanced Materials Interfaces****,* 6, 24, (2019), 1901410, doi: 10.1002/admi.201901410

IV. **Martin Grönke**, Ubed S.F. Arrozi, Nadine Bronkalla, Peer Schmidt, Martin Valldor, Steffen Oswald, Thomas G. Woodcock, Victoria Eckert, Qi Hao, Laura Plüschke, Albena Lederer, Kornelius Nielsch, Bernd Büchner, Stefan Kaskel and Silke Hampel*, Layered α-$TiCl_3$: Microsheets on YSZ substrates for ethylene polymerization with enhanced activity*, ***Chemistry of Materials***, 31, 14, (2019)*,* 5305-5313, doi: 10.1021/acs.chemmater.9b01818

III. **Martin Grönke**, Danny Pohflepp, Peer Schmidt, Martin Valldor, Steffen Oswald, Daniel Wolf, Qi Hao, Udo Steiner, Bernd Büchner and Silke Hampel, *Simulation and synthesis of α-$MoCl_3$ nanosheets on substrates by short time chemical vapor transport*, ***Nano-Structures and Nano-Objects***, 19 (2019), 100324, doi: 10.1016/j.nanoso.2019.100324

II. **Martin Grönke**, Peer Schmidt, Martin Valldor, Steffen Oswald, Daniel Wolf, Axel Lubk, Bernd Büchner and Silke Hampel, *Chemical vapor growth and delamination of α-$RuCl_3$ nanosheets down to the monolayer limit*, ***Nanoscale,*** 10, 40 (2018), 19014-19022, doi: 10.1039/c8nr04667k

I. Marcel Haft, **Martin Grönke**, Markus Gellesch, Sabine Wurmehl, Bernd Büchner, Michael Mertig and Silke Hampel, *Tailored nanoparticles and wires of Sn, Ge and Pb inside carbon nanotubes*, ***Carbon***, 101, (2016), 352-360, doi: 10.1016/j.carbon.2016.01.098

Oral lectures at scientific conferences

VI. Materials Chemistry Conference **(MC14)**, Aston University, Birmingham, U.K., 08.-11.07.19, „*Layered transition metal trihalides MX_3 (X= Cl, Br, I): simulation and synthesis by chemical vapor transport of bulk flakes and nanosheets on substrates*“

V. **Naturwissenschaftstag BTU CS**, Senftenberg, 14.06.19, „*Simulation und Kristallzüchtung von Mikroschichten von 2D-Materialien MX_3“*

IV. Sixth European Conference On Crystal Growth **(ECCG6)**, Varna, Bulgaria, 17.-19.09.2018, „*Crystal growth of 2D honeycomb transition metal halide MX_3 nanosheets by chemical vapor transport (CVT)*“

III. **DPG Frühjahrstagung**, TU Berlin, 11.-16.03.18, „*Chemical vapor growth and delamination of α-MCl_3 nanosheets (M = Ru, Mo, Ti)*“

II. Advanced Nanomaterials Conference **(ANM 2017)**, Aveiro University, Portugal, 19.-21.07.17, „*Synthesis of α-$RuCl_3$ crystals on the nanoscale via chemical vapor transport (CVT)*“

I. **Naturwissenschaftstag BTU CS**, Senftenberg, 16.06.17, „*Synthesis of α-$RuCl_3$ crystals on the nanoscale via chemical vapor transport (CVT)*“

Poster contributions at scientific conferences

IV. European Conference on Chemistry of Two-dimensional Materials **(Chem2DMat)**, TU Dresden, 03.-06.09.2019, „*Chemical vapor growth and delamination of 2D honeycomb MCl_3 (M = Ru, Mo, Ti, Cr) nanosheets down to the monolayer limit*“

III. 21st JCF Frühjahrssymposium and 2nd European Young Chemists' Meeting **(FJS | EYCheM)**, Bremen University, 20.-23.03.2019, „*Layered transition metal trihalides MX_3 (X = Cl, Br, I): simulation and synthesis by chemical vapor transport of bulk flakes and nanosheets on substrates*“

II. **Graphene Conference**, International Congress Center Dresden, 26.-29.06.18, „*Chemical vapor growth and delamination of 2D honeycomb transition metal halide MX_3 nanosheets*“

I. **DPG Frühjahrstagung**, TU Dresden, 19.-24.03.17, „*Synthesis and controlled growth of α-$RuCl_3$ crystals on the nanoscale via chemical vapor transport (CVT)*“

Contents

„I pick about 2020 as the earliest thing where I think we can call Moores Law dead. I am picking 7 nm - maybe you can talk me into 2022 and you might even be able to talk me into 5 nm – I don't know, but you're not gonna talk me into 1 nm. I think physics dictates against that.“

Dr. Robert Colwell (former main architect of the P6 processor family of Intel and current Deputy Director of Microsystems Technology Office, DARPA) in 2013 on the minimum feature size of future silicon based transistors.

1 Introduction

A key to success related to recent technological progress is the discovery and understanding of new materials. Promising candidates are specially tailored quantum materials, such as topological insulators, *Weyl* semimetals or spin liquids, whose physical properties are dictated by the quantum nature of the valence electrons and their collective behavior. It is only a matter of time before grasping and exhibiting physical synergies will facilitate path-breaking lossless electronics based on spin currents or quantum computing.[1]

With the recent investigation of graphene and its unique properties the interest for non-carbon, but isostructural materials with only a single honeycomb layer was not been long in coming.[2–5] *Van der Waals* bonded transition metal trihalides (TMTHs) with formula MX_3 (M = transition metal, X = Cl, Br or I), deployed since decades as catalysts in organic synthesis procedures, feature incomplete filled *d* orbitals that are strongly correlated due to the *Coulomb* repulsions of electrons. This results in the formation of various, partly coexisting, phases e.g. Mott-insulators, (anti)ferromagnets, ferroelectrics or multiferroics, only energetically separated by small differences. Thus, a manipulation of cooperative exchange interactions by application of an external magnetic or electric field is easily feasible.[1] These TMTHs were recently reexamined with respect to their layered nature and their consequent potential as ultrathin magnetic layers or improved catalysts with enlarged surface-to-volume ratio.[6,7]

As the macroscopic physical properties of MX_3 structures are determined by the stacking order of weakly coupled adjacent layers, small microscopic shifts or distortions of individual layers or several stacks may change further the overall contribution of exchange interactions (see Figure 1, page 2). For a comprehensive understanding of competing mechanisms scientists are searching for synthesis procedures with the outcome of crystallographic ideal structures, since conventional exfoliation attempts are *per se* associated with the introduction of structural defects.

This thesis is an approach to generate as-grown MX_3 structures directly on substrates and thus approximate ideally layered structures. To avoid a time consuming trial-and-error synthesis and for determination of optimal growth conditions, the vapor transport of each system was simulated initially by using CalPhaD methods (CALculation of PHAse Diagrams). By modelling, transport efficient gas species and the vapor transport equilibria were unveiled in order to a rational synthesis planning. The synthesis of MCl_3 (M = Ru, Mo, Ti and Cr), as well as of CrX_3 (X = Cl, Br and I) bulk- and nanostructures was realized by chemical vapor

transport (CVT). The adjustable parameter by CVT (time, temperatures or weighed portion of the starting material) were investigated for the targeted synthesis of either thicker MX_3 bulk platelets, or thin MX_3 nanosheets directly on suitable substrates. The deposited structures were subsequently characterized by several analytical methods proving their morphology, composition, phase purity and crystallinity. Finally, the physical properties (magnetic and catalytic) of the new functional materials with respect to the thin sheets of MCl_3 were determined experimentally and compared to those of the respective bulk materials.

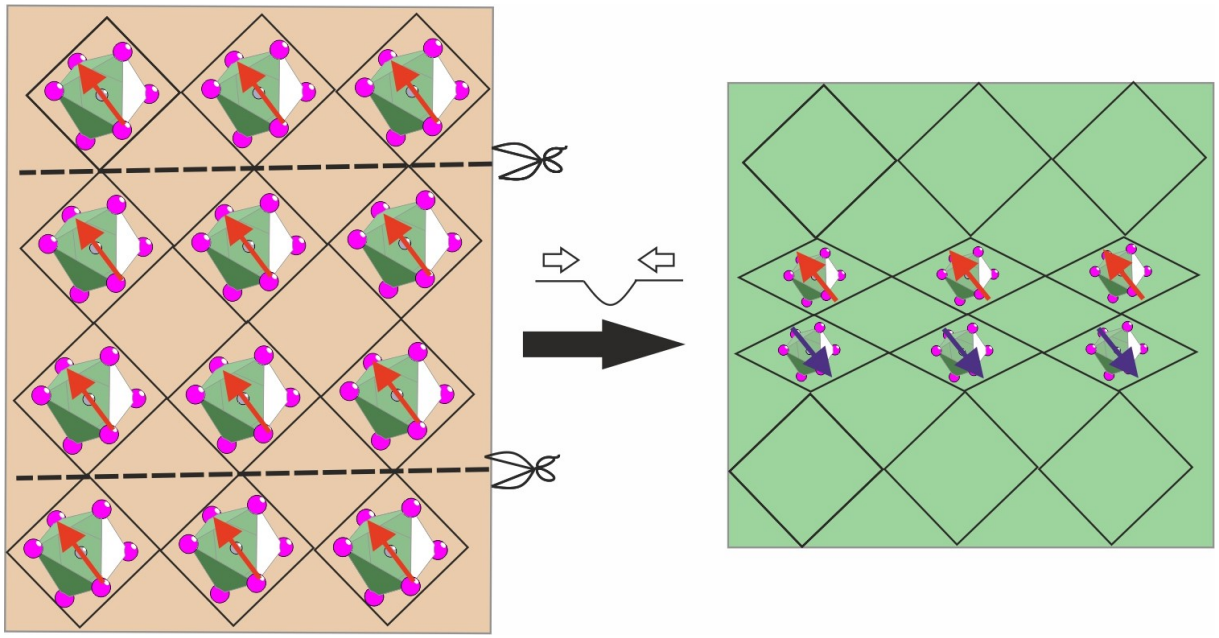

Figure 1: Modification of materials by distorting its crystal structure due to a lattice mismatch with a second material; by confinement of electronic and magnetic properties on a few atomic layers, new material properties are introduced (in this case the formation of a quasi two-dimensional antiferromagnet from an isotropic ferromagnet), simplified by cutting of few layers of a first material and incorporation into another material with different spatial pattern or likewise alignment on a substrate with different crystal structure, reproduced from [1].

2 Theoretical background

The history of metal halides dates back thousands of years, with rock salt (NaCl) as the most prominent candidate. Nowadays, a multitude of halide structures feed the curiosity of physicists and chemists to priorly predict- or subsequently explain experimental investigated phenomena by theoretical simulations and calculations. To limit the vast amount of structures and to highlight the subject of this work, the following chapters are mainly focused on the synthesis (see chapter 2.1), structural aspects & applications (see chapter 2.2, page 6) and vapor transports (see chapter 2.3, page 14) of binary halides with composition MX_3 (M = transition metal; X = halide), more precisely on MCl_3 (M = Ru, Mo, Ti and Cr), as well as CrX_3 (X = Cl, Br and I).

2.1 Synthesis of transition metal trihalides MX_3

2.1.1 Synthesis of $RuCl_3$ and CrX_3 by reaction of the pure elements

Considering plenty of transition metals, a myriad of transition metal halides MX_3 occur with each compound exhibiting different fascinating chemical and physical properties. The preparation of TMTHs is achieved via several approaches and well-known in literature. However, due to their volatility, halogens X (X = Cl, Br, I) are suitable reagents by utilizing them simply as pure elements in the desired stoichiometric composition (M:$X \approx 1$:3 for MX_3 compounds). Nevertheless, the synthesis approach has to be carefully considered depending on the respective halogen, since chlorine is gaseous, while bromine appears in a mainly liquid phase and iodine is solid at room temperature. The synthesis approaches differ from each other, whether chlorine is added as a flowing gas (open system) or related to fixed introduced amount (e.g. closed system).

$RuCl_3$ was prepared 1845 for the first time by *Claus* by direct reaction of ruthenium powder and chlorine gas, highly likely in an open system.[8] Referring to [9] *Wang* et al. synthesized α-$RuCl_3$ by pure ruthenium powder and a flowing gas stream of Cl_2 mixed with CO at 1073 K (800 °C).[10] *Fletcher* et al. were the first that reported on the reaction of the elements (Ru and Cl_2) in closed siliceous vessels at temperature above 873 K (600 °C).[11] Additionally, they recognized that a temperature above 723 K (450 °C) is important to produce mainly α-$RuCl_3$ and to avoid contaminations, for instance Ru_2OCl_6, $RuOCl_2$, unreacted ruthenium powder, or β-$RuCl_3$.[11,12] Recently, *Roslova* et al., as well as *Wellm* et al, described the preparation of α-$RuCl_3$ crystals and even mixed $Ru_{1-x}Cr_xCl_3$ ($0 \leq x \leq 1$) solid solutions from the pure elements in a sealed system under the usage of chlorine encapsulated in small glass capillaries.[13,14]

Morosin and *Carrivaburu* et al. presented the preparation of $CrCl_3$ by a reaction of chromium powder and a flowing chlorine gas stream at 1273 K (1000 °C) [15], respectively at 1223 K (950 °C).[16] Analogously, the synthesis of the bromides (MBr_3) is achieved by brominating the pure metal powder. *Cotton* et al. showed the synthesis of $RuBr_3$ from ruthenium powder and bromine at 723 K (450 °C) at higher pressures (20 bar).[17] *Tsubokawa* and *Gossard* et al. displayed the synthesis of chromium tribromide ($CrBr_3$) single crystals by reaction of the elements at 1023 K (750 °C) [18–20], or 1073 K (800 °C).[21] *Hansen* et al. prepared $CrBr_3$ by an analogous approach at 1073 K (800 °C), but mixed elemental Br_2 with helium to slow down the initial reaction.[22,23] *Cobb* et al. described the growth of larger chromium tribromide single crystals by varying the temperature in the reaction container loaded with chromium powder, from 1023 K (750 °C) on the one side to 873 K (600 °C) on the other side, with an additional gaseous stream of bromine and argon.[24] Later, chromium tribromide was prepared usually similar to *Tsubokawa´*s approach.[25,26] In 1994 *Nocker* and *Gruehn* established the synthesis of $CrBr_3$ by direct reaction of the elements in a chemical vapor transport approach (1023 K → 923 K).[27] Recently, *Richter* et al. produced $CrBr_3$ by reaction of the pure elements in evacuated quartz tubes analogously to *Nocker* and *Gruehn*.[28]

Especially the synthesis of the iodides MI_3 is favored by an elemental approach (M + pure iodine), since I_2 is solid at room temperature and can be handled easily. Chromium triiodide (CrI_3) was prepared for the first time by *Handy* and *Gregory* from pure chromium powder and iodine at 773 K (500 °C). Additionally, they added a sublimation step at 973 K (700 °C) to remove unreacted elemental chromium.[29] *Hansen* and *Griffel* synthesized CrI_3 by a modified approach of *Handy* to enlarge the produced quantities. They placed glass beads with the chromium powder in the tube and rotated the tube at the initial reaction.[22] *Dillon* and *Olson* sealed the elements (Cr and I_2) in a closed silica ampoule in opposite ends and initially formed CrI_2. Thereby, the temperature at the iodine end were held at 463 K (190 °C), respectively 1123 K (850 °C) at the chromium end, similar to a vapor transport reaction. Subsequently, CrI_3 formed by decreasing the temperature at the chromium end to 723 K (450 °C).[30] Recently the CrI_3 crystal synthesis is commonly related to *Handy´s* approach.[28,31–33] *McGuire* et al. prepared chromium triiodide single crystals by reaction of chromium powder and iodine in the desired molar ratio by application of chemical vapor transport (923 K → 823 K).[34–36] Similarly, *Wang* et al. directly synthesized CrI_3, but at higher temperatures (993 K → 913 K).[37] In 2017 *Huang* et al. reported on the production of large size CrI_3 single crystals by application of a three-zone furnace.[38–42]

2.1.2 Synthesis of $MoCl_3$, $TiCl_3$ and related compounds by reduction of precursors

$MoCl_3$ is commonly prepared by reduction of $MoCl_5$ with hydrogen [9,43], or instead with pure molybdenum powder at around 773 K (500 °C) [44–46], or $SnCl_2$ at 573 K (300 °C) as reducing agent under pure nitrogen atmosphere.[47] Moreover, $MoCl_3$ was synthesized by *Drobot* and *Sapranova* by a reaction of $MoCl_5$ with red phosphorus at 493 K (220 °C) in an evacuated ampoule, yielding in a mixture of $MoCl_3$ and PCl_5 [47], or even with PCl_3 in a CCl_4 solution at 338 K (65 °C).[48]

Schäfer et al. reported on the reduction of $TiCl_4$ with elemental aluminum or titanium at 923 K (650 °C), or even with mercury at room temperature for preparation of $TiCl_3$ powder.[49–51] *Coutinho* et al. described the synthesis of $TiCl_3$ by reduction of $TiCl_4$ with di-n-buthyl ether and diethylaluminum chloride in an iso-octane solution or with triethylaluminum in toluene solution.[52] It is shown, that depending on the applied reaction system, different modifications of $TiCl_3$ (α, β, γ or δ) were obtained, which was confirmed later by *Costa*.[53] *Lewis* et al. reported on the preparation of $TiCl_3$ by reduction of $TiCl_4$ with hydrogen at 1173 K (900 °C).[54] Likewise, *Higuchi* et al. used commercial $TiCl_3$, but noted that this batch was prepared by electrolysis of $TiCl_4$ with elemental titanium.[55] Similarly, *Miyaoka* et al. described α-$TiCl_3$ was synthesized by reduction of $TiCl_4$ vapor in the plasma arc generated by several titanium electrodes.[56],[54] *Natta* et al. stated that high reduction temperatures mainly lead to the alpha modification (α-$TiCl_3$), while lower temperatures lead to primarily β-$TiCl_3$ by application of any reducing agents, that was confirmed by further investigation.[57–60] In contrast to α- and β-$TiCl_3$, γ-$TiCl_3$ was prepared by reduction of $TiCl_4$ with organometallic compounds at 448 K (175 °C).[57]

Since it is challenging to weigh out bromine exactly, especially while preparing reactions in closed systems (for instance in a sealed ampoule), bromine precursors are widely applied. *Schäfer* et al. prepared the α- and β- modification of $TiBr_3$ by reaction of pure titanium and $TiBr_4$ or Al_2Br_6.[61] Moreover, $CrBr_3$ was synthesized by *Abramchuck* et al. by reaction of pure chromium powder with $TeBr_4$.[32]

Industrially, $RuCl_3$ is fabricated by dissolving RuO_4 in hydrochloric acid (HCl) to a mixture of ruthenium oxochloro- and hydroxochloro species that is reduced to $RuCl_3$ subsequently.[17,62] Similar to $RuCl_3$, RuI_3 was prepared by dissolving RuO_4 in an aqueous solution of HI.[17] By reduction of RuF_5 with iodine, RuF_3 can be obtained.[17] *Knox* et al. described the synthesis of higher, anhydrous chlorides (MX_n; $n \geq 4$) by reaction of the respective metal oxide and CCl_4 as chlorine precursor at around 400 °C in sealed glass tubes.[63]

2.1.3 Direct preparation of MX_3 monolayers and nanotubes

There are some interesting approaches discussed in literature for the direct formation of MX_3 single layers. *Sandoval* et al. reported on the formation of monolayers of CeI_3, $CeCl_3$, $TbCl_3$ and ZnI_2 by template-assisted growth utilizing multi-walled carbon nanotubes (CNT) as confinement containers. Thus, not only sheets, but mainly metal halide nanotubes were formed, especially by increasing the reaction temperature.[64] Similarly, *Moaied* et al. discussed an anomalous optical dispersion in CrI_3 nanotubes.[65] *Wang* et al. reported on the synthesis of monolayer suspensions of α-$RuCl_3$, by reaction with $LiBH_4$ under formation of Li_xRuCl_3 ($x \approx 0{,}2$), for the formation of nanocomposites by intercalation of polymers like polyaniline.[10] Likewise, *Preda* et al. intercalated non-transition metal trihalide BiI_3 with pyridine.[66]

2.2 Structural aspects and applications of MX_3 structures

2.2.1 General remarks on layered MX_3 structures

In the last decade several layered materials were put into the spotlight of structural two dimensionality. In addition many investigations were revisited according to the arising interest in materials with a honeycomb structure, similar to recently observed graphene. As previously described, TMTHs are as well layered, two-dimensional (2D) structures[1] that became initially only minor attention as 2D honeycomb compounds, probably due to the strong sensitivity to ambient conditions of some of them. The diversity of composition, structures and properties of TMTHs is very complex. The binding between *M* and *X* can be described as rather ionic. Typically, the halide anions (*X*) are large in both size and electronegativity, while the cations (*M*) are smaller. TMTHs were investigated with innumerable studies for review of several ligand field and crystal field theories.[67,68] Transition metal trihalides MX_3 consist of stacked layers that are only coupled weakly by *van der Waals* forces. Each individual layer consists of a honeycomb pattern, similar to graphene. The honeycombs are formed by an organized occupation of 2/3 of the octahedron vacancies within the closest packing of halogen atoms (either cubic or hexagonal) with respect to the transition metal atoms (see Figure 2).[2]

[1] Two dimensional (2D) materials are compounds with one or several layers stacked upon each other. The atoms of each layer are strongly bonded to their neighboring atoms by *intralayer* covalent forces, while the *interlayer* forces are of *van der Waals* nature and weaker. Each layer has a thickness in the nanoscale or smaller, while the lateral dimensions are generally larger, mostly in the micro-meter (µm) range. Since there are a variety of 2D materials with several properties, it is not specifically defined at which layer number a 2D material becomes a bulk compound. For instance, with respect to graphene, it is a 2D material up to ten layers.[196]

[2] Within a cubic closest packing (ccp) of halogen atoms and assuming a full occupation with cations the $CdCl_2$ structure type finally results. *Vice versa* assuming a hexagonal closest packing of halogen atoms the CdI_2 structure type is formed (assuming a likewise full occupation of metal ions).

Each metal atom is thus surrounded by six halogen ions, while every halogen ion is angled by two metal ions (coordination number 6:2). Thus the edge-linked octahedral environment is formed. Interestingly, a monolayer is often associated with the *c*-axis of an individual unit cell. In fact, two individual layers are part of one unit cell related to a *c*-axis of about 6 Å. Thus, a single layer has indeed a thickness of about 3 Å (see Figure 2).

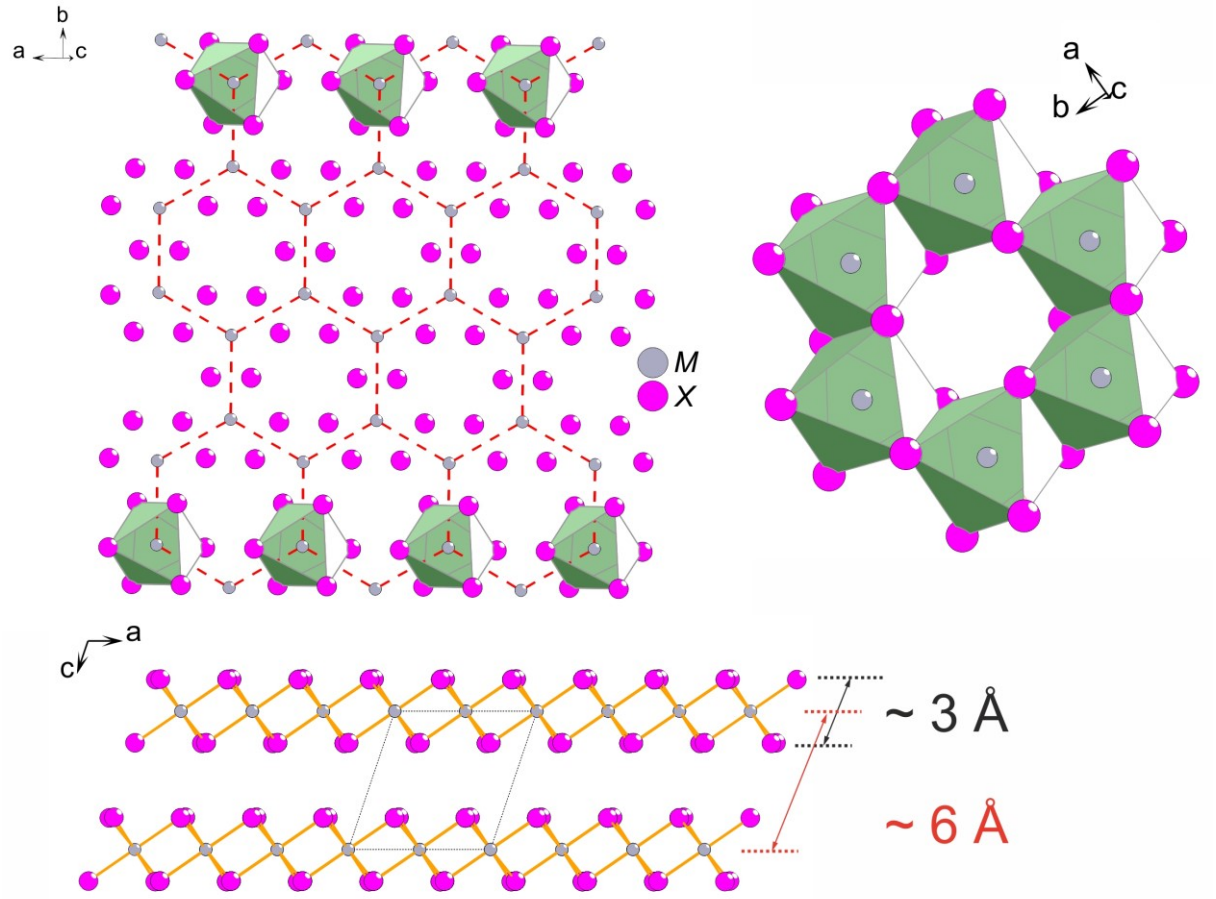

Figure 2: **(top left):** Structure of an individual MX_3 layer (*M* = Ru, Mo, Cr, Ti; *X* = Cl, Br, I), the honeycomb nature is implied by the red dashed line, **(top right):** visualization of an MX_6 edge-sharing octahedra, **(bottom):** two individual layers stacked upon each other, one MX_3 layer has a thickness of about 3 Å, the *c*-axis of the unit cell is associated with two MX_3 layers and an extent of about 6 Å.

2.2.2 Polytypism and polymorphism of layered MX_3 structures

The nature of TMTHs is heavily shaped by *polytypism*. Polytypism means that unless the honeycomb layers are isostructural within each other, independent from an either cubic or hexagonal close packing of halogen atoms, significant structural differences result of diverse stacking orders. The stacking order of halogen atoms can be realized in either AB- (with respect to a hexagonal close packing of halogen ions) or ABC sequences (with respect to a cubic close packing of halogen ions, see Figure 3). These stacking sequences are associated with the appearance of either a trigonal BiI_3 structure type (with respect to an AB stacking order) or a monoclinic $AlCl_3$ structure type (or likewise HT-$CrCl_3$ type with respect to an ABC stacking order). The stacking order was also reported to be temperature dependent.[69] Further stacking orders can be driven by the individual stacking of "voids" within the hexagonal layers, which is associated with the appearance of further trigonal symmetries. Thus, the occurrence of different crystallographic types are only a result of the stacking order of halogen atoms (see Figure 3). As the cleavage energies of individual MX_3 layers are commonly low, especially non-periodic shifts of periodic stacking sequences are easy to realize, which is associated with the prompt introduction of stacking faults by application of conventional exfoliation approaches.

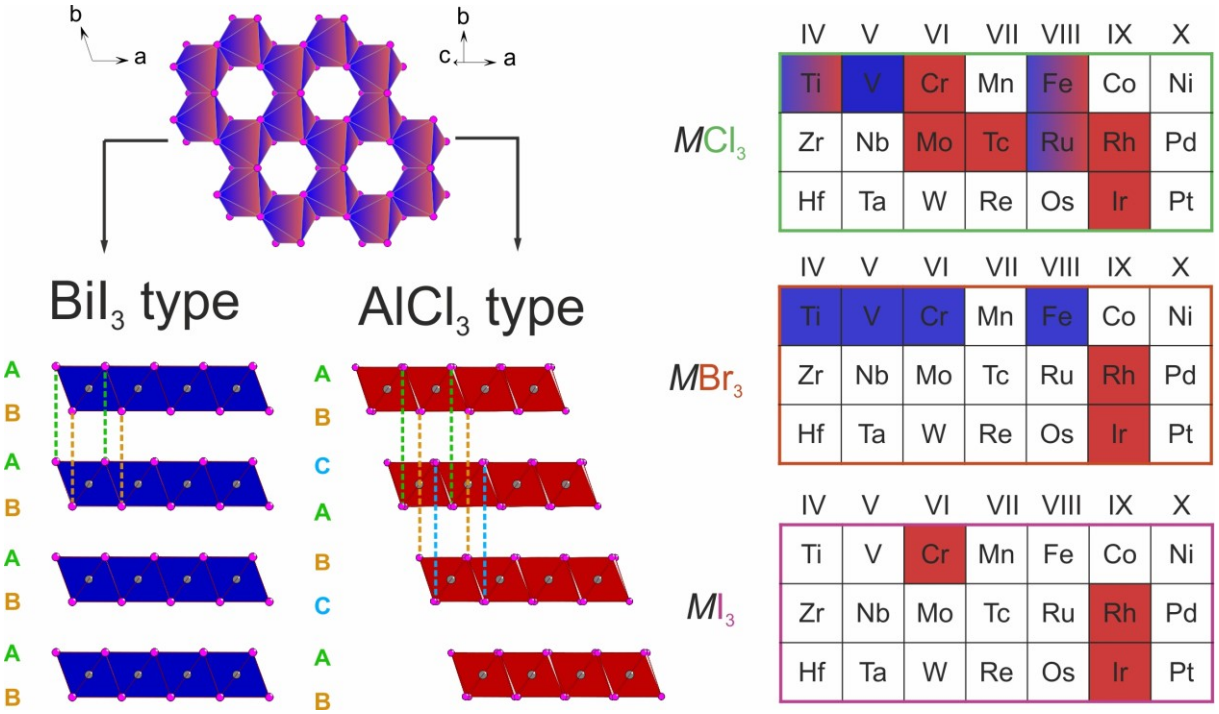

Figure 3: Preferred stacking orders of MX_3 compounds related to either the BiI_3- or $AlCl_3$ structure type according to reported literature data [70], the right part of the figure concerning the periodic tables was reproduced from [70].

Beyond polytypism, MX_3 compounds can adopt several *polymorphic* structure types. Meaning, the compounds structure not only differ in the stacking order of layers, but in the conjunction of individual MX_6 octahedra. Besides layered arrangements (see Figure 4, page 10), transition metal chlorides, bromides and iodides especially exhibit chain structures.[71] Thus, the observed crystals appear as thin needles. These compounds crystallize by adopting the TiI_3 (or ZrI_3) structure type with space group $P6_3/mcm$. In the hexagonal unit cell with two formula units the cations, in contrast to layered structures, occupy only 1/3 of the octahedron vacancies. With a hexagonal close packing of anions the resulting MX_6 octahedra are linked by opposing triangle planes. Due to symmetry reasons, the metal cations prefer a linear alignment with two equidistant neighbors. Hence, the *van der Waals* bonded chain nature of structures MX_3 result (see Figure 4, page 10, using the example of β-$RuCl_3$).[72]

The observed structure type is determined by the coordination geometry of the halogen and the *d* electron configuration of the transition metal. While the polarizability increases with heavier halides (e.g. I_2), the *M-X-M* angle decreases due to steric effects. The compositions of metal halides are controlled by the stable oxidation states of the metal. Characteristically, these compounds have extremely narrow ranges of homogeneity (but non-zero), since large variations of the chemical potential goes along with negligible changes in the chemical composition. Thus, from a thermodynamic point of view these compounds can be described as "line" compounds.[73] However, polymorphic variations occur due to variations in the *M*/*X* ratio.

With respect to the Mo/Cl phase diagram [74], α-$MoCl_3$, which exhibits Mo-Mo dimers at room temperature [45], (present at 25 at-% Mo and 75 at-% Cl) coexists with polymorphic β-$MoCl_3$ (space group $C2/c$) in the range between 75 and 77 at-% chlorine. In fact, α-$MoCl_3$ exits in the phase width of 2.98-3.00 Cl/Mo. In the range between 77 and 80 at-% chlorine β-$MoCl_3$ occurs with discrete composition up to 550 K (277 °C) that appear as black-brown fibrous like crystals. At higher temperatures β-$MoCl_3$ disproportionates irreversibly into α-$MoCl_3$(s) and $MoCl_4$(g). Thus, β-$MoCl_3$ represents a "chlorine-rich" molybdenum trichloride ($MoCl_{3.08}$).[75] Similar to $MoCl_3$, $TiCl_3$ exhibits a "low-temperature" β-polymorph (β-$TiCl_3$) with chain structure, dimerized titanium atoms and brown color (space group $P6_3/mcm$).[57,76,77] The octahedra of β-$TiCl_3$ are plane-linked but similar temperature sensitive. The transformation of β- to α-$TiCl_3$ occurs irreversible (and thus monotropic) at 217 K (-56 °C).[76,77] Anyhow, $TiCl_3$ initially seem to be a special case, since in literature even additional structure types are claimed (γ-$TiCl_3$ and δ-$TiCl_3$). In fact, this "modifications" are just other *polytypes* of α-$TiCl_3$ with either trigonal stacking ($P3_112$, γ-$TiCl_3$) or mixed stacking sequences (δ-$TiCl_3$).[57]

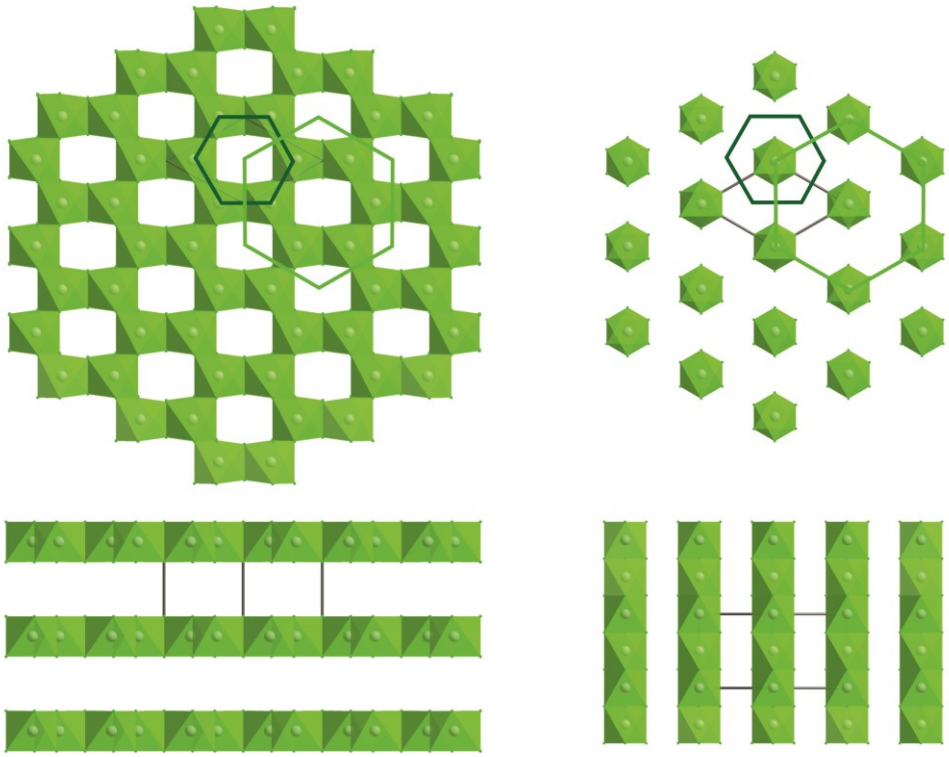

Figure 4: Layered structure of α-$RuCl_3$ **(left)** and chain structure of β-$RuCl_3$ **(right)** with both *ab*-plane (honeycomb vs. isolated octahedra) on the top and the stacking along *c* (with filled and empty layers vs. octahedral chains/strands) at the bottom; the beta polymorph could be assumed as an inverse alpha form: the octahedral chains now occupy the positions of the empty octahedral voids within the honeycomb layer; β-$RuCl_3$ irreversibly transforms into the α polymorph (α-$RuCl_3$) applying temperatures higher than 723 K (450 °C).[17]

2.2.3 Catalytic utilization of MX_3 structures

Transition metal trihalides are widely used in industry as heterogeneous catalysts. $RuCl_3$ is used largely in organic chemistry as oxidation catalyst of ethylene, or as a precursor for a variety of organo ruthenium complexes. For instance, tertiary phosphine complexes are utilized as catalysts for hydrogenation of alkenes.[17,78,79] Furthermore, $Ru(CO)_3(PPh_3)_2$ is applied as hydroformylation catalyst for the conversion of ethylene to propionaldehyde.[78] Moreover, $RuCl_3$ is implemented as an electroplating agent in processes of catalytic conversion of acetylene to acetaldehyde, of propylene to acetone, or for the polymerization of olefins and acetylenes.[78] *Xia* et al. described a significant improvement in hydrogen storage properties of a $LiBH_4$-MgH_2 composite by addition of anhydrous $MoCl_3$.[80] Moreover, *Mannei* et al. presented studies according to the introduction of $MoCl_3$ into zeolites as catalysts for the ammoxidation (process for the preparation of nitriles utilizing ammonia and oxygen) of C_2 hydrocarbons prepared by solid state ion exchange.[81] Furthermore, *Song* et al. described the application of $MoCl_3$, respectively $MoCl_3$ accompanied with LiCl and KCl salts, as catalyst for the hydrogenation of anthracene with improved selectivity.[82]

However, especially $TiCl_3$ is one of the most important Ziegler-Natta catalysts for the synthesis of stereospecific olefins (mainly polyethylene and polypropylene).[83] Titanium(III) chloride is used either unsupported (first generation of Ziegler-Natta catalyst), or supported on other materials together (newer generation) with mainly aluminum alkyls.[53,58] *Coutinho* et al. described, that the properties of the catalysts are determined by the defects present in their structures.[52] Hence, the properties of the products obtained by the polymerization reaction are strictly depending on the modification of $TiCl_3$ (α-, β-, γ- or δ- $TiCl_3$) applied.[52] In fact, the first catalyst invented by *Ziegler* was fibrillary β-$TiCl_3$, whereas later industrial implemented $TiCl_3$ by *Natta* was α-, γ- and δ- $TiCl_3$.[84] In organic synthesis, $TiCl_3$ is also utilized as reagent for reductive coupling reactions.[85] Similar to titanium trichloride, $CrCl_3$ is used in organic synthesis, for instance as a catalyst for the continuous conversion of xylose to furfural.[86] Moreover, chromium trichloride acts as a precursor for chromium-based organic complexes as catalysts for the oligomerization of ethylene.[87,88] *Sun* et al. claimed that the application of $CrCl_3$ based complexes give rise to ultra-high molecular weight polyethylene.[88] *Jouini* et al. described the implementation of $CrCl_3$ as precursor for chromium/zeolithe catalysts (Cr-ZSM-5) for selective reductions of NO with NH_3.[89] All examined pathways of MX_3 catalysts above are mainly focused on the implementation of bulk crystals. Recently, *Tao* et al. described the application of two-dimensional nanosheets as catalysts for electrocatalysis in energy generation and conversion, but gave no hints for the usage of MX_3 structures.[90]

2.2.4 Magnetic anisotropy in MX_3 layers and their relation to the Kitaev model

The basis of magnetism of MX_3 compounds is the existence of an electron angular momentum (orbital motion and spin) and consequent partially filled *d* orbitals. In MX_3 systems the metal cations are surrounded by the halogen anions in octahedral geometry. Hence the five *d* orbitals split into three t_{2g} levels at lower energy (d_{xy}, d_{xz}, d_z) and two e_g levels ($d_{x^2-y^2}$, d_{z^2}) at higher energy which are occupied related to *Hund´*s rules.[70] The magnetic anisotropy describes the magnetic properties of structures in dependence of the orientation of the applied magnetic field.[204] The magnetocrystalline anisotropy, originating mainly from spin orbit coupling (SOC) of *X* atoms and thus important for MX_3 compounds, couples the preferential ordering of spins (magnetic moments, e.g. Cr^{3+}) along specific crystallographic orientations as function of orientation of the external field (decreases from I to Br to Cl due to SOC effects).[200,204] The in-plane anisotropic magnetic interactions (*M-M*) in strongly correlated MX_3 structures are mediated by superexchange interactions via shared coordinating halogen anions (*M-X-M*).[203]

If the *M*-*X*-*M* angle is near 90° (as it is the case for MX_3 compounds) the superexchange between *M* and *X* is rather of ferromagnetic (↑↑) type (if 180° it favors antiferromagnetic (↑↓) alignment).[70] Due to relative large distances between the metal atoms direct *M*-*M* exchange interactions tend to be relatively weak. If nevertheless *M*-*M* bonds exist there are hints that a preferential dimerization of metal atoms lead to a rather diamagnetic behavior of compounds, for instance in case of $MoCl_3$.[70] The trihalides of chromium (CrX_3, *X* = Cl, Br, I) are very interesting candidates related to future ultrathin sensors since their magnetic properties are very anisotropic (and thus allow long-range magnetic ordering in 2D) and additionally layer dependent. [93] *Hansen* started to study the paramagnetic susceptibilities and *Curie* temperatures of anhydrous chromium halides CrX_3.[22,91] He showed that the susceptibilities follow the *Curie-Weiss* law over a remarkable temperature range with spin-only values of 3.87 and a predominant ferromagnetic coupling (increases from $CrCl_3$ to CrI_3). In fact among MX_3 structures, the CrX_3 family is the only class that exhibit three dimensional ferromagnetic structures at lower temperatures which is also sustained in a single layer, experimentally confirmed by *Huang* et al. using the example of CrI_3.[38,70] Likewise, *Zhang* et al. reported on intrinsic ferromagnetism in monolayer $CrBr_3$.[92] In CrX_3 structures chromium is in the $3d^3$ electronic configuration with $S = 3/2$.[22] However the predominant orientation of spins is different within the CrX_3 family. CrI_3 and $CrBr_3$ exhibit out-of-plane chromium spins (alignment along the crystallographic *c* axis). In contrast $CrCl_3$ prefers an in-plane spin alignment (parallel to *a*/*b*).[69] Very importantly, these compounds are paramagnets that can exhibit anisotropic ferromagnetic or antiferromagnetic properties at lower temperatures and low external magnetic fields (see Figure 5). Recently, *Sivadas* et al. showed that also the stacking order of CrX_3 sheets determines the magnetic properties due to a competition between ferromagnetic and antiferromagnetic interlayer superexchange interactions using the example of CrI_3.[93] Thus, the interlayer exchange can be switched from ferromagnetic to antiferromagnetic by changing the stacking order.[93] This makes the CrX_3 structures very interesting for e.g. future spintronic applications.

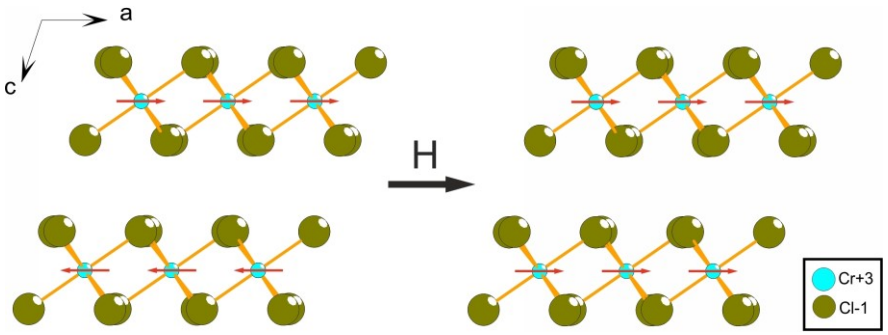

Figure 5: Sketch of magnetic moments of $CrCl_3$ (red arrows) aligned in the *a*/*b*-plane; *without* an external magnetic field a single layer of $CrCl_3$ is ferromagnetic, while two $CrCl_3$ layers couple antiferromagnetic **(left)** and in contrast *with* an external magnetic field $\mu_0 H \geq 0.1$ T **(right)**; by application of a small field the spins of the second layer polarize (until reaching the saturation magnetization) and thus induce an overall ferromagnetic state.

With the description of the *Kitaev* model MX_3 layers gained also the recent attention of quantum physics.[94] The *Kitaev* model allows the solution of a strongly correlated quantum mechanical problem under consideration of a special type of quasi particles, so called *Majorana* fermions. These *Majorana* fermions are formed due to fractionalization of spins. The model describes the interaction of spins with ½ degrees of freedom on a two-dimensional honeycomb lattice and is characterized by a "spin liquid" ground state. The structural honeycombs of MX_3 compounds serve as excellent model systems (see Figure 6a). A spin liquid is distinguished by the absence of any type of classical magnetic order, even down to a temperature of absolute zero, and requires strongly frustrated spin properties. The magnetic moments of these systems are thus characterized by the non-existence of any preferred orientation and hence symmetry breaking due to enlarged quantum fluctuations.[95] The frustration in MX_3 honeycomb systems arises from anisotropic exchange interactions, for instance the compass type interaction (see Figure 6b). The nearest-neighbor exchange interactions J^{α} of ferromagnetically coupled spins are of *Ising*-like type between sites *i* and *j*. The main characteristic of the *Kitaev* model is that the individual spin components $\alpha = x,y,z$ are coupled by an exchange that is depending on the anisotropy and bond direction (see Figure 6c). Since the model is exactly solvable for MX_3 structures it consequently prognosticates the existence of exotic excitations like *Majorana* fermions in these systems under specific circumstances. These quasiparticles, that are likewise their own anti-particles, are predicted to contribute to future topological quantum computation applications.[95] However, the search for signatures of these excitations is still ongoing. Initially A_2IrO_3 (A = Na, Li) compounds were investigated.[96] In 2014 *Plumb* et al. proposed the *Mott* insulator α-$RuCl_3$ as outstanding model system for studying *Kitaev* physics due to it substantial contributions of spin-orbit coupling and strong electron-electron correlating nature.[97] From that point on many efforts were undertaken to observe signatures of these exotic excitations in $RuCl_3$. However, the investigation of interesting physical phenomena require high crystalline solids, which may be introduced by vapor transport techniques.[97]

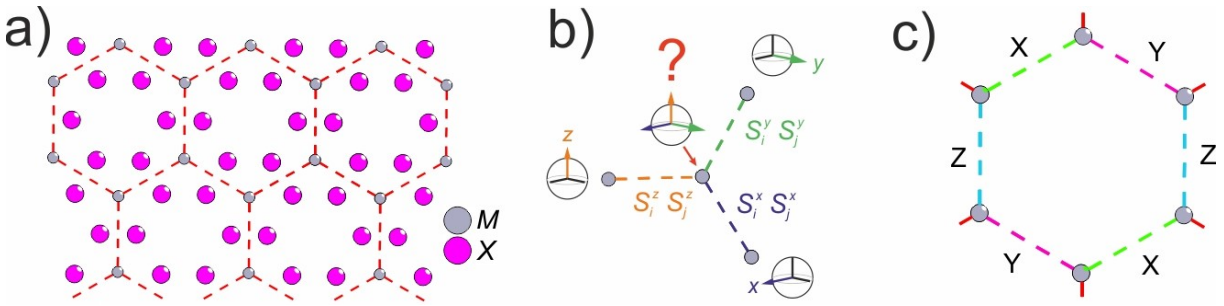

Figure 6: (a) Excerpt of a MX_3 honeycomb structure, **(b)** coupling of M spins ($S_{i/j}$) with a ferromagnetic *Ising* type interaction in *x,y,z*-direction with its neighbors, the central spin cannot be parallel to the *x,y,z*-axis simultaneously, thus it is frustrated due to its exchange interaction, **(c)** the basic of the *Kitaev* model: direction-dependence of exchange interactions, the figures b) and c) are reproduced from [95].

2.3 Vapor transports of transition metal halides

2.3.1 Chemical vapor transport and the purpose of halogens X_2 or halides M_nX_m

Chemical vapor transport (CVT) refer to a wide group of chemical reactions with a main similarity: a *condensed phase* (e.g. a solid) vaporizes in presence of a gaseous reactant (the *transport agent*) and recrystallizes on another side in form of well-defined single crystals (see Figure 7). The requirement for crystallization are altered thermodynamic conditions, mostly realized by application of a temperature gradient in a two-zone furnace. In contrast to chemical vapor deposition (CVD), CVT processes are most often related to closed systems, typically a silica glass (quartz) ampoule.

In 1925 *van Arkel* and *de Boer* became the first scientists that used specific CVT reactions to purify metals.[98] From 1950 on, *Schäfer* investigated and described vapor transport reactions systematically of many chemical families with outstanding scope.[99] CVT is nowadays used as a prominent tool in preparative work for the synthesis pure crystalline phases and purification processes.[100] Additionally, vapor transport techniques may be exhibited to analyze unknown gas-species, for specification of thermal data and determination of limiting solubility and phase ranges, or to formulate phase diagrams of solid state systems.[101] An extensive description of CVT processes by *Binnewies* et al. describes the vapor transport of different chemical families and its theoretical background.[100]

However, the utilization of this chemical approach is not limited to research, but achieved broad application in industrial processes also, for instance related to the *Mond-Langer*-process for production of high quality nickel.[12,100] Halogens X_2, metal halides M_nX_m and their complexes are very common in CVT processes.[101] More precisely, chlorine (Cl_2), bromine (Br_2) and iodine (I_2) are either utilized as pure elements or as part of compounds (halides), mainly as transport additions. In contrast to this, fluorine (F_2) is negligible as transport addition, due to an extreme equilibrium position for the formation of the most fluorides MF_x. Moreover, fluorine is problematic, because its reacts with the ampoule material (silica glass).[102]

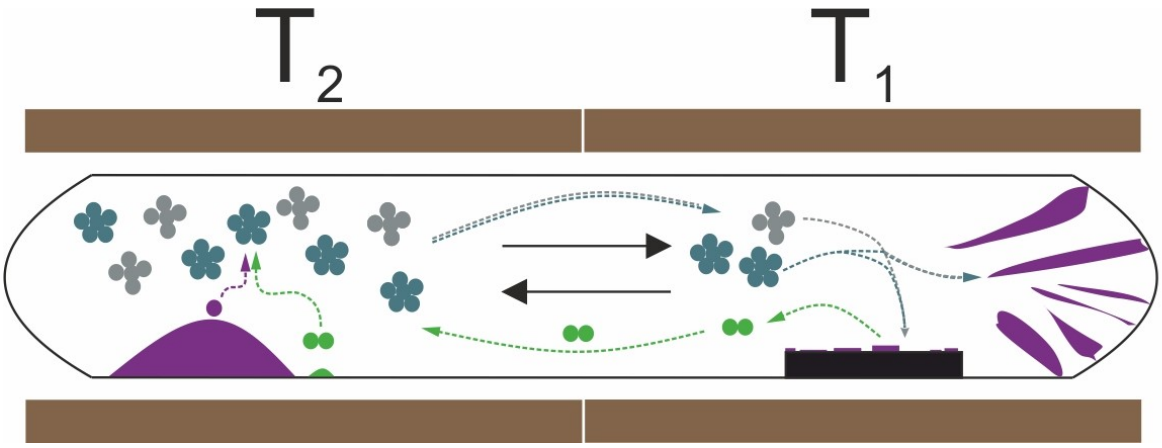

Figure 7: Principle of chemical vapor transport (CVT) for an endothermic vapor transport (T_2 or $T_{source} \rightarrow T_1$ or T_{sink}) in a two-zone furnace; by application of a temperature gradient (ΔT) different gas species are forming, proceeding from the starting materials (T_2, purple) and a transport agent (green), that are moving mainly by means of diffusion (and convection) processes to the sink (T_1), the gas-species condense at T_1 under formation of well-defined crystals at the ampoule wall and/or on an additional introduced substrate (black); finally the transport agent is released at T_1 and can interfere again at T_2 temperature.

In general, pure halogens (X_2) or their halides (M_nX_m) may overtake several assignments in vapor transport processes (see Table 1). An extensive review on the purpose of halogens and halides in vapor transport processes is given by *Oppermann*.[101] The most famous assignment of halogens is the transport of metals, such as the *Van Arkel de Boer* process, exhausted over years in commercial halogen lamps. The transport of W with elemental iodine lead to formation of several gaseous species (WX_6, WO_2X_2, WOX_4 and WX_2) that are responsible for the regenerative effect on the tungsten filaments.[101]

Table 1: Solid-gas reactions (via CVT) for the formation of MX_3 structures [100].

Heterogeneous gas phase equilibria of X_2 (X = Cl, Br, I) or M_nX_m	
(1) Halogens as transport agent for the formation of higher halides	**(2) Synproportionation reactions**
$RuCl_3(s) + {}^1/_2\ Cl_2(g) \rightleftharpoons RuCl_4(g)$	$MoCl_3(s) + MoCl_5(g) \rightleftharpoons MoCl_4(g)$
(3) Formation of gaseous complexes	**(4) Halogen transfer reactions**
$TiCl_3(s) + {}^1/_2\ Al_2Cl_6(g) \rightleftharpoons AlTiCl_6(g)$	$4\ AlF_3(s) + 3\ SiCl_4(g) \rightleftharpoons 4\ AlCl_3(g) + 3\ SiF_4(g)$
(5) Formation of interhalogen compounds	
$5\ MgF_2(s) + 6\ I_2(g) \rightleftharpoons 5\ MgI_2(g) + 2\ IF_5(g)$	

2.3.2 Thermodynamic characteristics of MX_3 and vapor transport without transport addition

Fundamentally, many metal halides MX_n are highly volatile and easy convertible from the solid into the gas phase (sublimation).[100] From this thermodynamic point of view, MX_3 vaporize, e.g. by application of a temperature lower than their decomposition temperature (see Equation 1). Thus, under consideration of sufficient high partial pressures ($p(i) > 10^{-5}$ bar) and transport efficiency (change of partial pressure $\Delta p(i)_{source \rightarrow sink}$) solid MX_3 can be consequently re-deposited by means of altered thermodynamic conditions in vapor transport processes due to ***sublimation*** (see Equation 1 and Figure 8). As a special feature of metal halides (in particular if M = Al, Ga, In, Fe, Sc) gaseous MX_3 molecules tend to form dimer M_2X_6 species or even oligomer molecules (see Equation 2). In homo gas phase complexes dimer M_2X_6 metal atoms are connected via halogen bonds.[100]

By exceeding the decomposition temperature the MX_3 structures decompose in either the respective element M and halogen X_2 (see Equation 4), or a lower halide MX_{3-x} and a minor amount of the respective halogen $x/2\ X_2$ (see Equation 3). As a rule of thumb, the tendency of decomposition with analogue temperature rises from MF_x to MI_x.[100] The released halogen X can function as an immanent transport agent for the system and form a potentially more transport efficient halide MX_4 (see Equation 5). If solid MX_3 does not exhibit a transport efficient partial pressure (gaseous MX_3), the transport of MX_3 can be realized instead with the formation of the higher valence halide MX_4. Hence, vapor transport is realized as ***auto- (or self) transport*** (see Equation 5).[103]

Sublimation:

$$MX_3(s) \rightleftharpoons MX_3(g) \quad (1)$$

Dimerization:

$$2\ MX_3(g) \rightleftharpoons M_2X_6(g) \quad (2)$$

Decomposition:

$$MX_3(s) \rightleftharpoons MX_2(s) + 1/2\ X_2(g) \quad (3)$$

$$MX_3(s) \rightleftharpoons M(s) + 3/2\ X_2(g) \quad (4)$$

Autotransport (self-transport):

$$MX_3(g) + 1/2\ X_2(g) \rightleftharpoons MX_4(g) \quad (5)$$

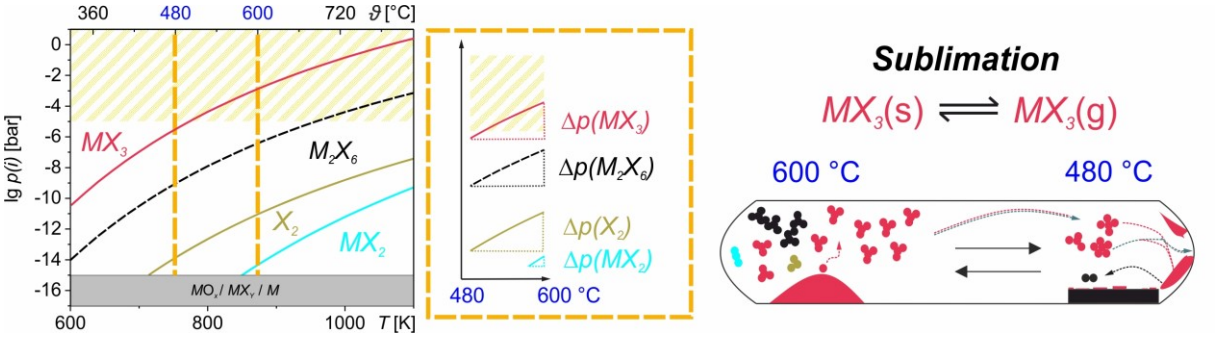

Figure 8: Gas phase of a hypothetical introduced material MX_3 (with amounts of MO_x and M due to potential reaction with fractional amounts of oxygen and decomposition processes) with a high partial pressure of MX_3 (highly volatile) that reaches transport relevant values (see yellow hatched area in the **left part of the figure**) and thus may be suitable for vapor transport by pure sublimation without the need of an additional transport agent; a significant change of partial pressure $\Delta p(MX_3)_{source \rightarrow sink}$ of more than 10^{-5} bar at $T_2 \rightarrow T_1$ (600 → 480 °C, see the orange dashed lines in the left part of the figure) indicates transport efficiency, highlighted by the **middle part of the figure**; the **figure located on the right** typifies a hypothetical vapor transport without any transport agent.

Sublimation and self-transport of MX_3 structures is a common approach used in literature (see references in the appendix, Table A 15 – Table A 17, page 141) because of its facileness for precipitation of high quality MX_3 single crystals without the need to introduce an additional transport agent (see Figure 9, page 18). Especially trihalides (MCl_3, MBr_3 and MI_3) of transition metals of the IUPAC groups five (V) to seven (VII) were prepared single crystalline by application of suitable temperatures (see Figure 9, page 18).

The CrX_3 (X = Cl, Br, I) compounds are showpiece candidates in this manner (see Figure 9, page 18). Depending on the applied temperature the vapor transport of $CrCl_3$ is achieved via sublimation or autotransport, or amount of both of them.[103] *Yu* et al. described the preparation of $CrBr_3$ single crystals from commercial powder ($CrBr_3$) by application of elevated temperatures (1163 K → 1046 K).[104] CrI_3 single crystals were grown by *McGuire* et al. by using instead stoichiometric ratios of elemental Cr and I_2.[34] *Weber* et al. described the preparation of $RuCl_3$ single crystals via sublimation (1023 K → 948 K).[105]

Even likely exotic compounds e.g. TcX_3 (X = Cl, Br, I) were already prepared without an additional transport agent (see Figure 9, page 18).[106] Similarly, the trihaldies of vanadium (VX_3) were synthesized without transport agents by *Oppermann*, *Kong* and *Juza*.[100,103,107]

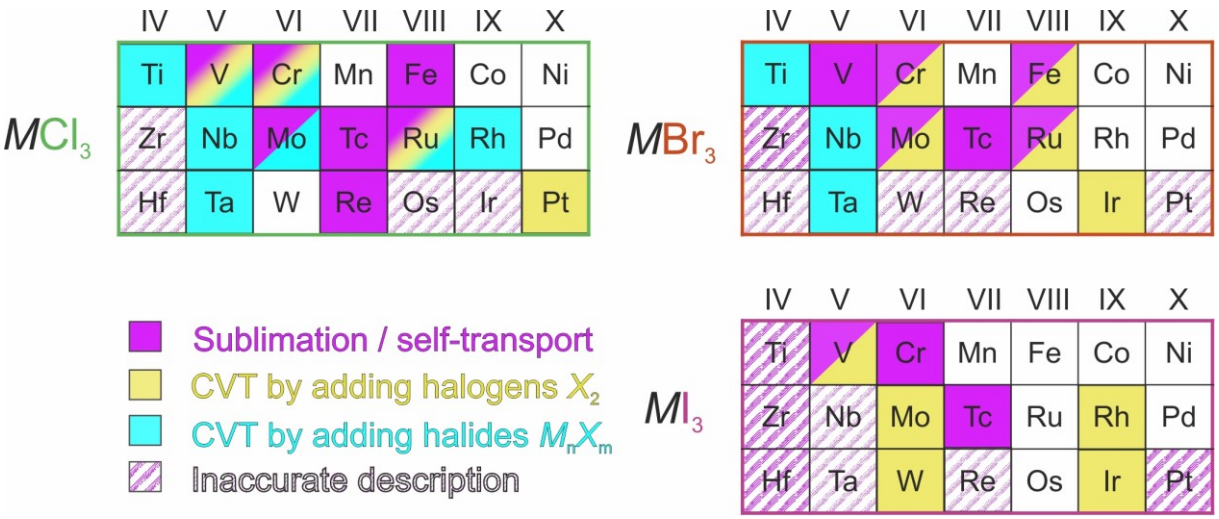

Figure 9: Screening of previously executed vapor transports of MX_3 by either sublimation or auto- (self) transport (marked in purple), CVT by adding the respective halogens X_2 as transport agents (marked in yellow) or CVT by adding halides M_nX_m as transport additions (marked in turquoise); inaccurate descriptions by literature that prevent an assignment to one of the prior categories are shaped in purple; the respective literature can be found in the appendix (see Table A 15 − Table A 17, page 141).

2.3.3 CVT of MX_3 with halogens X_2 or halides M_nX_m as transport additions

A common utilization of halogens X_2 or other halides M_nX_m is the transport of trihalides MX_3. Using transport additions of this kind may be necessary if the partial pressures of the introduced compounds MX_3, or their decomposition products, are too low for efficient vapor transport (see Figure 10). By utilization of ***halogens*** X_2, the formation of transport efficient halides with higher valence (e.g. MX_4) occurs (see Equation 6) due to the oxidizing properties of X_2.

$$MX_3(s) + {}^1/_2\ X_2(g) \rightleftharpoons MX_4(g) \qquad (6)$$

MX_4 compounds are more volatile than MX_3 because of an increasing covalent character of the *M-X* bond. Still, higher halides tend to decompose, more than halides with lower oxidations states of the metal. Hence, sufficient high halogen partial pressure are necessary for efficient formation of MX_4.[100] Elemental iodine is largely solid at room temperature. Because of that, it is often a well suited transport agent if used in excess (according to MX_{3+x}). Although the experimental handling is more difficult with bromine, some reports describe the vapor transport by using excess amounts of Br_2 (see Figure 9). Nevertheless, even MCl_3 structures were prepared previously by utilization of elemental chlorine as transport agent. Common examples are the vapor transport of $CrCl_3$ [108], $RuCl_3$, or VCl_3 with Cl_2, see Figure 9.[100]

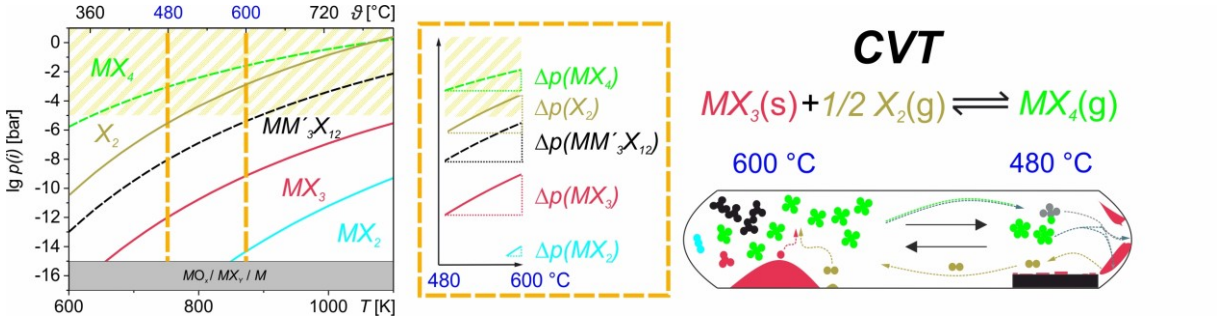

Figure 10: Gas phase of a hypothetical introduced material MX_3 and additional transport agent X_2 (with amounts of MO_x and M due to potential reaction with fractional amounts of oxygen and decomposition processes) with a low partial pressure of MX_3 (low volatile) that do not reach transport relevant values (yellow hatched area in the **left part of the figure**) and thus is not suitable for vapor transport by pure sublimation; the introduction of an additional transport agent becomes necessary and results in the formation of the transport efficient gas species MX_4; a significant change of partial pressure $\Delta p(MX_4)_{source \rightarrow sink}$ of more than 10^{-5} bar at $T_2 \rightarrow T_1$ (600 → 480 °C, see the orange dashed lines in the left part of the figure) indicates transport efficiency, highlighted by the **middle part of the figure**; the **figure located on the right** typifies a vapor transport using a transport agent (X_2).

Analogously, the introduction of ***higher valence halides M_nX_m*** may lead to the formation of more volatile halides with semi-high valence (MX_4) associated with a synproportionation reaction (see Equation 7). In particular MX_3 with M = V, Nb, Ta, Cr, Mo or W permit the coexistence of halides with more than two oxidations states of the respective metal.[100]

$$MX_3(s) + MX_5(g) \rightleftharpoons MX_4(g) \quad (7)$$

A well-known characteristic of transition metal halides is the formation of stable homo- (dimerization) and ***hetero gas phase complexes***, e.g. of MX_3 and M'_2X_6, and consequent formation of MM'_2X_9, MM'_3X_{12} or MM'_4X_{15} in particular with M'= Al, Ga or Fe and X = Cl, Br, I (see Equation 8-10).[100] By formation of gas phase complexes, transport of especially nonvolatile MX_3 compounds becomes possible. With respect to Figure 9 (see page 18) especially MCl_3 and MBr_3 of early transition metals (group IV – VI) were described in literature to be suitable for the formation of higher valence halides M_nX_m or gas phase complexes by adding halides as transport addition. Thus, *Lascelles* et al. reported on the vapor transport of $CrCl_3$ with Al_2Cl_6.[109]

$$MX_3\,(s) + M'_2X_6\,(g) \rightleftharpoons MM'_2X_9\,(g) \quad (8)$$

$$MX_3\,(s) + M'_3X_9\,(g) \rightleftharpoons MM'_3X_{12}\,(g) \quad (9)$$

$$MX_3\,(s) + M'_4X_{12}(g) \rightleftharpoons MM'_4X_{15}\,(g) \quad (10)$$

In a similar manner halogens and halides are suitable for the transport of the respective metal oxide halogenides $M_nO_mX_p$ and metal oxides M_nO_m.[101]

2.3.4 Short-term vapor transport for deposition of MX_3 micro- and nanosheets on substrates

A crucial aim of thin layer synthesis is the subsequent implementation of MX_3 structures in devices or circuits, e.g. used in the semiconductor industry.[5,110] Nevertheless these applications demand high quality materials.[111] Reduced dimensions such as wires or thin sheets with thicknesses in the *nm* range or even *monolayers* (below 1 nm) are usually desired.[112] Exfoliation (mechanical or liquid) of thicker flakes is utilized traditionally to prepare thin layers.[3,5,7] Though, this top-down approach is associated with the introduction of crystals defects, e.g. stacking faults.[113,114] Additionally, this delamination is fairly not reproducible.[115] Materials of lower dimensions are synthesized as well by vapor phase epitaxy and technical challenging bottom-up methods, for instance molecular beam epitaxy (MBE) or atomic layer deposition (ALD) on specific substrates.[5,111] Anyhow, these methods are very system specific and require time consuming device preparations.[116] Independent from the synthesis approach, a vital relevance is the choice of substrate.[111,117] Basically, assuming an epitaxial layered growth, the crystallographic orientation of the synthesized material depends on the predefined orientation by the substrate. The requirements in this case are similar lattice parameters (substrate and deposited material). The advantage in this manner is the preparation of thin layers with single orientation (see Figure 11). In contrast to this, the orientation of the deposited layer may be non-epitaxial (or random orientated) due to a significant tilted structure and/or lattice mismatch between the as-prepared material on top and the substrate (see Figure 11).[111,112] On the first sight this may seem a disadvantage because of variable oriented structures. However, this situation may also induce lattice strains due to shifted layer periodicities because of the mismatch situation and thus consequently altered physical properties.[118–121]

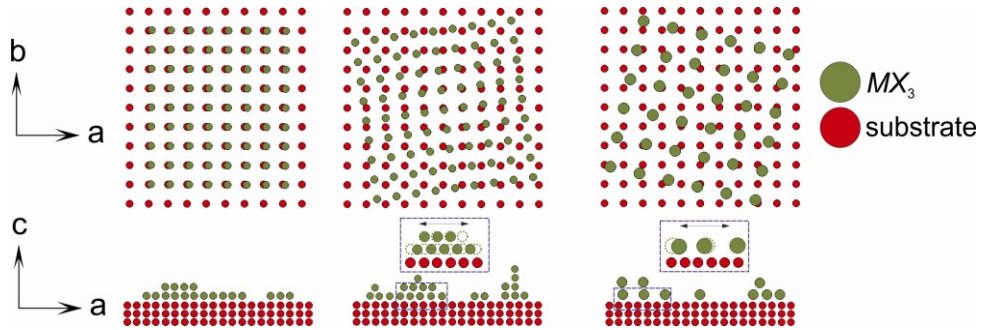

Figure 11: Simplified scheme about the influence of the substrates structure (red color) to the as-prepared MX_3 material on top of it (dark green color); three cases are basically explained: **(1)** on the left part the crystallographic structure of MX_3 fits pretty close to this of the substrate, thus an ideal (epitaxial) growth is expected; **(2)** in the middle the structure of MX_3 is titled, the depositing layers are stretched or clinched due to *van der Waals* interactions between the substrate and MX_3 atoms, though layer growth may proceed; **(3)** similar to the second case the crystals structure of MX_3 on the right part does not correspond to those of the substrate, though isolated atoms may be deposited that form structures with shifted layer periodicities and rather random crystallographic orientation with respect to the orientation of substrate.

Surprisingly, the CVT approach for formation of thin sheets was obviously rather neglected, since vapor transport in sealed ampoules is traditionally known for the preparation of larger (lateral dimensions around some *mm*), phase-pure single crystals.[122] However, CVT also allows thin layer preparations under consideration of suitable parameters.[123] The synthesis of few-layered materials by vapor transport technique is associated with many advantages in comparison to conventional applied exfoliation. For instance, vapor transport permits the growth of high crystalline nanostructures with a well-defined morphology directly on a substrate.[124] A high crystal quality implies that the defect density is rather low. Furthermore vapor growth in closed systems needs no additional precursors or carrier gases, since all required gaseous species are formed by the previously introduced materials.[125] A low transport rate of deposited structures (< 1 mg/h), depending on the applied temperatures, is intended. In due consideration of all parameters, the growth of isolated island-like thin sheets of 2D materials is feasible.[126] There are only a few reports in literature about the preparation of thin nanosheets on substrates by this manner. *Nowka* et al. described the synthesis of single crystalline Bi_2Se_3 nanostructures on Si/SiO_2 substrates (p-type, 300 nm oxide-layer).[115] Despite the application of CVT is challenging for the synthesis of few-layered materials directly on substrates under consideration of various technical limits, process optimization allows the deposition of thin structures (see Figure 12). The most important CVT parameter are the amount of the weighed starting materials (few mg), the transport duration (minutes to hours), the applied temperatures ($T_2 \rightarrow T_1$) and the type of substrate (see Figure 11, page 20). By systematic and stepwise optimization of these parameters, the synthesis of isolated, few-layered sheets on substrates becomes possible (see Figure 12).

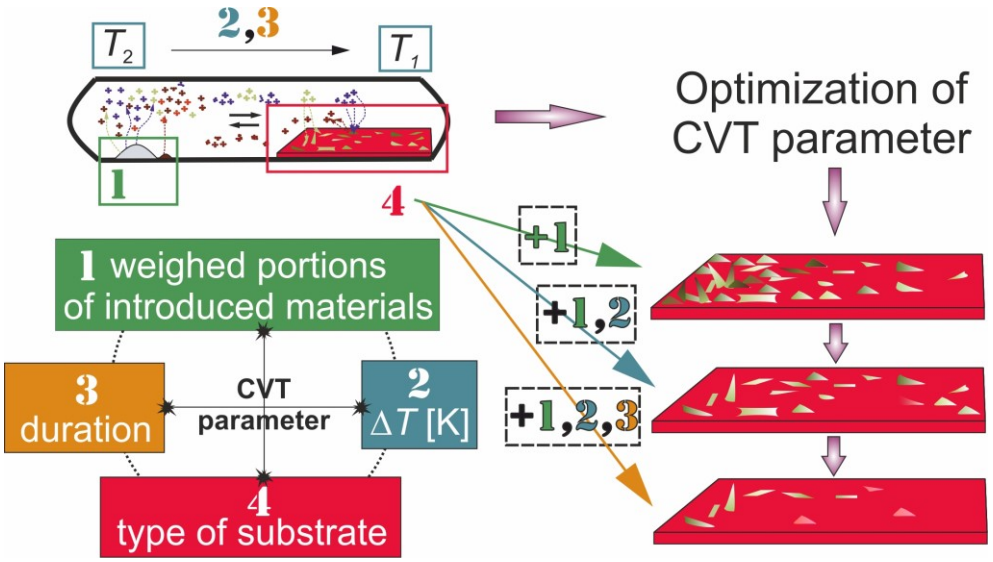

Figure 12: Optimization of CVT parameter for deposition of few-layered MX_3 materials on top of substrates, fundamentally the deposition of thin layers is depending on the crystallographic type of the substrate, by systematic optimization of parameters an incremental improvement is achieved for production of isolated thin MX_3 sheets.

3 Materials and Methods

3.1 Starting materials and substrates

All utilized starting compounds (see Table 2) were used without any initial purification step. MX_3 bulk crystals were synthesized proceeding from powders in sealed silica glass (quartz) ampoules of ca. 12 cm length and about 1 cm inner diameter (wall thickness: 0.1 cm). For the deposition of the respective thin MX_3 micro-/nanosheets an additional substrate was introduced into the ampoule prior to sealing (see Table 3).

Table 2: Starting materials for CVT experiments for the synthesis of MX_3 structures (bulk and nanosheets).

Starting compounds	Total formula	Purity [%]	Customer
Molybdenum(III)- chloride	$MoCl_3$	99.5	Alfa Aesar
Molybdenum(V)- chloride	$MoCl_5$	99.6	Alfa Aesar
Tellurium(IV)-bromide	$TeBr_4$	99.9	Alfa Aesar
Tellurium(IV)-chloride	$TeCl_4$	99.9	Alfa Aesar
Titanium(III)- chloride	$TiCl_3$	99.999	Merck
Gallium(III)- chloride	$GaCl_3$	99.999	Alfa Aesar
Ruthenium(III)- chloride · 6 H_2O	$RuCl_3$	98.5	Merck
Chromium(III)- chloride (anhydrous)	$CrCl_3$	99.9	Alfa Aesar
Aluminum(III)- chloride	$AlCl_3$	99.99	Alfa Aesar
Mercury(II)- chloride	$HgCl_2$	99.5	Alfa Aesar
Iodine (double resublimed)	I_2	-	Merck
Bromine	Br_2	99.6	Acros Organics
Chromium powder (≈ 100 mesh)	Cr	99	Alfa Aesar

Table 3: Substrates utilized in CVT experiments for the deposition of thin MX_3 structures (micro- and nanosheets).

Substrate material	Total formula	Dimensions [mm³]	Orientation	Customer
Yttrium stabilized zirconia (YSZ)	ZrO_2:Y_2O_3	10 x 10 x 0.5	[100]	CrysTec
Sapphire	Al_2O_3	10 x 10 x 0.5	[0001]	Crystal
Silicon	Si	10 x 10 x 0.5	[100]	Crystal
Silicon/silicondioxide	Si/SiO_2	5 x 3 x 0.1	[100]	Crystal
Silicondioxide	SiO_2	10 x 10 x 0.5	[0001], [10-10]	Crystal
Lanthanum aluminate	$LaAlO_3$	10 x 10 x 0.5	[100]	Kelpin
Lithium fluoride	LiF	10 x 3 x 0.4	[111]	Crystal
Barium fluoride	BaF_2	10 x 10 x 0.5	[100]	Crystal
Strontium titanate	$SrTiO_3$	10 x 10 x 0.5	[100]	Kelpin
Magnesium oxide	MgO	10 x 10 x 1	[100]	Kelpin
Silver	Ag	10 x 10 x 0.5	[100]	Kelpin

It has to be remarked that some of the starting compounds are heavily hygroscopic and oxygen sensitive (e.g. $TiCl_3$ and $GaCl_3$) and thus have to be handled with great care. These compounds including $MoCl_5$, $MoCl_3$, $TeBr_4$, $TeCl_4$, $CrCl_3$, $HgCl_2$ and consequently synthesized $CrBr_3$ and CrI_3 were handled under inert gas atmosphere (Ar) in a glovebox environment.

3.2 Methods

3.2.1 Thermodynamic simulations using TRAGMIN software

To avoid time consuming trial-and-error synthesis approaches, thermodynamic simulations were utilized for clarifications of heterogeneous and homogeneous gas phase equilibria and for a rational synthesis planning of investigated systems. Applying the CalPhaD method using the freeware TRAGMIN (www.tragmin.de) led to a calculation of the occurring gas phase composition and respective partial pressures of individual components in a "one-room" system within a temperature series. For vapor growth processes transport efficient gas species are necessary. Therefore, changes in partial pressures $\Delta p(i)_{source \rightarrow sink} \approx 10^{-4} \ldots 10^{-5}$ bar signalize a potential suitability[3] as efficient gaseous molecules (see Figure 8, page 17).[102] Moreover, the gas phase solubilities of elements and theoretical transport rates (mg/h) of deposited crystals were determined related to CVT processes ($T_2 \rightarrow T_1$).[127]. By calculating the transport efficiency $w(i)$ of gaseous molecules it is possible to determine the transport agent (negative $w(i)$) and transport efficient gas species (positive $w(i)$). The transport agent (negative $w(i)$) is consumed in the source and released in the sink. *Vice versa*, the transport efficient gas species (positive $w(i)$) are evaporated in the source and condensed at the sink (see Figure 17, page 41). The main benefit by application of the software (TRAGMIN) is to comprehend the backgrounds of vapor growth mechanisms and assess optimum growth conditions before starting subsequent experiments. It is possible to deduce the main transport relevant homogeneous and heterogeneous gas phase equilibria. By implementing modeling subsequent to the experiment additional simulation results may reveal that the vapor transport is realized by not only one, but several mechanisms (sublimation and/or auto-/self-transport and/or chemical vapor transport reaction) occurring simultaneously. The comprehensive description of the vapor growth mechanism allows for a specified optimization of applied CVT parameters (see Figure 12, page 21).

[3] There is controversy in literature about if even gaseous molecules with a very low partial pressure (down to 10^{-6} bar) can be transport relevant. For simplification this thesis is focused on 10^{-5} bar as transport relevant border (see Figure 17, page 41).

3.2.2 Preparation of silica glass (quartz) ampoules for vapor transport experiments

Silica glass (quartz) ampoules of about 12 cm length (inner diameter: 1 cm) were preheated at 1000 °C to minimize the amount of attached water. Subsequently, fixed amounts of starting materials and transport agents (powders) were funneled into the ampoules in ambient conditions ($RuCl_3$, Cr, I_2) or by using glove box techniques (MB200B, MBRAUN company, $O_2 < 0.5$ ppm, $H_2O < 1$ ppm) in inert (Ar) atmosphere ($TiCl_3$, $GaCl_3$, $MoCl_3$, $MoCl_5$, $CrCl_3$, see Figure 13). For $CrBr_3$ experiments, Br_2 was encapsulated into small glass capillaries (mark-tubes glass no. 14, length: 8 cm, inner diameter: 0.7 mm, Hilgenberg company) and transferred into the transport ampoules at ambient conditions (see Figure 13).

For the preparation of micro- and nanosheets, substrates were additionally placed at the cold side of the ampoule (in opposite to the powders) to deposit thin structures on. The transport ampoules were sealed at a Schlenk line under vacuum (about 0.002 mbar).

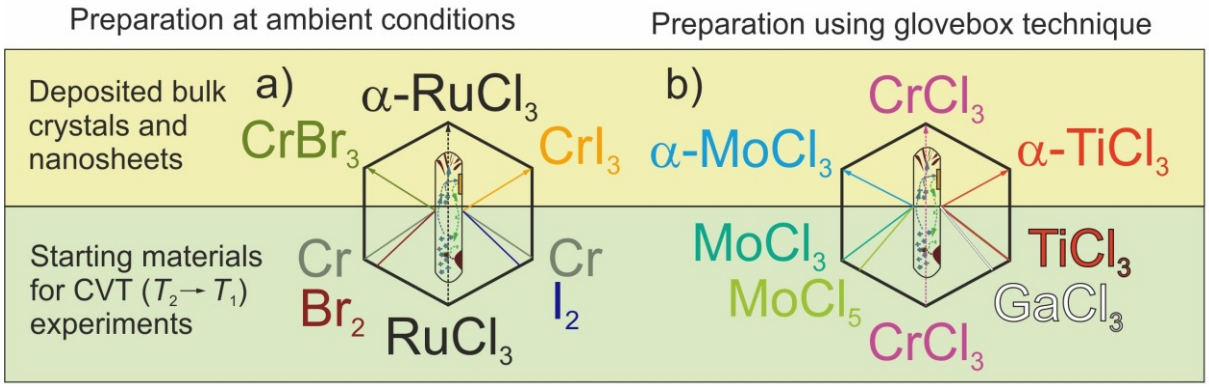

Figure 13: Sketch of preparation of silica glass (quartz) ampoules for CVT experiments with starting materials (powders and bromine encapsulated in glass capillaries) for the deposition of MX_3 bulk crystals and thin nanosheets at **(a)** ambient conditions and **(b)** in inert atmosphere using glove box technique (oxygen sensitive specimen); note that $CrBr_3$ and CrI_3 crystals were synthesized by using the pure elements (chromium and iodine (CrI_3) or bromine ($CrBr_3$)) at ambient conditions, yet the finally deposited structures ($CrBr_3$ and CrI_3) were kept under inert atmosphere due to oxygen and moisture sensitivity both in bulk and especially micro-/nanosheet dimensions.

3.2.3 MX_3 vapor transports in two-zone high temperature LOBA furnaces

CVT experiments were realized in horizontal mounted two-zone furnaces (LOBA, HTM Reetz GmbH, 620 x 205 x 255 mm) by application of endothermic temperature gradients ($T_2 \rightarrow T_1$). The high temperature furnace consists of a KVS 126 isolation (Microtherm), a heat conducting tube (made of an aluminum oxide ceramic) coiled with an heating conductor made of a KANTHAL wire (diameter: 1.2 mm) of quality A1 (alloy made of Cr 22%, Al 5.8%, Fe 72.2%) which allows a maximum working temperature of 1200 °C. The temperature control is achieved by using both thermocouples located on the heating conductor and on movable

Minitec profiles (EUROTHERM type). Additional temperature monitoring is realized by an external thermocouple. The length of the heating zone is 180 mm with an inner diameter of 32 mm. The temperature program was set by utilizing an external console unit.[4]

The as-prepared (and sealed) ampoules were introduced into the furnace and placed at the center of the heat conducting tube. The two movable Minitec thermocouples were fixed at the source and sink locations of the ampoule. The open heating tube (heating zone/furnace) was closed with glass wool at both ends and the predefined temperature program was started. After processing (with fixed temperatures and time) the hot ampoules were deterred in water (with respect to $RuCl_3$, $TiCl_3$, $CrBr_3$ and $CrCl_3$ systems). In contrast, $MoCl_3$ and CrI_3 ampoules were not quenched [5] but naturally cooled down in the open-ended furnace, while the source protruded about 1 cm out of the oven to prevent a gas phase condensation. The cooled-down ampoules were re-introduced into the glove box ($MoCl_3$, $TiCl_3$, CrI_3, $CrBr_3$ and $CrCl_3$) and opened with a glass cutter. Transport ampoules of $RuCl_3$ were opened in ambient conditions, since analytics verified that oxygen does not affect the deposited crystals significantly. The experimental transport rates were determined by quantifying the mass of deposited crystals (mg/h) inside the ampoule and subsequently compared to the calculated values (extracted from simulation data).

3.2.4 Delamination techniques

One main goal of this work was to get access to isolated MCl_3 *single layers*. As-grown MCl_3 nanosheets were prepared using CVT (see Figure 14, page 26). To further reduce the thickness and gain structures in *monolayer dimensions*, the MCl_3 samples on substrates, synthesized by vapor transport, were subsequently delaminated. TMTHs are layered structures and thus allow for cleaving down to only a monolayer (about 0.6 nm thickness). It is well known that the delamination of *van der Waals* crystals by traditional mechanical exfoliation, proceeding from bulk flakes with an adhesive tape, introduces defects e.g. stacking faults. To overcome this issues, *Nicolosi* et al. claimed that metal halides MX_3 are suitable for liquid exfoliation with appropriate dispersing agents.[6]

[4] For more technical details visit: https://www.htm-reetz.de/rohroefen/
[5] The deterrent effect led to the condensation of the gas phase that contaminated the deposited crystals.

With the help of several dispersing agents, liquid exfoliation was realized with as-prepared MX_3 specimen subsequently to vapor transports using ultrasonication (see Figure 14). The "liquid delamination" was executed using as-prepared MCl_3 micro- and nanostructures on substrates (M = Ru, Cr) that were suspended in 2 mL of different dispersing agents (iso-propanol, distilled water, ethanol, benzene, n-methyl-2-pyrrolidone and *n*-hexane). The specimen were sonicated in small laboratory ultrasonication vessels (HILGENBERG company) without any cooling steps for ten seconds up to longer exposure times of 60 minutes at room temperature. At the end of this process, the substrate was taken out of the device and dried under air.

Despite of the known disadvantages, conventional exfoliation using several tapes (substrate exfoliation) was established, too (see Figure 14). For substrate exfoliation conventional scotch tape, and several PF Film tapes (Gel-Pak company, USA), composed of a gel coated on a clear removable polyester substrate covered by a polyethylene coversheet, with different retention levels (XT, X4 and X8) were used. For conventional exfoliation the as-prepared substrate (with $RuCl_3$, $TiCl_3$ or $CrCl_3$ micro- and nanosheets on top) was fixed to an object slide with double-ended adhesive tape. The tape utilized for exfoliation was placed onto the substrate, smoothly appressed and quickly released. The substrate exfoliation of $TiCl_3$ was realized in a glove box. In contrast to this, dry delaminations of $CrCl_3$ and $RuCl_3$ were executed at ambient atmosphere.

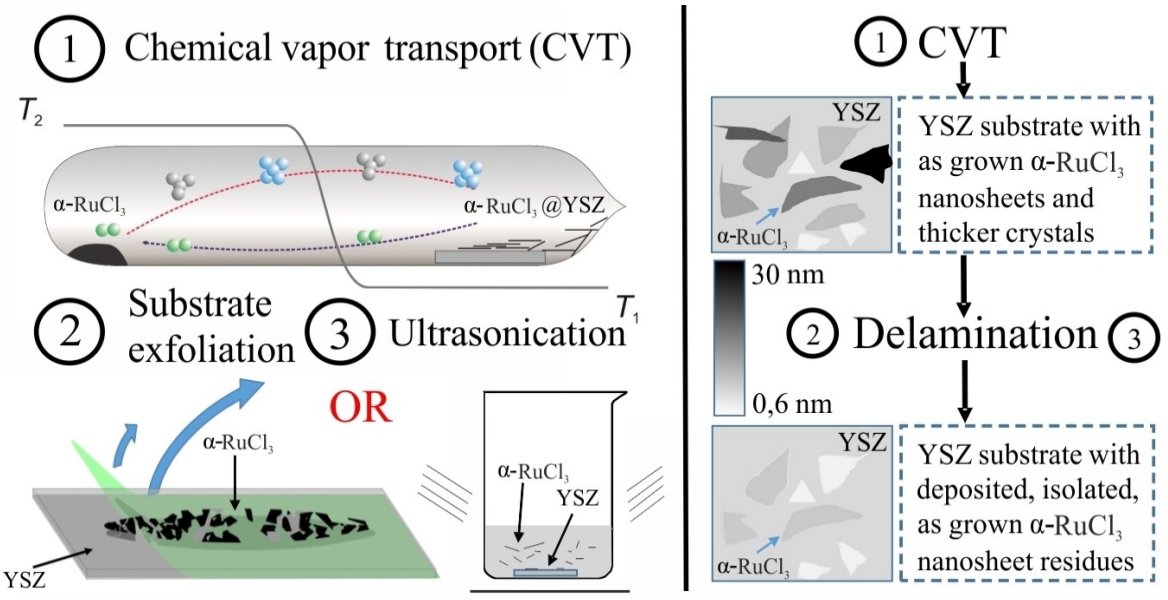

Figure 14: Concept of experimental approach using the example of α-$RuCl_3$ for the synthesis of MX_3 nanosheets and monolayers; firstly as-grown MX_3 nanosheets and thicker crystals (microsheets) are deposited on substrates by chemical vapor transport (CVT) following the delamination of thicker structures by two different approaches (substrate exfoliation or ultrasonication) resulting in isolated, as-grown MX_3 nanosheets and thin residues from thicker structures (few-layer down to monolayer); figure from reference [123].

3.2.5 $TiCl_3$ catalyst tests

As synthesized $TiCl_3$ bulk flakes and microsheets on YSZ substrates were implemented for catalytic reactions. The gas-phase polymerizations of ethylene were realized in a glovebox (O_2 < 0.1 ppm and H_2O < 0.1 ppm) and a static pressure of ethylene of 10 bar at room temperature. The catalyst tests were performed in a 25 mL stainless steel reactor. Initially the catalyst ($TiCl_3$ in bulk dimensions or $TiCl_3$ microsheets on top of YSZ) was dipped into a triethylaluminum solution (25% w/w in hexane, Alfa Aesar, purity 95%) used as a co-catalyst. The coated catalyst was placed in the reactor, activated at vacuum at room temperature, flushed with ethylene (1 bar) for three times and then pressurized with ethylene to 10 bar. The reaction time was one hour. At the end the ethylene feed was turned off and the product (polyethylene at top of $TiCl_3$) was transferred to the glovebox.[128]

3.3 Characterization techniques

The as-prepared MX_3 bulk flakes and respective micro- and nanosheets were analyzed with various analytics including microscopy, spectroscopy and diffraction techniques (see Figure 15). The used devices including sample preparation steps are presented in the subsequent subheadings.

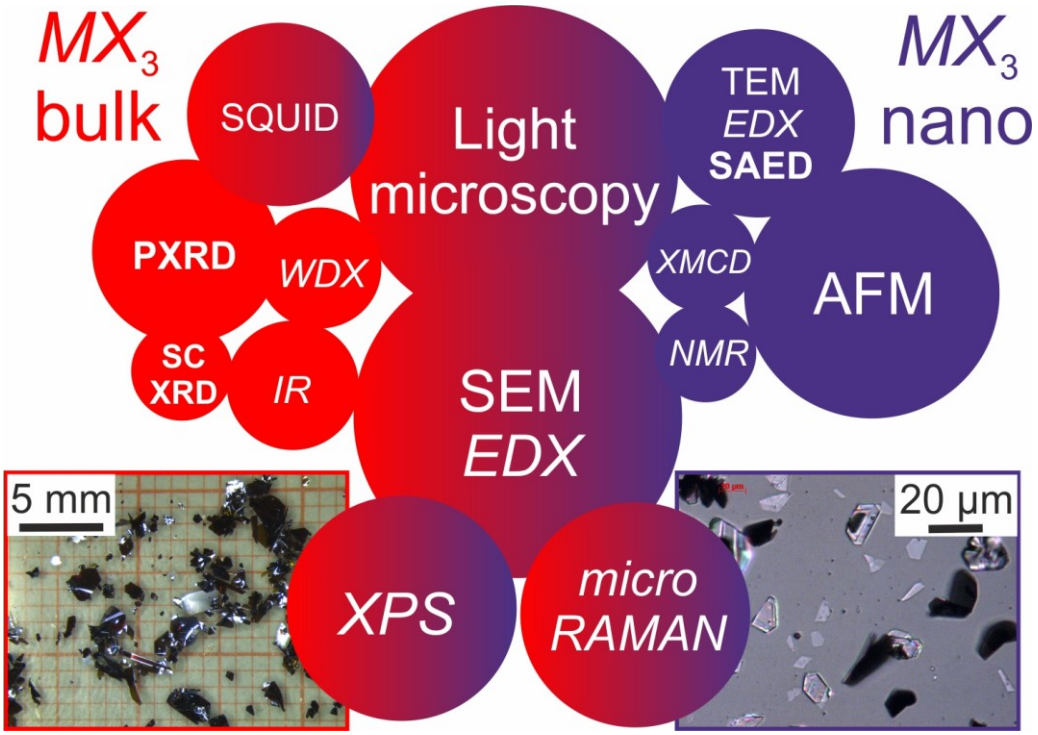

Figure 15: Utilized characterization techniques for determination of e.g. morphology, composition, phase-purity or magnetic properties of MX_3 bulk flakes (red) and respective micro- and nanosheets (blue), analytics with both colors indicate that as well both bulk flakes and nanosheets were investigated; the size of the circles point towards the perceived amount of utilization; *italic* letters indicate spectroscopy techniques and **bold** letters are utilized diffraction tools.

3.3.1 Light microscopy

Optical images of synthesized MX_3 crystals and overview recordings of as-prepared substrates were captured with a LEICA M80 optical microscope and an integrated camera in ambient atmosphere using the Leica Application Software (v.4.8.0). An additional LEICA M60 was used in glovebox atmosphere to take images of oxygen sensitive samples (e.g. $TiCl_3$). In particular synthesized MX_3 nanosheets on substrates (20x- and 100x magnification) and bulk crystals on the ampoule wall (5x magnification) were investigated by utilizing a further light microscope (AXIO Imager.A1m, ZEISS company, Germany) in bright- (morphology and dimensions) and dark-field mode (edge contrast for investigation of height differences between the surfaces of the substrate and crystals). Furthermore, the EPI-CDIC image mode (EPIplan objective category and differential interference contrast with circular polarized light) was applied to investigate very small height differences. Similar to the images acquired with LEICA devices, the figures observed with the ZEISS microscope were recorded with an integrated camera.

Preparation of MX_3 samples for optical microscopy

For analysis of MX_3 bulk crystals (M = Ru, Mo, Cr; X = Cl, Br, I) and micro- or nanosheets ($RuCl_3$, $MoCl_3$, partly $CrCl_3$) by means of optical microscopy the respective crystals and/or the coated substrate was extracted from the silica glass (quartz) ampoule and investigated as is in ambient atmosphere. With respect to $TiCl_3$ (bulk and micro/nanosheets), as well as CrX_3 micro- and nanosheets, the microscope images were acquired by taking images of specimen in the inside of the sealed ampoules (to fairly maintain the inert gas atmosphere).

3.3.2 Scanning electron microscopy (SEM) and energy-dispersive X-ray spectroscopy (EDX)

Visualizing structures in the nanometer dimension requires electron microscopy approaches (the resolution limit of optical devices is about 0.24 µm).[129] By scanning electron microscopy (SEM) it is possible to investigate the morphology and topography of MX_3 crystals at the micro- and nanometer scale (resolution limit of about 2.3 nm).[129] In this thesis two separate SEM devices have been utilized. For most of the SEM investigations (α-$RuCl_3$, α-$MoCl_3$, $CrCl_3$, $CrBr_3$ and CrI_3) a Nova NanoSEM 200 (FEI company) was used with xTm microscope control software (v. 1.3.5, FEI company). The microscope is equipped with an ET (Everhard-Thornley) detector, a TL (through-the-lens) detector to detect secondary electrons and a BSE (back

scattered electron) detector for better elemental contrast. For investigation of bulk crystals acceleration voltages of 3-15 kV have been used. Since mostly insulating substrates were applied (e. g. yttrium stabilized zirconia, YSZ) very low acceleration voltages of 2-4 keV were applied also to minimize occurring and obstructive charging effects. The spot size was set to around 4.5. Crystals and nanosheets of α-$TiCl_3$ were investigated with a Leo 1530 Gemini (ZEISS company, Germany) with an ET detector, an acceleration voltage between 3-15 keV and a spot size of 5.

Both devices are combined with an energy-dispersive X-ray (EDX) spectrometer for qualitative and quantitative elemental analysis. For EDX analysis a QUANTA 200/400 (AMATEX) with an acceleration voltage of 15 keV has been utilized together with "EDAX Genesis Spectrum" software (v. 6.32).

Preparation of *MX*$_3$ samples for SEM/EDX

For SEM measurements prior as-grown MX_3 crystals, respectively MX_3 micro- and nanosheets on substrates, were directly affixed to carbon tape on a SEM sample holder (diameter: ca. 1 cm) and introduced into the device. The preparation was realized either in ambient conditions (α-$RuCl_3$) or in a glovebox under inert atmosphere (α-$MoCl_3$, $CrCl_3$, $CrBr_3$ and CrI_3). Specimen of $MoCl_3$ were coated with a thin layer of carbon by means of sputtering prior the SEM/EDX analysis to minimize charging effects. For investigation of α-$TiCl_3$ a transfer module by Kammrath & Weiss (Germany) has been used to avoid any oxygen and moisture contamination. $TiCl_3$ micro- and nanosheets at substrates were transferred into the transfer module inside a glovebox under inert atmosphere and subsequently investigated at the SEM. After reaching final vacuum conditions the transfer chamber was opened and the micro- and nanosheets were investigated by SEM and EDX.

3.3.3 Transmission electron microscopy (TEM) coupled with EDX, electron nanodiffraction (END) and selected area electron diffraction (SAED)

For investigation of thin MX_3 nanosheets, transmission electron microscopy (TEM) was applied. By TEM it is possible to analyze ultrathin samples (resolution limit of about 0.2 nm).[129] The measurements were performed with two different devices. For visualizing thin nanosheets a Tecnai F30 (FEI company) has been used. The microscope is equipped with a field emission cathode, a Gatan GIF 200 energy filter, a Gatan MSC 794 multiscan CCD camera and super-twin alpha objective lenses. Acceleration voltages up to 300 kV were applied. For

EDX measurements (local probes and linescan) a X-ray spectrometer (EDAMIII, EDAX company) has been used. Further, electron nanodiffraction (END) measurements were performed using this instrument, to investigate the localized crystallinity of deposited $TiCl_3$ in micro- and nano dimensions. END diffraction patterns are generated from very small regions of specimen diameters of 1 nm or little less. This is realized by application of strong electromagnetic lenses that form electron probes of sub-nanometer diameter by demagnification of a small and bright electron source and electrons of a few hundred thousand eV. END pattern are pointing towards hints of a particles structure and orientation.[130]

For electron microscopy down to atomic resolution HR-TEM (high-resolution TEM) measurements were utilized. The high resolution measurements were performed with a Titan³ 80-300 (FEI company, USA) with acceleration voltage of 300 keV. For atomic resolution an aberration corrector was established, resulting in resolutions down to 0.08 nm. Further, selected area electron diffraction (SAED) investigations of MCl_3 (M = Ru, Mo, Cr) were applied by using this TEM. In contrast to END, SAED pattern are generated from specimen regions larger than 100 nm. However, considering specimen with high crystallinity SAED provides sharp diffraction spots, high resolution in reciprocal space and high accuracy with respect to the dimensions of the acquired pattern.[130]

Preparation of MX_3 samples for TEM/EDX/END/SAED investigations

In preparation of TEM measurements prior as-grown MCl_3 (M = Ru, Mo, Cr) specimen (bulk or micro- and/or nanosheets at adjacent substrates) were sonicated in 2 mL isopropanol for five minutes in a conventional BANDELIN ultrasonication bath in laboratory scale without application of any cooling or heating steps. The dispersion was pipetted (about five drops) onto lacey-carbon copper grids (diameter: 3 mm). Then, the solvent was volatilized at ambient conditions for about one hour and inserted into the TEM sample holder (using a Titan³ 80-300).

For TEM investigations of α-$TiCl_3$, the respective nanocrystals were deposited directly onto lacey-carbon copper grids by CVT (700 → 600 K, 1 hour transport duration). Subsequent to the CVT process the ampoule (with the coated lacey-carbon copper grid inside) was cracked in a glovebox under argon atmosphere, and the grid was inserted into the TEM sample holder (also placed in the glovebox). The sample holder was closed, additionally fairly sealed and transferred to the device (Tecnai F30).

3.3.4 Wavelength-dispersive X-ray spectroscopy (WDX)

Since the energy of emitted X-ray quanta may be in the same range for specific elements, respectively their elemental lines (e. g. Ru-L and Cl-K with respect to $RuCl_3$, or Cr-K, I-L and O-K considering CrI_3) exact quantification by EDX becomes difficult. Hence, selected MX_3 crystals were further investigated by means of wavelength-dispersive X-ray spectroscopy (WDX). For WDX measurements an EVO MA15 scanning electron microscope (Zeiss, Germany) has been used, equipped with a Microspec WDX-3PC detector (Microspec Corporation, USA). The applied acceleration voltage of the SEM was 15 kV and the working distance 10.5 mm. Bulk flakes of α-$RuCl_3$, $CrBr_3$ and CrI_3 (lateral dimensions: 5-10 *mm*) have been measured by WDX. By WDX the application of a standard becomes necessary. Considering α-$RuCl_3$, pure ruthenium (Ru Lα) and NaCl (Cl Kα) were employed as suitable standards. For standardization of $CrBr_3$, pure chromium (Cr Kα) and KBr (Br Lα) were used. In case of CrI_3 we worked with pure chromium (Cr Kα) and CsI (I Lα).

Preparation of MX_3 samples for WDX investigations

Selected samples of $RuCl_3$, CrI_3 and $CrBr_3$ were fixed on a sample holder using carbon tape.

3.3.5 Powder- and single crystal X-ray diffraction (PXRD, SCXRD)

The deposited MX_3 crystals were characterized by powder X-ray diffraction (PXRD) for phase identification. For PXRD measurements a STOE STADI-P diffractometer in transmission geometry, a detector with 6° spatial resolution and a Ge (111)-primary beam monochromator (Johannes-type) were used. For excitation mainly Mo $K_{\alpha1}$-radiation (λ = 0.7093 Å) in angular range $2° \leq 2\Theta \leq 60°$, rarely Cu-$K_{\alpha1}$-radiation (λ = 1,5406 Å) in angular range $2° \leq 2\Theta \leq 90°$, has been utilized. The resolution was 0.02° 2Θ and the step width $\Delta 2\Theta = 0.2°$. For phase identification the standardized structure models of the ICSD (inorganic crystal structure database) or the ICDD (international center of diffraction data) were used. The evaluation of obtained diffraction data was performed with the software STOE WinXPOW (v. 2.08) or by ORIGIN 2018.

Selected MX_3 single crystals were investigated using single crystal X-ray diffraction (SCXRD) by utilizing a Bruker AXS with Mo $K_{\alpha1}$-radiation and a CCD detector (charge coupled device). The refinement was established by application of JANA 2006 software.

Preparation of MX_3 samples for PXRD and SCXRD investigations

For PXRD investigations in transmission geometry MX_3 crystals were introduced into glass capillaries (Hilgenberg, Germany) with a diameter of 0.7 mm or 0.3 mm, either in ambient atmosphere (α-$RuCl_3$) or inert atmosphere (α-$MoCl_3$, α-$TiCl_3$, $CrCl_3$, $CrBr_3$ and CrI_3). Rather rarely the MX_3 crystals were measured in reflection mode by fixing them with collodion glue on a (X-ray amorphous) polyacetate foil. The MX_3 crystals were not homogenized at all while preparing the samples due to their *van der Waals* nature. Thus, a strong preferential orientation was induced and had to be considered evaluating the obtained powder pattern. Thin single crystalline MX_3 platelets were prepared for SCXRD by affixing them with glue on a cactus needle (amorphous). The crystals were previously selected by means of optical microscopy.

3.3.6 Atomic force microscopy (AFM) and magnetic force microscopy (MFM)

The thickness and surface topography of MX_3 nanosheets were investigated with atomic force microscopy (AFM) in tapping mode with measuring probes (cantilever) made of a silicon single crystal (spring constant: 3 N/m) coated with a thin cobalt alloy. For very rarely applied magnetic force microscopy (MFM) measurements the lift mode[6] was combined with the tapping procedure. For AFM (and MFM) mainly a Dimension Icon (BRUKER, USA) has been used. Early AFM measurements were performed with a VEECO DI 3100 (Digital Instruments Veeco Metrology Group), also in tapping mode. The analysis of the detected height profiles was performed with NanoScope Analysis software (v. 1.8).

Preparation of MX_3 samples for AFM (MFM) investigations

Suitable MX_3 nanosheets (M = Ru, Mo, Cr; X = Cl, Br, I) were preselected using optical microscopy (even $CrBr_3$ and CrI_3 were temporary exposed to ambient conditions). The distance between the nanolayers and an edge of the substrate was defined and noted. This numeric values were subsequently used to localize the thin sheets in the AFM. Thin sheets of $TiCl_3$ could not be measured by means of AFM due to their extreme strong sensitivity to moisture and oxygen (the approximate thicknesses were measured using SEM and a transfer chamber).

[6] In lift-mode every scan-line is measured a second time, but with a distance of 60 nm (surface-cantilever).

3.3.7 Micro-RAMAN spectroscopy

By RAMAN spectroscopy vibrational frequencies (stretching vibrations) of solids are measured due to radiation with energy rich quanta, which are not absorbed by the specimen. By means of micro-RAMAN it is possible to measure stretching vibrations of thin nanosheets on a substrate, since the device is coupled to an integrated camera. In this thesis a LabRAM HR Evolution (HORIBA Scientific) has been used, equipped with a solid state laser (Coherent Innova Model 306) for measurements of α-$MoCl_3$ (λ = 458 nm), α-$TiCl_3$ (λ = 488 nm), $CrCl_3$, $CrBr_3$ and CrI_3 (all CrX_3: λ = 458 nm) with laser intensities of 1-5 % and an acquisition time of 30 seconds. Micro-RAMAN measurements of α-$RuCl_3$ were performed using a T64000 (Horiba Jobin Yvon GmbH) with an argon laser (Coherent Innova Model 306). Laser intensities of 1-5 % and measurement times of 400 seconds have been applied.

Preparation of MX_3 samples for micro-RAMAN investigations

MX_3 (M = Ru, Mo, Cr; X = Cl, Br, I) samples were placed on a sample holder and measured immediately. For measurements of α-$TiCl_3$ microcrystals, thin titanium trichloride structures (deposited at Si substrates) were incorporated between two microscope object slides in glove box atmosphere. The object slides were sealed with epoxy glue to avoid oxygen contamination. Next to nanosheets, MX_3 bulk crystals, as well the pure substrates (for comparison of micro- and nano samples) were measured also.

3.3.8 X-ray photoelectron spectroscopy (XPS)

X-ray photoelectron spectroscopy (XPS) is a useful tool for detailed investigation of surface atoms of specimen, their chemical environment, as well as binding- and their oxidation state. The method is based on a radiation of the sample by monochromatic X-rays and a resulting photoionization (separation of electrons if X-ray energy is equal or more than their binding energy). Since the binding energy of electrons is characteristic for every element, a shift of this energy (± 10 eV depending on the effective nuclear charge) due to ionization is detected. The measurements were performed with a PHI 5600 (Physical Electronics, USA) and an excitation using monochromatic Al Kα-radiation (350 watt). For the detection a hemispherical analyzer has been used. For surface cleaning all samples were sputtered with argon ions (3.5 keV, Ar purity: 99.999 %). The sputter rate was set to 3.5 nm/min.

Preparation of MX_3 samples for XPS investigations

For XPS analysis typical cylindrical shaped sample holders (diameter about 10 mm) were used. MX_3 bulk crystals were transferred into semicircular shaped recesses on the specimen holder for direct investigation. MX_3 thin layers on their respective substrates were fixed on the holder using a small clamp, which was already preinstalled. In this thesis XPS was especially utilized to determine the origin of the oxygen signal, detected by prior applied EDX (if oxygen is only adsorbed at the surface or incorporated into the crystal lattice). Thus it was important to maintain the absence of oxygen and moisture while preparing the samples. For this reason a transfer chamber was used. With respect to all investigated $M\mathrm{Cl}_3$ and $\mathrm{Cr}X_3$ structures, the sample holder (and transfer chamber) was thus introduced into the glovebox, mounted with the respective specimen, introduced into the transfer chamber and closed under inert conditions. The transfer chamber was introduced into the XPS device and opened under vacuum conditions.

3.3.9 Infrared spectroscopy (IR)

Bulk crystals of investigated MX_3 and compounds were further characterized by infrared spectroscopy (IR). The measurement is based on the absorption of electromagnetic radiation by solid specimen. Absorption occurs if the incoming energy is in the same range as symmetric molecular vibrations or rotations and herein characteristic for chemical bondings. The spectra were recorded in transmission geometry by a Vertex 80v FT-IR (BRUKER) with Globar radiation source, a T222 mylar-multilayer-radiation splitter and a DLaTGS detector. By Fourier transformation the detected data were converted to visualize the absorption (or vice versa transmission) of radiation in dependence of the wavenumber. The experiments were realized in the far-to-mid infrared regions (wave number range 700…40 cm^{-1}), a resolution of 2 cm^{-1} and 128 scans.

Preparation of MX_3 samples for IR investigations

MX_3 crystals were either dispersed in 2 mL isopropyl alcohol and dropped (three drops) onto a polyethylene (PE) substrate (in case of $\mathrm{Cr}X_3$) or utilized as a pressed powder sample (KBr + $M\mathrm{Cl}_3$ flakes). In case of a KBr approach, the transmittance drastically rises at low wave numbers (< 250 cm^{-1}) due to the measurement limit originating from KBr. By application of the PE substrate covered by MX_3 layers, the spectrum resulted in a much better resolution (smaller background) and a greater measurement range.

3.3.10 Magnetic measurement (SQUID)

To measure the magnetic properties of MX_3 samples a SQUID (superconducting quantum interference device) of MPMS type (magnetic properties measurement system, Quantum Design) in VSM mode (vibrating sample magnetometer) has been used. The method is based on the detection of the magnetic moment of a specimen in dependence of an external magnetic field (-5 T … 5 T) at specific temperatures (room temperature down to 2 K) in either field cooled (fc) or zero field cooled (zfc) mode. With respect to bulk MCl_3 (M = Ru, Mo, Ti, Cr) the $m(T)$ curves of crystals (powders) were measured in random orientation (see preparation part below) at 0.1 T ($RuCl_3$ and $CrCl_3$) or 1 T ($MoCl_3$ and $TiCl_3$). Considering bulk CrX_3 specimen (X = Cl, Br, I), additional $m(H)$ curves were acquired at 2 K. Here, instead selected CrX_3 crystals were aligned parallel or perpendicular to the external magnetic field to analyze the anisotropic properties. The $m(T)$ curves of CrX_3 samples were recorded at two different magnetic field intensities (0.1 and 3 T), also with crystals aligned in both orientations (parallel or perpendicular to the external magnetic field).

As-grown $CrCl_3$ micro- and nanosheets on YSZ (yttrium stabilized zirconia) substrates were as well analyzed by SQUID magnetometry. In this case, the magnetic field was applied perpendicular to the crystallographic c-axis of $CrCl_3$. To reduce the influence of the underlying YSZ, the magnetization of the empty substrate (without $CrCl_3$) was measured initially and the diamagnetic signal was then subtracted from the overall measurement data ($CrCl_3$ on top of YSZ). The $m(H)$ curve was acquired at 5 K. The $m(T)$ curve of $CrCl_3$ micro- and nanosheets was measured using external magnetic fields from 30 Oe up to 5 kOe (5 T).

Preparation of MX_3 samples for SQUID investigations

Depending on the morphology of MX_3 samples, MCl_3 specimen were either measured in small plastic capsules (powders, ≈ 1…5 mg) or in specific gelatin capsules (platelets, ≈ 1…5 mg), that were further fixed in the middle of a plastic straw. This plastic straw was introduced into the device and the measurement sequence was started. CrX_3 crystals were fixed between two stripes of adhesive tape. The plastic straw was cut in the middle and the tape (with crystals in between) was aligned either parallel or perpendicular to the external magnetic field ($H \parallel c$ or $H \parallel ab$). As-grown $CrCl_3$ micro- and nanosheets on top of YSZ were also positioned in a plastic straw (H aligned perpendicular to the crystallographic c axis) and mounted in the device.

3.3.11 Nuclear magnetic resonance spectroscopy (NMR)

$CrCl_3$ micro- and nanosheets were investigated by ^{53}Cr nuclear magnetic resonance spectroscopy (NMR) with zero-field. An attenuator optimization was done prior to the measurement. The measurement was done for several frequencies in 0.1 MHz steps with a solid echo pulse repetition (p90 pulse – tau – p90 pulse) to obtain the NMR spin echo (the p90 pulse, or 90-degree-pulse, flips the core magnetization of chromium by 90 degrees). The p90 pulse had a length of 0.6 µs with a tau of 9 µs. Each measurement (for each frequency) was repeated for 10000 times with a time gap of 10 ms between the frequencies. The single measurements were added up and Fourier transformed. As a rule of thumb 10^{16} nuclear spins are desired to get a decent NMR signal.[131] If less nuclear spins are present, the enhancement effect of zero-field NMR provides a sufficient signal, though. As comparison bulk crystals of $CrCl_3$ were utilized. Although thicker $CrCl_3$ flakes were prepared during the period of this work as well, the bulk crystals related to the NMR investigations were provided by the TU Dresden (in particular thanks to Prof. A. Isaeva and Dr. M. Roslova).

Preparation of $CrCl_3$ micro- and nanocrystals for NMR investigations

$CrCl_3$ micro- and nanosheets on substrates (YSZ) were at first wrapped round with Teflon tape and secondly with a small wire of Manganin. Thus, a coil was formed. This coil was implemented in the NMR sample holder, cooled down (1.4 … 8 K) and measured.

3.3.12 X-ray magnetic circular dichroism (XMCD)

The magnetic properties of $CrCl_3$ microsheets were analyzed by X-ray magnetic circular dichroism (XMCD) at the X-Treme station at Paul Scherrer Institute, Swiss Light Source. XMCD is a polarization-dependent X-ray absorption spectroscopy (XAS) technique. These approaches allow the determination of the local electronic and magnetic structure of 3*d* transition metal atoms due to their valence-, site-, and symmetry-selectivity.[132] The beamline used produces soft X-rays with variable polarization (circular left (parallel) or right (anti-parallel) and linear in any angle between 0 and 90°) from an Apple-II undulator source. The X-ray absorption is analyzed and XMCD is the result of the difference of the XAS spectra of both left and right helicity of absorbed X-ray quanta. The device is equipped with a superconducting 2D vector magnet operating up to 7 T single direction or 2 T vectorial field at low temperatures of 2 K. The beamline is focused on measurements at the $L_{2,3}$ edges of elements (transition 2p→3d) at an energy range of 400…2000 eV.[133] The XAS (XMCD) measurements

were performed at the chromium $L_{2,3}$ edge at two external magnetic fields (0.15 and 6.8 T). Additionally, the XMCD spectra were analyzed at different incidence angels (0, 14, 28, 42 and 56°). Moreover, the magnetization data of $CrCl_3$ microsheets could be extracted of the normalized XMCD signal at temperatures of 2, 10 and 18 K at a beam incidence of 0 and 70°.

Preparation of $CrCl_3$ micro- and nanocrystals for XMCD investigations

$CrCl_3$ micro- and nanosheets were transferred by means of ultrasonication on top of a Si/SiO_2 substrate (200 nm oxide layer). Herein as-grown $CrCl_3$ micro- and nanosheets (on top of YSZ) were sonicated for 3 minutes in 2 mL isopropanol. The YSZ substrate was extracted subsequently and replaced by a Si/SiO_2 substrate. The Si/SiO_2 substrate with micro- and nanosheets on top was obtained after repeated sonication for 3 minutes, extracted from the bath and dried under air. The sample was stored under argon and then transferred into the device.

4 Results and discussion

To ensure a rational synthesis planning and avoid time consuming trial-and-error approaches the vapor transport of each investigated system MCl_3 (M = Ru, Mo, Ti, Cr) and CrX_3 (X = Cl, Br, I) was simulated using CalPhaD methods (see chapter 4.1). The calculation of optimum synthesis conditions consequently allowed a targeted preparation and following characterization of MCl_3 (see chapter 4.2, page 47) and CrX_3 (see chapter 4.3, page 79) structures. This thesis is focused on the *layered* candidates of transition metal trihalides. Starting from chapter 4.1, the demonstrated results of $RuCl_3$, $MoCl_3$ and $TiCl_3$ hence refer to the α-polymorph of these compounds.[7]

4.1 Simulation of vapor transports of transition metal trihalides MX_3

The vapor transports of MCl_3 (M = Ru, Mo, Ti, Cr, see chapter 4.1.1, page 39) and CrX_3 (X = Cl, Br, I, see chapter 4.1.2, page 44) were simulated by utilizing the software TRAGMIN. The modeling was achieved by considering thermodynamic data (standard formation enthalpy, standard entropy and the function of the heat capacity) of all possible condensate and gaseous species within a heterogeneous system *solid-vapor* (both of the introduced material and a potential transport agent). The thermodynamic data sets were compiled using the TRAGMIN data base. By applying the CalPhaD method, occurring homogeneous- and heterogeneous gas phase equilibria were calculated within the systems *M*-*X*-O, thus considering potential contamination by oxygen or moisture under real synthesis conditions. The foundation of this method is the minimization of the free reaction enthalpy by *Eriksson*, considering that this enthalpy within an assumed equilibrium condition is zero. A profound understanding about the growth of MX_3 structures and phase relations of systems *M*-*X*-O became possible by clarification of dominating transport mechanisms, accompanied with a derivation of a ternary *M*-*X*-O phase diagram (see Figure 16, page 39). This phase diagram exemplifies the type of vapor transport depending of the amount of introduced *M*, *X* and O. Considering both, the introduced materials (composition, see Figure 16) and applied temperatures (thermodynamics, see Figure 17, page 41; Figure 18, page 44 and Figure 19, page 46) a detailed description of MX_3 vapor transport was achieved.

[7] There are several chemical polymorphs or modifications known for $RuCl_3$ (α,β), $MoCl_3$ (α,β) and $TiCl_3$ (α,β,γ,δ), but up to the process time of this work there were no reports concerning $CrCl_3$, $CrBr_3$ or CrI_3

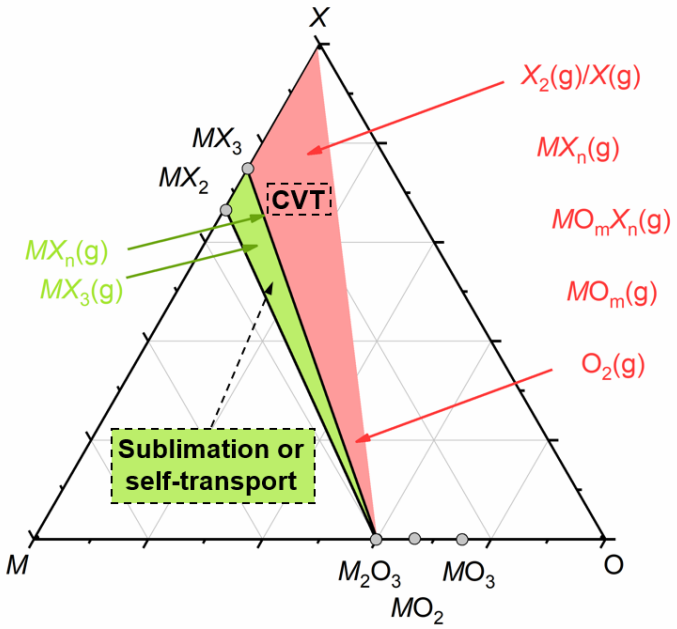

Figure 16: Ternary phase diagram of *M*/*X*/O with *X* = Cl, Br or I, the composition of *M*-*X*-O determines whether the vapor growth is realized as sublimation, auto- or self-transport (both green area) without addition of a suitable transport agent or as chemical vapor transport reaction (CVT, red area) with an excess of halide, either by the pure halogen X_2 (*X* = Cl, Br, I) or other halides MX_n; the figure was reproduced from reference [126].

4.1.1 *M*Cl$_3$ (*M* = Ru, Mo, Ti, Cr)

The simulations prove that vapor transport of $RuCl_3$ and $CrCl_3$ is possible without a transport addition, while in contrast $MoCl_3$ and $TiCl_3$ need a transport addition. Thus, the modeling results of MCl_3 are compared in detail between both *M* = Ru/Cr and *M* = Ti /Mo and within a combination of either $RuCl_3$/$CrCl_3$ or $TiCl_3$/$MoCl_3$ (see Figure 17, page 41 and appendix, Table A 1, page 123). Thereby both, the composition of the gas phase (see e.g. Figure 17a) and the transport efficiencies (see e.g. Figure 17b) were calculated for every system separately.

Considering a thermal treatment of pure $RuCl_3$ and $CrCl_3$ and assuming a stoichiometric approach (*M*:Cl = 1:3, according to MCl_3), several heterogeneous and homogeneous gas phase equilibria occur (see appendix, Table A 1, page 123). With respect to $RuCl_3$, the remaining solid is homogeneously composed of RuO_2, $RuCl_3$ and Ru formed by several heterogeneous equilibria (see Figure 17a and appendix, Table A 1, page 123). Contrary to that, $CrCl_3$ residues are composed still of the oxide (Cr_2O_3) and the trihalide ($CrCl_3$), but no elemental chromium (see appendix, Table A 1, page 123). However, due to a heterogeneous equilibrium $CrCl_2$ accumulates the residue material, starting from temperatures above 940 K (see Figure 17c). Below 940 K the decomposition equilibrium of $CrCl_3$ is strongly shifted to the “educt” side. Thus, the accumulation of $CrCl_2$ in the starting material is negligible. The $RuCl_3$ vapor phase is dominated by Cl_2(g), $RuCl_3$(g), $RuCl_4$(g) and monoatomic Cl(g) (see Figure 17a). Initially, Ru(s) and Cl_2(g) are formed by a heterogeneous equilibrium (see appendix, Table A 1,

page 123, Equation E1). Fractional amounts of oxygen lead to RuO_2(s). Further homogeneous equilibria (see appendix, Table A 1, page 123, Equation E5-6) form Cl(g) and $RuCl_4$(g). Although HCl, shaped by reaction with minimum amounts of water, has a high absolute partial pressure, its pressure change between sink and source is low and thus its efficiency in vapor transport is almost non-relevant (see Figure 17b). For the deposition of thin $RuCl_3$ nanosheets directly on substrates, low transport rates of less than 1 mg/h (deposited $RuCl_3$ in mg/h) are desired. By calculation of the CVT process, a temperature gradient of ΔT = 200 K (973 → 773 K) proved to be suitable for $RuCl_3$ nanosheets with a transport rate of around 0.5 mg/h. Similar low transport rate values were determined by using ΔT = 100 K (873 → 773 K) for $CrCl_3$. By application of this temperatures (973 → 773 K) with respect to $RuCl_3$ two vapor transport mechanisms occur simultaneously: sublimation of pure $RuCl_3$ and auto- or self-transport (see Figure 17b and appendix, Table A 1, page 123). However, due to the temperature dependency of vapor equilibria, the growth of $RuCl_3$ sheets is achieved by different amounts of these mechanisms. At 973 → 773 K thin sheets form mainly by a $RuCl_3$ sublimation. The $RuCl_3$ auto-transport has a minor, but still significant, amount (see Figure 17b). In auto-transport prior released gaseous chlorine (see Equation E12 in the appendix) forms $RuCl_4$(g), that re-condensates to $RuCl_3$(s) and Cl_2(g), see appendix, Table A 1, page 123. The calculation of transport efficiencies verified, that Cl_2(g) acts as the transport agent, in accordance with Equation E12 (see negative slope in Figure 17b). Further, $RuCl_3$(g) and $RuCl_4$(g) proved to be the transport efficient gas species in harmony with Equation E11 and E12 (see positive slope in Figure 17b). At higher temperatures (1073 → 873 K) the amount of auto-transport is more negligible and at 1373 → 1173 K the sublimation is the by far the dominant mechanism accompanied with an enlargement of transport rates to be about 1 mg/h. Considering an excess of chlorine, either pure or chemically bonded e.g. by $AlCl_3$, $RuCl_3$ vapor transport is also viable due to a chemical vapor transport reaction.

The main difference of $RuCl_3$ vapor transports in relation to $CrCl_3$ is that at temperatures of ΔT = 100 K (873 → 773 K) and assuming a stoichiometric ratio ($CrCl_3$), self-transport has no influence on the $CrCl_3$ vapor transport, and the sheets growth is achieved completely by sublimation. This can be comprehended with the course of partial pressure of $CrCl_3$(g) that is slightly entering the transport efficient area above 773 K and thus enables sublimation. However, the main reason why the auto-transport of $CrCl_3$ fails is the initial thermodynamic formation of $CrCl_2$(s) in low amounts, instead of Cr(s), additionally only at temperatures higher than 940 K. Thus, the partial pressure of Cl_2(g) and its temperature dependent change is poor, preventing self-transport. The $CrCl_3$ calculations further show that an enhancement of transport

temperature to 1023 → 923 K solely leads to an additional influence of auto-transport due to slight shift of Cl_2(g) coming into force, but in fact, sublimation still dominates the CVT process. Moreover, high transport rates of $CrCl_3$ were determined for temperatures of 1023 → 873 K. Furthermore calculations prove that neither low amounts of chromium oxides nor oxychlorides suppress the growth of $CrCl_3$ sheets. By introduction of an excess of chlorine (n_{Cr}:n_{Cl} = 1:3.05) vapor transport is instead achieved due to a chemical vapor transport reaction (see Figure 16, page 39). In this case Cl_2(g) acts as transport agent and $CrCl_4$(g) as transport efficient gas species at ΔT = 100 K (873 → 773 K). Although an excess of chlorine is present, the amount of sublimation starts to increase at elevated temperatures and at 1123 → 1023 K sublimation of $CrCl_3$ dominates the transport behavior again. Furthermore the amount of sublimation increases by decreasing the chlorine excess. Similar to the prior discussed stoichiometric approach, a shortfall of chlorine ($CrCl_{3-x}$ ($x \geq 0.05$)) favors the sublimation, too.

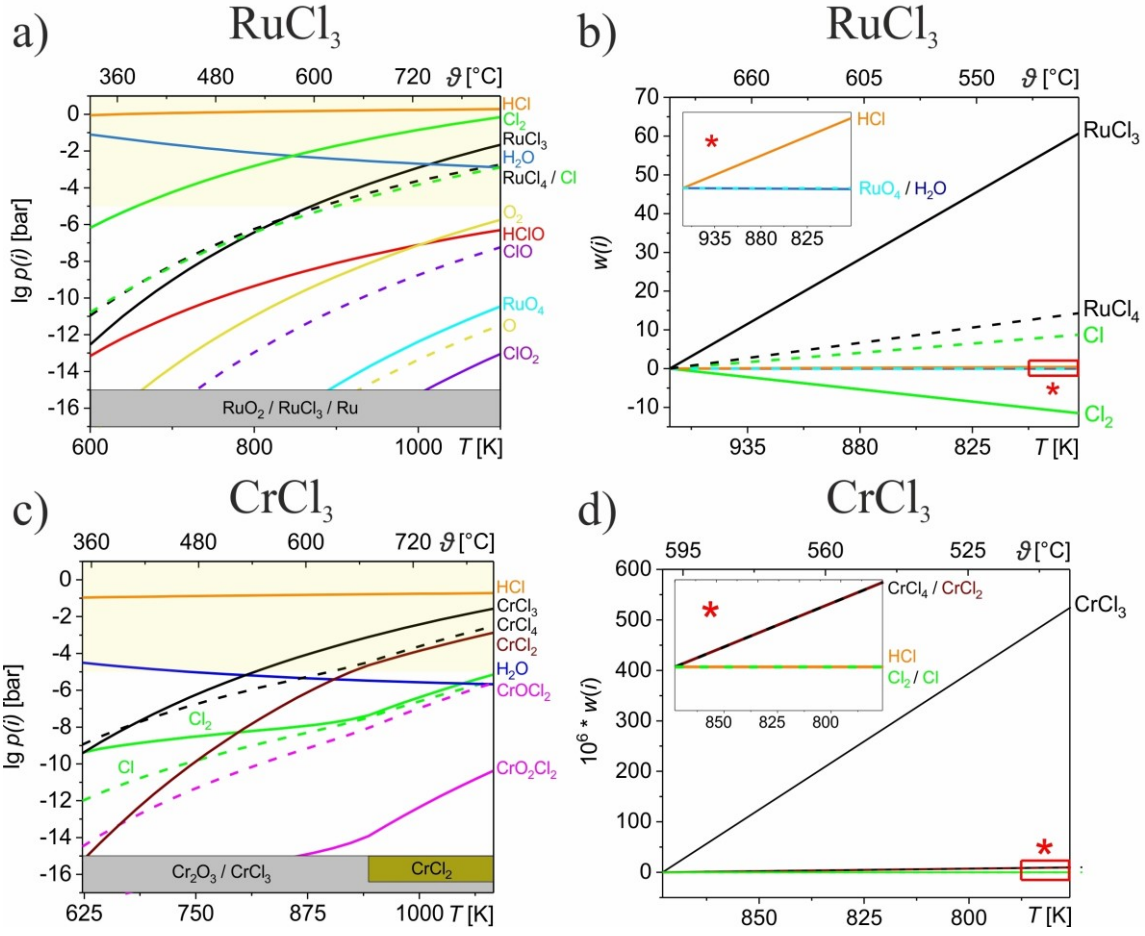

Figure 17: Thermodynamic simulations using TRAGMIN of: **(a)** $RuCl_3$ system: partial pressures of the component species in the one-room-gas phase; the yellow area indicates the transport relevant area for species with a partial pressure higher than 10^{-5} bar (with respect to the logarithmic application of values) and **(b)** $RuCl_3$ system: transport efficiencies for temperatures 973 → 773 K (ΔT = 200 K) with transport agent Cl_2 and transport efficient gas species dominated by the sublimation of $RuCl_3$ and small amounts of $RuCl_4$ and Cl, the inset is showing low transport efficiencies for rather negligible components, **(c)** $CrCl_3$ system: partial pressures of the component species in the one-room-gas phase and **(d)** $CrCl_3$ system: transport efficiencies for temperatures 873 → 773 K (ΔT = 100 K) dominated by sublimation of $CrCl_3$, the inset is showing low transport efficiencies for negligible components; figures partly reproduced from references [123,126].

Unlike $RuCl_3$ and $CrCl_3$, the simulations of MCl_3 (M = Mo, Ti) revealed that the addition of a suitable transport agent is necessary for successful vapor transport of $MoCl_3$ and $TiCl_3$ with rather low, but still efficient transport rates. A low partial pressure of $MoCl_3$(g) prevents a pure transport relevant sublimation (see Figure 18a and b, page 44). For the deposition of $MoCl_3$ crystals the introduction of $MoCl_5$ promotes the formation of several heterogeneous and homogeneous gas phase equilibria (see appendix, Table A 2, page 124 and Figure 18a) in accordance with literature by *Schäfer*.[134,135] The implemented calculations prove that even Cl_2, instead of $MoCl_5$, is suitable as transport addition, as it forms immediately $MoCl_4$ and $MoCl_5$. As a result $MoCl_3$ can react (in the sense of CVT) with $MoCl_5$ as the active transport agent to form volatile $MoCl_4$. In fact, it is important to ensure the presence of an excess of chlorine, either by the pure element or other chlorides, such as $AlCl_3$. Assuming a stoichiometric approach, without Cl_2 excess, the equilibrium of introduced $MoCl_3$ is controlled by decomposition into solid $MoCl_2$ and gaseous $MoCl_4$. Unlikely to $RuCl_3$, the partial pressure of $MoCl_5$ is too low for a pure auto-transport.[124] Supposing the introduction of low amounts of $MoCl_5$, the calculations reveal that temperatures of 743 → 673 K (ΔT = 70 K) are favorable for deposition of $MoCl_3$ crystals. $MoCl_5$(g) acts as the transport agent, while $MoCl_4$(g) is the transport efficient gas species (see appendix, Table A 2, page 124 and Figure 18b). The inherence of minimal amounts of water supports the evaporation of molybdenum oxychlorides like $MoOCl_3$(g), MoO_2Cl_2(g) and $MoOCl_4$(g) (see Figure 18a, page 44). By a further heterogeneous equilibrium MoO_2Cl_2(g) and $MoOCl_4$(g) additionally functions as transport agents and $MoOCl_3$(g) as transport efficient component. However, the efficiency of this equilibrium is very low and in comparison to the main transport equilibrium ($MoCl_5$(g) and $MoCl_4$(g)) in fact insignificant (see Figure 18b).

With respect to $TiCl_3$ the situation is somewhat different and more complex. $TiCl_3$ sublimes at elevated temperatures (T_d = 1017 K) by formation of both $TiCl_3$(g) and Ti_2Cl_6(g) with partial pressure > 10^{-5} bar above 700 K. Indeed, calculations prove that vapor growth of $TiCl_3$ can be achieved by pure sublimation at temperatures 900 → 800 K (ΔT = 100 K) assuming a stoichiometric approach of Ti:Cl = 1:3 (according to $TiCl_3$). However, these elevated temperatures are accompanied with rather high transport rates, advantageous for thicker flakes but adverse for the formation of thin sheets. By decreasing the temperatures down to 700 → 600 K vapor transport fails without addition of a transport agent due to too low partial pressures of $TiCl_3$(g) and Ti_2Cl_6(g). Moreover, an auto-transport of $TiCl_3$ is foreclosed thermodynamically, similar to $MoCl_3$. Modeling showed that Al_2Cl_6(g) and Cl_2(g), in theory suited as potential transport agents of $TiCl_3$, are less convenient for efficient crystal growth.

Thereby addition of $AlCl_3$ acts as a chlorinating agent (oxidizing $TiCl_3$). With respect to pure chlorine, the free *Gibbs* energy exhibit a rather high negative value ($\Delta_r G^0_{700} = -110.8$ kJ·mol^{-1}) and thus a high equilibrium constant K_p, preventing efficient recondensation of $TiCl_3$ at the sink zone. Vice versa, applying Al_2Cl_6(g) the free *Gibbs* energy is positive ($\Delta_r G^0_{700} = +113.9$ kJ·mol^{-1}) but the equilibrium constant K_p is low. Thus, only a low amount of transport necessary $TiCl_4$(g) is formed. Vapor transport under softer conditions was successfully calculated by introduction of low amounts of $GaCl_3$. By adding of $GaCl_3$ (respectively Ga_2Cl_6) the transport reactions reach almost equilibrium conditions ($\Delta_r G^0_{700} = +13.5$ kJ·mol^{-1}), meaning an equalized ration between $TiCl_3$(s) and $TiCl_4$(g). This characteristic is pointing towards a well-suited transport agent, since dissolution and condensation can be realized effectively. Moreover, $GaCl_3$ is more volatile (and less stable) than Al_2Cl_6, that favors vapor transport since the equilibrium is shifted to the product side (formation of $TiCl_4$(g) and GaCl(g)).

By adding minor amounts of $GaCl_3$ several heterogeneous and homogeneous gas phase equilibria are formed (see appendix, Table A 2, page 124 and Figure 18c, page 44). The thermal treatment of powders initially form $GaCl_3$(g) and Ga_2Cl_6(g). These gaseous molecules are important to generate the volatile molecule $TiCl_4$(g). In two reversible equilibria both molecules ($GaCl_3$(g) and Ga_2Cl_6(g)) function as transport agents, while $TiCl_4$(g) and GaCl(g) are transport efficient gas species (see appendix, Table A 2, page 124 and Figure 18d). These two equilibria dominate the vapor transport of $TiCl_3$ (with respect to the addition of low amounts of $GaCl_3$). Thereby, Ga_2Cl_6(g) is the dominating transport agent (see Figure 18d, page 44) since its partial pressure is more temperature dependent, than those of $GaCl_3$(g) and thus causing higher efficiency. Further homogeneous equilibria form more negligible components like Ga_2Cl_2(g) and Ga_2Cl_4(g). Assuming minimum amounts of residual water, titanium oxychlorides (TiOCl and $TiOCl_2$) form besides TiO_2(g), but with low partial pressures. By increasing the transport temperatures up to 800 → 700 K, with respect to the prior addition of $GaCl_3$, the amount of sublimation starts to increase. By further enhancement to 900 → 800 K the sublimation of $TiCl_3$(g) dominates the vapor transport, and the actual transport equilibria of $GaCl_3$(g) and Ga_2Cl_6(g) are suppressed. The calculations confirm *Schäfers* early assumptions ($GaCl_3$ is a suitable transport agent for crystallization of $TiCl_3$).[61] Additional transport effect by formation of gas complexes $TiGaCl_6$ or $TiGa_2Cl_9$ can be assumed. However, the knowledge on these individual complexes is vague and thermodynamic data are not available, so that modeling of respective gas phase equilibria is currently impossible.

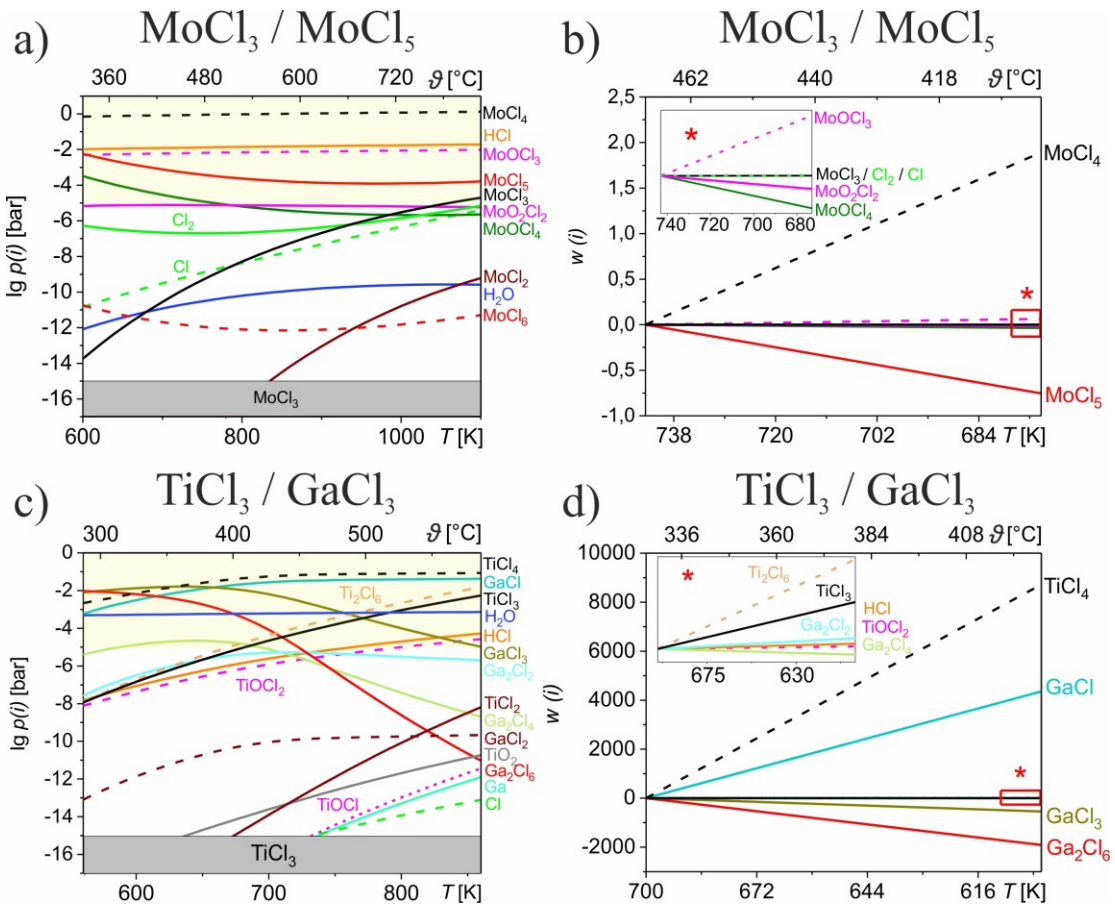

Figure 18: Thermodynamic simulations using TRAGMIN of: **(a)** $MoCl_3$ system (using $MoCl_5$ as transport agent): partial pressures of the component species ($n_{MoCl3/MoCl5} \approx 5{:}1$) in the one-room-gas phase; the yellow area indicates the transport relevant area for components with a partial pressure higher than 10^{-5} bar (with respect to the logarithmic application of values) and **(b)** $MoCl_3$ system (using $MoCl_5$ as transport agent): transport efficiencies for temperatures 743 → 673 K (ΔT = 70 K) determining $MoCl_5$ as transport agent and $MoCl_4$ as main transport efficient gas species due to the main vapor transport equilibrium, the inset is showing low transport efficiencies for rather negligible components. **(c)** $TiCl_3$ system (using $GaCl_3$ as transport agent): partial pressures of the component species ($n_{TiCl3/GaCl3} \approx 5{:}1$) in the one-room-gas phase, **(d)** $TiCl_3$ system (using $GaCl_3$ as transport agent): transport efficiencies for temperatures 700 → 600 K (ΔT = 100 K) pointing towards Ga_2Cl_6 and $GaCl_3$ as transport agents, while $TiCl_4$ and GaCl are the main transport efficient gas species; the inset is showing low transport efficiencies for rather negligible components; figures partly reproduced from references [124,128].

4.1.2 CrX_3 (X = Cl, Br, I)

For rational prediction of suitable synthesis conditions the vapor transport of CrX_3 (X = Cl, Br, I) compounds was modeled, similar to MCl_3 structures. The calculations revealed that an excess of halide X (X = I, Br) of about 0.05 mmol is suitable for the vapor growth of chromium halides (CrI_3 and $CrBr_3$) with rather low transport rates. By modeling CrI_3 vapor transports, applicable transport temperatures proved to be in the temperature region 550-750 K. By applying this temperatures, several homogeneous and heterogeneous gas phase equilibria occur (see appendix, Table A 3, page 125). The decomposition equilibrium of CrI_3 is remarkable heavily shifted to the product side (formation of CrI_2(s) and I_2(g)). Further, fractional amounts of O_2(g) form Cr_2O_3(s). Thus, the residual source material is composed of CrI_2 and Cr_2O_3 (see Figure 19a, page 46). Besides iodine species (I_2(g) and I(g)), formed by

decomposition of CrI_3, the main gas phase is dominated by both $CrI_3(g)$ and $CrI_4(g)$, see Figure 19a. Well-suited CrI_3 modeling results were achieved under consideration of temperatures 923 → 823 K (ΔT = 100 K). The modeling of transports prove that at this temperatures CVT is mainly achieved by sublimation of CrI_3 (see Figure 19b, page 46). The negative slope of $I_2(g)$, respectively positive slope of I(g), arises from a homogeneous equilibrium and does not hint at a decent transport relevance. In comparison to $CrI_3(g)$ the temperature dependency of the CrI_4 partial pressure $\Delta p(CrI_4)_{source \rightarrow sink}$ is somewhat smaller. Thus, the transport efficiency of $CrI_4(g)$ is lower and vapor transport does mainly function as sublimation, not vapor transport reaction. Nevertheless, there is a small amount of $CrI_4(g)$ present at transport efficient gas species, but in fact the contribution is negligible in comparison to the sublimation of CrI_3 (see Figure 19b). However, CVT becomes transport relevant in theory at very low temperatures (623 → 523 K). In fact the transport rates, achieved at this temperatures, are too low for efficient condensation of CrI_3 crystallites. Considering further both a stoichiometric approach of Cr:I = 1:3 (CrI_3) and a shortfall of iodine CrI_{3-x} ($x \geq 0.05$) sublimation still dominates the vapor growth of CrI_3 sheets. However, by rapid increase of transport temperatures (e.g. 1123 K → 1023 K) the partial pressure of $CrI_2(g)$ and $CrOI_2(g)$ rise to be transport relevant. Thus, condensation of CrI_2, instead of CrI_3, is achieved.

Considering $CrBr_3$ and a slight excess of bromine (Br_2), the situation is exactly *vice versa* to CrI_3. Although the gas phase is dominated by elemental- and monoatomic bromine ($Br_2(g)$ and Br(g)) the ratio of CrX_3/CrX_4 (X = Br) is almost exactly reversed in comparison to CrI_3. Meaning, that even though the temperature dependency of the $CrBr_3(g)$ partial pressure is somewhat larger than in case of $CrBr_4(g)$, its absolute value starts to get transport relevant only at temperatures higher than 940 K (see Figure 19c, page 46). Since modeling showed that preferred transport rates are achieved at 923 → 823 K (ΔT = 100 K), analogously to CrI_3, vapor transport of $CrBr_3$ is realized almost completely by CVT in this temperature regime, in clear contrast to CrI_3. This can be comprehended by calculation of transport efficiencies (923 → 823 K) indicating $Br_2(g)$ as transport agent and $CrBr_4(g)$ as transport efficient gas species (see Figure 19d). Due to a homogeneous equilibrium Br(g) likewise acts as transport efficient gas species. Likely to CrI_3, there is an indicator of a very low amount of the other (negligible) transport mechanism – in case of $CrBr_3$ it is sublimation (see positive slope in the inset in Figure 19d). If higher transport temperatures are considered (1323 K → 1223 K), sublimation supersedes CVT and becomes the dominant transport mechanism. The influence of chromium oxide bromides (e.g. $CrOBr_2(g)$) are basically negligible. However, they become slightly transport relevant, but with low amounts, applying temperatures higher than 1023 K.

In further distinction to CrI_3, the dominant transport mechanism of $CrBr_3$ can be altered even at medium temperatures (923 → 823 K) by changing the amount of inserted halogen (bromine). Assuming a stoichiometric approach of $CrBr_3$ (n_{Cr}:n_{Br} = 1:3) vapor transport proceeds as self-transport. Here bromine, released due to initial decomposition of $CrBr_3$, acts as inherent transport agent that forms $CrBr_4$(g). Similar to $CrCl_3$, sublimation becomes transport relevant, instead of auto-transport, with respect to little higher temperatures (1023 → 923 K). The situation is similar under consideration of a shortfall of introduced bromine $CrBr_{3-x}$ ($x \geq 0.05$). Due to the presence of less amounts of bromine species, vapor transport is realized as sublimation (923 → 823 K). By decreasing the temperatures (723 → 623 K) vapor transport fails at bromine shortfall conditions.

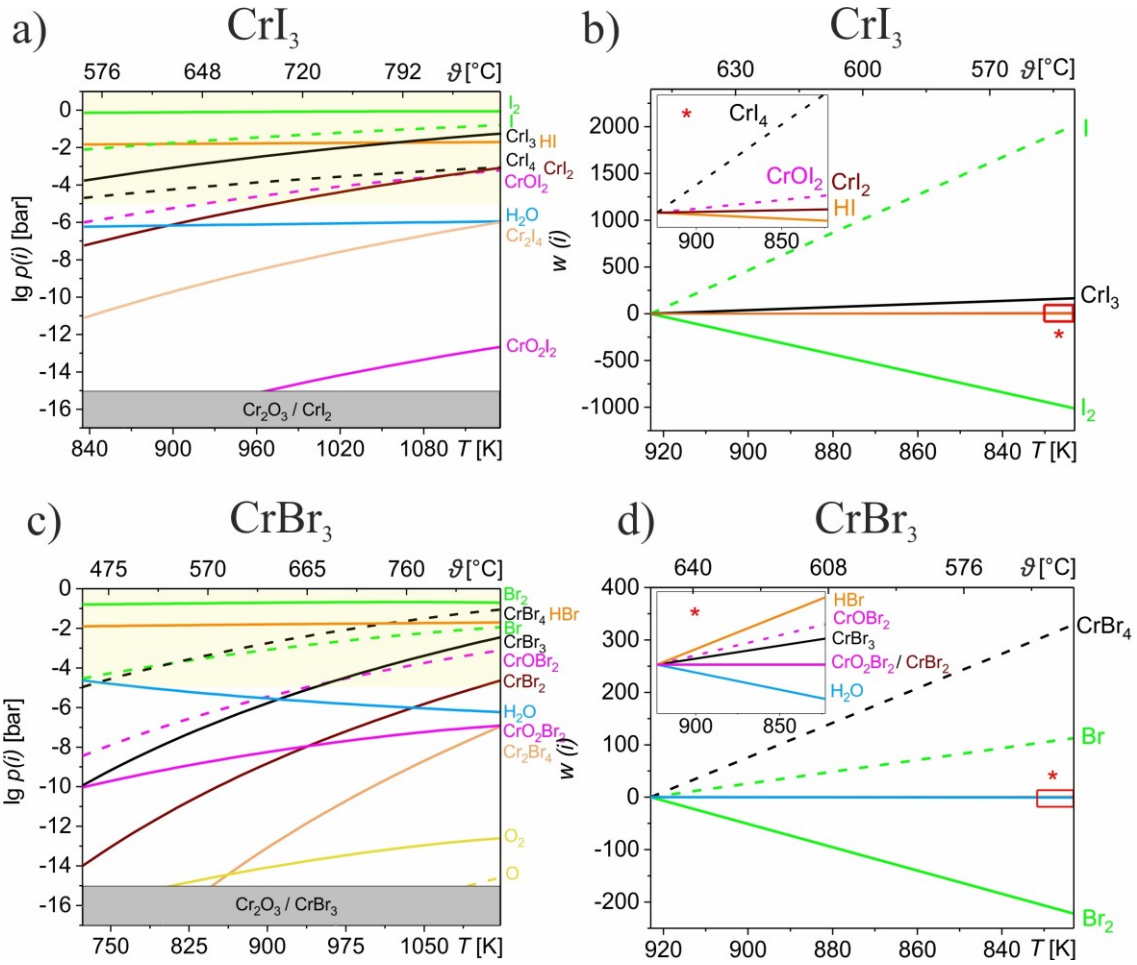

Figure 19: Thermodynamic simulations using TRAGMIN of: **(a)** CrI_3 system (proceeding from pure chromium and elemental iodine): partial pressures of the component species ($n_{Cr/I}$ ≈ 1:3.05) in the one-room-gas phase; the yellow area indicates the transport relevant area for components with a partial pressure higher than 10^{-5} bar (with respect to the logarithmic application of values) and **(b)** CrI_3 system (proceeding from pure chromium and elemental iodine): transport efficiencies for temperatures 923 → 823 K (ΔT = 100 K) determining CrI_3 as main transport efficient gas species due to sublimation (the negative and positive slopes of I_2 and I arising from a homogeneous equilibrium), the inset is showing low transport efficiencies for rather negligible components, **(c)** $CrBr_3$ system (proceeding from pure chromium and elemental bromine): partial pressures of the component species ($n_{Cr/Br}$ ≈ 1:3.05) in the one-room-gas phase and **(d)** $CrBr_3$ system (proceeding from pure chromium and elemental bromine): transport efficiencies for temperatures 923 → 823 K (ΔT = 100 K) determining Br_2 as transport agent and $CrBr_4$ and smaller amounts of Br as main transport efficient gas species, the inset is showing low transport efficiencies for rather negligible components; figures partly reproduced from reference [126].

4.2 Synthesis and characterization of bulk flakes and nanosheets of MCl_3 (M = Ru, Mo, Ti, Cr)

4.2.1 Synthesis of MCl_3 bulk flakes

Based on the assessment of suitable thermodynamic conditions by simulation (see page 39) MCl_3 bulk flakes were synthesized using chemical vapor transport in an endothermic temperature gradient. Fundamentally different parameters, like temperatures, gradients, amounts of introduced materials or the transport time, were investigated and their influence on the shape and dimensions of synthesized crystals was assessed (see overview of parameters at Figure 20, page 48).

4.2.1.1 Synthesis of $RuCl_3$ flakes

The preparation of blackish-silvery α-$RuCl_3$ platelets succeeded by using about 55 mg of $RuCl_3$ powder at mainly both 973 → 773 K (see Figure 21a, page 51) and little higher temperatures (1003 → 933 K) for at least 24 hours (see Table 4, page 50). With respect to the transport time, the amount of deposited flakes was much higher by using 72 hours, as expected by vapor transport theory. By increase of transport temperatures (1073 → 873 K) the amount of deposited material was enlarged ($TR_{exp} \approx 1$ mg/h) in consistence with simulation results. By decreasing the temperatures to 873 → 773 K the crystallite sizes was considerably reduced as well as the total amount of platelets. Under consideration of very low temperatures (773 → 673 K) no two-dimensional material was formed, which may be attributed to the crystallization of β-$RuCl_3$, which has no layered but a needle-like habitus and is formed below 773 K.[72] Basically, longer transport durations (> 24 h) and smaller temperature gradients (ΔT = 50 or 100 K) favored a crystallization of rather µm- up to mm-sized crystals. Vice versa, lower transport durations (≤ 24 h) and larger temperature gradients (e.g. ΔT = 200 K) caused crystallization alongside the whole ampoule length with much more fine crystallites. With respect to the simulated transport rates, the experimental determined values matched quite close to be about 1 mg/h or little less (see appendix, Table A 4, page 126).

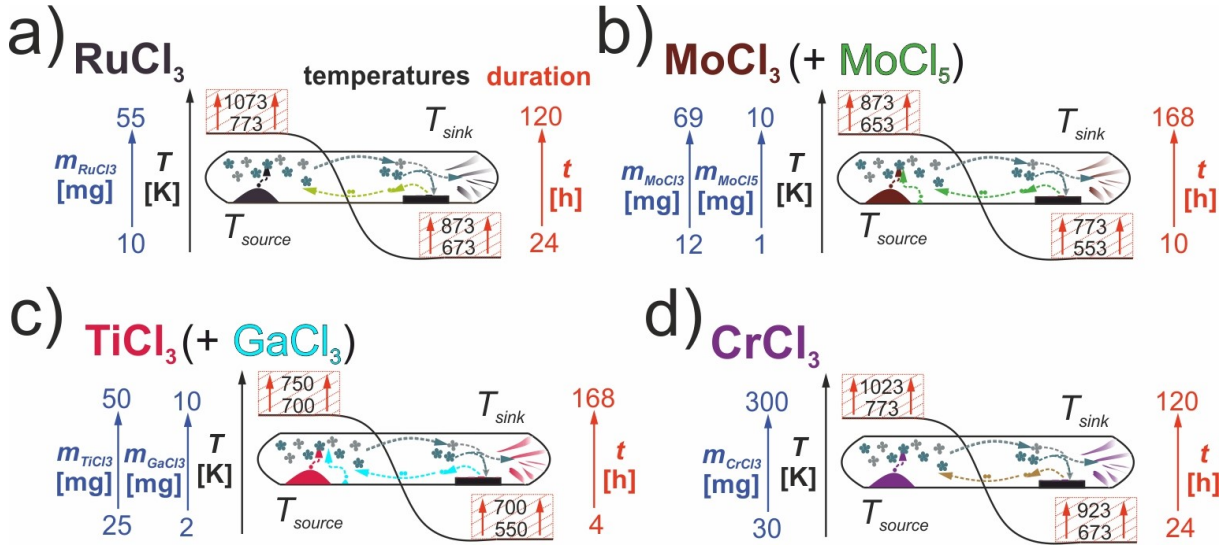

Figure 20: Scheme of applied and investigated CVT parameter (furnace temperatures in red colored dashed boxes, transport duration as well in red color, mass of introduced material MCl$_3$ and possible transport agent in blue color) for the preparation of MCl$_3$ bulk structures (M = Ru, Mo, Ti, Cr).

4.2.1.2 Synthesis of $MoCl_3$ flakes

In contrast to $RuCl_3$, the vapor transport of $MoCl_3$ was achieved by using a transport agent ($MoCl_5$), in accordance with simulation results. Typically about 50 mg of $MoCl_3$ and 5 mg of $MoCl_5$ were utilized for the synthesis of overgrown rose-like $MoCl_3$ bulk flakes (see Figure 21b, page 51) with µm-mm lateral dimensions using a temperature gradient of ΔT = 70 K (743 → 673 K) for 24 hours (see Table 4, page 50). The crystallite size could be successfully decreased to sub-mm or few µm by two approaches changing the ratio of introduced $MoCl_3/MoCl_5$. The first attempt is a decrease of amount of inserted $MoCl_3$ (e.g. down to 12.5 mg $MoCl_3$ and constant 5 mg $MoCl_5$) due to a prevention of an oversaturation of the gas phase. Moreover downsizing ($MoCl_3$ crystallites) becomes possible by reduction of the chlorine excess (e.g. by introduction of only 1 mg $MoCl_5$ and 50 mg $MoCl_3$). Thus the formation of transport relevant $MoCl_4$ is reduced and the transport rate is decreased, accompanied with no overgrown polycrystals or agglomerates but isolated, smaller $MoCl_3$ sheets.

Similar to $RuCl_3$, larger temperature gradients (ΔT = 150 K) prefer the growth of structures with smaller surface areas. However, the small platelets further form intertwining agglomerates which may be attributed to the presence of Mo-Mo dimers.[45] Particular importance comes along with the choice of the sink temperature. By application of T_{sink} > 673 K formation of $MoCl_2$ slightly starts, instead of $MoCl_3$, with a discernible yellow color (of $MoCl_2$). This is achieved due the disproportion equilibrium of $MoCl_3$ (to $MoCl_4$(g) and $MOCl_2$(s)). At T_{sink} > 773 K the disproportion is heavily strengthened and a yellow to brown condensation indicates the formation of $MoCl_2$. Further details concerning the bulk synthesis (see Figure 20)

can be checked at [75]. The experimental transport rates are in general about two powers of ten larger than the calculated ones which might be attributed to several reasons, e.g. not fully consistent thermodynamic data were used for modeling potentially. There might be even some unconsidered gas species (e.g. H_2MoO_4) under real (experimental) conditions.

4.2.1.3 Synthesis of $TiCl_3$ flakes

For crystallization of $TiCl_3$ bulk crystals thermodynamically favorable conditions were achieved by utilization of $GaCl_3$ as respective transport agent. In consensus with simulation results advantageous thermodynamic conditions were gained by usage of about 25 mg $TiCl_3$ powder and 2 mg $GaCl_3$ (see Figure 20, page 48). Crystal growth of dark purple platelet-shaped $TiCl_3$ hexagons or half-hexagons succeeded at relatively low temperatures (700 → 600 K, ΔT = 100 K) for around 4 hours (see Figure 21c, page 51 and Table 4, page 50). An enlargement of the transport temperatures (750 → 650 K) led to the deposition of a higher amount of $TiCl_3$ crystals with larger lateral dimensions due to a higher transport rate. In consistence with observations made with $RuCl_3$ and $MoCl_3$, and in accordance with basic nucleation theory, low temperature gradients (ΔT = 50 K) and larger transport durations (> 4 h) resulted in the emergence of thicker flakes, mainly located at the end of the ampoule. On the contrary larger temperature gradients (ΔT = 150 K) and lower transport times (e.g. 1 h) led to the deposition of thinly dispersed crystallites alongside the whole ampoule.

Similar to observations made with $MoCl_3$, the $TiCl_3$ crystallites lateral dimensions could be altered by changing the ratio of inserted $TiCl_3/GaCl_3$. By decreasing the chlorine excess (with respect to inserted $GaCl_3$) the crystallite sizes could be slightly reduced. Furthermore the lateral extent (of $TiCl_3$ platelets) receded significantly by reduction of introduced $TiCl_3$ powder (e.g. only 5 mg instead of 25 mg) from mm to µm sizes, which can be attributed to the thermodynamic laws of nucleation and growth. Further details with respect to the bulk crystal growth of $TiCl_3$ can be checked at reference [136]. The calculated transport rates of $TiCl_3$ are much higher than the experimentally achieved (see appendix, Table A 6, page 126). Although the aim was to prepare bulk flakes, the amount of inserted material ($TiCl_3$ + $GaCl_3$) is quite low (several milligrams). Thus, the rate-determining step might not be the diffusion of the gas phase, as assumed by the simulation, but additional kinetic effects at the dissolution of the starting materials and precipitation of crystals (see appendix, Table A 5, page 126). This might explain the experimental observed low yields of $TiCl_3$.

4.2.1.4 Synthesis of $CrCl_3$ flakes

Highly crystalline $CrCl_3$ bulk flakes with few hundred µm lateral extent were prepared, just as $RuCl_3$, without the application of a respective transport agent from about 150 mg $CrCl_3$ powder and the utilization of a temperature gradient of ΔT = 100 K (873 → 773 K) for at least 24 hours (see Figure 20, page 48). By enlarging the transport duration up to 7 days, the flakes appeared as large purple platelets with several mm in diameter. Likewise the size of flakes could be enlarged by increasing the amount of introduced material ($CrCl_3$), e.g. chromium(III) chloride flakes with diameters of around 5 mm could be observed by utilization of 300 mg $CrCl_3$ (starting material, powder). Particular details on the growth of bulk $CrCl_3$ sheets can be checked at reference [137]. Similar to $TiCl_3$, the calculated transport rates are higher than the experimentally determined (see appendix, Table A 7, page 127). Based on the evaluation of assessed transport parameters, optimal growth conditions could be determined (see Table 4).

Table 4: Experimentally determined optimum vapor transport parameter for the growth of MCl_3 bulk flakes.

MCl_3	$m(MCl_3)$ [mg]	Transport agent (TA)	m(TA) [mg]	Temperatures [K]	Duration [h]
$RuCl_3$	50	-	-	973 → 773	24
$MoCl_3$	50	$MoCl_5$	5	743 → 673	24
$TiCl_3$	25	$GaCl_3$	5	700 → 600	4
$CrCl_3$	150	-	-	873 → 773	24

4.2.2 Characterization of MCl_3 bulk flakes

4.2.2.1 Morphology of MCl_3 bulk flakes (Light microscopy and SEM)

The morphology of MCl_3 bulk flakes was initially characterized by optical microscopy. Fundamentally, MCl_3 flakes appear as weakly coupled *van der Waals* platelets with lateral dimensions of a few hundred micrometer and thicknesses in the *µm* range (see Figure 21). Occasionally, investigating $MoCl_3$ bulk flakes led to the observation of a second manifestation in terms of rather polycrystalline rosette-shaped crystals, which could be caused by the dimerization of molybdenum atoms present in this structure (see Figure 21b).[45] Bulk sheets of $RuCl_3$ and $MoCl_3$ appeared with either silver-shiny or black color, depending on the incidence of light (*pleochroism*, see Figure 21a). Similarly, thick $TiCl_3$ flakes were black colored but usually appeared in its characteristic red-purple color, only by decreasing the samples thickness to a few *µm* (see Figure 21c). The color of $CrCl_3$ differs from the three other chlorides due to its striking pink-purple color (see Figure 21d).

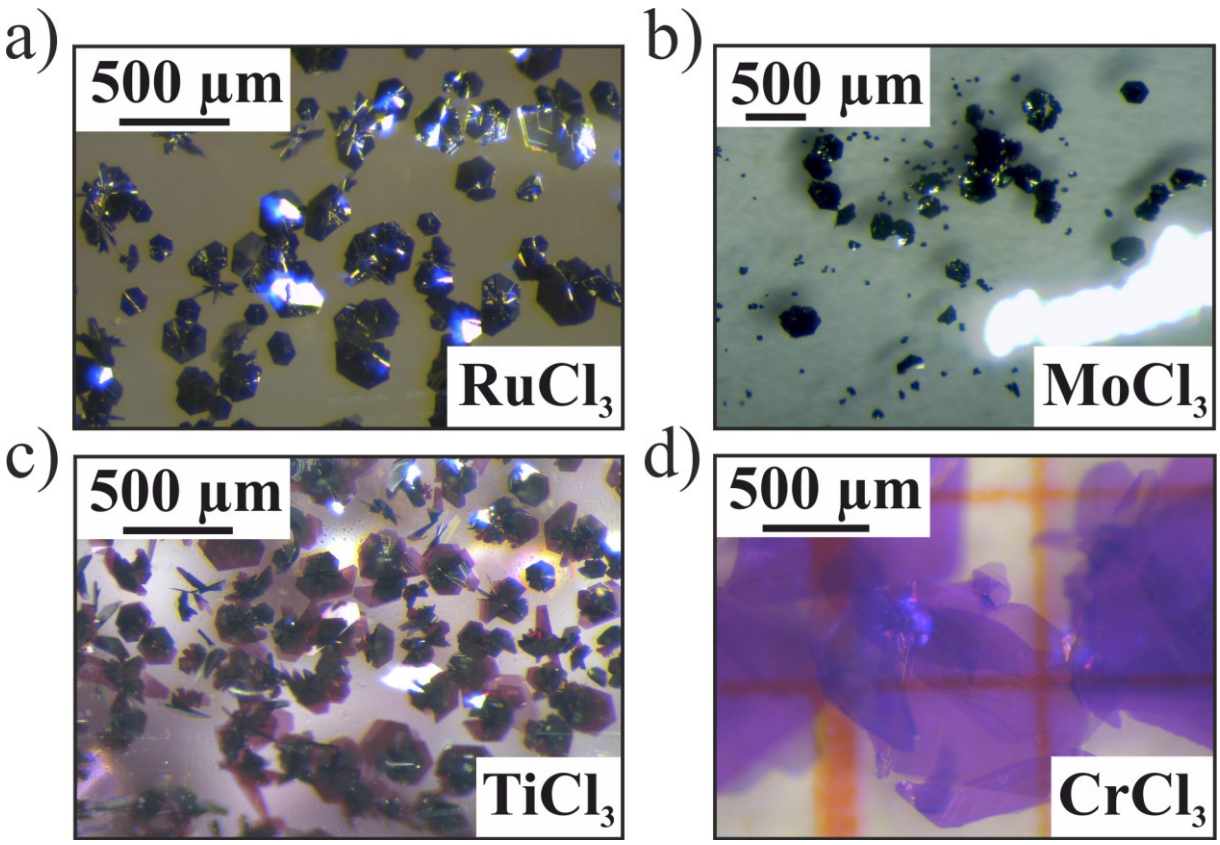

Figure 21: Optical microscopy of as-prepared MCl_3 flakes: **(a)** silvery-blackish colored $RuCl_3$, **(b)** black rosette-shaped $MoCl_3$ (these samples appeared rather as overgrown polycrystals), **(c)** black-purple, oxygen-sensitive $TiCl_3$ and **(d)** pink $CrCl_3$ with larger platelets (nearly with lateral dimensions in the mm range).

Investigating MCl_3 flakes by SEM in secondary electron contrast revealed the crystalline character of the deposited flakes with sharp edges and the typical layered nature (see Figure 22a, page 52). Further, the two-dimensionality of individual stacks of layers is highlighted by SEM imaging (see the cascade shapes in Figure 22b-d). Few specimen surface inhomogeneities (e.g. the crack in Figure 22b) could be caused by mounting the sample on the respective carbon tape due to induced strain. Additional charging effects (see Figure 22d) caused by electron beam penetration aggravated the analysis, in consequence of the electrical (mott-) insulating properties of MCl_3[8] (M =Ru and Cr) compounds.[69,138] By analyzing the morphology of MCl_3 platelets the structures were exposed to air, at least for some seconds, during the sample preparation. Thus, the appearance of "bubbles" on the MCl_3 surface was an indirect proof of air or moisture sensitivity due to ambient conditions (preparation and transfer into the device). It was found that $RuCl_3$, $MoCl_3$ and $CrCl_3$ bulk flakes are stable in air, at least of some minutes. In contrast to this, $TiCl_3$ reacts immediately with the surrounding environment (mainly oxygen and water) which becomes noticeable by emerging "dots" at the flakes surface (see Figure 22c).

[8] $CrCl_3$ exhibits insulating properties (*Mott-Hubbard*-insulator) [197], $RuCl_3$ is likewise a *Mott*-insulator.[198] An analogue was calculated for $TiCl_3$ [84], but experiments revealed semiconducting properties.[147] The investigation of the electronic properties of $MoCl_3$ are still pending, but we assume an insulator due to heavy charging effects.

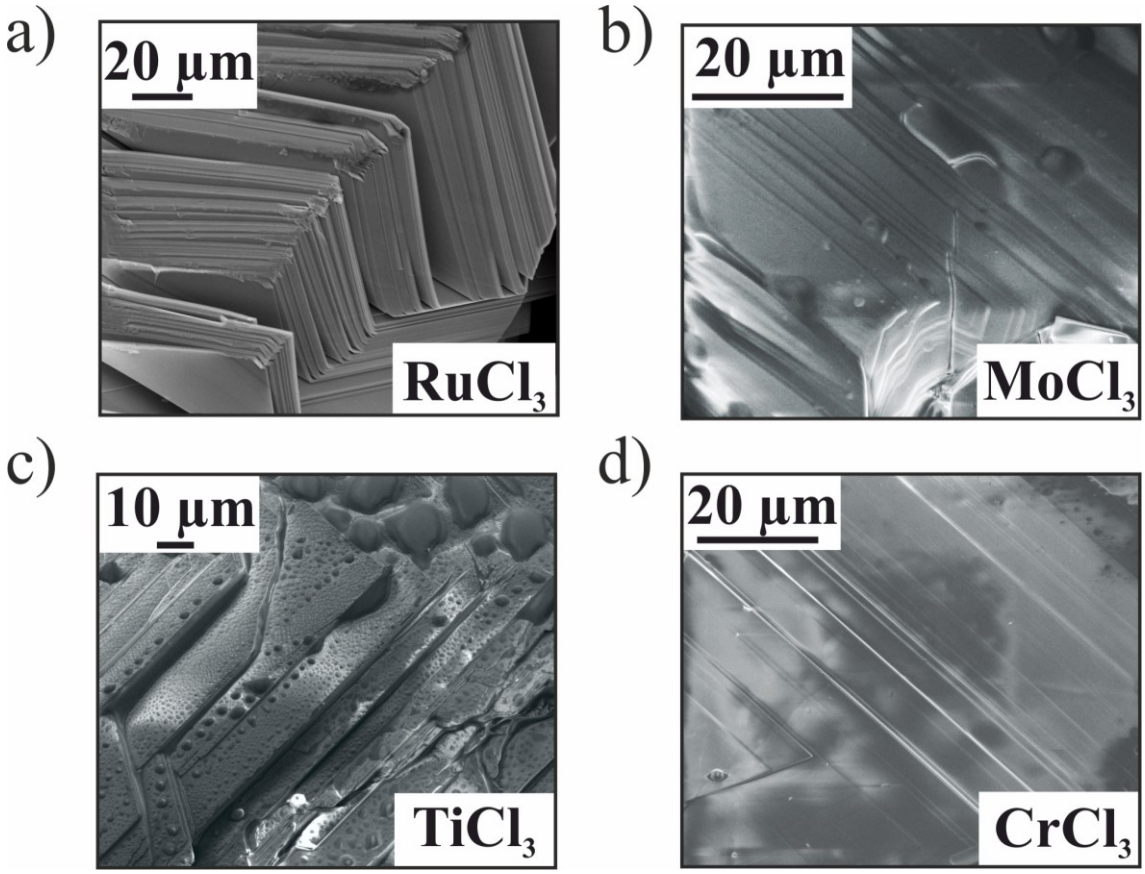

Figure 22: Two-dimensional structure of MCl_3 bulk flakes investigated by SEM: **(a)** stacks of $RuCl_3$ layers, **(b)** $MoCl_3$ layers with charging effects caused by SEM (the respective $MoCl_3$ specimen were sputtered with a thin layer of carbon previous to the SEM analysis), **(c)** $TiCl_3$ with "dotted" surface that points towards incorporation of ambient water and **(d)** the layered nature of $CrCl_3$ with minor charging effects due to electron beam penetration.

4.2.2.2 Composition of *M*Cl₃ bulk flakes (SEM/EDX, WDX, IR)

The composition of MCl_3 flakes was investigated by several spectroscopy techniques. With respect to "$RuCl_3$" samples the elemental analysis (EDX) indicated a composition close to $RuCl_3$ (Ru:Cl ≈ 1:3) by taking into account the superimposing elemental lines (Cl-*K* and Ru-*L*, see Figure 23a). Likewise, the composition of $MoCl_3$ and $CrCl_3$ fitted very well to the desired 1:3 ratio (see Figure 23b,c). Contrary to the other three systems, the observed sensitivity of $TiCl_3$ to oxygen and moisture (see Figure 22c) was confirmed by an emerging oxygen peak in the EDX spectrum (see Figure 23c). Assuming that oxygen affects the $TiCl_3$ sheets by starting its penetration from the surface, it could be assumed that $TiCl_3$ is oxidized to either an oxychloride (e.g. $TiOCl_2$) or even the pure oxide (highly likely TiO_2 or Ti_2O_3). Within all four spectra an *escape peak* of the most intense Cl-*K* line was detected looming at around 0.9 keV (see Figure 23a-d). Except for $TiCl_3$, the recorded spectra clearly show that the crystals are not affected by impurities and demonstrate the requested quantification results, fitting to a MCl_3 stoichiometry (see Figure 23a,b,d).

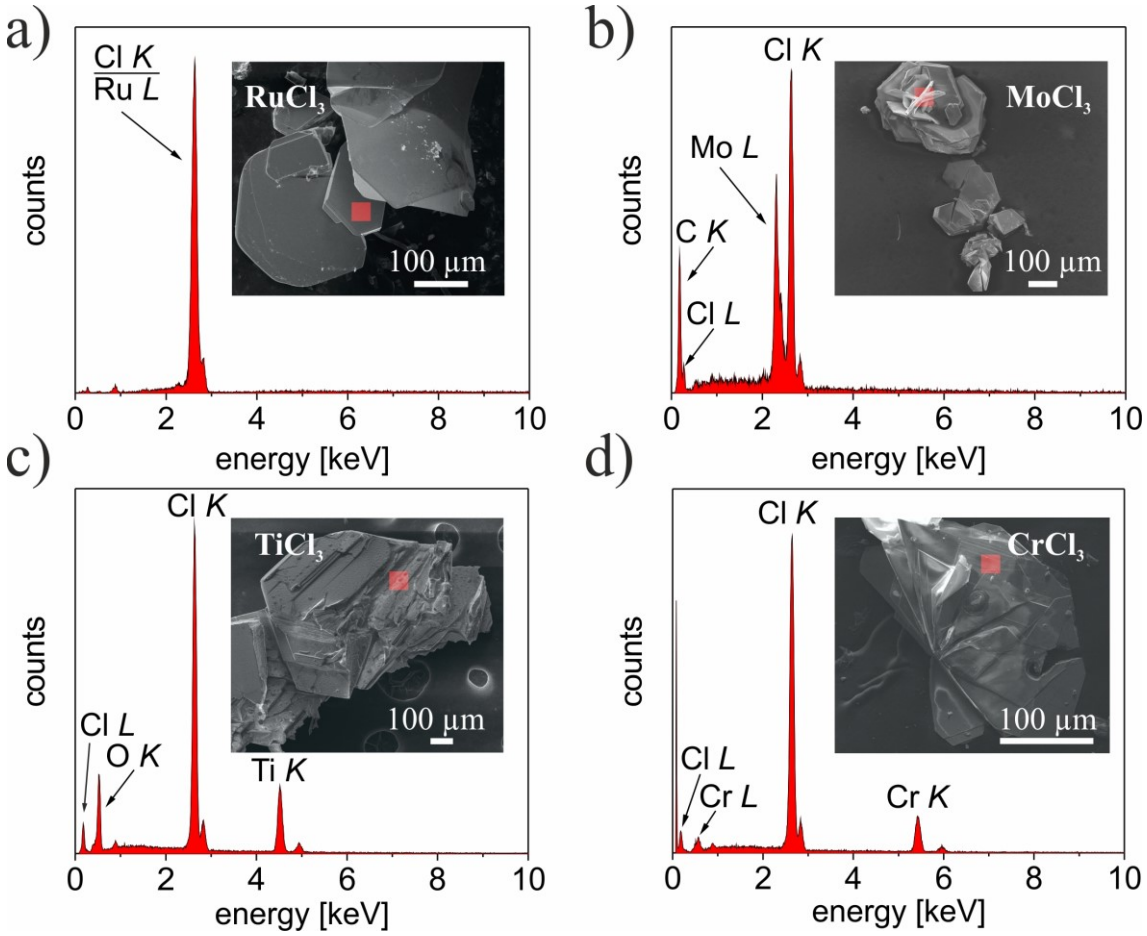

Figure 23: EDX spectra of deposited MCl_3 bulk flakes: **(a)** $RuCl_3$, **(b)** $MoCl_3$, **(c)** $TiCl_3$ and **(d)** $CrCl_3$); the inset shows the investigated MCl_3 bulk crystals, the red box is indicating the locating of the EDX measurement.

The Ru-*L* and Cl-*K* lines overlap in the energy range of 2-3 keV with respect to "$RuCl_3$" samples. Therefore additional WDX analysis was applied to confirm the EDX quantification results ($RuCl_3$). The application of wavelength dispersive resolutions led to identification of Ru-*L*α, Ru-*L*β and Cl-*K*α peaks (see appendix, Figure A 9, page 131). Moreover, the quantification results approved the EDX calculations to fit to the desired $RuCl_3$ composition.

The vibrational lattice behavior of the four investigated chlorides MCl_3 were determined by IR spectroscopy (see Figure 24, page 54). The observed spectra give detailed hints about the type of vibration. Vibrations of type E_u and A_{2u} correspond to asymmetric stretchings. Further, A_{1g} and E_g are related to symmetric lattice vibrations. Focusing $RuCl_3$, the appearance of peaks at 313 cm^{-1} and the small shoulder at 323 cm^{-1}, originating from stretching vibrations between the Ru and Cl atoms, confirming $RuCl_3$ (α-modification) due to consensus with reported literature data (see Figure 24a).[139] Similarly, the recorded spectrum of $MoCl_3$ is in good accordance with previous reported findings (see Figure 24b).[74] In case of $MoCl_3$ no comments were suggested for the type of lattice vibrations (stretching or deformation). The experimentally detected peaks of $TiCl_3$ fit noticeable good to the previous reports (see Figure 24c).[140] The absorption band of $CrCl_3$ agrees well with literature data (see Figure 24d).[25] Some reference

peaks lower in intensity (e.g. the $CrCl_3$ absorption band at 413 cm^{-1}) could not be detected. No unknown vibrations were observed, which could be probably indicators of crystal impurities.

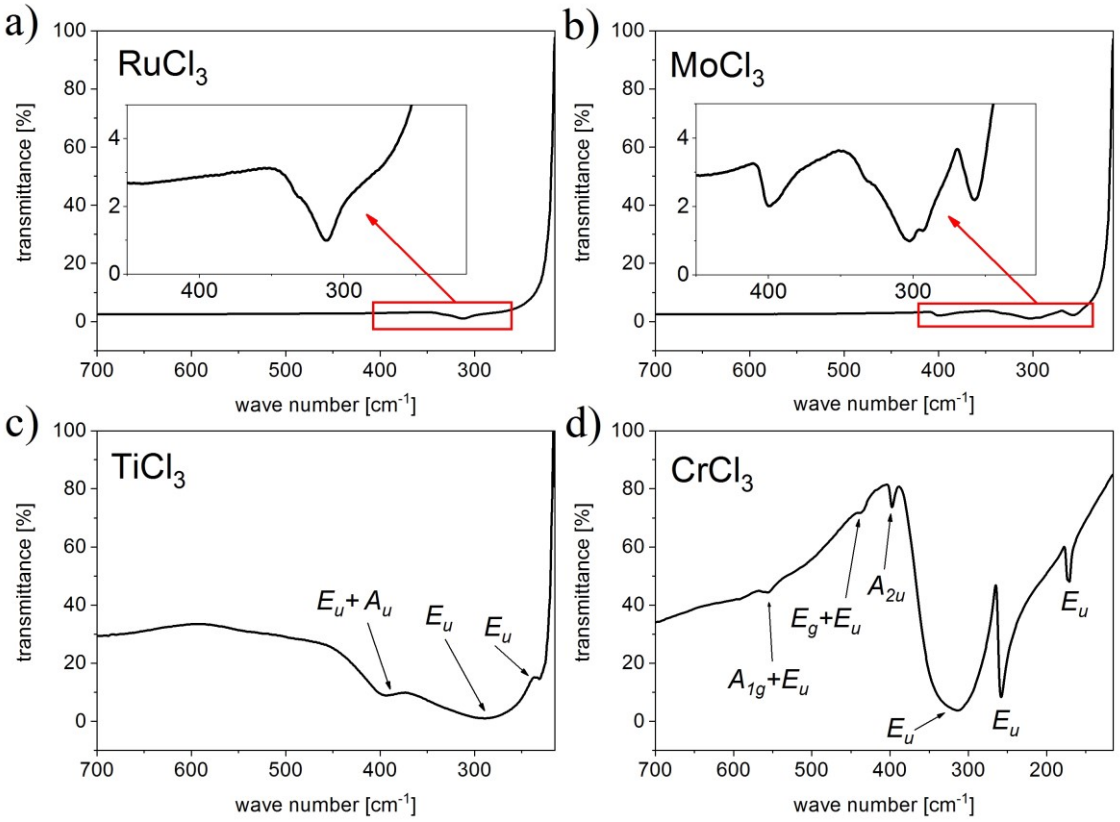

Figure 24: Infrared spectra (IR) of MCl_3 bulk flakes: **(a)** $RuCl_3$, **(b)** $MoCl_3$, **(c)** $TiCl_3$, **(d)** $CrCl_3$, in case of $RuCl_3$, $MoCl_3$ and $TiCl_3$ the spectra were obtained by application of a powder sample (KBr + MCl_3 flakes). Thus, the transmittance at low wave numbers drastically rises due to the measurement limit originating form KBr. The spectrum of $CrCl_3$ was obtained differently (crystallites from a suspension dropped onto PE foil). This resulted in a much better resolution (smaller background) and a greater measurement range of the corresponding IR spectrum.

4.2.2.3 Crystallinity of MCl_3 bulk flakes (PXRD, SCXRD)

The deposited MCl_3 platelets were investigated by means of PXRD. The diffraction pattern of all four chlorides MCl_3 are characterized by a high amount of recorded reflexes (see Figure 25, page 56). Thus, a high crystallinity of flakes is confirmed. Specifically related to $RuCl_3$, $TiCl_3$ and $CrCl_3$, the observed *Bragg* reflexes are compared with previously reported MCl_3 diffraction pattern of either monoclinic or trigonal crystal systems, which can be found in both the ICSD and ICDD database. As explained in the theory part of this thesis (see chapter 2.2.2, page 8) the crystal systems and therefore different space groups (monoclinic and trigonal) are a result of a distinct stacking order of individual sheets and thus only *polytypes* of isostructural compounds with respect to the honeycomb arrangement. Moreover, with respect to CrX_3 compounds (and also applicable to MCl_3) it was claimed that these structures undergo a temperature dependent crystallographic phase transition (α-$RuCl_3$ ≈ 150 K [141], α-$MoCl_3$ ≈ 585 K [45], α-$TiCl_3$ ≈ 217 K [142] and $CrCl_3$ ≈ 240 K [15]).[69] The high temperature phase is typically of

monoclinic ($C2/m$) symmetry.[15,45,141] The respective low temperature phase is distinguished by a higher symmetrical trigonal- (e.g. $P3_112$ [141] in case of $RuCl_3$ or $R\bar{3}H$ [15] related to $CrCl_3$) or lower symmetrical triclinic space group, which is partly associated by formation of metal dimers (e.g. Ti-Ti in case of $TiCl_3$).[77] It indicates that $MoCl_3$ is an exception, because the "phase transition" at 585 K, associated with Mo-Mo dimer breaking, maintains its monoclinic symmetry, probably due to its distorted honeycomb net at room temperature.[45]

In fact, this "phase transitions", related to $RuCl_3$, $TiCl_3$ and $CrCl_3$, are a shift of a dominating stacking order (either AB → ABC or ABC → AB). However, it must be assumed that, independently of the type of dominating stacking, there are still few amounts of a second *non*-dominating stacking order, present anytime in the structures due to the weak *van der Waals* bonding between the layers. Due to that, especially with $RuCl_3$ samples, many reflex positions overlap between "monoclinic $RuCl_3$" and "trigonal $RuCl_3$" (see Figure 25a, page 56). An exact determination of a single "space group" and thus the conformation of "phase purity", analogously with powder samples, proves to be impossible.

Commonly, reflexes and herein amounts of both stacking types (monoclinic and trigonal) were found to be present in thicker structures of $RuCl_3$ and $CrCl_3$ (see Figure 25a and d). Nevertheless, both crystal systems were often reported independently from each other for both compounds ($RuCl_3$ and $CrCl_3$) without a remark of a second stacking and the discussion about this topic is in general rather obscure.[143,144] By taking into account the theoretical reflexes of $CrCl_3$ ($C2/m$ and $R\bar{3}H$) and the sharp reflex (131) at around 16° 2θ (see Figure 25d) in the observed diffraction pattern, one could tentatively assume that the monoclinic space group $C2/m$ dominates the crystal structure, in accordance with reported literature of the high-temperature polytype.[69] In fact, the reflex positions of the theoretical pattern overlap too much for a final assignment. With respect to $TiCl_3$ the situation is clearer than for $RuCl_3$ and $CrCl_3$. In accordance with literature [57,85] it was found that the preferential crystallization of $TiCl_3$ flakes is realized by the trigonal space group $P\bar{3}m1$ (see Figure 25c) with only very little amounts of a "monoclinic stacking". In contrast to the other three halides but in consensus with literature [45], $MoCl_3$ adopts only a monoclinic $C2/m$ space group (and thus ABC stacking), confirmed by the realized experiments (see Figure 25b). In general it has to be remarked that the application of PXRD of MX_3 platelets is challenging since the two-dimensionality of sheets is associated with some measurement impairments, e.g. preferential orientations or intensity loss. Further, the stacking order can be easily changed unintended, possibly by the influence of mechanical force, e.g. by the preparation of samples for XRD measurements in capillaries.

Nonetheless the observed measurements proofed the high crystallinity and the desired phase identification of the MCl_3 structure without impurities, e.g. various oxychlorides or oxides.

Individual flakes of $RuCl_3$, $MoCl_3$ and $CrCl_3$ were further characterized using SCXRD (see example of $CrCl_3$ in the appendix, Figure A 1, page 128). The results indicated that, at least the majority of the investigated crystals, crystalized in the monoclinic space group ($C2/m$). Though, some few platelets of $CrCl_3$ matched also to the trigonal space group ($P3_112$). Considering the powder- and single crystal X-ray diffraction results $RuCl_3$, $CrCl_3$ and $MoCl_3$ are probably dominated by the monoclinic space group $C2/m$, while $TiCl_3$ crystallized preferably in a trigonal crystal system. Eventually, SCXRD experiments with $TiCl_3$ failed due its extreme oxygen sensitivity.

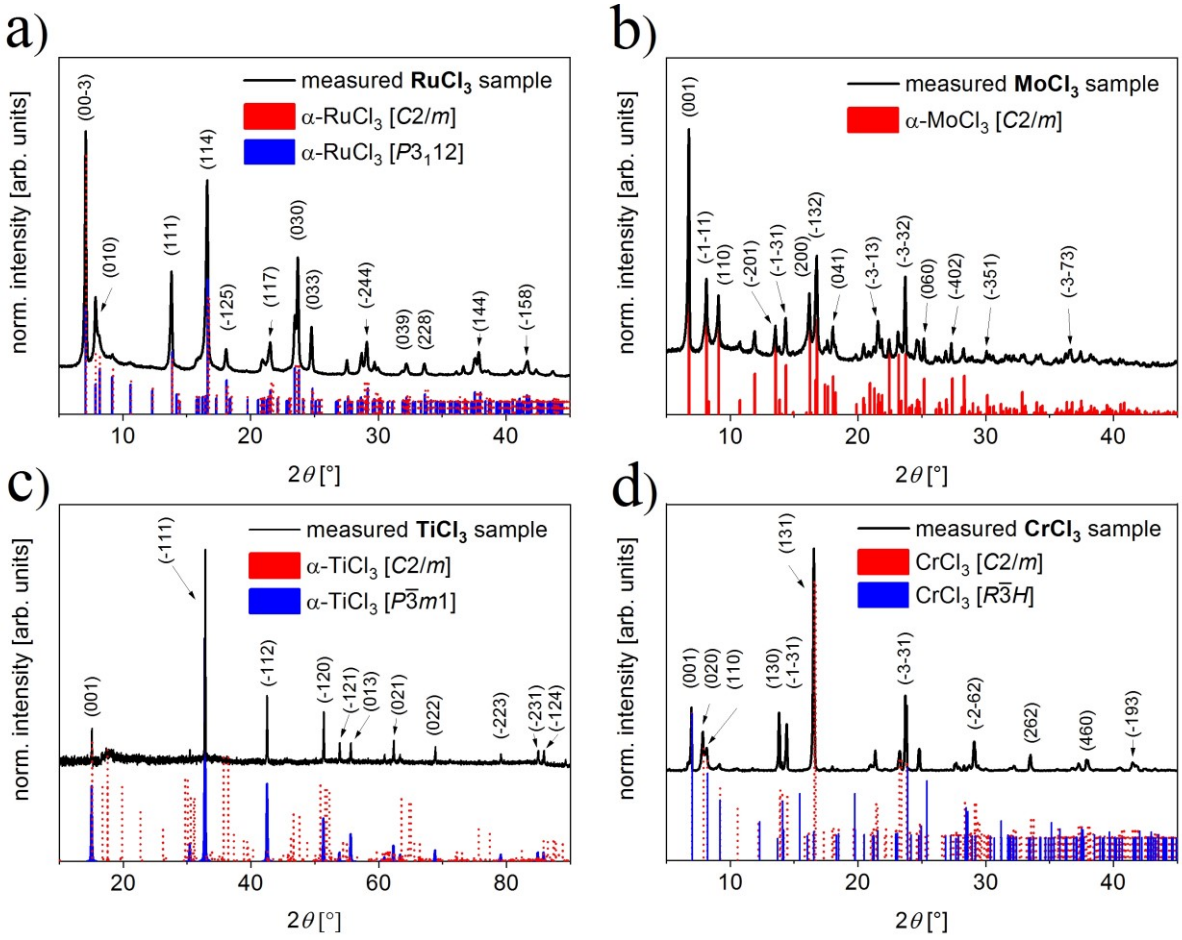

Figure 25: PXRD pattern of MCl_3 bulk flakes: **(a)** $RuCl_3$, **(b)** $MoCl_3$, **(c)** $TiCl_3$ and **(d)** $CrCl_3$ with indexed reflexes in brackets and experimental observed powder pattern (black) and either monoclinic (red) or trigonal (blue) reference pattern that associate an ABC (red) or AB stacking of MCl_3 layers (blue).

4.2.2.4 Magnetic properties of MCl_3 bulk flakes (SQUID)

The magnetic properties of MCl_3 platelets were determined by VSM-SQUID magnetometry. Related to as-prepared $RuCl_3$ polycrystals, the $m(T)$ curve (respectively $\chi_g(T)$) indicated an antiferromagnetic ground state (↑↓) with respect to an external magnetic field of $\mu_0 H$ = 0.1 T, considering the drop of magnetization below 14 K (see Figure 26a, page 58). In accordance with previous experimental observations [12,145] two magnetic transitions at *Néel* temperatures (T_N) of 7 K and 14 K are clearly visible (see Figure 26a). As stated in the literature [146], these transitions can be attributed to a coincident occurrence of ABC and AB stacking sequences of individual $RuCl_3$ layers, in accordance with observed PXRD results (see Figure 25a, page 56).

In contrast, $MoCl_3$ shows a diamagnetic behavior at $\mu_0 H$ = 1 T (see Figure 26b) in consistency with previous reported magnetic data.[135] *Schäfer* et al. showed that the composition of Mo/Cl do not need to be exactly 1/3 (according to $MoCl_3$) and actually exhibits a phase width ranging from $MoCl_{2.98}$ to $MoCl_{3.08}$.[135] By changing the amount of chlorine the magnetic behavior switches from dia- to paramagnetic (ratio of Cl/Mo ≥ 2.99) and thus the type of magnetism emerges at a threshold.[135]

Concerning $TiCl_3$, the interpretation of the measured data is somewhat more difficult. The literature is rather inconsistently with respect to magnetic data of $TiCl_3$, probably due to the existence of many polymorphs (α-δ).[54] Early assumptions of an antiferromagnetic behavior (T_N = 265 K) by *Cavallone* et al. [147] were discarded due to contradictory neutron diffraction experiments.[142] *Tsutsumi* et al. and *Motizuki* et al. observed two anomalies in the susceptibility data, respectively magnetic phase transitions at 60 and 217 K.[142,148] They attributed the latter (217 K) to a first-order phase transition by a discontinuous decrease of *a* and increase of *c* lattice parameters, accompanied with indications by differential thermal analysis. Later, *Angelkort* described that the 217 K transition is related to a reduction of symmetry and dimerization of titanium atoms in-plane of the honeycomb layers and thus indicating antiferromagnetic coupling.[77] Further calculations again contradict the dimerization of Ti atoms and the complete absence of strong magnetic interactions in α-$TiCl_3$.[84] In this work similarly no phase transitions or signs of antiferromagnetic low temperature coupling between $TiCl_3$ layers were observed using an external magnetic field of $\mu_0 H$ = 1 T (see Figure 26c). The occurrence of the paramagnetic phase could be associated with non-established magnetic spin interactions between Ti atoms.[77] A possible explanation of the absence of the transitions would probably be the contamination of α-$TiCl_3$ with β-$TiCl_3$ or even TiO_2, which are paramagnetic.[59,149] Most likely, the transfer of the $TiCl_3$ platelets to the device affected the measurement, since *Schäfer*

and *Fritz* described the observation of a pure paramagnetic susceptibility of $TiCl_3$ incorporated with six moles of crystal water ($TiCl_3 \cdot 6\ H_2O$).[150]

The magnetic properties of $CrCl_3$ (see Figure 26d) are more complex and are presented in detail alongside with the CrX_3 (X = Br, I) structures (see chapter 4.3.2.4, page 85).

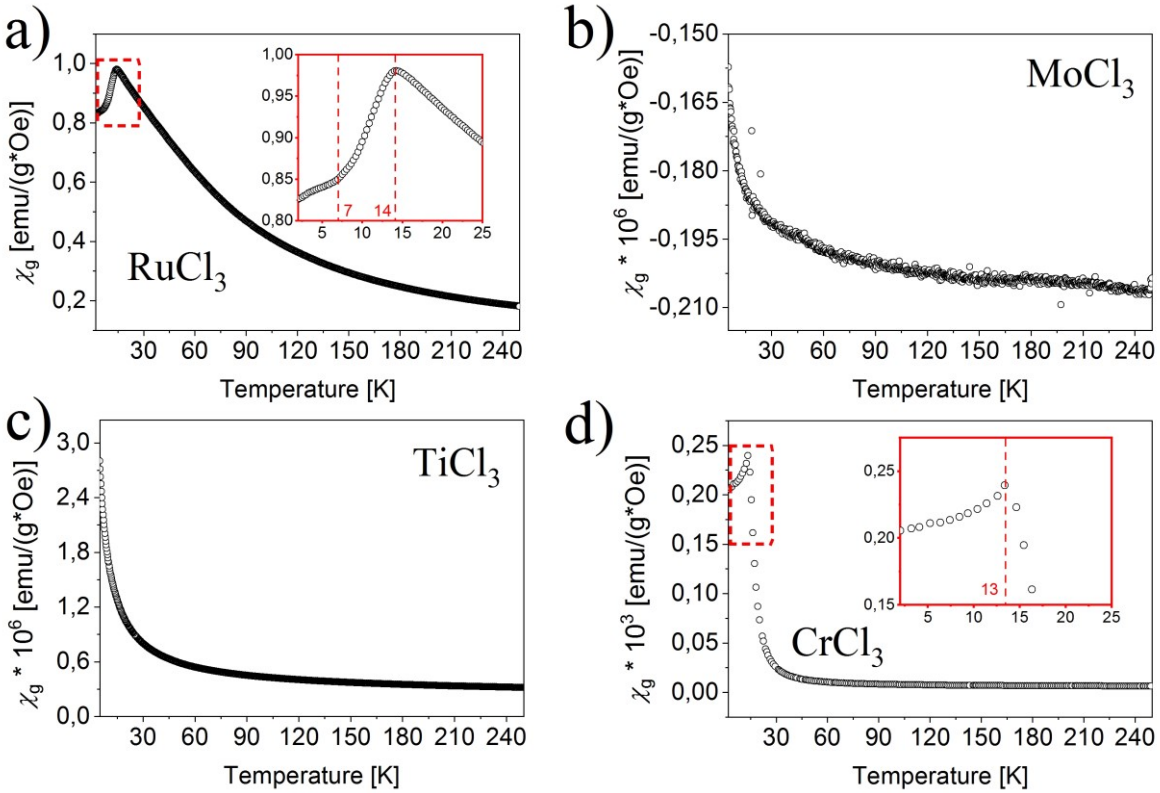

Figure 26: Magnetic properties ($\chi_g(T)$ curves) of MCl_3 platelets determined by SQUID magnetometry, the trend of the mass susceptibility indicates an antiferromagnetic (AFM) ground state (↑↓) present at **(a)** $RuCl_3$ at $\mu_0 H$ = 0.1 T and **(d)** $CrCl_3$ at $\mu_0 H$ = 0.1 T. In contrast, **(b)** $MoCl_3$ and **(c)** $TiCl_3$ show diamagnetic, respectively paramagnetic behavior using an external magnetic field of $\mu_0 H$ = 1 T.

4.2.3 Synthesis of MCl_3 nanosheets on substrates

4.2.3.1 Synthesis of $RuCl_3$ micro- and nanocrystals

Based on the modeling results (see chapter 4.1.1, page 39), MCl_3 micro- and nanosheets were grown by vapor transport in an endothermic temperature gradient. The utilization of about 1 mg of $RuCl_3$ powder was sufficient for deposition of "phase pure" micro- and nanosheets on top of YSZ substrates without the addition of a transport agent (see Figure 28, page 62). For $RuCl_3$ nanosheet transports the experimentally determined (ideal) temperature gradient of 973 → 773 K (ΔT = 200 K) proved to be successful (see Table 5, page 61). By reaching constant final temperatures (973 and 773 K) the entire furnace was switched-off and the hot ampoule was quenched with water. Application of higher temperatures (1373 → 1173 K, ΔT = 200 K) led to the crystallization of fewer structures on top of the YSZ substrate (see appendix, Figure A 2, page 129). In contrast to this, utilizing lower temperatures (873 → 673 K,

ΔT = 200 K) resulted in no crystal growth at all and the color of the YSZ substrate changed to brown, possibly due to a deposition of β-$RuCl_3$ (which has a brown color). By application of another type of substrate, e.g. sapphire (Al_2O_3), substituting YSZ, a deposition of thin $RuCl_3$ nanolayers was possible by using adequate parameters (973 → 773 K, ΔT = 200 K). Fairly good results were further obtained using $LaAlO_3$ as substrate material (see appendix, Figure A 4, page 129). Utilizing $SrTiO_3$ led to the deposition of rather thick $RuCl_3$ micro-, but no nanosheets (see appendix, Figure A 3, page 129). The application of Si/SiO_2 substrates, instead of YSZ, resulted in a complete failure of crystal growth, possibly due to formation of Ru_nSi_m or Si_nCl_m species (see Figure 27). Likewise, the utilization of Ag, BaF_2 or LiF surfaces (substrates) for deposition of $RuCl_3$ nanosheets was associated without any observation of crystals.

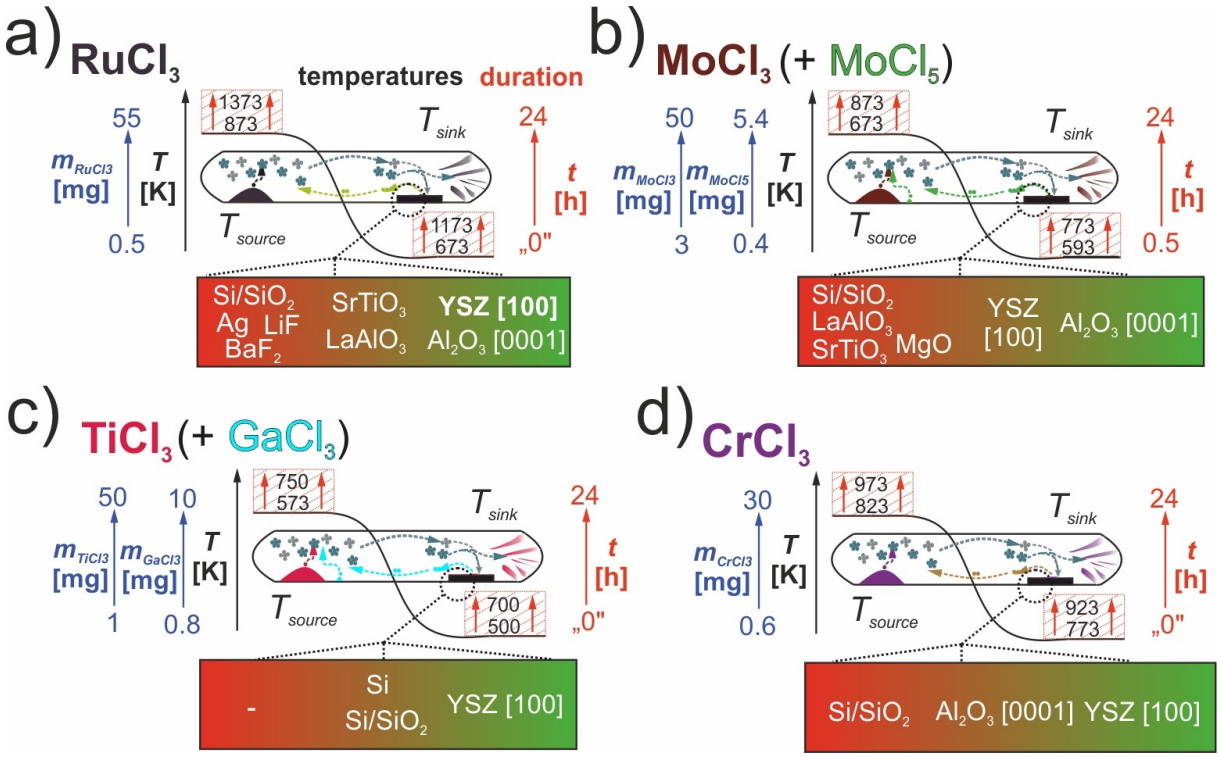

Figure 27: Scheme of investigated CVT parameter (temperatures in red dashed boxes, transport duration in red color, mass of introduced materials in blue color) for the preparation of MCl_3 micro- and nanostructures on suitable substrates: **(a)** $RuCl_3$, **(b)** $MoCl_3$, **(c)** $TiCl_3$ and **(d)** $CrCl_3$; the color bar below indicates the observed suitability of individual substrates with the focus on the deposition of highly crystalline and isolated MCl_3 micro- and nanosheets (green color means very well-suited); in contrast red color indicates a failure of crystal growth; subjectively perceived average results (with respect to layer thickness, isolated deposition and morphology) are located in the middle of the color bar (orange area).

4.2.3.2 Synthesis of $MoCl_3$ micro- and nanocrystals

In contrast to $RuCl_3$, the vapor growth of $MoCl_3$ micro- and nanocrystals was utilized by implementation of a transport agent ($MoCl_5$), similar to experiments for vapor growth of bulk $MoCl_3$ flakes (see chapter 4.2.1.2, page 48). Well-defined, isolated nanosheets were prepared on sapphire (Al_2O_3, [0001]) substrates by using a temperature gradient of ΔT = 70 K (743 → 673 K), analogously to parameters applied for the formation of thicker sheets (see Figure 27). The primary difference to the former bulk parameters is the utilization of less material (both $MoCl_3$ and $MoCl_5$) and fewer transport duration. For synthesis of thin $MoCl_3$ sheets on top of Al_2O_3 about 6 mg of $MoCl_3$ and 0.6 mg of $MoCl_5$ were used. In addition, a transport duration of one hour proved to be sufficient for the deposition of $MoCl_3$ micro- and nanosheets (see Table 5, page 61).

The deposition was also investigated utilizing Si/SiO_2, instead of sapphire. Although the vapor transport of $MoCl_3$ did not completely fail, in comparison to $RuCl_3$ and Si/SiO_2, it showed to be inhibited by some side reaction. It was obvious that the Si/SiO_2 substrate was affected mainly at the edges. XRD investigations confirmed the formation of Mo_5Si_3. Similar to $RuCl_3$, $MoCl_3$ was deposited on YSZ using temperatures 743 → 643 K (ΔT = 100 K) and 24 hours transport duration. By using YSZ large and thick microsheets (up to sub-mm sizes) crystallized on top of the substrate (see appendix, Figure A 5, page 130). Furthermore, the $MoCl_3$ vapor transport failed using MgO, $LaAlO_3$ or $SrTiO_3$ substrates (see Figure 27).

4.2.3.3 Synthesis of $TiCl_3$ microcrystals

Similar to preparations of $MoCl_3$ micro- and nanosheets and in accordance to the synthesis of bulk $TiCl_3$ flakes, the utilization of a transport agent proved to be appropriate for thinner $TiCl_3$ sheets. In accordance with thicker layers, $GaCl_3$ was applied, but in case of microsheets lower amounts were used (about 1 mg). Besides, about 5 mg of $TiCl_3$ was used principally. Similar to $RuCl_3$, YSZ was suitable for deposition of a large amount of microsheets, but at lower temperatures 700 → 600 K (ΔT = 100 K). The transport duration was set to be about one hour (see Table 5). Surprisingly, the vapor transport succeeded also by application of Si/SiO_2 (200 nm oxide layer), in contrast to MCl_3 (M = Ru, Mo, Cr) structures (see appendix, Figure A 6, page 130). Obviously, the relative low temperatures in the range 700-600 K are kinetically inconvenient for the formation of the respective titanium silicides (see Figure 27). Even the deposition on pure Si succeeded (see appendix, Figure A 7, page 130). In definite contrast to the other three investigated chlorides MCl_3 (M = Ru, Mo, Cr), the described preparation of $TiCl_3$

layers led towards sheets with thicknesses in the μm range, not thinner nanosheets (see chapter 4.2.4.1, page 62). The main reason is that the occurring transport rates are still high under consideration of the implementation of volatile $GaCl_3$ (see appendix, Table A 6, page 130).

4.2.3.4 Synthesis of $CrCl_3$ micro- and nanocrystals

The growth of $CrCl_3$ micro- and nanolayers was realized, similar to $RuCl_3$ experiments on YSZ substrates, without any addition of a transport agent, but by application of lower temperatures (873 → 773 K) and smaller temperature gradients (ΔT = 100 K), analogously to bulk $CrCl_3$ flakes (see Figure 27). Further, it was observed that very low transport durations of 30 minutes are sufficient for the deposition of mainly microsheets and few amounts of nanolayers (see chapter 4.2.4.1, page 62). A pure heating-up process similar to $RuCl_3$ (by switching-off the furnace at reaching final temperatures 873 and 773 K) yielded in the condensation of acceptable amounts of thin $CrCl_3$ structures on top of YSZ. *Vice versa*, with an enhanced transport time (1 hour) the $CrCl_3$ microsheets tended to agglomerate to even thicker structures.

The crystallite size of individual $CrCl_3$ microsheets increased by using higher amounts of $CrCl_3$ as starting material (e.g. 15 or 30 mg instead of 1 mg). By using slightly lower temperatures (848 → 748 K) the quantity of crystallized sheets was heavily decreased due to a too low partial pressure of $CrCl_3$ (see Figure 17c, page 41) at the bottom limit of transport efficiency. By implementing even lower temperatures (823 → 723 K) vapor transport failed. Similar to $RuCl_3$ and especially $MoCl_3$, the utilization of Al_2O_3 also resulted in the deposition of well-defined $CrCl_3$ microsheets by using parameters, equally implemented with YSZ (see appendix, Figure A 8, page 131). Table 5 concludes the experimentally determined optimum CVT parameters for the deposition of thin MCl_3 micro- and nanolayers directly on respective substrates.

Table 5: Experimentally determined optimum vapor transport parameter for the growth of MCl_3 micro- and nanosheets on substrates.

MCl_3	$m(MCl_3)$ [mg]	Transport agent (TA)	m(TA) [mg]	Substrate	Temperatures [K]	Duration [min]
$RuCl_3$	1	-	-	YSZ	973 → 773	5
$MoCl_3$	6	$MoCl_5$	0.6	Sapphire	743 → 673	60
$TiCl_3$	5	$GaCl_3$	1	YSZ	700 → 600	60
$CrCl_3$	1	-	-	YSZ	873 → 773	30

4.2.4 Characterization of *M*Cl$_3$ nanosheets on substrates

4.2.4.1 Morphology and dimensionality of *M*Cl$_3$ nanosheets (Light microscopy, SEM, TEM, AFM)

Similar to their bulk counterparts (see chapter 4.2.2.1, page 50), *M*Cl$_3$ nano- and microsheets appear as platelets of individual shape and color, but much thinner, on top of their respective substrates (see Figure 28). As demonstrated in Figure 29b the color of thin *M*Cl$_3$ sheets vary with downsizing the sample thickness that can be well monitored by light microscopy in bright-field mode. Basically, *M*Cl$_3$ microsheets (> 200 nm) exhibit clear individual colors and sharp edges (see Figure 29b). Based on the prior described preparations (see chapter 4.2.3, page 58) about 55 % ($RuCl_3$) and 65 % ($MoCl_3$) of investigated layers on substrates were microsheets with thicknesses > 200 nm (see Figure 29a). Even thicker sheets were found for $CrCl_3$ and $TiCl_3$ on top of the substrates. About 80 % of analyzed $CrCl_3$ layers showed thicknesses > 2 µm and nearly all $TiCl_3$ structures were microlayers with thicknesses > 4 µm (see Figure 29a).

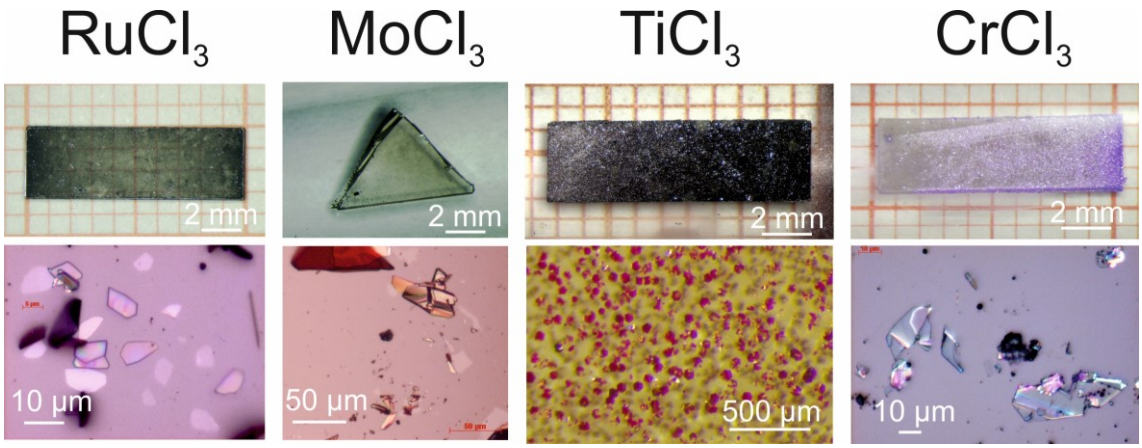

Figure 28: Optical microscopy applying the bright-field mode of both a survey of the respective substrate subsequent to the CVT process **(above)** and **(below)** the respective individual *M*Cl$_3$ micro- and nanosheets (*M* = Ru, Ti, Cr on YSZ and $MoCl_3$ on sapphire); while individual micro- and nanolayers of *M*Cl$_3$ (*M* = Ru, Mo and Cr) were investigated using a Zeiss microscopy, the magnification of the microscope image of $TiCl_3$ microsheets is lower due to another type of used microscope (LEICA M60 microscope inside a glovebox); figures partly reproduced from references [123,126, 128].

By decreasing the *M*Cl$_3$ specimen thickness to the threshold between micro and nano (75-200 nm) the edges of small *M*Cl$_3$ crystallites are still sharp but with black color (*M* = Ru, Mo, Cr). Furthermore, the color of the whole *M*Cl$_3$ platelets starts to shift to grey ($RuCl_3$), dark grey ($MoCl_3$), shiny purple ($TiCl_3$) and colorful ($CrCl_3$). More than 20 % of deposited $RuCl_3$ layers belong to this semi-thick structures and about 15 % with respect to $MoCl_3$ and $CrCl_3$. Common to all the four chlorides *M*Cl$_3$ is, if the sheets get even thinner (< 75 nm) they get *transparent* and the prior colorful appearances fade, accompanied with barely discernable edges (see Figure 29b). Ultrathin nanosheets of 25 nm or less are harder to localize as the effect of transparency is drastically enhanced. Only a few of the deposited $CrCl_3$ sheets were obtained

as real nanosheets with thicknesses less than 75 nm. In contrast, about 20 % of the investigated thinner $RuCl_3$ and $MoCl_3$ layers showed thin (25-75 nm) or ultrathin (> 25 nm) layer thicknesses (see Figure 29a).

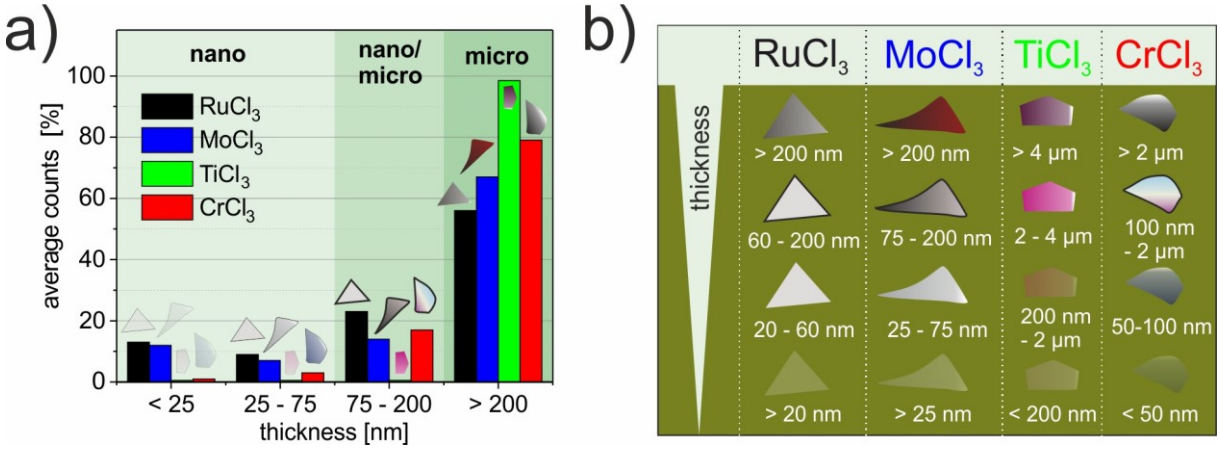

Figure 29: **(a)** Distribution of thicknesses of MCl_3 micro- and nanosheets on their respective substrates, **(b)** appearance and color of MCl_3 micro- and nanosheets ($RuCl_3$, $TiCl_3$ and $CrCl_3$ on YSZ and $MoCl_3$ on top of sapphire substrates) depending on its individual thickness observed by optical microscopy in bright field mode.

Thin nanosheets composed of MCl_3 (M = Ru, Mo, Cr) deposited by CVT on respective substrates, were investigated by AFM (see Figure 30). By means of this technique representative layer thicknesses of 18 nm (about 30 stacked layers), 23 nm (about 38 stacked layers) and 26 nm (about stacked 44 layers) could be confirmed with respect to $RuCl_3$, $MoCl_3$ and $CrCl_3$. The light green dashed line indicates the approximate minimal thickness of $TiCl_3$ microsheets deposited by CVT, but determined instead by point-to-point SEM measurements. AFM measurements of $TiCl_3$ were not practicable due to the extreme sensitivity of $TiCl_3$ to ambient conditions, which is even again enhanced at micro- and nano dimensions. The thicknesses of $TiCl_3$ were basically much larger due to the used experimental procedure implementing volatile $GaCl_3$ as transport agent and the occurrence of higher transport rates.

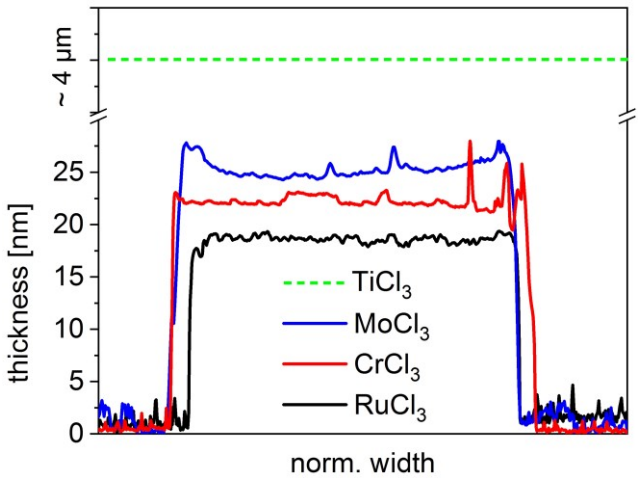

Figure 30: Thickness of individual representative deposited MCl_3 nanosheets ($RuCl_3$, $MoCl_3$ and $CrCl_3$) determined by AFM, to ease the comparison of distinct layer thicknesses the latitudinal dimensions were normalized (the absolute values are in the range of several micrometers); the thickness of as-grown $TiCl_3$ microsheets were determined by SEM point-to-point measurements in inert atmosphere and added for comparison.

The morphology and lateral dimensions of MCl_3 micro- and nanosheets were further investigated by SEM (see Figure 31). Thinner sheets of MCl_3 composition mainly form hexagons, half-hexagons or structures with arbitrary shape (see Figure 31). By utilizing secondary electron contrast it is demonstrated that the lateral dimensions of thinner $RuCl_3$, $MoCl_3$ and $CrCl_3$ sheets are mainly in the range of 25-50 µm. The deposited $TiCl_3$ structures are thicker (see Figure 30) and as a consequence their longitudinal extension is as well larger and in the range of about 100 µm (see Figure 31). The SEM images of $RuCl_3$ and $CrCl_3$ are acquired with a tilted sample holder (tilt angle 45°). Thus, it could be demonstrated that the micro- and nanosheets are not entirely oriented "plane" to the substrate surface in [100] (in case of YSZ) or [0001] orientation (with respect to sapphire). In fact, roughly estimated about half of the deposited layers are randomly orientated and do not match to the orientation of the substrate (see Figure 31). The main reason of these effect is that the vapor growth of thin MCl_3 sheets is not realized epitaxial, since the unit cell of the substrate surface (YSZ: cubic) is not entirely compatible to those of the respective MCl_3 sheets (monoclinic or trigonal, see chapter 2.3.4, page 20). This fact might also indicate that the lattices of MCl_3 structures are influenced by mechanical strain due to the lattice mismatch between the bottom MCl_3 layer and the substrate surface. Additionally, due to the formation of initial MCl_3 nuclei and growth of further MCl_3 structures, the sheets are frequently not deposited as isolated layers but grown into each other (see Figure 31) and thus partly forming agglomerates.

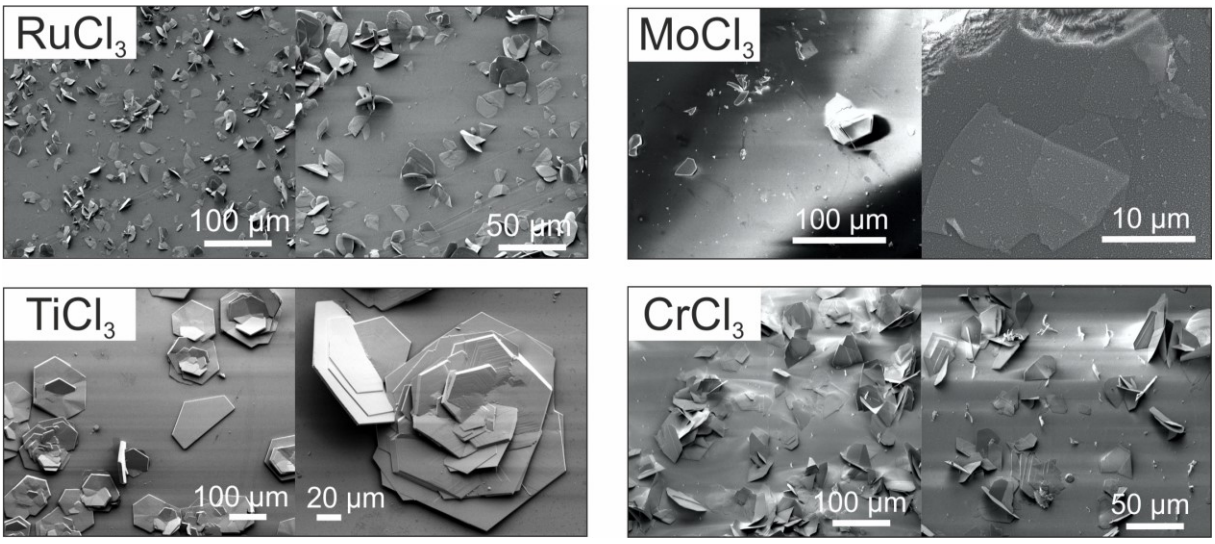

Figure 31: SEM investigations of MCl_3 micro- and nanosheets (M = Ru, Mo, Ti, Cr) on top of YSZ- ($RuCl_3$, $TiCl_3$ and $CrCl_3$) or sapphire substrates ($MoCl_3$) in secondary electron contrast; the figures of $RuCl_3$ and $CrCl_3$ were acquired by using a tilted sample holder (tilt angle: 45°) and thus also show randomly oriented MCl_3 layers; the measurement conditions were complicated by the fact that YSZ is an insulating substrate, thus it was necessary to either work with low acceleration voltages (2-5 keV) or to perform a previous sputtering, e.g. by coating the substrate and deposited layers with a thin (some nm) layer of carbon (graphite); figures partly reproduced from references [124,128].

By depositing MCl_3 nanosheets on lacey-carbon copper grids and applying TEM the atomic lattice planes could be made visible (see Figure 32). In terms of $RuCl_3$ and $MoCl_3$ the edges of nanosheets were investigated in detail (see Figure 32). Hence, the magnified pictures are showing regions of fewer and greater intensity that is related to the underlying layers of different thicknesses. As the specimen of $RuCl_3$, $MoCl_3$ and $CrCl_3$ were prepared including ultrasonication, the slightly wavy surface layers (e.g. in terms of $RuCl_3$) could be assigned to the influence of sonication step (see Figure 32). However, the well-arranged atomic planes point towards a high specimen homogeneity and crystallinity of MCl_3 nanosheets (see Figure 32).

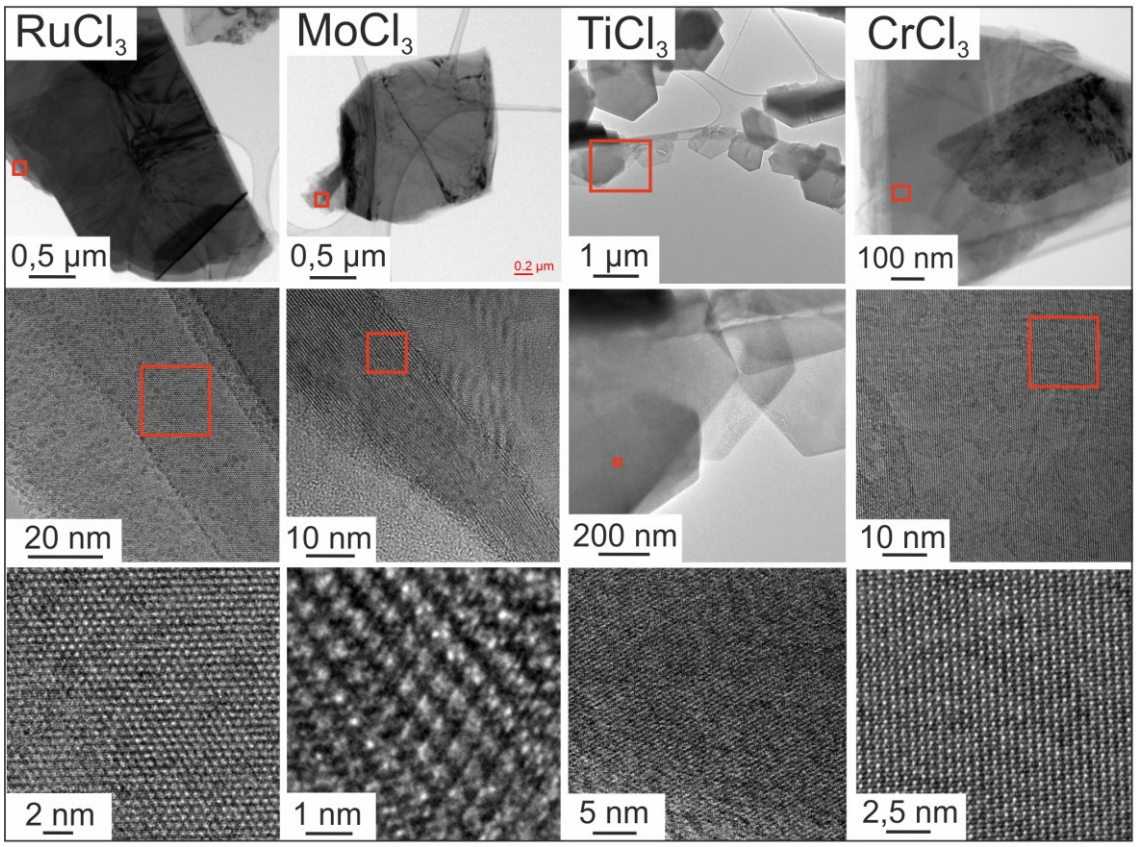

Figure 32: HR-TEM investigations of $RuCl_3$, $MoCl_3$, $CrCl_3$ and STEM investigations of $TiCl_3$ including visualizations of atomic planes and individual darker M- (M = Ru, Mo, Ti, Cr) and Cl-atoms (white circles); figures partly reproduced from references [123,124,126,128].

4.2.4.2 Composition and thickness dependent measurements of MCl_3 nanosheets (SEM/TEM-EDX, micro-RAMAN, XPS)

To analyze the composition of deposited MCl_3 micro- and nanosheets, SEM-EDX measurements were performed (see Figure 33, page 66). By investigating nanolayered $RuCl_3$, as expected, the Ru-L and Cl-K lines were acquired and the elemental quantification suggested a ratio of Ru:Cl ≈ 1:3 (according to $RuCl_3$). Further quantitative measurements confirmed MCl_3 compositions also for $MoCl_3$, $TiCl_3$ and $CrCl_3$ (composition that fitted closely to the assumed 1:3 (M:Cl) ratio, see appendix, Table A 12, page 139). Additional elemental peaks

(e.g. Zr-*L*, Al-*K*) originated from the underlying substrate. As already described, especially $TiCl_3$ microsheets proved to be heavily oxygen sensitive in ambient atmosphere. The oxygen sensitivity of $RuCl_3$, $MoCl_3$ and $CrCl_3$ was quite moderate and allowed an exposure to oxygen atmosphere for at least some minutes. By utilization of a transfer module with respect to $TiCl_3$ specimen (see page 29) any oxygen contaminations could be excluded and highly probable neither $TiCl_3$ microsheets nor MCl_3 (M = Ru, Mo, Cr) nanosheets proved to be oxidized to either oxyhalides or oxides. Still, there were some amounts of oxygen detected (see Figure 33a, b, d). However, on the single basis of EDX, the origin of this oxygen signal present in $RuCl_3$, $MoCl_3$ and $CrCl_3$ could not be accurately defined. It cannot be excluded that X-ray quanta are detected also from the underlying substrate due to a remarkable penetration depth. By comparing the approximate ratios of the acquired signals of the substrate elements (e.g. Zr/O) to the MCl_3 materials on top (e.g. Ru/Cl) a slight indication on the flakes thickness could be obtained. Meaning, that the intensity of the Zr-*L* line (from the YSZ substrate) in the $CrCl_3$ EDX spectra (see Figure 33d) is almost at the same level as of the Cl-*K* line (arising from $CrCl_3$). This points to a very thin $CrCl_3$ sheet. In contrast to this Ti-*K* and Cl-*K* lines were acquired by analyzing $TiCl_3$ microsheets without any substrate signal. This is another proof that the $TiCl_3$ sheets are thicker than the other three deposited chlorides ($RuCl_3$, $MoCl_3$ and $CrCl_3$).

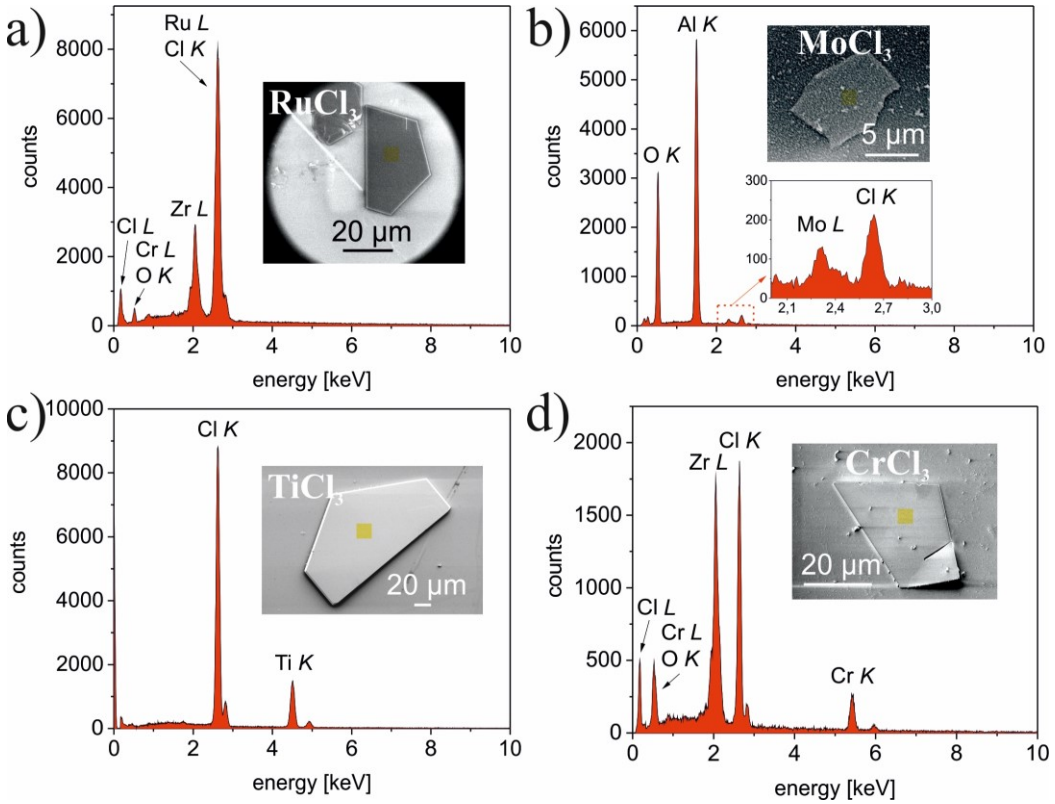

Figure 33: SEM-EDX investigations of MCl_3 micro- and nanosheets on substrates: **(a)** $RuCl_3$/YSZ, **(b)** $MoCl_3/Al_2O_3$, **(c)** $TiCl_3$/YSZ, **(d)** $CrCl_3$/YSZ; the inlay figures demonstrate the investigated nanocrystals, the yellow spot is indicating the location of the respective measurement, in contrast to bulk MCl_3 EDX results, the total number of acquired X-ray quanta (counts) was added to get a better idea of the signal-to-noise ratio; figures partly reproduced from references [123,124,126,128].

The composition of $RuCl_3$ nanosheet samples was subsequently reconfirmed by applying TEM-EDX to be about 1:3 (according to see $RuCl_3$, appendix, Figure A 27d, page 138). With respect to $RuCl_3$ an EDX linescan was realized indicating a homogeneous composition of ruthenium and chlorine (according to $RuCl_3$) with few variations along the longitudinal axes of the thin sheet (see appendix, Figure A 27a, b, page 138). As the flakes thickness started to increase at the end (on the edge), the intensity of both Ru-*K* and Cl-*K* lines increased as well, as expected. The homogeneous distribution of both elements (Ru and Cl) could be additionally confirmed by implementing a TEM-EDX mapping (see appendix, Figure A 27c, page 138). By EDX mapping it is demonstrated that the elements (Ru and Cl) are both distributed homogeneously within the $RuCl_3$ nanolayer. The darker areas on both mappings could arise from minor variations in thicknesses or a presence of smaller defects on the $RuCl_3$ surface. In a similar manner MCl_3 (M = Mo, Ti, Cr) were investigated and the composition of 1:3 according to MCl_3 was confirmed by TEM-EDX (see appendix, Figure A 28, page 139).

By using surface sensitive XPS related to both MCl_3 bulk- and microsheets (respectively nanosheets) the elemental composition specifically of the upper layers of thin sheets was investigated subsequently (see Figure 34, page 68). For practical comparison the XPS spectra of the pure substrates (YSZ or sapphire) was measured as well. It was obtained that the spectra of bulk- and micro/nanolayers within the MCl_3 compounds are rather identical with respect to the characteristic elemental features of M and Cl and assumed compositions (with respect to MCl_3, see Figure 34). More importantly, the observed binding energies of M were in good agreement with previously observed values for $RuCl_3$, $MoCl_3$ and $CrCl_3$.[151] The intensity of the O1s peaks were enhanced in MCl_3 micro/nanosheet dimensions due to the influence of the underlying oxygen-containing substrate (YSZ or Al_2O_3). A main reason for applying this measurements was to assign the prior located oxygen signal by EDX (see Figure 33) to either the substrate (YSZ, Al_2O_3) or a probable (partly) oxidized MCl_3. By reason of surface sensitivity and sample transfer small amounts of oxygen (5…10 at-%) were recorded within all MCl_3 XPS measurements, although prepared using a transfer chamber. Though this amount of oxygen could be minimized by application of sputtering with argon ions (for 3 min) to 2 at-% in case of $RuCl_3$, $MoCl_3$ and $CrCl_3$. By using elemental quantifications (done by XPS software) subsequent to sputtering, it was confirmed that MCl_3 bulk and nanosheet samples (M = Ru, Mo, Cr) exhibit the desired stoichiometry (MCl_3) and that the structures are not significantly oxidized in accordance with simulation results. The main amount of detected oxygen (measured by EDX) arises from the substrate. The fractional amounts of oxygen (≈ 2 at-%) were still located at the MCl_3 sheets but assigned as rather adsorbed on the crystals surface than

incorporated in the lattice. As noticed in case of $MoCl_3$, the sputtering process was associated with the deformation of the crystal structure (shift of binding energy of $Mo3d_{5/2}$ from 229 eV to 228 eV). Moreover the occurrence of the substrate peaks (Zr, Y or Al) in the nanosheets spectra indirectly proved the thin sheets dimensionality. In contrast, the enhanced intensity of the O1s peak related to $TiCl_3$ clearly pointed towards surface oxidation in case of both bulk and microsheets to highly probable TiO_2 (see Figure 34c), which reflects the observations of microscopy and EDX. In addition, small amounts of gallium species were located which may correspond to minimum residues of the transport agent.

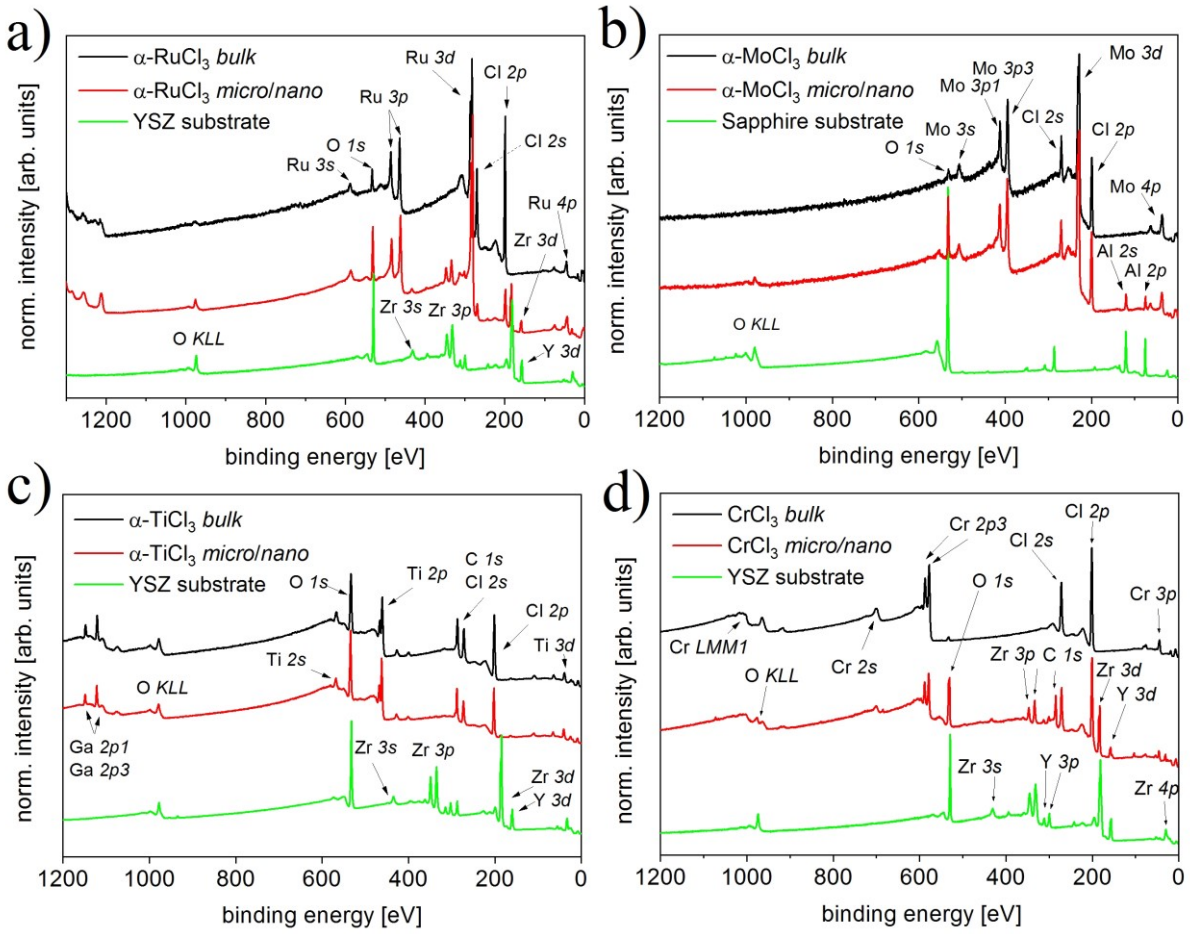

Figure 34: Thickness dependent XPS measurements of MCl_3 compounds: **(a)** $RuCl_3$, **(b)** $MoCl_3$, **(c)** $TiCl_3$ and **(d)** $CrCl_3$ with respective MCl_3 bulk flakes in black, MCl_3 micro- and nanosheets deposited at the respective substrate (red color) and the underlying, pure substrate without any structures on top (light green); XPS irradiates specimen with monochromatic soft X-rays while measuring the kinetic energy of the emitted electrons (photoelectrons, e.g. Ru 3*d*) due to photoemission; as a result, the binding energy can be calculated; each element has unique binding energies and thus allows for elemental identification and quantification; differences in the chemical potential and polarizability cause chemical shifts (variations of the binding energy) which again permit the determination of the chemical state of an element; photoemission further causes the emission of Auger electrons (e.g. O *KLL*) as a result of a relaxation of excited ions (an outer electron falls into an inner electron vacancy and a second electron is emitted coincidentally due to the excess energy).[151] The figures were reproduced from references [123,124,126,128].

Furthermore, thickness dependent measurements of MCl_3 sheets were performed utilizing micro-RAMAN (see Figure 35, page 70) to investigate the composition and crystallinity of thin structures and to compare them with their bulk counterparts (MCl_3). The occurrence of RAMAN-active peaks requires the change of the polarizability of investigated M (M= Ru, Mo, Ti, Cr) and Cl molecules due to vibrations of the MCl_6 octahedra. The RAMAN results clearly indicated a high crystalline structure, both in bulk and micro- and nanosheets, of $RuCl_3$ (on top of YSZ) with four double-degenerated sharp and clear E_g peaks (110 cm^{-1}, 160 cm^{-1}, 265 cm^{-1}, 292 cm^{-1}) and one A_{1g} peak (308 cm^{-1}) at the expected energies (see Figure 35a).[152] The determined spectroscopic features are in the same energy range for all three sample thicknesses of $RuCl_3$ (bulk, micro and nano). As an indirect proof of a decreasing $RuCl_3$ layer thickness, the broad (YSZ) substrate peak at about 600 cm^{-1} emerges in $RuCl_3$ samples at the same energy range, especially in thin nanosheets. Additionally, a minor shift of about 2 cm^{-1} to higher energies (with respect to the 160 cm^{-1} E_g peak) was detected for micro- and nanosheets of $RuCl_3$ which could be caused by strain that is present in thinner $RuCl_3$ structures due to the lattice mismatch (≈ 20 %) of the $RuCl_3$ crystals to the YSZ substrate.[123] Similar strain effects were recently investigated using MoS_2 and 2H-$TaSe_2$.[153,154] With respect to the slight RAMAN-shift there are also possible influences of finite size effects, that were likewise observed in thin layers of MoS_2, or stacked induced changes in the intralayer Cl-M-Cl bonding.[123]

The detected sharp RAMAN peaks of $MoCl_3$ samples at 150 cm^{-1}, 261 cm^{-1}, 296 cm^{-1}, 331 cm^{-1} and 351 cm^{-1} are in good agreement with previously reported data by *McGuire* et al (see Figure 35b).[45] As expected, the peaks intensity is decreasing with narrowed $MoCl_3$ layer thickness but the most prominent peaks at 150 cm^{-1}, 296 cm^{-1} and 351 cm^{-1} are still visible. Similar to RAMAN measurements of $RuCl_3$, a peak shift of bulk $MoCl_3$ (150 cm^{-1}) to higher energies of $MoCl_3$ micro- (152 cm^{-1}) and nanosheets (157 cm^{-1}) was obtained.[124]

RAMAN results acquired using $TiCl_3$ samples are more difficult to analyze since the influence of the object slides of the measurement set-up, used to ensure absence of oxygen, cannot be excluded (see Figure 35c). The most prominent peak at 247 cm^{-1} could not be observed in thinner sheets. Likely to $RuCl_3$ and $MoCl_3$, the intensity of thinner sheets is rapidly decreased.

Similar to $RuCl_3$ and $MoCl_3$, the RAMAN results obtained with $CrCl_3$ are in good agreement with previously published literature.[25,155–157] By analyzing very thin $CrCl_3$ nanosheets, only the most intense A_{1g} peak at 298 cm^{-1} is still identifiable and the underlying YSZ influences the obtained signal heavily. In contrast to $RuCl_3$ and $MoCl_3$, the RAMAN signals of thinner $CrCl_3$

nanolayers at 246 cm^{-1} and 298 cm^{-1} are shifted to lower energies, probably induced by additional lattice strain but this should be more investigated in the near future.

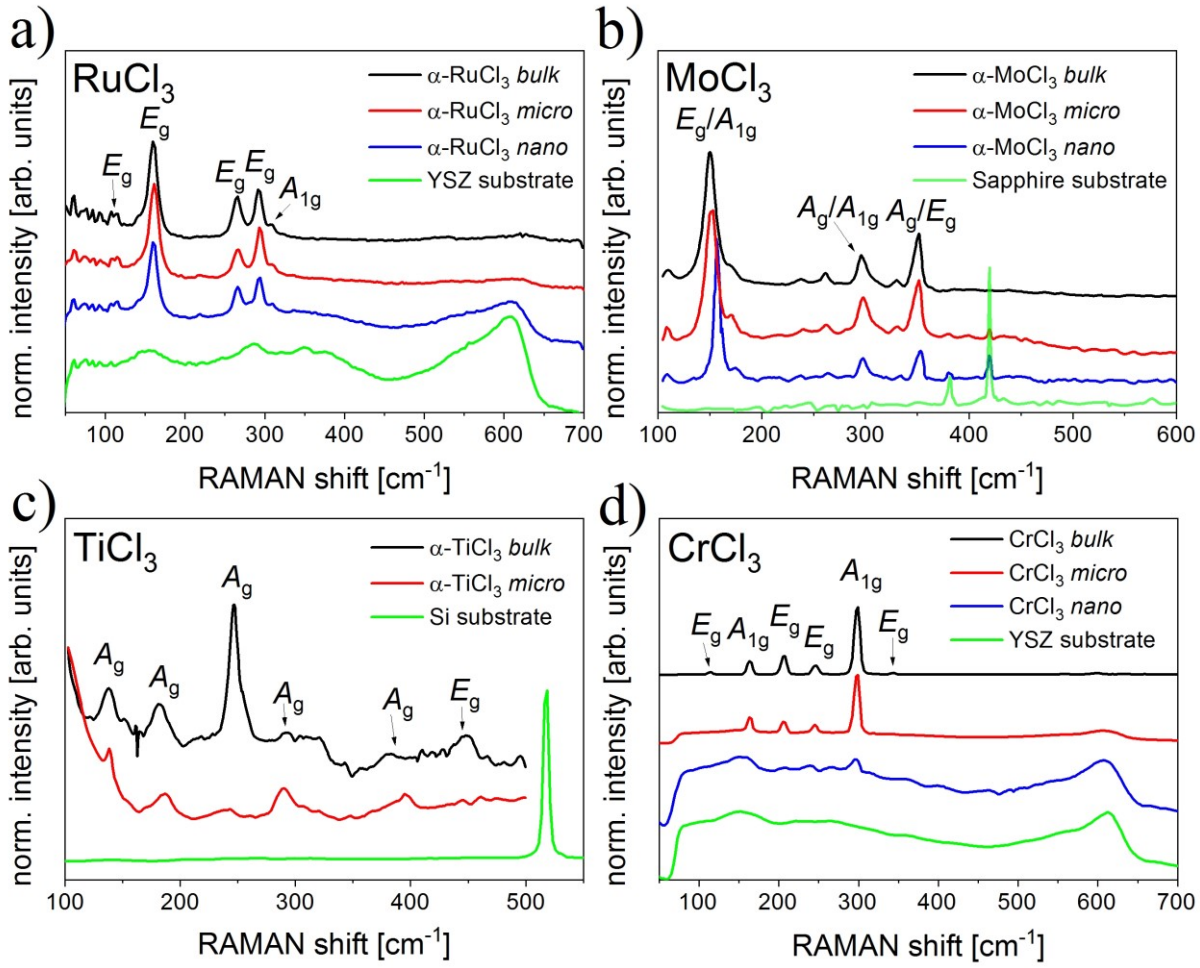

Figure 35: Thickness dependent micro-RAMAN measurements of MCl_3 compounds: **(a)** $RuCl_3$, **(b)** $MoCl_3$, **(c)** $TiCl_3$ and **(d)** $CrCl_3$ with respective MCl_3 bulk flakes in black color, MCl_3 micro- (red color) and MCl_3 nanosheets (blue color) and the underlying pure substrate without any structures on top (light green color). The figures were reproduced from references [123,124,126,128].

4.2.4.3 Crystallinity of MCl_3 nanosheets (SAED & END)

The crystallinity of thin MCl_3 nanolayers was further investigated, with respect to the thinnest obtained micro- or nanosheets, by using electron diffraction techniques (SAED and END). By means of SAED, MCl_3 (M = Ru, Mo, Cr) nanosheets were confirmed to be high crystalline due to obtained sharp diffraction spots of MCl_3 samples occurring in the reciprocal space (see Figure 36). The recorded $MoCl_3$ and $CrCl_3$ electron diffraction pattern coincided with those of the respective theoretical MCl_3 pattern (M = Mo, Cr) with monoclinic space group $C2/m$. Thus, at least the investigated $MoCl_3$ and $CrCl_3$ nanosheets confirmed the PXRD results of bulk MCl_3 flakes (see chapter 4.2.2.3, page 54). In contrast to this, the obtained diffraction pattern of nanolayered $RuCl_3$ matched to those of the trigonal $RuCl_3$ space group $P3_112$. As only the stacking order of MCl_3 layers determines the formation of an individual space group, and even

by PXRD it is difficult to ascertain a single unit cell, it could be tentatively assumed that both types of stacking orders (ABC and AB) are highly probable present in both bulk MCl_3 flakes and their respective nanosheets. Further, the space trigonal space group $P3\bar{m}1$ was obtained with thin layered $TiCl_3$ using END. Similar to SAED, sharp diffraction spots of smaller regions, used to be applied in END, demonstrating high crystallinity of individual MCl_3 layers. Likewise to MCl_3 (M = Ru, Mo, Cr) the finding of the trigonal $P3\bar{m}1$ space group ($TiCl_3$) is in good agreement with the analysis of thicker $TiCl_3$ flakes by PXRD (see chapter 4.2.2.3, page 54).

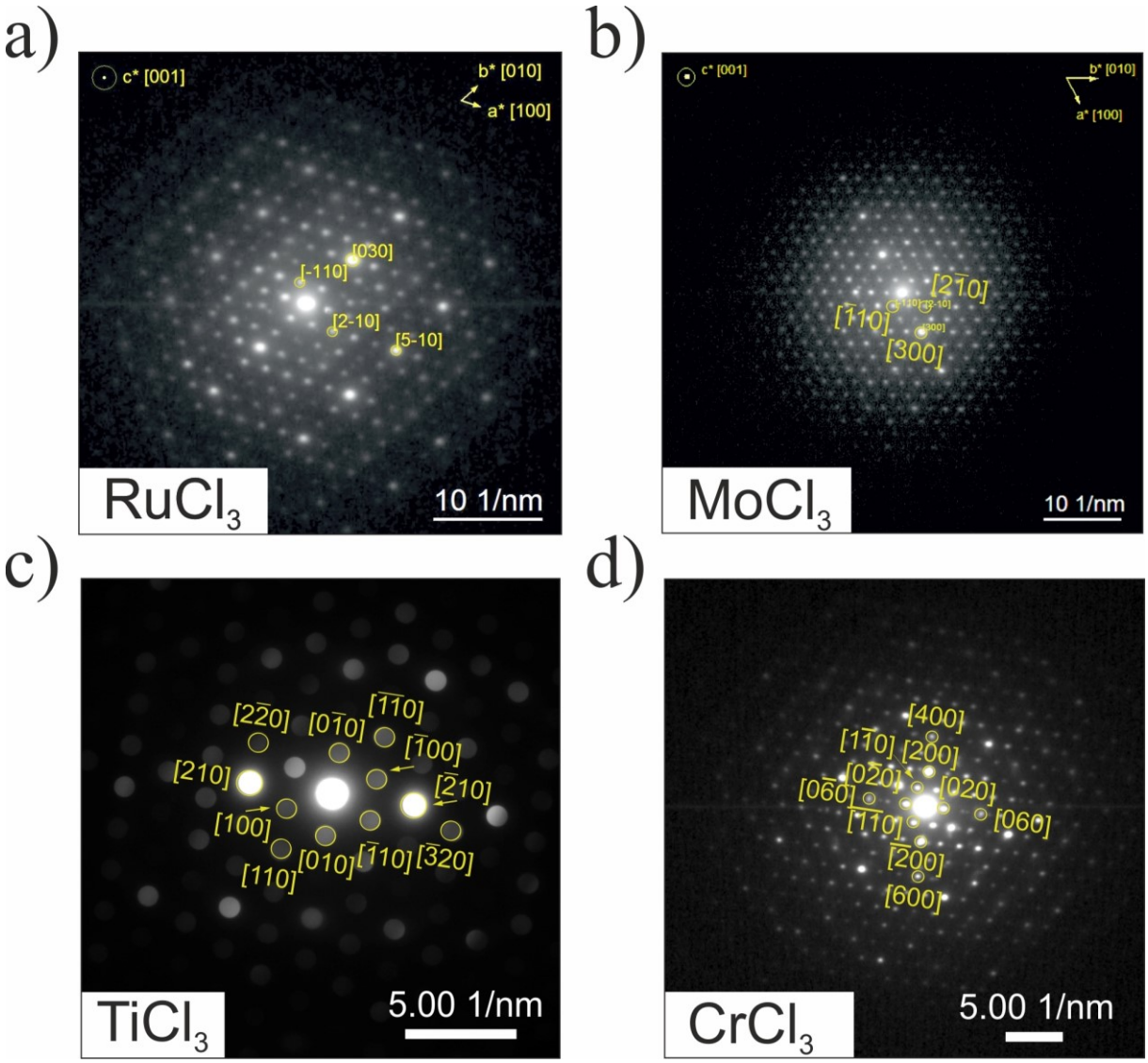

Figure 36: Investigation of crystallinity of as-prepared MCl_3 nanosheets using SAED (selected area diffraction): **(a)** $RuCl_3$, **(b)** $MoCl_3$ and **(d)** $CrCl_3$ and by means of END (electron nanodiffraction) with respect to **(c)** $TiCl_3$ microsheets acquired in [001] orientation, the occurrence of sharp diffraction spots indicated the high crystallinity of as-grown structures; the diffraction spots were indexed (visible in yellow numbers and square brackets) which match to the *Miller* indices of the corresponding lattice planes and their integer multiples. The figures were reproduced from references [123,124,126,128].

4.2.4.4 Catalytic properties of $TiCl_3$ microsheets

$TiCl_3$ is one of the most prominent *Ziegler-Natta* catalysts for the polymerization of olefins (mainly ethylene and propylene). Prior as-grown $TiCl_3$ microsheets on YSZ substrates were implemented as catalysts for the gas-phase polymerization of ethylene. The idea behind the downscaling approach by CVT is providing more $TiCl_3$ active catalyst sites which results in the emergence of an enlarged catalytic activity (determined by $m_{product}$ / $m_{catalyst}$) due to a higher surface-volume-ratio.

By comparing the catalytic performance of microsheets with as well investigated bulk $TiCl_3$ (catalytic activity of 5.0 $g \cdot g^{-1}$), it was proven that thinner sheets (with thicknesses of about 4 µm) enhanced the catalytic activity significantly by about 16 % to 5.8 $g \cdot g^{-1}$ (see Figure 37 and appendix, Table A 14, page 140).

In addition, the prior as-synthesized $TiCl_3$ microsheets were mechanically exfoliated in inert atmosphere (see chapter 4.2.5.3, page 77) to further decrease the crystallite sizes and thicknesses (to be finally about 200 nm thin). Utilizing the nanolayered and delaminated sample (one exfoliation) led to an even higher catalytic performance with a significant 24 % increase of activity (6.2 $g \cdot g^{-1}$) in comparison to the initial $TiCl_3$ bulk material (see Figure 37 and appendix, Table A 14, page 140). Thus, a proof of concept was established (an enlarged surface-to-volume-ratio increases the catalytic activity).

By prolonged exfoliations (up to five times) the amount of $TiCl_3$ heavily decreased and thus the catalyst mass could not be determined exactly due to the limit of the balance used, which would be essential for calculation of the catalytic activity. Further details on the catalytic process and the characterization of the synthesized polyethylene on top of $TiCl_3$ microsheets can be checked at reference [128].

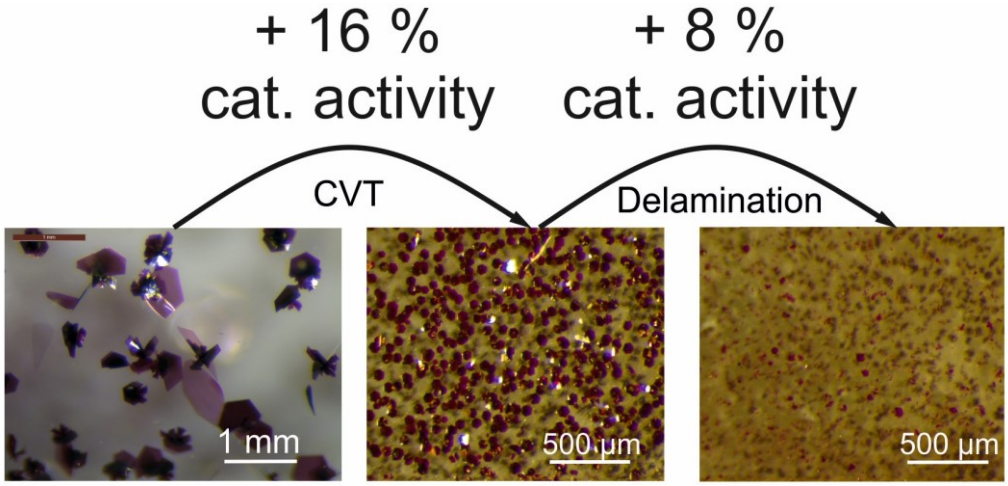

Figure 37: Downscaling of $TiCl_3$ bulk sheets to micro thicknesses by short-term CVT resulted in an enhancement of the catalytic activity by 16 %, further delamination led to even thinner nanosheets and final 24 % improvement in comparison with the initial bulk $TiCl_3$ catalyst; reproduced form reference [128].

4.2.5 Delamination of as-grown MCl_3 (M = Ru, Cr, Ti) structures on top of YSZ

To further reduce the MCl_3 micro- and nanosheets thicknesses and to get access to e.g. isolated $RuCl_3$ monolayers (and hence probable new playgrounds for *Kitaev* physics, see chapter 2.2.4, page 11) the as-grown MCl_3 structures on top of YSZ substrates were delaminated subsequently. Two delamination approaches were realized by using 1) a "conventional" tape-based exfoliation and 2) a liquid technique (ultrasonication). The subsequent chapter reveal that the delamination process is system specific for MCl_3 (M = Ru, Cr, Ti). The delamination parameter e.g. repetitions of exfoliation (substrate exfoliation) or the choice of a suitable dispersing agent (sonication) have to be optimized and tailored for an individual MCl_3 compound. The delamination of $MoCl_3$ was skipped for time reasons.

4.2.5.1 Delamination of $RuCl_3$ micro- and nanosheets

With respect to the conventional exfoliation approach, which is associated with mechanical ablation of layers of prior as-grown $RuCl_3$ sheets, a gel tape on a polyester substrate with different retention levels (X4 and X8) was tested. Utilizing this tapes especially individual $RuCl_3$ microsheets (thickness > 200 nm) could be removed satisfactorily (see Figure 38a and Figure 39a-c). By applying six repetitions of exfoliation the amount of microsheets could be decreased by about 85 % (see Figure 38a). The intention to significantly enlarge the number of thin layers (< 60 nm) reproducibly rather failed and no monolayers could be generated by this technique (see Figure 38a). Furthermore, no crucial differences regarding the different retention levels (X4 and X8) were found. However, in one particular case it was possible to isolate a structure of only about 1 nm thickness, which correlates to a $RuCl_3$ bilayer (see Figure 39d-f).

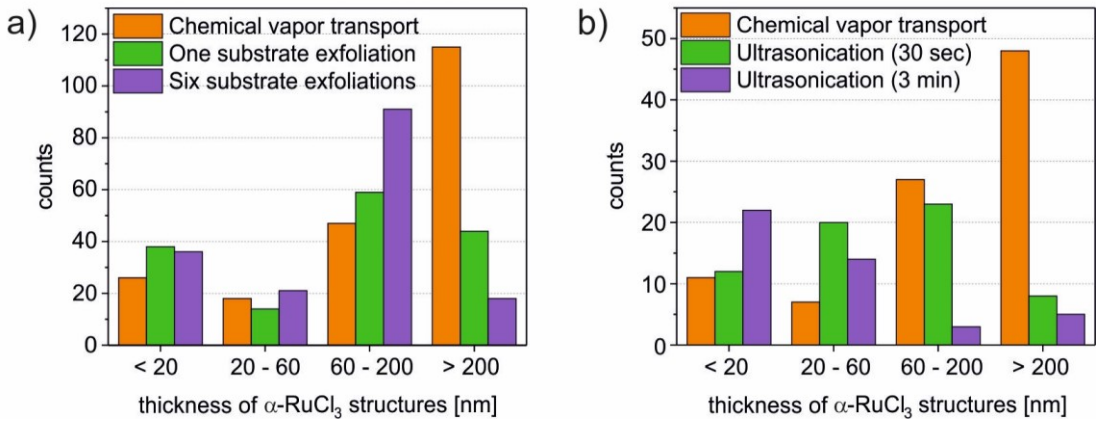

Figure 38: (a) Size distribution of α-$RuCl_3$ structures after pure chemical vapor transport (orange), after one substrate exfoliation (green) and after six substrate exfoliations (purple) related to Figure 39a-c, **(b)** size distribution of α-$RuCl_3$ structures after pure chemical vapor transport (orange), after 30 seconds ultrasonication with *n*-Methyl-2-Pyrrolidone (green) and after 3 minutes of ultrasonication with *n*-Methyl-2-Pyrrolidone (purple) related to Figure 41a-c; figure extracted from reference [123].

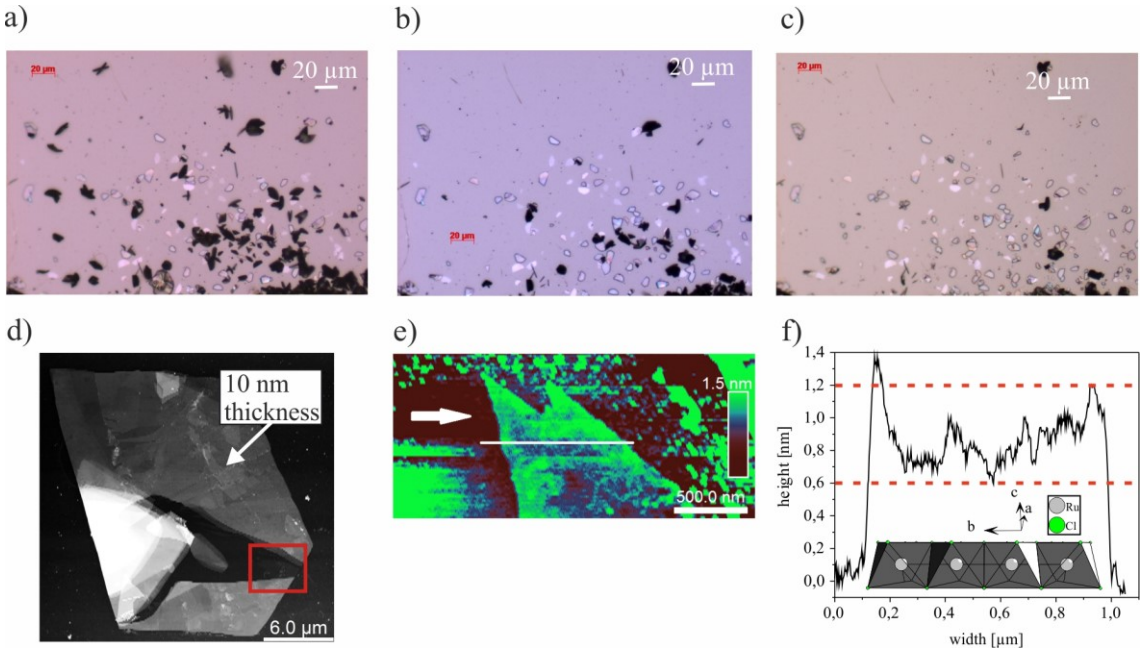

Figure 39: (a) Optical microscopy of the YSZ substrate with α-$RuCl_3$ nanocrystals deposited before exfoliation (after CVT), **(b and c)** exfoliation of thicker α-$RuCl_3$ crystals with X8 retention tapes 1 time **(b)** and 6 times **(c)**, **(d)** investigated α-$RuCl_3$ nanosheet (the red area indicating the AFM measurement), **(e)** investigated α-$RuCl_3$ nanosheet by means of AFM (the white line indicates the measurement) and **(f)** AFM measurement of the bilayer (the red dashed line indicating the theoretical layer thickness of a monolayer); figure taken from reference [123].

In addition ultrasonication studies of prior as-grown $RuCl_3$ nanostructures were performed referring to a liquid exfoliation procedure (see sample and suspension preparation procedure on page 25). In consideration of a vast count of sonication parameters (e.g. nature of material, sonication time as well as the intensity and frequency) the focus was set to an alteration of dispersing agents and sonication time.

It was observed that distilled water is not suited as dispersing agent since even smaller $RuCl_3$ crystals agglomerated to thicker ones (see appendix, Figure A 12, page 133). Likewise, using ethanol led to the result that $RuCl_3$ sheets were removed from the substrate after sonication process, probably due to the partly solubility of $RuCl_3$.[17] Using nonpolar *n*-hexane with rather low viscosity revealed that the resulting $RuCl_3$ crystals agglomerate easily (see appendix, Figure A 13, page 133). However, few $RuCl_3$ nanosheets with thicknesses of about 18 nm could be confirmed by AFM (see appendix, Figure A 13, page 133). Applying higher viscous benzene led to the isolation of few $RuCl_3$ thin sheets of only 4 and 15 nm (see Figure 40d-f). Nevertheless, by utilizing benzene it was observed that thicker $RuCl_3$ crystals mainly burst into smaller ones due to sonication effect which is associated with the emergence of rather less isolated structures (see Figure 40a-c).

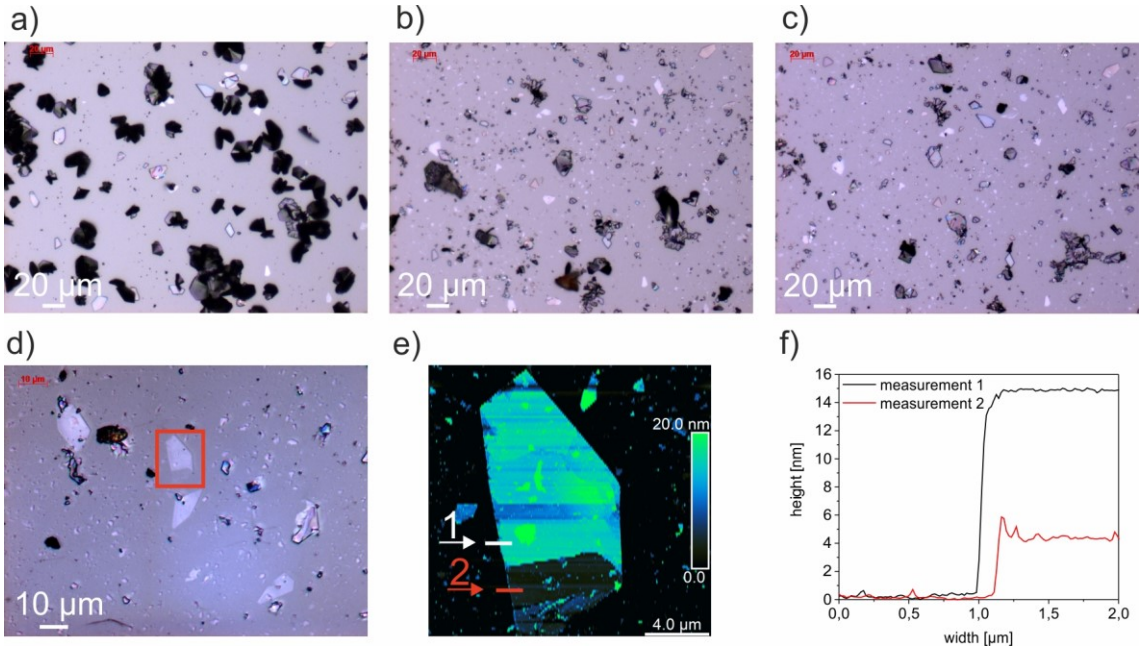

Figure 40: (a) Optical microscopy of the YSZ substrate with deposited α-$RuCl_3$ nanocrystals before sonication (after CVT); **(b)** after 30 seconds of ultrasonication with benzene, **(c)** after 3 minutes of ultrasonication with benzene, **(d)** investigated α-$RuCl_3$ nanocrystal by means of AFM (the red area is indicating to location of the measurement), **(e)** investigated α-$RuCl_3$ nanocrystal by means of AFM (the white and red lines are indicating the AFM measurements) and **(f)** AFM height profiles of (e), figure originates from reference [123].

Very good results were achieved by application of high viscous NMP (*n*-methly-2-pyrrolidone), which is a frequently applied dispersing agent in liquid exfoliation with various kinds of 2D materials, e.g. graphite, black phosphorus, graphene (derivatives) HfS_2 and MoS_2.[158–164] Besides viscosity, the polarity and the molecule size might be an important parameter in liquid exfoliation, which proves NMP to be advantageous due to a high polarity and big molecule size. By the use of NMP, short sonication times of only 30 seconds are sufficient to remove about 85 % of $RuCl_3$ structures with thicknesses greater than 200 nm attached at the substrate surface (see Figure 41b, page 76 and Figure 38b, page 73). By enlargement up to three minutes, almost every thicker $RuCl_3$ flake (microsheet) is removed (see Figure 41c). After three minutes about 90 % of the semi-thick flakes (60 – 200 nm thickness) were eliminated from the YSZ substrate (see Figure 38b).

In contrast to conventional tape exfoliation, ultrasonication with NMP enables an enlargement of amounts of thinner structures (20 – 60 nm) after 30 seconds, and an almost doubled emergence of ultrathin flakes (< 20 nm) after three minutes of sonication time (see Figure 38b). Particularly monolayers of $RuCl_3$ were isolated reproducibly (see Figure 41d-f). A possible explanation why $RuCl_3$ monolayers remain on the substrate surface after successful exfoliation (either by tape or liquid media) is that the adhesion force of the first (bottom) deposited layer of $RuCl_3$ at the interface substrate/crystal is quite strong, especially compared to the *van der Waals* forces between adjacent layers. It was observed that ultrasonication is way more efficient

to generate ultrathin or monolayer structures of $RuCl_3$. A tentative explanation could be that in ultrasonication processes many delaminating mechanisms interfere, e.g. liquid streams causing micro-bubbles and thus cavitation or fragmentation.[160]

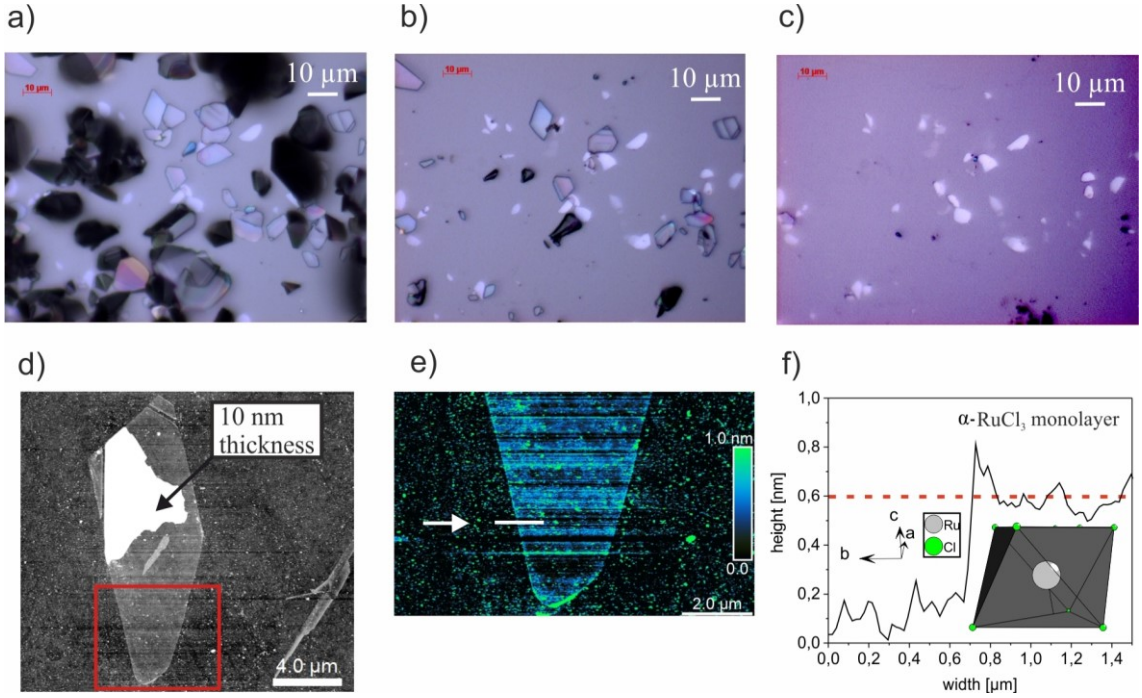

Figure 41: (a) Optical microscopy of the YSZ substrate with deposited α-$RuCl_3$ nanocrystals before sonication (after CVT), **(b)** after 30 seconds of ultrasonication, and **(c)** after 3 minutes of ultrasonication with NMP, **(d)** investigated α-$RuCl_3$ nanocrystal by means of AFM (the red area indicates the AFM measurement), **(e)** investigated α-$RuCl_3$ monolayer by means of AFM (the white line indicates the measurement) and **(f)** AFM measurement (inset: crystal structure of α-$RuCl_3$, the red dashed line is indicating the theoretical layer thickness of a monolayer), figure originates from reference [123].

4.2.5.2 Delamination of $CrCl_3$ micro- and nanosheets

Based on the successful isolation of monolayers of $RuCl_3$, chromium(III) chloride ($CrCl_3$) was delaminated likewise. Basically isolating monolayers by both approaches (ultrasonication and conventional exfoliation) proved to be more difficult in comparison to $RuCl_3$. Ultrasonication studies were performed with respect to three different dispersing agents (NMP, isopropanol and distilled water) and a timescales of 30 seconds up to three minutes using as-grown $CrCl_3$ micro- and nanosheets on YSZ substrates.

Peeling off individual layers by application of distilled water failed and no liquid exfoliation could be observed. By using isopropanol the micro- and nanostructures rather agglomerated. However, few thinner nanostructures could be determined on substrate surface subsequent to the sonication process. With respect to NMP on the one hand the isolation of thinner sheets became possible. On the other hand, the $CrCl_3$ sheets surface were affected due to the contact with the dispersing agent by an obvious formation of brown edges and residues on the substrate surface. Furthermore, the suitable application of substrate exfoliation was examined. With the

use of Gel-Pak tapes (both retention levels X4 and X8) the $CrCl_3$ structures partly smeared upon the substrate and the crystals were rather destroyed subsequently.

However, conventional scotch tape proved to be more suitable for the detachment of $CrCl_3$ structures of the substrate. In general it was possible to remove the entire number of $CrCl_3$ structures with different thicknesses (see Figure 42a). Nevertheless, the purpose to detach individual layers of micro- and nanosheets to enlarge the number of ultrathin structures rather failed. By analysis of the remaining $CrCl_3$ sheets thicknesses a $CrCl_3$ monolayer could be confirmed by means of AFM (see Figure 42b and c). Thus substrate exfoliation of prior deposited $CrCl_3$ sheets on YSZ substrates using scotch tape proved to be successful.

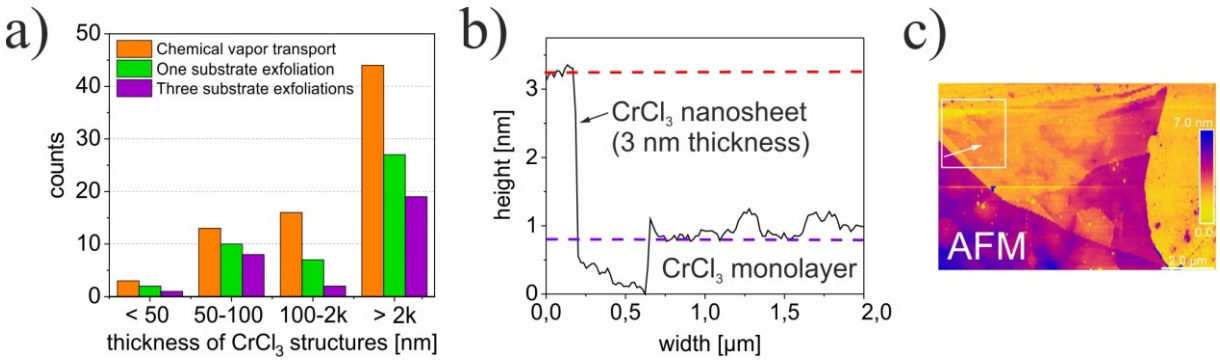

Figure 42: (a) Distribution of $CrCl_3$ thicknesses after pure vapor transport (orange color), after one substrate exfoliation using scotch tape (green color) and after three repetitions (purple color), **(b)** AFM measurement of a monolayer of $CrCl_3$ (purple) and ultrathin sheet (red) after substrate exfoliation of prior as-grown $CrCl_3$ micro- and nanosheets on YSZ substrates, **(c)** the white arrow is indicating the direction of the monolayer AFM measurement of (b), the figures were partly extracted from reference [126].

4.2.5.3 Delamination of $TiCl_3$ microsheets

Surface sensitive as-prepared $TiCl_3$ microsheets (located on YSZ substrates) were delaminated using the substrate exfoliation approach and conventional scotch tape in glovebox (inert) atmosphere (see Figure 43b-g, page 78). The application of delamination resulted in the emergence of much thinner micro- and even nanosheets (see Figure 43a). Moreover the total number of crystals decreased due to delamination effects. Using a single delamination step, the amount of thicker structures (> 4 µm) was decreased by about 77 % (see Figure 43a). In clear contrast to e.g. $CrCl_3$, when the amount of thicker $TiCl_3$ structures (2-4 µm) decreased, the number of thinner structures (< 200 nm) was heavily increased by repeated exfoliation (see Figure 43a). Under consideration of five times of exfoliation, more than the half of investigated $TiCl_3$ crystals are thin nanolayered sheets (thickness < 200 nm).

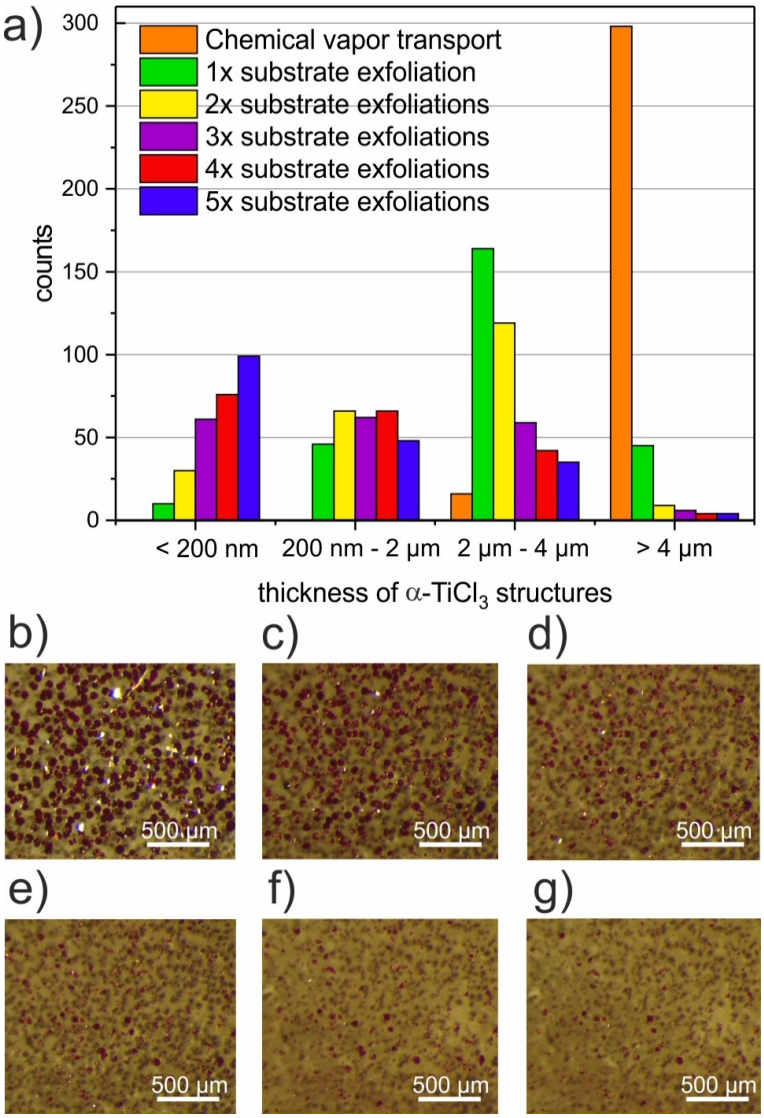

Figure 43: (a) Distribution of thicknesses of $TiCl_3$ structures without delamination (after CVT) in orange color, with one time of exfoliation (green color), after 2 repetitions (yellow), after 3 repetitions (purple), after 4 repetitions (red) and after 5 repetitions (blue); it has to be remarked that the $TiCl_3$ thicknesses could not be determined by AFM (as it was the case with e.g. $RuCl_3$ and $CrCl_3$) due to the sensitivity of $TiCl_3$ to ambient conditions - instead the approximate thicknesses were measured by point-to-point measurements using a SEM and a tilted sample holder; by comparison of individual $TiCl_3$ layer colors with their respective approximate thicknesses a classification of thickness distributions could be drawn (see Figure 29, page 63), **(b)** $TiCl_3$ on top of YSZ after pure chemical vapor transport, **(c)** $TiCl_3$ on top of YSZ after one time of substrate exfoliation, **(d)** $TiCl_3$ on top of YSZ after two times of substrate exfoliation, **(e)** $TiCl_3$ on top of YSZ after three times of substrate exfoliation, **(f)** $TiCl_3$ on top of YSZ after four times of substrate exfoliation, **(g)** $TiCl_3$ on top of YSZ after five times of substrate exfoliation, figures extracted from reference [128].

4.3 Synthesis and characterization of bulk flakes and nanosheets of CrX_3 (X = Cl, Br, I)

This part is mainly focused on $CrBr_3$ and CrI_3, since the vapor growth and characterization of $CrCl_3$ bulk flakes and nanosheets was described extensively in the MCl_3 part (see chapter 4.2, page 47). However, on suitable text passages a comparison of results of CrX_3 (X = I or Br) structures to previously studied $CrCl_3$ is adduced.

4.3.1 Synthesis of CrX_3 bulk flakes

Based on the simulation results (see page 44) CrX_3 bulk flakes were synthesized using chemical vapor transport in an endothermic temperature gradient. In contrast to the prior discussed MCl_3 compounds, CrI_3 and $CrBr_3$ were initially prepared from the elements (Cr and I_2, respectively Cr and Br_2, for further details check chapter 3.2.2, page 24). Both the preparation and vapor transport were realized as a "one-step approach", meaning the initial formation of CrX_3 structures (Cr + X) was directly followed by the vapor transport using a temperature gradient without the application of any prior isothermal step.

4.3.1.1 Synthesis of CrI_3 flakes

Basically, bulk flakes of CrI_3 were grown by application of a temperature gradient of ΔT = 100 K (923 → 823 K, see Figure 44, page 80). CrI_3 platelets with few mm in diameter were obtained by using about 20 mg of chromium powder and a slight excess of iodine of about 160 mg (with respect to a CrI_3 stoichiometry) and transport durations of 72 hours (see Figure 45a, page 81). The amount of deposited CrI_3 was not significantly different by applying either less (24 hours) or more (168 hours) transport duration. Likewise, the reduction of mass of starting materials (10 mg Cr and 80 mg I_2) did not considerably change the morphology of deposited CrI_3 structures. However, applying larger temperature gradients ΔT = 200 K (1023 → 823 K) resulted in the formation of mainly overgrown CrI_3 platelets (see appendix, Figure A 14, page 134) or mm-sized greenish structures (923 → 723 K, see Figure A 16, page 134). The greenish color might be induced by partial oxidation and slight formation of Cr_2O_3, e.g. in case of significant remaining amounts of oxygen in the ampoule. In accordance to observations of MCl_3 bulk flakes, smaller temperature gradients of ΔT = 50 K (923 → 873 K) promoted the formation of agglomerated few-mm polycrystals (see appendix, Figure A 15, page 134).

4.3.1.2 Synthesis of $CrBr_3$ flakes

In contrast to CrI_3, and especially $CrCl_3$, slightly increased temperatures were used for the crystallization of chromium(III) bromide ($CrBr_3$) crystals based on modeling results (see page 44). Few-mm sized $CrBr_3$ bulk platelets were prepared by using about 10 mg chromium powder and 50 mg of bromine and applying basically temperature gradients of ΔT = 100 K (1023 → 923 K, see appendix, Figure A 18, page 135) for 24 hours (see Figure 44). The main amount of structures was located at the end of the colder side of the ampoule. Little thinner (more transparent) and smaller $CrBr_3$ flakes (mm to µm) were obtained by application of temperatures 923 → 823 K (see appendix, Figure A 19, page 135). As the $CrBr_3$ flakes thickness decreased, the color changed from silvery-blackish to dark green. The crystallite lateral dimensions could be further reduced (mainly in the µm range) by decreasing the transport duration down to 12 or even 6 hours (see appendix, Figure A 20, page 136).

Applying larger gradients (ΔT = 200 K, 1023 → 823 K) led to a more uniformly distributed condensation of few-mm $CrBr_3$ flakes alongside the sink zone (see Figure 45b, page 81). Decreasing the temperatures down to 873 → 773 K resulted in very few, small $CrBr_3$ structures and thus is rather inappropriate for the growth of thicker sheets. An enlargement of the transport duration (e.g. up to 168 hours) led to the crystallization of few-mm polycrystalline $CrBr_3$ layers, located at the end of the ampoule (see appendix, Figure A 21, page 136). With respect to both systems, CrI_3 and $CrBr_3$, the calculated transport rates are higher than the experimental ones which could be correlating particularly with the difficult experimental handling of individual CrX_3 flakes (extraction from the ampoule, see appendix, Table A8 and A9, page 127), similar to observations made with $CrCl_3$.

Table 6 summarizes the determined optimum vapor transport parameter of CrX_3 bulk flakes (X = I or Br).

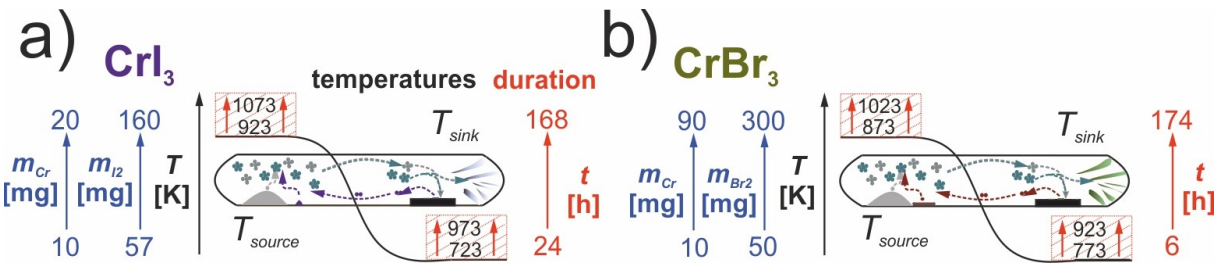

Figure 44: Scheme of applied and investigated CVT parameter (temperatures in red colored dashed boxes, transport duration as well in red color, mass of introduced material Cr and X_2 (X = I or Br) in blue color) for the synthesis of CrX_3 bulk structures: **(a)** CrI_3 and **(b)** $CrBr_3$.

Table 6: Experimentally determined optimum vapor transport parameter for the growth of CrX_3 bulk flakes.

CrX_3	m(Cr) [mg]	$m(X_2)$ [mg]	Temperatures [K]	Duration [h]
CrI_3	10	80	923 → 823	24
$CrBr_3$	10	50	1023 → 923	24

4.3.2 Characterization of CrX_3 bulk flakes

4.3.2.1 Morphology and dimensionality of CrX_3 bulk flakes (Light microscopy and SEM)

As previously described (see chapter 4.3.1, page 79) the CrX_3 bulk flakes lateral dimensions are mainly in the few-millimeter range while forming thicknesses of only some micrometer (see Figure 45a-c). CrI_3 bulk platelets exhibit silvery-shiny or blackish colors, depending on the incidence of light (see Figure 45a). Similar to MCl_3 sheets, all the three CrX_3 compounds show pleochroistic properties. The color of $CrBr_3$ apparently seems to be brown (see Figure 45b). In fact, the color of the sheets varies from dark green to shiny black (see appendix, Figure A 19, page 135) and the brown appearance is made by the remaining bromine atmosphere. As described previously $CrCl_3$ adopts a characteristic pink color (see Figure 45c). Utilization of SEM of CrX_3 structures elucidated the two dimensional composition of individual CrX_3 layers stacked upon each other (see Figure 45a-c).

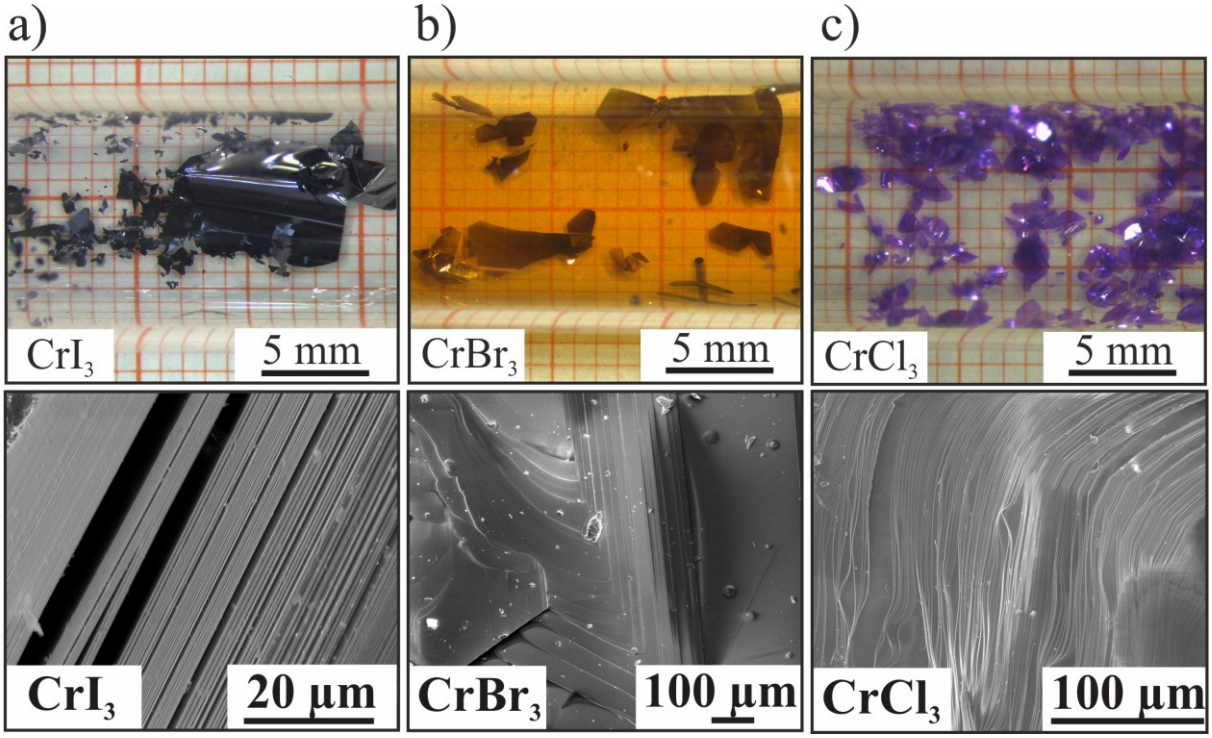

Figure 45: Light microscopy and SEM investigations of CrX_3 bulk flakes highlighting their two dimensional structure: **(a)** CrI_3, **(b)** $CrBr_3$ and **(c)** $CrCl_3$. The figures were partly extracted from reference [126].

4.3.2.2 Composition of CrX_3 bulk flakes (SEM-EDX, WDX, IR)

To investigate the elemental composition of deposited CrX_3 bulk flakes[9], individual samples were analyzed by SEM-EDX (see Figure 46, page 83). With respect to CrI_3 (see Figure 46a), the EDX quantification indicated a ratio of about 1:3 (according to CrI_3) by comparing the atomic ratios of chromium (Cr-*K*, 24 at-%) and iodine (I-*L*, 76 at-%). The situation is pretty close to EDX results obtained with thicker $CrBr_3$ crystals (see Figure 46b) revealing quantifications of 22 at-% (Cr-*K*) and 78 at-% (Br-*L*) and thus showing a ratio near 1:3 (according to $CrBr_3$). Nevertheless, it has to be remarked that especially in $CrBr_3$ samples the atomic percentage of bromine was regularly over-detected (Br-*L* atom percentages higher than 80 %, see appendix, Table A 11, page 131). The situation of $CrCl_3$ was already mentioned in chapter 4.2.2.2 (page 52). As demonstrated in Figure 46c, $CrCl_3$ EDX quantifications proved to fit to the 1:3 ratio (according to $CrCl_3$).

To demonstrate the elemental distribution of Cr and *X* (*X* = I, Br, Cl) additional EDX mapping was realized (see Figure 47, page 83) using the SEM device. The mapping revealed a homogeneous distribution of Cr and *X* (*X* = Cl, Br, I) within all three investigated halides (CrX_3, see Figure 47). Based on experimental observations CrI_3 tend to oxidize under ambient conditions during minutes, while the oxygen sensitivity decreases drastically from the iodide to the chloride ($CrCl_3$). This was confirmed by taking the elemental contrast of oxygen also into account for the respective EDX mapping results (see light green accentuations in Figure 47a). It is shown that oxygen is also distributed mainly homogeneously on the surface of CrI_3 sheets, which is not the case for $CrBr_3$ and $CrCl_3$ (see Figure 47a-c).

In view of the fact that the quantification of oxygen (O-*K* line) is difficult by EDX due to overlapping with Cr-*L* (all CrX_3) and additionally I-*M* (CrI_3) elemental lines, the composition of CrX_3 (*X* = I and Br) bulk flakes was further analyzed by WDX (see appendix, Figure A 10, page 132). Under the use of few-millimeter CrX_3 platelets (*X* = I or Br) the stoichiometry of around 1:3 (Cr:*X*), previously determined by EDX, could be reconfirmed to fit to the desired CrX_3 stoichiometry. Considering at least three measuring points, quantitative WDX analysis indicated the average atomic percentage of chromium is 23.8 at-% (± 0.2 at-%) and 76.2 at-% (± 0.2 at-%) for iodine (according to CrI_3). With respect to investigated $CrBr_3$ the average atomic percentages acquired by WDX are 22.8 at-% (± 1.3 at-%) for chromium and 77.2 at-% (± 1.3 at-%) for bromine (according to $CrBr_3$).

[9] Similar to $CrCl_3$, $CrBr_3$ and CrI_3 are *Mott*-insulators due to strong exchange correlations. [32,34,197]

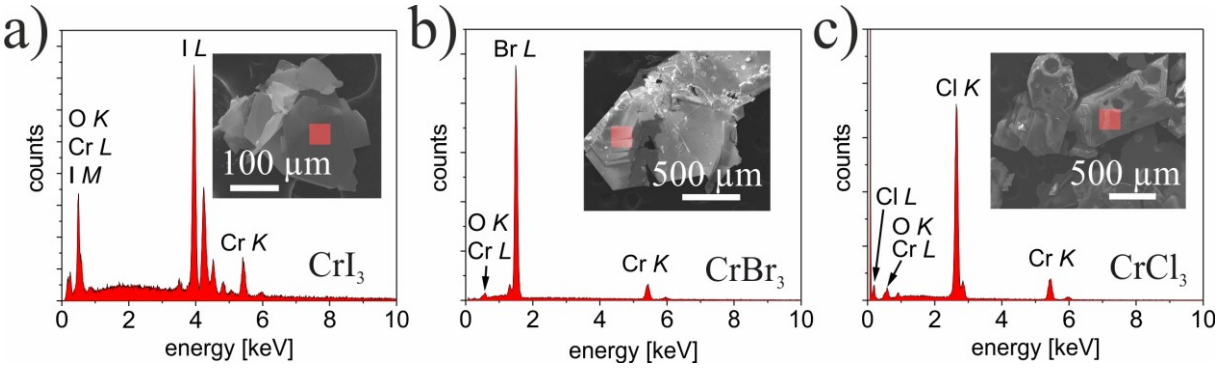

Figure 46: EDX spectra of deposited CrX_3 bulk flakes: **(a)** CrI_3, **(b)** $CrBr_3$ and **(c)** $CrCl_3$; the insets shows the investigated CrX_3 crystal, the red box is indicating the location of the respective EDX analysis.

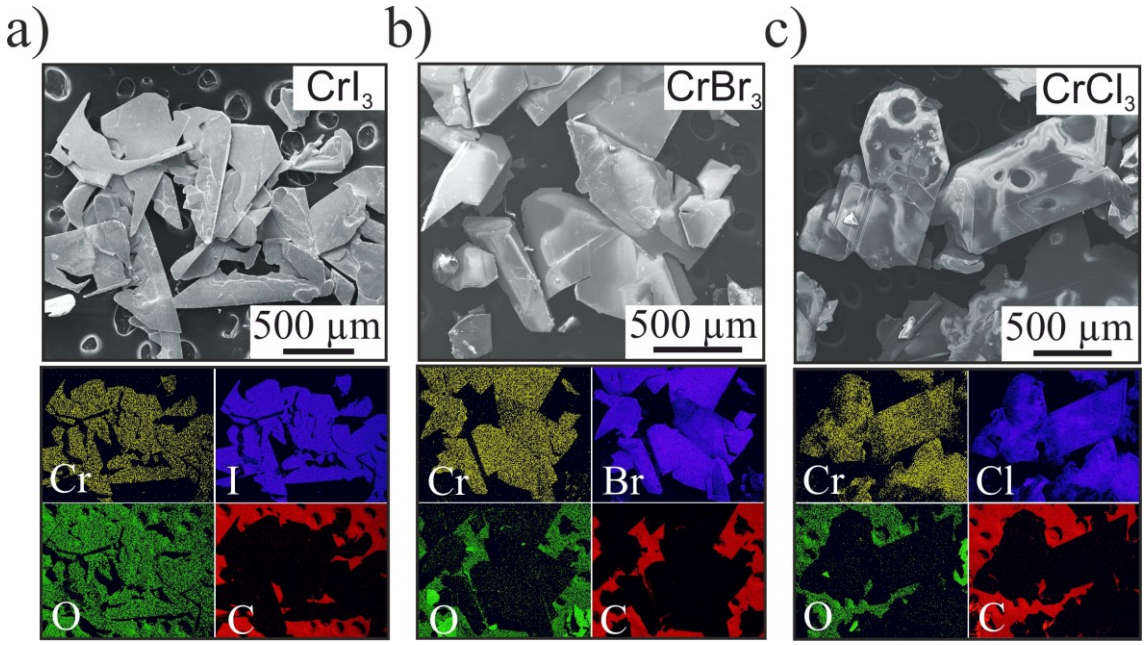

Figure 47: Elemental distribution of CrX_3 bulk flakes demonstrated by EDX mapping: (**a)** CrI_3, **(b)** $CrBr_3$ and **(c)** $CrCl_3$ for confirmation of a homogeneous Cr/X distribution; as an indicator of a decreasing sensitivity to O_2 (from $CrI_3 \rightarrow CrCl_3$) and for elemental contrast the elemental distributions of O and C were mapped in addition.

Further sample identification was realized by application of infrared spectroscopy in transmission geometry (see Figure 48, page 84). The acquisition of satisfying spectra of CrI_3 was challenging since there were almost no clear peaks that could be detected, except a distinct one at 222 cm^{-1} (see Figure 48a). There is also no literature available for a suitable comparison, which might be related to the absorption and incorporation of water between the Cr-I layers that disturb the infrared measurements. Utilizing instead $CrBr_3$ was accompanied with the observation of sharp peaks, similar to $CrCl_3$ (see Figure 48b). The most dominant peaks were observed at 159 cm^{-1} (E_u vibration) and 259 cm^{-1} (A_{1g}/E_u lattice vibrations), which were also detected in $CrCl_3$ specimen. Further peaks, but smaller in intensity, could be detected at 316 cm^{-1}, 375 cm^{-1}, 400 cm^{-1}, 420 cm^{-1} and 437 cm^{-1} that concords with literature data.[25,155] However, some particular peaks at 105 cm^{-1} and 217 cm^{-1} observed by *Borghesi* et al. and *Bermudez* were not observed which might also be related to partial moisture contaminations.

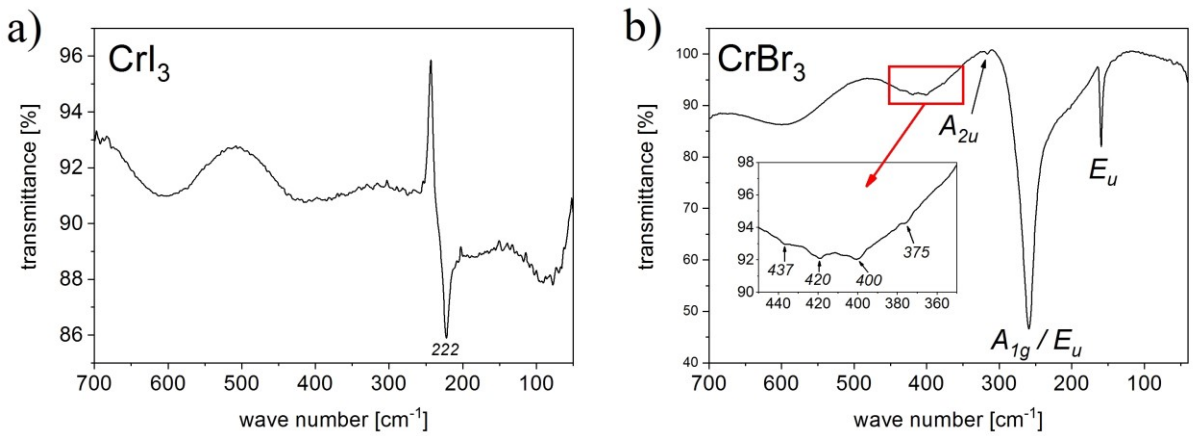

Figure 48: Infrared spectra (IR) of CrX_3 bulk flakes: **(a)** CrI_3 and **(b)** $CrBr_3$, the spectra were obtained similar to $CrCl_3$ specimen (CrX_3 crystallites from a prior prepared suspension dropped onto the PE foil).

4.3.2.3 Crystallinity of CrX_3 bulk flakes (PXRD)

Similar to MCl_3 structures (see chapter 4.2.2.3, page 54), CrX_3 flakes were investigated by PXRD. As well as MCl_3 layers, CrX_3 crystals exhibit several *polytypes*, which are characterized by a dominating stacking order (ABC or AB). The type of dominating CrX_3 stacking order is likewise temperature dependent and may change from monoclinic (ABC) to trigonal (AB) or vice versa (and thus is described in the literature as crystallographic phase transition of first order) with transition temperatures of 210-220 K for CrI_3 [34] and 423 K for $CrBr_3$.[15]

The obtained CrX_3 diffraction pattern signalized a high crystallinity of as-grown deposited flakes due to the occurrence of many detected reflexes (see Figure 49, page 85). The reflex positions of both CrI_3 and $CrBr_3$ are in good agreement with previously determined monoclinic or trigonal CrX_3 structures (see Figure 49). As the crystallographic structures are only determined by the occurring stacking order, none of the obtained reflexes can be assigned to a phase beyond CrX_3, the samples can be described as "phase pure". Additionally, it has to be considered that especially in real materials the stacking order may change within a given sequence of layers, meaning several types of stacking may coexist (a dominating and non-dominating stacking order). With respect to CrI_3, both reflex positions of *C*2/*m* (monoclinic) and $P3_112$ (trigonal) CrI_3 references fit well to the measured diffraction data (see Figure 49a).[29,34] As even the reflex intensity ratios are in the same orders of magnitude, it is difficult to assign the acquired data to the emergence of a single crystallographic unit cell (and thus preferential stacking order). More likely is the coincident presence of amounts of both stackings, similar to the situation in MCl_3 structures.

Considering $CrBr_3$ samples, the acquired data are as well characterized by a decent amount of recorded reflexes and thus point towards high crystallinity of specimen (see Figure 49b). The situation of $CrBr_3$ is slightly different to those of CrI_3. Although *Morosin* and *Narath* stated that

they detected the monoclinic crystal structure of $CrBr_3$ [15] (with respect to the 423 K transition temperature), up to now no proof and respective data are available (with respect to "monoclinic" $CrBr_3$). However, the measured data fitted well to trigonal $CrBr_3$ references ($R\bar{3}H$ and hexagonal $P3$) and all acquired diffraction reflexes can be allocated to fit to those of the corresponding $CrBr_3$ structures (see Figure 49b). Though, by comparing the ratios of reference reflex intensities with the measured data, the trigonal space group $R\bar{3}H$ seems to dominate the structure of bulk $CrBr_3$, in accordance with previously reported literature.[28,104,120,155,165–167]

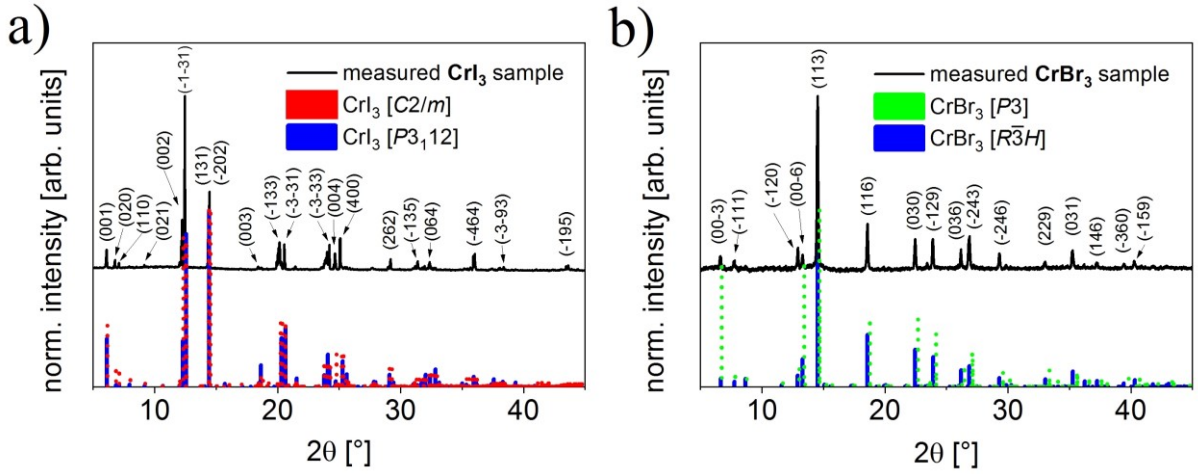

Figure 49: PXRD pattern of CrX_3 bulk flakes: **(a)** CrI_3 and **(b)** $CrBr_3$ with experimental observed powder pattern (black) and either monoclinic (red) or trigonal/rhombohedral (blue or green) CrX_3 reference pattern.

4.3.2.4 Magnetic properties of CrX_3 bulk flakes (SQUID)

CrX_3 are very interesting structures due to their intrinsic magnetic properties[10] down to single layer dimensions.[38] The magnetic properties of CrX_3 bulk platelets were determined by SQUID magnetometry (see Figure 50, page 88). With respect to literature, CrI_3 and $CrBr_3$ are a ferromagnets with T_C = 61 K (respectively T_C = 37 K for $CrBr_3$) and $CrCl_3$ is an antiferromagnet with two ordering temperatures (T_N) of about 14 and 17 K.[69] The magnetic ordering temperatures of CrX_3 enhances from the chloride to the iodide as the halogen size increases while the electronegativity decreases.[69] As a consequence of both larger halogen atoms and lowered electronegativity, the Cr-Cr distance is enlarged and the bonding becomes more covalent, which both supports superexchange interactions in the near 90° Cr-X-Cr bonds (instead of direct exchange), which should favor a ferromagnetic alignment of Cr^{3+} moments (important for the explanation of ferromagnetic properties of CrI_3, the influence of the ferromagnetic coupling is thus decreased for $CrBr_3$ but especially for $CrCl_3$).[69] Moreover,

[10] In reference [199] *Burch*, *Mandrus* and *Park* gave an overview about the fascinating variety of application possibilities of 2D *van der Waals* materials with layer dependent magnetic properties, e.g. in terms of specifically tailored multiferroics, magnetic sensors, magneto-optical devices or spintronics.

halogen associated spin-orbit coupling increases from $CrCl_3$ to the CrI_3 which is the predominant origin of magnetic anisotropy[11] of the CrX_3 family.[69,168]

Due to the proposed anisotropic properties of CrX_3 [70] (see chapter 2.2.4, page 11) the measurements of both $m(H)$ (at 2 K) and $m(T)$ using external magnetic fields of $\mu_0 H = 0.1$ T and $\mu_0 H = 3$ T were realized by applying the external magnetic field parallel ($H \parallel c$) as well as perpendicular ($H \perp c$) to the crystallographic c axis of CrX_3 specimen.

Related to CrI_3, the detected $m(H)$ curve revealed a strong magnetocrystalline anisotropy, in accordance with published literature [34], confirming the *easy axis* (preferred alignment) of Cr^{3+} spins is along the c axis of the unit cell ("out-of-plane"). This can be comprehended by a drastic increase of magnetization (the slope of magnetization is more rising than by aligning the magnetic field perpendicular to c) by applying the field parallel to the c axis of CrI_3 (see Figure 50b). This matches pretty close to similar observations made by *Liu* and *Petrovic*.[42] The magnetization saturates at relatively low fields ($\mu_0 H \approx 0.25$ T, see Figure 50b) along the preferred orientation of spins. It was observed that both ZFC and FC curves are identical for all three CrX_3.

Considering $CrBr_3$ the anisotropy is weaker than in CrI_3, but still clearly present in the $m(H)$ curve with the same preferred direction of spins (see Figure 50d), which also correlates with literature.[70]

The measurements demonstrated a converse situation, as predicted by literature [69], for $CrCl_3$ specimen. Here, the *easy axis* is localized in the a/b-plane of $CrCl_3$ ("in-plane"), detected by a larger slope of increasing magnetization with respect to this alignment of samples in the device (H perpendicular to c, see Figure 50f). It has to remarked that the absolute values of effective moments μ_B for Cr^{3+} should be about 3. This fitted pretty well for measurements of $CrBr_3$, but CrI_3 and $CrCl_3$ cases revealed significant deviations from the expect value, which could originate from not applied demagnetization corrections within all magnetic experiments of CrX_3 or weighing errors of utilized CrX_3 platelets.

Commonly similar in all three CrX_3 compounds, the Cr^{3+} spins are less ordered at higher temperatures (see the respective ordering temperatures in the beginning of this chapter) in the paramagnetic regime (see Figure 50a,c,e).[22] At a particular low temperature (see values for T_C or T_N on page 85) the individual Cr^{3+} spins start to align (second order phase transition) in their respective single layers "out-of-plane" (CrI_3 and $CrBr_3$) or "in-plane" ($CrCl_3$). Thus, a CrX_3 single layer is suspected to behave like a ferromagnet. The potential formation of long range

[11] The magnetocrystalline anisotropy describes the preferential ordering of spins (magnetic moments, e.g. Cr^{3+}) along a specific crystallographic orientation, meaning it is easier to magnetize a specimen in a particular "direction".[200]

magnetic order in one layer (intralayer) affects again the alignment of spins of neighboring layers (interlayer).[12] By analyzing the recorded $m(T)$ curves of as-prepared CrX_3 flakes it is demonstrated that variations of intensity of the external applied magnetic field results in different alignments of Cr^{3+} spins. Two following scenarios are presented.

With respect to the first scenario a relatively low external magnetic field ($\mu_0 H$ = 0.1 T) was applied. Considering $CrCl_3$ specimen it is shown that the magnetization decreased below 14 K (in good agreement with the reference ordering temperature) for both alignments of crystals (see Figure 50e). This means the magnetic interlayer coupling is of *A*-type anti-ferromagnetic manner (despite the Cr^{3+} spins of an individual layer are aligned ferromagnetic, the overall contribution of the structure is *anti*-ferromagnetic, since the spins of neighboring layers are aligned *anti*-parallel). Considering CrI_3, as initially of the chapter described, the magnetization is increasing consistently below T_C with only a minor decrease which should highly probable point towards a ferromagnetic alignment of Cr^{3+} spins, independent of the alignment of specimen with respect to the external magnetic field (see Figure 50a). As demonstrated in Figure 50c, the magnetic situation of $CrBr_3$ is located somewhere between those of CrI_3 and $CrCl_3$. The alignment of $CrBr_3$ flakes with respect to their crystallographic *c* axis parallel to the external field led highly probable to the induced ferromagnetic state, similar to CrI_3 samples (Figure 50c). Nevertheless, mounting the $CrBr_3$ sample in the opposite direction (*H* parallel to *a*/*b* or likewise perpendicular to *c*) resulted in a decrease of magnetization at about 33 K (see Figure 50c). The means the magnetic field of 0.1 T was too low to induce a long range interlayer ferromagnetic regime and the ground state of *A*-type anti-ferromagnetism persisted.

Related to the second scenario, a higher magnetic field ($\mu_0 H$ = 3 T) was applied considering all three CrX_3 compounds. By application of this external field the ferromagnetic state was induced (accompanied with fully aligned Cr^{3+} spins, even between several layers) with respect to all three CrX_3 structures (see Figure 50a,c,e), as expected from the literature.[28,34,69] A further final proof of ferromagnetic properties of CrX_3 materials would be an additional measurement of a potential hysteresis loop which could not be finalized due to time reasons.

[12] The description of the detailed mechanisms of formation and collapse of long range magnetic order in these systems are very complex and not part of this thesis. Particular focus on these topics are mentioned in the following references: [18,42,69,93].

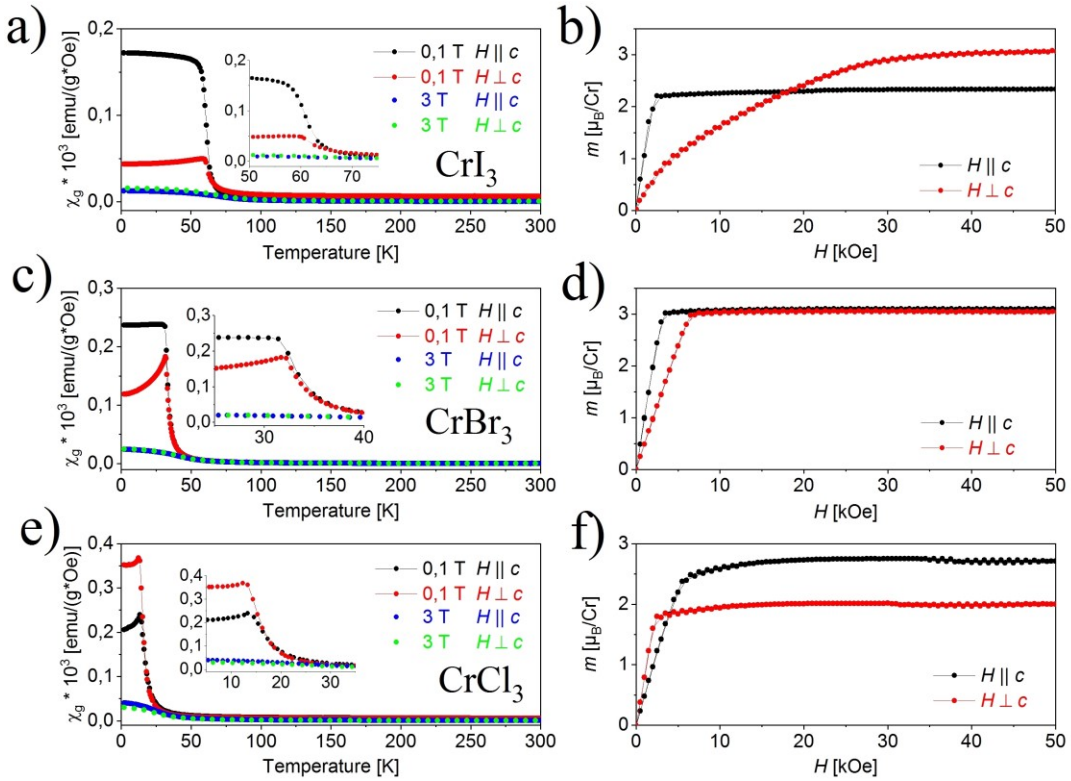

Figure 50: Magnetic properties of CrX_3 platelets determined by SQUID magnetometry with observed mass susceptibilities of CrI_3, $CrBr_3$ and $CrCl_3$ **(a, c and e)** at rather smaller (0.1 T) and higher (3 T) external magnetic fields ($m(T)$ curves) and various orientations of individual crystals (H parallel or perpendicular to the c axis) and the respective magnetization curves $m(H)$ **(b, d and f)** at low temperature (2 K) with different CrX_3 crystal orientations; it has to be remarked, that no demagnetization correction was applied within all measurement, which could change the trend of the $m(H)$ curves; additionally, the error in the absolute values of absolute moments of CrX_3 crystals of both orientations (parallel and perpendicular to c) could stem from an error of the mass of applied CrX_3 platelets. The figures were extracted from reference [126].

4.3.3 Synthesis of CrX_3 nanosheets on substrates

In contrast to the prior discussed thin layers of MCl_3, CrI_3 and $CrBr_3$ micro- and nanosheets were prepared from the elements (Cr and Br_2, respectively Cr and I_2, for further details check chapter 3.2.2, page 24). Both the preparation and vapor transport were realized as a "one-step approach", meaning the initial formation of CrX_3 structures (Cr + X) was directly followed by the vapor transport using a temperature gradient without the application of any prior isothermal step.

4.3.3.1 Synthesis of CrI_3 micro- and nanocrystals

Based on the modeling results (see chapter 4.1.2, page 44) CrX_3 micro- and nanosheets were deposited on suitable substrates (see Figure 51, page 89). Similar to thicker CrI_3 flakes (bulk) a slight excess of iodine (≈ 0.05 mmol) was utilized (resulting in introduced masses of 10 mg chromium powder and about 80 mg of iodine). The furnace temperatures (T_2 and T_1) were set to be 923 → 823 K (ΔT = 100 K) but with way lower transport duration of only one hour

(in contrast to bulk CrI_3, see Table 7, page 90). Deposition of CrI_3 nanosheets with thicknesses less than 40 nm and a lateral extents of about 20 µm (see Figure 52d, page 91) succeeded on YSZ substrates (see Figure 54, page 92). The application of a smaller gradient of ΔT = 50 K (923 → 873 K) resulted in the formation of sheets with similar thickness, but larger lateral extent of few hundred µm (see Figure 52c). As a unique feature of CrI_3 within the investigated systems MCl_3 and CrX_3, an enlargement of the temperature gradient up to ΔT = 200 K (1023 → 823 K) led to the crystallization of mm-sized microsheets (thickness ≥ 200 nm) on top of YSZ (see Figure 52b, page 91). A reduction of transport time to 30 minutes (see Figure 52a), but especially of introduced material (1 mg of chromium powder and 8 mg of iodine) led to the observation of a higher amount and laterally smaller nanocrystals (see Figure 52d). Replacing YSZ with Si/SiO_2 or pure Si led to a failure of crystal growth (see Figure 51). Furthermore using SiO_2 [0001], $LaAlO_3$, or sapphire, instead of YSZ, resulted in the observation of very few CrI_3 micro- (SiO_2 [0001], $LaAlO_3$) or nanosheets (sapphire) on top of the respective substrate (see appendix, Figure A 26, page 138).

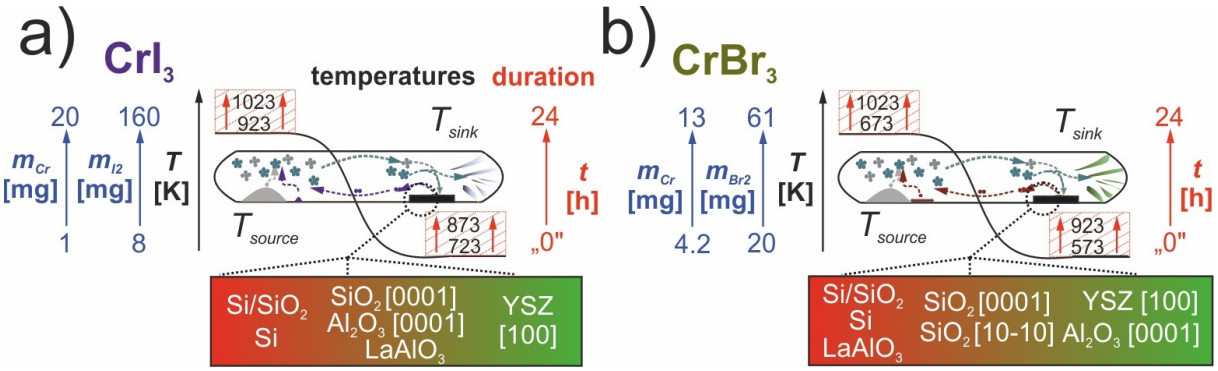

Figure 51: Scheme of investigated CVT parameter (temperatures in red dashed boxes, transport duration also in red color, mass of introduced material in blue color) for the synthesis of CrX_3 micro- and nanostructures on suitable substrates: **(a)** CrI_3 and **(b)** $CrBr_3$; the color bar indicates the observed suitability of individual substrates with the focus on the deposition of highly crystalline and isolated CrX_3 micro- and nanosheets (green color); in contrast red color indicates a failure of crystal growth, subjectively perceived average results (with respect to layer thickness, isolated deposition and morphology) are located in the middle of the color bar (orange area).

4.3.3.2 Synthesis of $CrBr_3$ micro- and nanocrystals

By using a slight excess of bromine (≈ 0.05 mmol, respectively 7 mg Cr powder and 38 mg Br_2), $CrBr_3$ micro- and nanosheets with thicknesses less than 25 nm (see Figure 54, page 92) were prepared on YSZ substrates for 30 minutes (see Table 7, page 90) by using a temperature gradient of ΔT = 100 K (923 → 823 K) based on prior thermodynamic calculations (see chapter 4.1.2, page 44). An enhancement of introduced mass (10 mg Cr, 50 mg Br_2) and transport duration (24 hours) led to the condensation of mainly microsheets (see appendix, Figure A 22, page 136). In significant contrast to CrI_3, applying a temperature gradient ΔT = 200 K (1023 → 823 K) benefited both a growth of lots of microsheets (see Figure 52e, page 91) and

a sparse amount of ultrathin $CrBr_3$ layers with thicknesses less than 1 nm (see appendix, Figure A 23, page 137). The amount of deposited $CrBr_3$ on top of YSZ was further minimized by application of lower temperatures 873 → 773 K (ΔT = 100 K). Beyond to prior discussed experiments applying YSZ as substrate material, several investigations were performed using alternative surfaces for the deposition of thin $CrBr_3$ layers. By applying Si/SiO_2, pure Si, $LaAlO_3$ or a lacey-carbon copper (TEM) grid, instead of YSZ, crystal growth failed (see Figure 51). Utilizing SiO_2 [0001] or [10-10] resulted in micro- and thin agglomerated nanocrystals of $CrBr_3$ which could be analyzed by SEM (see appendix, Figure A 24, page 137). With respect to sapphire, the deposited thin $CrBr_3$ layers resembled those of investigated YSZ experiments (see appendix, Figure A 25, page 137). Additionally, by applying sapphire even a pure heating-up process (without duration of a constant end-temperature) was sufficient for condensation of $CrBr_3$ micro- and nanosheets.

Table 7: Experimentally determined optimum vapor transport parameter for the growth of CrX_3 micro- and nanosheets on substrates (X = I, Br), the parameter of $CrCl_3$ were already discussed in the MCl_3 part.

CrX_3	*m*(Cr) [mg]	*m*(X_2) [mg]	Substrate	Temperatures [K]	Duration [min]
CrI_3	10	80	YSZ	923 → 823	60
$CrBr_3$	7	38	YSZ	923 → 823	30

4.3.4 Characterization of CrX_3 nanosheets on substrates

4.3.4.1 Morphology and dimensionality of CrX_3 nanosheets (Light microscopy, SEM, AFM)

The morphology and thickness of deposited CrX_3 (X = I or Br) nano- and microsheets on YSZ substrates was investigated by optical microscopy, SEM (see Figure 52, page 91) and AFM (see Figure 54, page 92). Based on these microscopic observations it was concluded that thin CrX_3 layers with distinct colors accordingly exhibit different thicknesses. Thus, a distribution of thicknesses of CrX_3 micro- and nanolayers on a representative substrate area was determined (see Figure 53, page 92). Related to CrI_3, the majority (> 60 %) of deposited thin sheets are silvery-blackish microsheets with thicknesses greater than 200 nm (see Figure 53a, page 92). As the sheets get thinner, the color initially changes to silvery-grayish that subsequently becomes more transparent (see Figure 53b). About 20 % of investigated CrI_3 layers were nanosheets with thicknesses between 25 – 75 nm (see Figure 53a and Figure 54, page 92). Only few structures exhibited thicknesses below 25 nm (see Figure 53a).

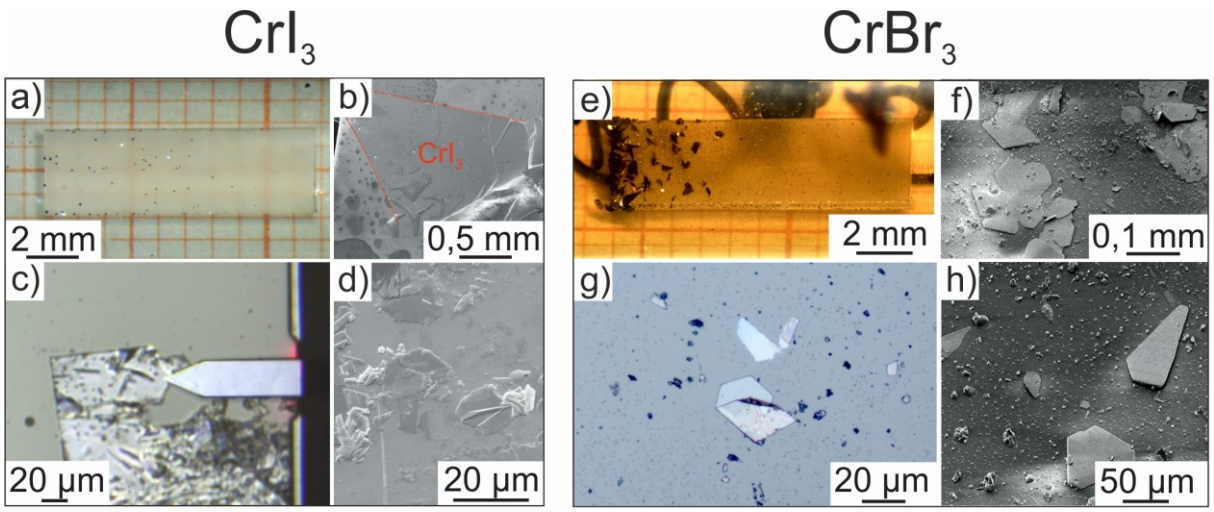

Figure 52: **(a)** CrI_3 micro- and nanosheets proceeding from 20 mg Cr powder and 160 mg of I_2 deposited at YSZ within a duration of 30 minutes, **(b)** CrI_3 microsheet proceeding from 10 mg Cr powder and 80 mg I_2 deposited with larger ΔT = 200 K (1023 → 823 K) within a duration of 1 hour, **(c)** CrI_3 nanosheets proceeding from 10 mg Cr powder and 80 mg I_2 deposited with smaller ΔT = 50 K (923 → 873 K) within a duration of 1 hour, **(d)** CrI_3 nanosheets proceeding from 1 mg Cr powder and 8 mg I_2 deposited with ΔT = 100 K (923 → 823 K) within a duration of 30 minutes, **(e)** $CrBr_3$ micro- and nanosheets proceeding from 7 mg Cr powder and 38 mg Br_2 deposited at YSZ substrate and residual bromine atmosphere, the $CrBr_3$ nanosheets were obtained applying parameters ΔT = 200 K (1023 → 823 K) within a durations of 30 minutes, **(f-g)** refer to experiments with a gradient of ΔT = 100 K (923 → 823 K) and same amounts of introduced materials (Cr & Br_2) as well as transport duration. The figures were extracted from reference [126].

With respect to $CrBr_3$, more than half of the investigated structures were dark-green colored microsheets with thicknesses of more than 200 nm (see Figure 53b, page 92). Similar to bulk $CrBr_3$, the microsheets mistakenly seem to appear brown due to the residual bromine atmosphere (see Figure 52e). As the layers get thinner (75 – 200 nm) the color changes to light-colorful-green (> 20 % of deposited layers, see Figure 53a, b, page 92). Further thickness reduction leads to a white-grey appearance (25 – 75 nm, ≈ 10 % of sheets) that becomes more transparent (< 25 nm, > 10 % of deposited $CrBr_3$) with decreasing thickness (see Figure 53b and Figure 54). The lateral dimensions of $CrBr_3$ micro- and nanolayers are about 20 µm (according to nanolayers) and several hundred µm (with respect to microsheets, see Figure 52e-h). It was further observed that both, $CrBr_3$, but especially CrI_3, microsheets are oxygen sensitive that is even enhanced at nanolayer dimensions (see appendix, Figure A 11, page 132).[13]

[13] From an experimental point of view, the oxygen sensitivity of $CrBr_3$ and CrI_3 thin layers initially did not seem to be as drastic as with comparable samples of e.g. $TiCl_3$. However, the change of the crystal habitus can be well monitored using an opical microscope within minutes in ambient atmosphere.

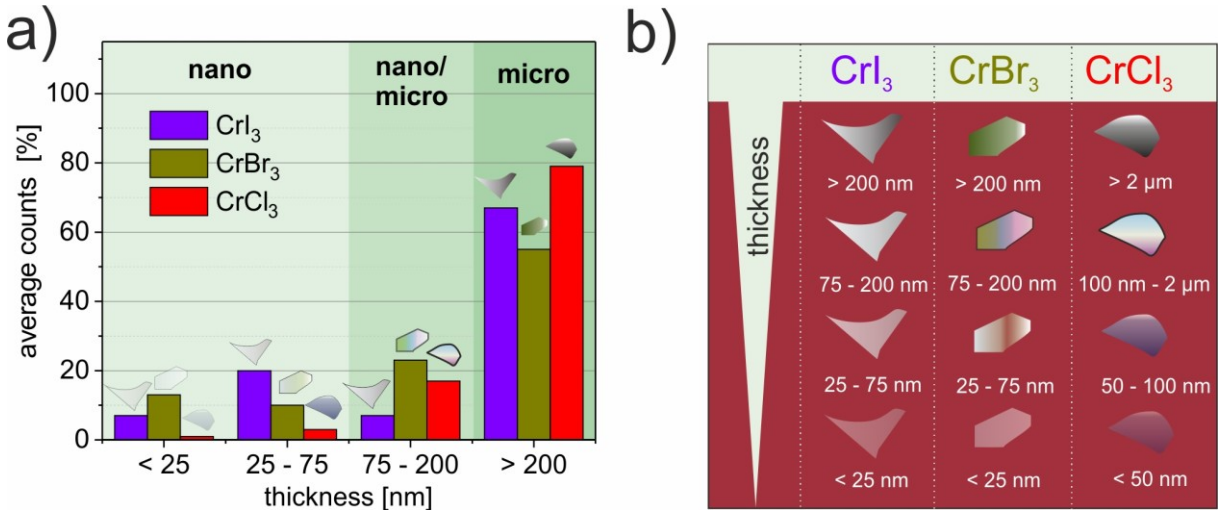

Figure 53: **(a)** Distribution of thicknesses of CrX_3 micro- and nanosheets on YSZ substrates, **(b)** appearance and color of CrX_3 micro- and nanosheets on top of YSZ depending on its individual thickness observed by optical microscopy in bright field mode.

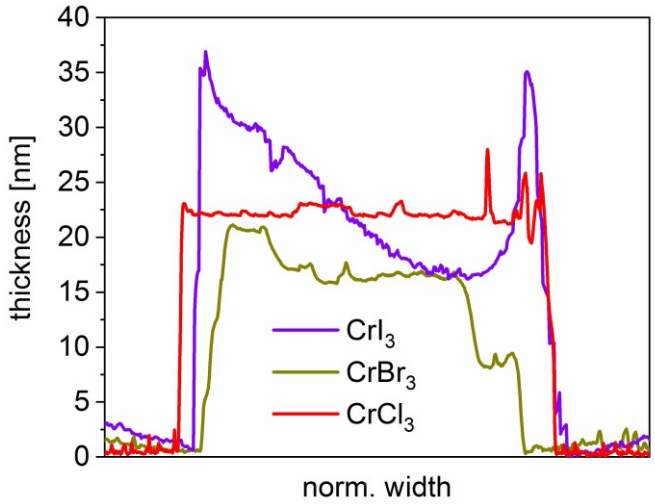

Figure 54: Thickness of individual representative deposited CrX_3 nanosheets (X = Cl, Br, I) determined by AFM, to ease the comparison of distinct layer thicknesses the latitudinal dimensions were normalized (the absolute values are in the range of several micrometers).

4.3.4.2 Composition and thickness dependent measurements of CrX_3 nanosheets (SEM-EDX, XPS, micro-RAMAN)

The composition of CrX_3 micro- and nanosheets was investigated by SEM-EDX and XPS. Related to CrI_3 on top of YSZ the expected elemental lines of Cr-*K*, I-*L*, Zr-*L*, Y-*L* and O-*K* were observed quantitatively (see Figure 55a, page 93). With respect to Cr-*K* and I-*L* the quantification results pointed towards CrI_3 (by a ratio of ≈ 1:3) similar to results obtained with $CrCl_3$, see appendix Table A 13, page 140. Analogical to EDX investigations of MCl_3 nanosheets it was not practicable to assign the origin of the oxygen signal (O-*K* line) to either a potential oxidized CrX_3 nanosheet or the YSZ substrate (as it contains oxygen). In further complexity, the Cr-*L* and I-*M* lines both overlap with the O-*K* line, due to similar energies of released X-ray quanta (see Figure 55a). Likewise the quantitative attribution of the elemental

lines of $CrBr_3$ fitted to the expected pattern composed of Cr-*K*, Br-*L*, Zr-*L* (Y-*L*), and O-*K* (see Figure 55b). By reason of an over-quantification of bromine signal (see appendix, Table A 13, page 140) the quantification fitted worse to a 1:3 ratio (Cr:Br according to $CrBr_3$), as already observed with bulk $CrBr_3$ (see chapter 4.3.2.2, page 82). A significant perturbance variable definitely was the emergence of charging effects due to the insulating behavior of the YSZ substrate (and highly probable also the *Mott* insulating behavior of $CrBr_3$, see Footnote 9 at page 82). Thus, the quantification results are only indicators of a potential composition of thin CrX_3 sheets, but needed to be re-confirmed by using more sensitive techniques, e.g. XPS.

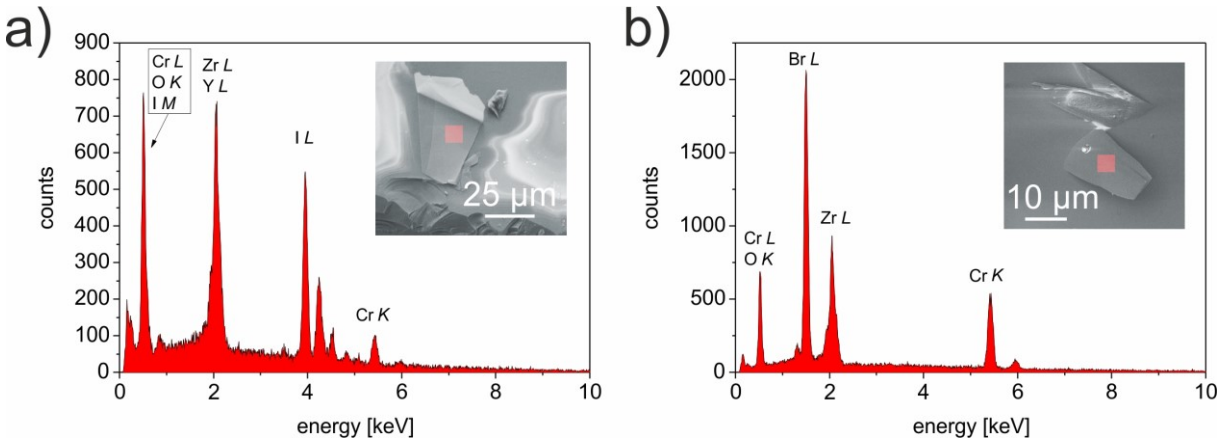

Figure 55: SEM-EDX investigations of CrX_3 micro- and nanosheets on top of YSZ substrates: **(a)** CrI_3 and **(b)** $CrBr_3$, the inlays are demonstrating the investigated CrX_3 thin crystals, the red spot is indicating the location of the respective EDX measurement, in contrast to bulk CrX_3 EDX results, the total number of acquired X-ray quanta (counts) was added to get a better idea of the signal-to-noise ratio. The figures were partly extracted (and reproduced) from reference [126].

To further clarify the origin of the oxygen signal detected by EDX (see Figure 55), CrX_3 micro- and nanosheets were investigated by surface sensitive XPS (see Figure 56, page 94). The obtained spectra were compared to those of the CrX_3 bulk flakes and the pure YSZ substrate (see Figure 56). With respect to CrI_3, the acquired XPS spectra of nanosheets and bulk were almost identical, excluding the increased oxygen peak in lower material dimensions (see Figure 56a). This proves the high quality of the as-prepared CrI_3 nanolayers. The Zr3p and Zr3d peaks arising from the YSZ substrate are also visible in the spectra of the thinner CrI_3 layers (see Figure 56a). Fairly good results were acquired using $CrBr_3$ bulk structures (see Figure 56b). In contrast to bulk $CrBr_3$, only signal of minor intensity could be detected investigating $CrBr_3$ micro- and nanosheets. This resulted in significantly decreased intensity of Cr and Br peaks (see Figure 56b). By means of XPS quantification calculations it could be confirmed that oxygen is mainly arising due to the underlying YSZ substrate related to both bulk and nano-layered CrI_3. Subsequently to a sputtering process with argon ions, the remaining oxygen amount was about 2 at-% and thus assigned as rather adsorbed at the CrI_3 nanosheets surface and not incorporated in the crystal lattice. This matched pretty close to a similar situation in

*M*Cl$_3$ nanosheets (*M* = Ru, Mo, Cr). The situation is much more difficult with respect to CrBr$_3$. The acquired data of CrBr$_3$ were not sufficient in quality to declare a quantitative evidence related to the origin of detected oxygen. Highly probable the investigated micro- and nanosheets were oxidized to Cr_2O_3. Since the oxygen sensitivity drastically increases with downsizing the sheets of CrBr$_3$, it could be assumed that oxygen contamination was induced by sample transfer (from the glovebox to the XPS device), although suitable transfer chambers were used.

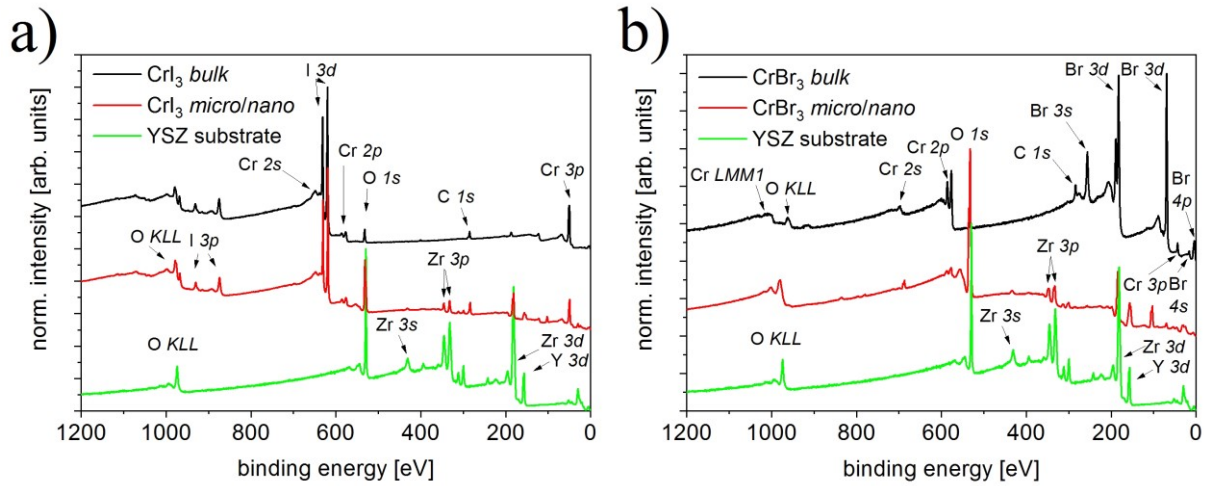

Figure 56: Thickness dependent XPS measurements of CrX_3 compounds: **(a)** CrI$_3$ and **(b)** CrBr$_3$ with respective CrX_3 bulk flakes in black color, CrX_3 micro- and nanosheets deposited at the respective substrate (red color) and the underlying, pure substrate without any structures on top (light green). The figures were partly extracted (and reproduced) from reference [126].

Subsequently, thickness dependent micro-RAMAN measurements of CrX_3 structures were carried out (see Figure 57, page 95). Initially starting with CrI$_3$, the acquisition of suitable data rather failed excluding one observed lattice vibration of A_g type at 110 cm^{-1} (see Figure 57a). This peak was also observed by *Shcherbakov* et al.[31] The utilized measurement setup was located in an ambient atmosphere and thus highly probable influenced by moisture contaminations as well as previously reported photocatalytic degradations of CrI$_3$.[31] It is reported that this degradation is accompanied with a photo induced ligand substitution with H_2O and formation of aqua chromium iodides, which are hygroscopic and water soluble.[31] As a result the acquired RAMAN peaks of nano- and microlayered CrI$_3$ were fairly broadened and decreased in total intensity (see Figure 57a).

Similar to well viable measurements of CrCl$_3$, micro-RAMAN spectra of CrBr$_3$ were observed for several layer thicknesses (see Figure 57b). It proved that the main spectroscopic features are identical for all thicknesses of the material (see Figure 57b). Moreover, the acquired data are in very good agreement with literature.[25,155] A particular change related to the intensity of individual CrBr$_3$ spectra was the decreasing A_{1g} peak at 108 cm^{-1} (see Figure 57b). The acquired RAMAN spectra of CrBr$_3$ confirmed the high crystallinity of as-prepared micro- and nanolayers on YSZ substrates.

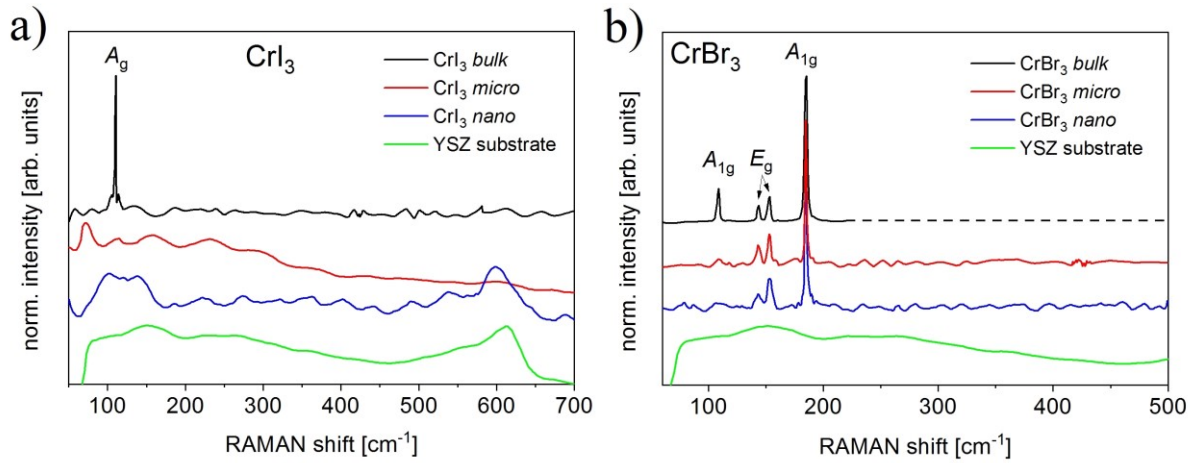

Figure 57: Thickness dependent micro-RAMAN measurements of CrX_3 compounds: **(a)** CrI_3 and **(b)** $CrBr_3$ with respective CrX_3 bulk flakes in black color, CrX_3 micro- (red color) and CrX_3 nanosheets (blue color) and the underlying pure YSZ substrate without any structures on top (light greencolor). The figures were partly extracted (and reproduced) from reference [126].

4.3.4.3 Magnetic properties of $CrCl_3$ microsheets (SQUID, XMCD, NMR)

The magnetic properties of as-grown $CrCl_3$ micro- and nanosheets on YSZ substrates were determined by SQUID magnetometry. The magnetic field was applied perpendicular to the crystallographic *c*-axis of $CrCl_3$ (easy axis). To reduce the influence of the underlying YSZ, the magnetization of the empty substrate (without $CrCl_3$) was measured initially and the diamagnetic signal was then subtracted from the overall measurement data ($CrCl_3$ on top of YSZ) assuming that there is no additional contribution stemming from (magnetic) interactions at the interface between $CrCl_3$ and the substrate.

The magnetization data of thin sheets significantly differ from those of the bulk flakes (see Figure 59b, page 97). In bulk $CrCl_3$ flakes (sample thickness in the *µm* range and width in the *mm* range), as described in chapter 4.3.2.4 (page 85), two magnetic transition occur at low external fields (e.g., $\mu_0 H \leq 0.1$ T).[69] The first transition at 16-18 K is indicating the *intralayer* "ferromagnetic" alignment of individual spins. By decreasing the temperatures to 13-14 K the *interlayer* antiferromagnetic interactions lead to the overall formation of an *A*-type antiferromagnetic ground state (see Figure 58, page 96). This is associated with a decrease in the magnetization below this temperature (see Figure 59b). By the application of higher external fields ($\mu_0 H \geq 3$ T) the overall ferromagnetic contribution dominates due to a very small spin-flop field.

With respect to $CrCl_3$ micro- and nanosheets (sample thickness in the *nm* range and width in the *µm* range), the investigations showed that the magnetic ordering transition from paramagnetic to *intralayer* "ferromagnetic" (16-18 K) is not affected by dimensionality as indicated by comparable transition temperatures in small external fields ($\mu_0 H \leq 0.1$ T),

see Figure 59b. The second transition (13-14 K) significantly differs in bulk compared to the micro/nano material. Our observations point towards non-trivial, complex magnetic interactions in micro- and nano dimensions of $CrCl_3$. While in bulk dimensions an *interlayer A*-type AFM ground state is preserved (see Figure 50e, page 88), it is speculated that $CrCl_3$ in micro/nano thicknesses support predominantly ferromagnetic interactions instead ("*interlayer*-ferro") below this temperature (13-14 K), in clear distinction to bulk $CrCl_3$ (see Figure 59a). One reason might be, that there is some competing interplay of anti- and ferromagnetic contributions in lower dimensions. Other explanations for the increasing magnetization could also be found in additional para- or ferrimagnetic impurities. Nevertheless, the overall magnetization of nano $CrCl_3$ does not drop to lower values with decreasing temperature, which would correspond to an AFM behavior (see Figure 59b).

Unless the situation is not finally clarified with respect to micro- and nano $CrCl_3$, we suppose from our investigations that even very small magnetic fields ($\mu_0 H \leq 0.1$ T) are sufficient to fully polarize the spins and to induce a ferromagnetic state (see Figure 58 and Figure 59a). With respect to $CrCl_3$ in micro- and nano thicknesses, no indicators of an *A*-type antiferromagnetic ground state is observed at low temperatures, as proven with bulk $CrCl_3$ samples.[169] For clarification of the magnetic situation in micro- and nano thicknesses of $CrCl_3$ it would be suitable to investigate if a hysteresis occurs at lower dimensions, which would (highly probable) consequently confirm ferromagnetic behavior. Another useful investigation to elucidate the magnetic properties of thin sheets would be a measurement of the spin-flop field at low fields.

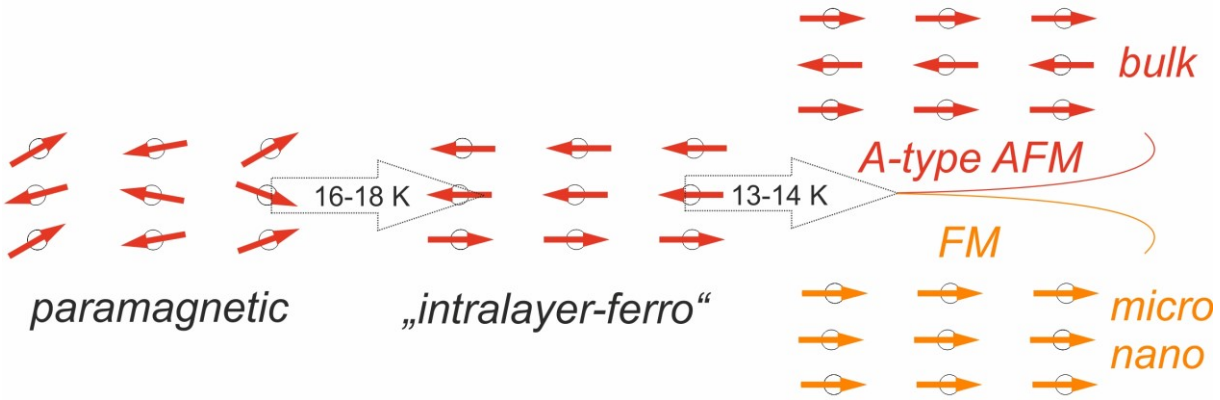

Figure 58: Simplified scheme about the tuning of magnetic properties of $CrCl_3$ bulk (red color) and $CrCl_3$ micro/nanosheets at YSZ substrates (orange color) with temperature by application of an external magnetic field ($\mu_0 H = 0.1$ T) aligned perpendicular to the crystallographic *c* axis of $CrCl_3$ (both bulk flakes and thin sheets).

The magnetization as function of field data ($m(H)$) of thin $CrCl_3$ sheets (see Figure 59c) clarifies that the magnetization (respectively magnetic ordering) shows no saturation even for fields $\mu_0 H = 5$ T. Instead, the investigated micro/nano $CrCl_3$ sample show a monotonous increase of the magnetization up to the highest accessible fields. This is in contrast to the bulk samples

where the full saturation is reached for $\mu_0 H \approx 1$ T (magnetic field perpendicular to c axis), or $\mu_0 H \approx 2$ T (magnetic field parallel to c axis). It has to be remarked, that no demagnetization correction was applied within the measurement, which could change the trend of the $m(H)$ curves. Additionally, the error in the absolute values of magnetization of $CrCl_3$ bulk crystals of both orientations (parallel and perpendicular to c) could stem from an error of the mass of applied platelets.

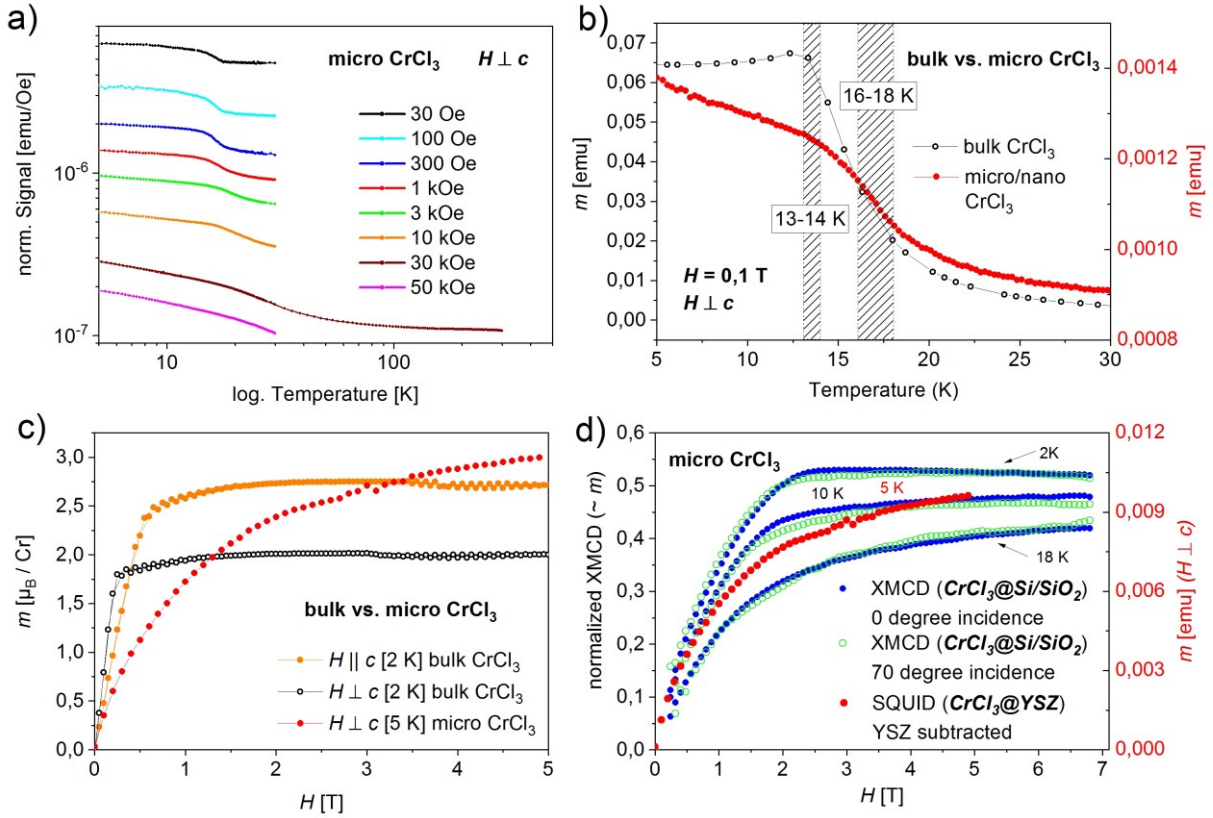

Figure 59: (a) Magnetization of $CrCl_3$ micro- and nanosheets at YSZ substrates determined by SQUID at various external magnetic fields ($\mu_0 H$ = 30 Oe…50 kOe) aligned perpendicular to the crystallographic c axis (parallel to a/b) of $CrCl_3$, **(b)** comparison of the magnetization of microsheets and bulk crystals of $CrCl_3$ at an external magnetic field of $\mu_0 H$ = 1 kOe (0.1 T) at low temperatures (5…30 K), **(c)** comparison of the magnetization of microsheets at 5 K and bulk crystals of $CrCl_3$ at 2 K at various external magnetic fields up to $\mu_0 H$ = 50 kOe (5 T), **(d)** comparison of magnetization of $CrCl_3$ microsheets at various low temperatures (2…18 K) determined by SQUID magnetometry ($CrCl_3$@YSZ) and XMCD ($CrCl_3$@Si/SiO_2, in 0 and 70 degree beam incidence).

X-ray magnetic circular dichroism (XMCD) is a useful tool to investigate ferromagnetism and is especially suitable for thin layer materials. For clarification of the $CrCl_3$ thin sheets magnetic properties, surface sensitive XCMD was utilized in fluorescence mode. The initial scheme to characterize $CrCl_3$ on YSZ, as in the SQUID case, failed, due to charging effects that aggravated reproducible measurements. The charging effects were caused by the insulating nature of the substrate, although a thin layer of conducting gold (5 nm) was sputtered on top of the substrate. To realize XMCD measurements thin flakes of $CrCl_3$ were transferred onto Si/SiO_2 substrates (200 nm oxide layer) by using ultrasonication. The X-ray absorption (XAS), and consequent XMCD spectra, were obtained by taking into account the Cr $L_{2,3}$ absorption edges at low

temperatures (2-3 K) and magnetic fields of both $\mu_0 H$ = 0.15 T and 6.8 T (see Figure 60, page 99). Absorption of circular-polarized X-rays by magnetic atoms depends on the polarization direction (caused by different absorption coefficients for a specific direction), which enables determination of element-specific magnetic properties from the difference of two absorption spectra (which is known as magnetic dichroism). The observed XAS spectra of $CrCl_3$ at the Cr $L_{2,3}$ edge show typical Cr^{3+} multiplets due to 2p→3d excitations, which exhibit strong circular polarization dependence in the magnetic field of 6.8 T (see Figure 60a). Basically the obtained summarized spectra (parallel and anti-parallel X-ray helicities) are in very good agreement to those of *Frisk* et al. that analyzed the XAS and XMCD of CrI_3 at the Cr $L_{2,3}$ edge.[132] The XMCD spectrum results of the difference between the XAS spectra of both circular polarization (clockwise and anti-clockwise). The XMCD signal of $CrCl_3$ micro- and nanosheets obtained in a magnetic field of 6.8 T points towards a ferromagnetic ordering (see Figure 60a). By decreasing the external magnetic field down to 0.15 T the ferromagnetic signal, and thus the differences between the X-ray absorption with respect to two polarization directions, and in turn the XMCD signal was reduced in intensity but is still present (see Figure 60c). This confirms that even small fields of 0.15 T are sufficient to stabilize an interlayer ferromagnetic ordering of $CrCl_3$ micro- and nanosheets.

To further analyze the type of long range magnetic order, the angle dependence of XMCD was studied. Both at high (6.8 T) and low fields (0.15 T) the XMCD is almost the same in energy and intensity with respect to beam incidences from 0° (initial measurements, see Figure 60a and c) to 56°. In case of an antiferromagnetic ordering the XMCD should be reduced or even vanish with an enlarged angle (grazing incidence). However, due to only very slight changes in the angle dependent XMCD data it is concluded that the thin $CrCl_3$ sheets order exclusively ferromagnetic (see Figure 60b and d). The magnetization data extracted from the measurements fit pretty well to those of the SQUID measurements and does not change significantly by application of an incidence angle of 70° (see Figure 59d).

To further explain the altered magnetic properties of $CrCl_3$ micro- and nanosheets ^{53}Cr zero field NMR was utilized. Initially, the NMR spectra of bulk $CrCl_3$ (sample from TU Dresden) was measured at various low temperatures (see Figure 61a, page 101). As expected for chromium with spin $^3/_2$ and an isostructural crystallographic environment, three lines are obtained related to transitions $[m = +\,^1/_2 \rightarrow m = -\,^1/_2]$, $[m = +\,^3/_2 \rightarrow m = +\,^1/_2]$, and $[m = -\,^1/_2 \rightarrow m = -\,^3/_2]$ that are clearly visible at 1.4 K (see Figure 61a, page 101).

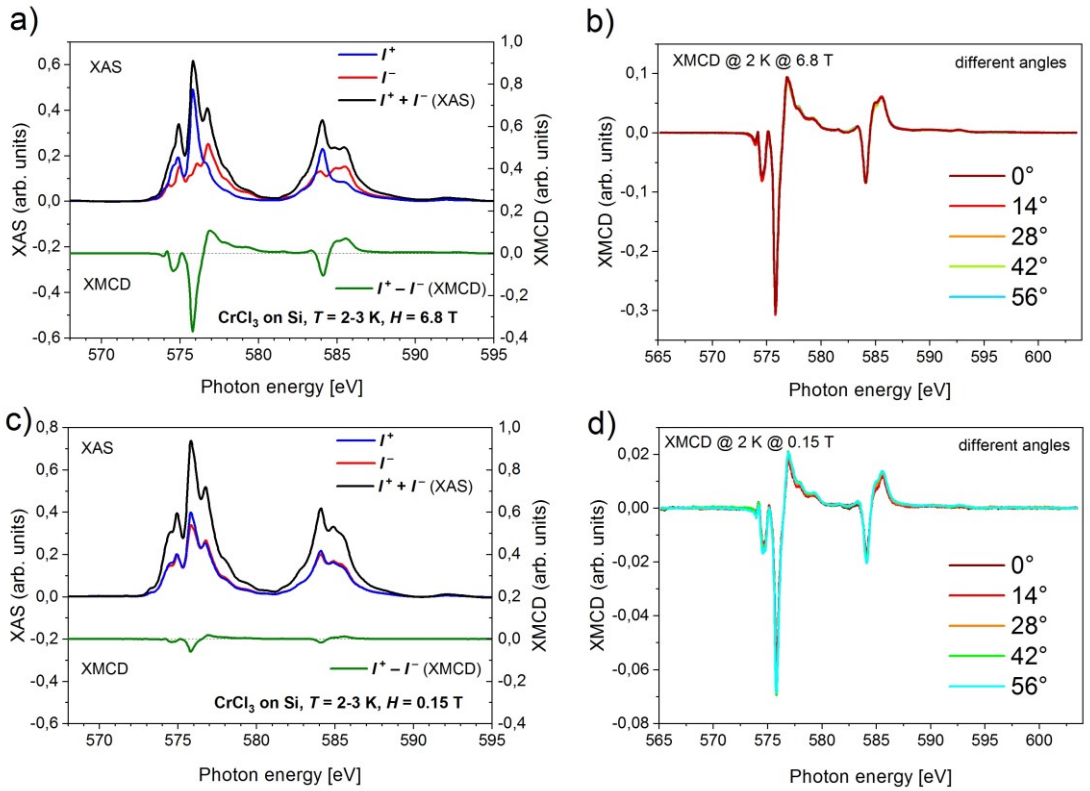

Figure 60: (a) XAS- (black) and XMCD spectra (green) of $CrCl_3$ microsheets at Si/SiO_2 substrate at the Cr $L_{2,3}$ edge at low temperatures (2…3 K) and a magnetic field of 6.8 T, the net X-ray absorption spectrum (black) is obtained by the sum of XAS with variable polarization (circular left (blue) or right (red) polarized light, **(b)** XMCD spectra of $CrCl_3$ microsheets at the Cr $L_{2,3}$ edge at 2 K and 6.8 T obtained at various angles of incidence (the XMCD data overlap), **(c)** XAS- (black) and XMCD spectra (green) of $CrCl_3$ microsheets at Si/SiO_2 substrate at the Cr $L_{2,3}$ edge at low temperatures (2…3 K) and a magnetic field of 0.15 T, the net X-ray absorption spectrum (black) is obtained by the sum of XAS with variable polarization (circular left (blue) or right (red) polarized light, **(d)** XMCD spectra of $CrCl_3$ microsheets at the Cr $L_{2,3}$ edge at 2 K and 0.15 T obtained at various angles of incidence (the XMCD data overlap).

At higher temperatures the Cr signals are shifted to lower frequencies, which results from the evolution of the hyperfine field that is associated with the electronic magnetization and mimics, hence, the magnetometry data. Concomitantly, the number of NMR lines is increasing from $T \geq 2.8$ K indicating a larger number of chromium environments. The observation of additional local environments could be explained as follows: $CrCl_3$ undergoes a first order structural phase transition at 240 K from monoclinic $C2/m$ (with respect to an ABC stacking order) to rhombohedral $R\bar{3}$ (related to an ABAB stacking).[15,70,170] This phase transition shows a substantial thermal hysteresis and is suspected to exhibit a wide coexisting range. It could be tentatively assumed, that there are still minor amounts of a second stacking order (e.g. ABC) in a dominating ABAB stacking of individual $CrCl_3$ layers at low temperatures (stacking faults), which would also confirm the investigations made by PXRD (see chapter 4.2.2.3, page 54). By decreasing the temperature (2.1 K and 1.4 K) the second magnetic environment seems to vanish indicating an ABAB stacking solely (see Figure 61a, page 101). NMR lines originating in chlorine are as well present but lower in intensity, for instance a single

broad peak at the 5 K spectrum at 59 MHz (related to the ABAB stacking), two Cl-NQR lines at 54.5 MHz and 56 MHz in the higher temperature 7.5 K NMR spectrum (related to minor amounts of ABC stacking still present in these structures), or a broad range where these three coexist, indicated by arrows in the corresponding spectra (see Figure 61a and b).

NMR measurements of $CrCl_3$ micro- and nanosheets on YSZ substrates point towards signals shifted to higher values in frequency compared to bulk (see Figure 61b). A reason for the shift of the micro/nano samples could be additional strain that is present in thinner sheets of $CrCl_3$. This strain might be induced due to a lattice mismatch between the monoclinic ($C2/m$) $CrCl_3$ unit cell (a = 5.9588(16) Å; b = 10.3206(13) Å; c = 6.1138(21) Å) and the cubic YSZ substrate crystal structure ($Fm\bar{3}m$; a = 5.21(2)). Apart from the shift, the spectra of single crystals and microsheets are rather similar at temperatures of 4.25 K, respectively 4.5 K (see Figure 61b). The small shoulder in the microsheets spectra at 4.5 K could be assigned to an enlarged surface-to-volume ratio, which is only present in micro/nano samples.

Another explanation would be the altered environment due to the additional interface with the YSZ substrate of one $CrCl_3$ layer. Furthermore, the individual peaks of the microsheets sample are blurred and not as sharp as they are in the single crystal case. This might be an indicator of many magnetic contributions that interact in thin sheets, more than in the bulk material. Related to the same spectra at 8 K, two peaks with similar intensities were observed instead of one peak as in the bulk material (see Figure 61b). Still, the origin of the second peak is unknown but could be assigned to an enlarged contribution of surface chromium atoms and conflated ^{53}Cr “bulk” peaks. Similar to the 4.5 K curve of microsheets, the influence of the interface with the substrate cannot be excluded. Related to isostructural $RuCl_3$, *Vatansever* et al. recently described that a biaxial in-plane tensile strain of higher than 2 % is sufficient to change an antiferromagnetic ground state of a monolayer to ferromagnetic.[121] Thus, this strain, present in micro- and nanosheets of $CrCl_3$, could explain the altered magnetic properties present in thin sheets.

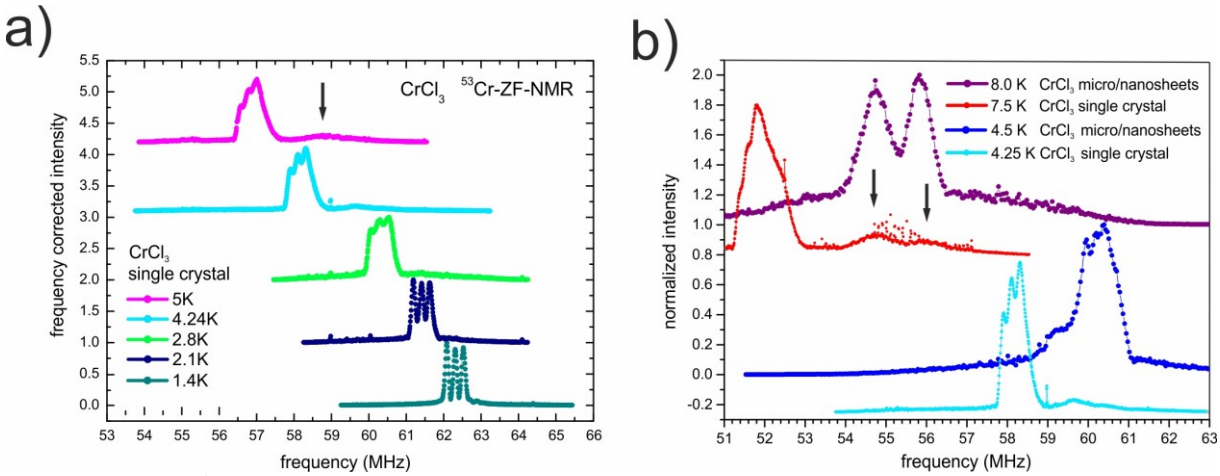

Figure 61: (a) ^{53}Cr zero field NMR of $CrCl_3$ single/bulk crystals at low temperatures (1.4…5 K) and **(b)** comparison of NMR spectra of $CrCl_3$ bulk crystals and $CrCl_3$ micro/nanosheets on YSZ substrates at similar temperatures; the black arrows in both figures are pointing towards additional contributions of chlorine, smaller in intensity, but still visible.

5 Conclusion and outlook

This thesis is focused on the simulation, synthesis and characterization of transition metal trihalides MCl_3 (M = Ru, Mo, Ti, Cr) and CrX_3 (X = Cl, Br, I) with respect to either the thicker bulk material or thinner micro- and nanosheets deposited on substrates.

For a rational synthesis planning of each system the vapor transport of MCl_3 and CrX_3 was initially simulated for a decent understanding of occurring heterogeneous and homogeneous gas phase equilibria. Simulation results revealed beneficial transport conditions applying stoichiometric compositions of $CrCl_3$ (873 → 773 K) and $RuCl_3$ (973 → 773 K) corresponding to a sublimation. Suitable transport rates of $CrBr_3$ and CrI_3 were calculated by introduction of a slight excess of X (X = Br, I) and temperatures of 1023 → 923 K. Lower temperature gradients (ΔT = 70 K) were calculated to be thermodynamically preferred for CVT of $MoCl_3$ with $MoCl_5$ (as transport addition) at temperatures 743 → 673 K. Similar temperatures, but a still slightly higher gradient (ΔT = 100 K), was calculated for CVT of $TiCl_3$ with $GaCl_3$ (700 → 600 K).

Based on prior simulation results MCl_3 (M = Ru, Mo, Cr) bulk flakes were synthesized in thermodynamic favorable regimes for at least 24 hours with respect to the introduction of 50 mg $RuCl_3$, 50 mg $MoCl_3$ (+ 5 mg $MoCl_5$) or 150 mg $CrCl_3$. With respect to CrX_3 (X = Br, I) about 10 mg of elemental chromium and 50 mg (Br_2) or 80 mg (I_2) were utilized. In case of $TiCl_3$ a vapor transport of about 4 hours proved to be sufficient for considerable crystal growth considering the utilization of 25 mg $TiCl_3$ and 5 mg $GaCl_3$.

Characteristic millimeter sized, platelet-shaped crystals were obtained with black-silvery- ($RuCl_3$, $MoCl_3$ and CrI_3), dark green- ($CrBr_3$) or dark purple to pink colors ($TiCl_3$ and $CrCl_3$). PXRD confirmed the high crystallinity and phase purity of MCl_3 and CrX_3 sheets with monoclinic or trigonal crystal systems according to ABC or AB stacking orders of the otherwise identical honeycomb layers. In consistence with literature the magnetic measurements pointed towards antiferromagnetic ground states of $RuCl_3$ while $TiCl_3$ showed para- and $MoCl_3$ diamagnetic behavior. The magnetic measurements of CrX_3 flakes confirmed the magnetic anisotropy and ferro- or antiferromagnetic ordering at lower external applied magnetic fields (0.1 T). Application of higher fields (3 T) led to an induced ferromagnetic state with respect to all three CrX_3 (X = Cl, Br, I) compounds.

MCl_3 nanosheets were basically prepared at the same temperatures as the respective bulk flakes, but additionally with suited substrates. MCl_3 (M = Ru, Ti, Cr) and CrX_3 thin sheets were deposited on YSZ substrates, while $MoCl_3$ was prepared on sapphire. The main focus for formation of thin layers were a considerable lower amount of introduced material ($RuCl_3$ and

$CrCl_3$: 1 mg, $TiCl_3$: 5 mg ($GaCl_3$: 1 mg) and $MoCl_3$: 6 mg ($MoCl_5$: 0.6 mg)) and a consequent way less transport time. While vapor transports of $MoCl_3$ and $TiCl_3$ were realized within 60 minutes transport duration (30 minutes related to $CrBr_3$), sublimation processes were successful using 30 minutes ($CrCl_3$), 60 minutes (CrI_3), or even a pure heating-up process considering $RuCl_3$.

Thin sheets of MCl_3 and CrX_3 composition exhibited systems specific and thickness dependent colors and got more transparent, the thinner they are. In fact, more than 50 % of deposited MCl_3 and CrX_3 structures were microsheets with thicknesses greater than 200 nm. About 20 % of deposited $RuCl_3$, $MoCl_3$, CrI_3 and $CrBr_3$ sheets were nanolayers with thicknesses less than 75 nm. One highlight of this work is the successful reproducible isolation of $RuCl_3$ monolayers by subsequent delamination using ultrasonication. Similarly, $CrCl_3$ monolayers were obtained by using the conventional scotch tape approach applied to prior as-grown thin sheets. SEM confirmed mainly randomly orientated as-prepared MCl_3 and CrX_3 nanoflakes deposited on the respective substrates. The investigated samples confirmed a high specimen homogeneity with well-arranged MCl_3 atomic planes. XPS confirmed the desired MCl_3 and CrX_3 composition of nanosheets without further impurities. Oxygen, detected by EDX, could be identified as rather adsorbed on the surface of MCl_3 and CrX_3 (X = Cl, I) nanosheets, which means O_2 did not incorporate the crystal lattice. RAMAN measurements and electron diffraction confirmed the high crystallinity of the nanosheets (MCl_3 and CrX_3). Slight shifts of phonon energies were determined to either higher- ($RuCl_3$, $CrCl_3$) or lower intensity ($MoCl_3$), which could be signatures of strain present in thinner MCl_3 (M = Ru, Mo, Cr) layers.

The magnetic data of as-prepared $CrCl_3$ micro- and nanosheets revealed ferromagnetic order even at very low external magnetic fields (e.g. $\mu_0 H$ = 30 Oe) without any signatures of an A-type antiferromagnetic ground state, in significant difference to the bulk $CrCl_3$ material. Another highlight of this work is the observed enhancement of catalytic activity of $TiCl_3$ by microstructuring by about 16 %. Further delamination down to nano dimensions enlarged the catalytic properties ones more by about 8 % (and thus a total improvement of 24 % in comparison to as well investigated bulk $TiCl_3$).

However, this thesis is only a cornerstone for following investigations. The occurring stacking sequence in as-grown MCl_3 and CrX_3 nanolayers is of great interest for further detailed comprehension of altered physical properties, such as varied cooperative magnetic interactions. Additional insights into crystallinity of thin layers could be revealed by polarized RAMAN measurements. In further consequence mixed halide systems such as $M_{1-x}M'_xX_3$, $M(X_{1-y}Y_y)_3$ or even $M_{1-x}M'_x(X_{1-y}Y_y)_3$ are chemically possible and should be investigated.

6 Bibliography

[1] E. Benckiser, *Phys. J.* **2019**, *18*, 146.
[2] A. K. Geim, K. S. Novoselov, *Nat. Mater.* **2007**, *6*, 183.
[3] K. S. Novoselov, A. K. Geim, S. V Morozov, D. Jiang, *Science* **2004**, *306*, 666.
[4] K. S. Novoselov, A. K. Geim, S. V Morozov, D. Jiang, M. I. Katsnelson, I. V Grigorieva, S. V Dubonos, *Nature* **2005**, *438*, 197.
[5] G. Fiori, F. Bonaccorso, G. Iannaccone, T. Palacios, D. Neumaier, A. Seabaugh, S. K. Banerjee, L. Colombo, *Nat. Nanotechnol.* **2014**, *9*, 768.
[6] V. Nicolosi, M. Chhowalla, M. G. Kanatzidis, M. S. Strano, J. N. Coleman, *Science.* **2013**, *340*, 1226419.
[7] P. Miro, M. Audiffred, T. Heine, *Chem. Soc. Rev.* **2014**, *43*, 6537.
[8] C. Claus, *Bull. Sci. St. Pdtersbg.* **1844**.
[9] G. Brauer, "Handbuch Der Präparativen Anorganischen Chemie", **1981**, Ferdinand Enke Verlag Stuttgart, ISBN: 3432878230.
[10] L. Wang, M. Rocci-Lane, P. Brazis, C. R. Kannewurf, Y.-I. Kim, W. Lee, J.-H. Choy, M. G. Kanatzidis, *J. Am. Chem. Soc.* **2000**, *122*, 6629.
[11] J. M. Fletcher, W. E. Gardner, E. W. Hooper, K. R. Hyde, F. H. Moore, J. L. Woodhead, *Nature* **1963**, *199*, 1089.
[12] H. B. Cao, A. Banerjee, J.-Q. Yan, C. A. Bridges, M. D. Lumsden, D. G. Mandrus, D. A. Tennant, B. C. Chakoumakos, S. E. Nagler, *Phys. Rev. B* **2016**, *134423*, 1.
[13] M. Roslova, J. Hunger, G. Bastien, D. Pohl, H. M. Haghighi, A. U. B. Wolter, A. Isaeva, U. Schwarz, B. Rellinghaus, K. Nielsch, B. Büchner, T. Doert, *Inorg. Chem.* **2019**, *58*, 6659.
[14] C. Wellm, J. Zeisner, A. Alfonsov, A. U. B. Wolter, M. Roslova, A. Isaeva, T. Doert, M. Vojta, B. Büchner, V. Kataev, *Phys. Rev. B* **2018**, *98*, 184408.
[15] B. Morosin, A. Narath, *J. Chem. Phys.* **1964**, *40*, 1958.
[16] B. Carrivaburu, J. Ferre, R. Mamy, I. Pollini, J. Thomas, *J. Phys. C Solid State Phys.* **1986**, *19*, 4985.
[17] S. A. Cotton, "Chemistry of Precious Metals", **1998**, Chapman & Hall, 2-6 Boundary Row, London, UK, ISBN: 07514 0413 6.
[18] I. Tsubokawa, *J. Phys. Soc. Japan* **1960**, *15*, 1664.
[19] J. R. Sime, N. W. Gregory, *J. Am. Chem. Soc.* **1960**, *82*, 93.
[20] J. F. Dillon, *J. Appl. Phys.* **1962**, *33*, 1191.
[21] A. C. Gossard, V. Jaccarino, J. P. Remeika, *J. Appl. Phys.* **1962**, *33*, 1187.
[22] W. N. Hansen, M. Griffel, *J. Chem. Phys.* **1959**, *30*, 913.
[23] L. D. Jennings, W. N. Hansen, *Phys. Rev.* **1965**, *139*, 1694.
[24] C. H. Cobb, V. Jaccarino, J. P. Remeika, R. Silberglitt, H. Yasuoka, *Phys. Rev. B* **1971**, *3*, 1677.
[25] V. M. Bermudez, *Solid State Commun.* **1976**, *19*, 693.
[26] V. M. Bermudez, D. S. McClure, *J. Phys. Chem. Solids* **1979**, *40*, 149.
[27] K. Nocker, R. Gruehn, *Z. Anorg. Allg. Chem.* (*ZAAC*) **1994**, *620*, 73.
[28] N. Richter, D. Weber, F. Martin, N. Singh, U. Schwingenschlögl, B. V. Lotsch, M. Kläui, *Phys. Rev. Mater.* **2018**, *2*, 024004.
[29] L. L. Handy, N. W. Gregory, *J. Am. Chem. Soc.* **1952**, *74*, 891.
[30] J. F. Dillon, C. E. Olson, *J. Appl. Phys.* **1965**, *36*, 1259.
[31] D. Shcherbakov, P. Stepanov, D. Weber, Y. Wang, J. Hu, Y. Zhu, K. Watanabe, T. Taniguchi, Z. Mao, W. Windl, J. Goldberger, M. Bockrath, C. N. Lau, *Nano Lett.* **2018**, *18*, 4214.

[32] M. Abramchuk, S. Jaszewski, K. R. Metz, G. B. Osterhoudt, Y. Wang, K. S. Burch, F. Tafti, *Adv. Mater.* **2018**, *1801325*, 1.
[33] C.-F. Shieh, N. W. Gregory, *J. Phys. Chem.* **1973**, *77*, 2346.
[34] M. A. McGuire, H. Dixit, V. R. Cooper, B. C. Sales, *Chem. Mater.* **2015**, *27*, 612.
[35] G. T. Lin, X. Luo, F. C. Chen, J. Yan, J. J. Gao, Y. Sun, W. Tong, P. Tong, W. J. Lu, Z. G. Sheng, W. H. Song, X. B. Zhu, Y. P. Sun, *Appl. Phys. Lett.* **2018**, *112*, 072405.
[36] L. Chen, J.-H. Chung, B. Gao, T. Chen, M. B. Stone, A. I. Kolesnikov, Q. Huang, P. Dai, *Phys. Rev. X* **2018**, *8*, 041028.
[37] Z. Wang, I. Gutiérrez-Lezama, N. Ubrig, M. Kroner, M. Gibertini, T. Taniguchi, K. Watanabe, A. Imamoğlu, E. Giannini, A. F. Morpurgo, *Nat. Commun.* **2018**, *9*, 2516.
[38] B. Huang, G. Clark, E. Navarro-Moratalla, D. R. Klein, R. Cheng, K. L. Seyler, D. Zhong, E. Schmidgall, M. A. McGuire, D. H. Cobden, W. Yao, D. Xiao, P. Jarillo-Herrero, X. Xu, *Nature* **2017**, *546*, 270.
[39] Y. Liu, C. Petrovic, *Phys. Rev. B* **2018**, *97*, 1.
[40] S. Djurdjić-Mijin, A. Šolajić, J. Pešić, M. Šćepanović, Y. Liu, A. Baum, C. Petrovic, N. Lazarević, Z. V. Popović, *Phys. Rev. B* **2018**, *98*, 104307.
[41] B. Huang, G. Clark, D. R. Klein, D. MacNeill, E. Navarro-Moratalla, K. L. Seyler, N. Wilson, M. A. McGuire, D. H. Cobden, D. Xiao, W. Yao, P. Jarillo-Herrero, X. Xu, *Nat. Nanotechnol.* **2018**, *13*, 544.
[42] Y. Liu, C. Petrovic, *Phys. Rev. B* **2018**, *97*, 1.
[43] D. E. Couch, A. Brenner, *Natl. Bur. Stand. A* **1959**, *63A*, 185.
[44] A. V. Nikolaev, A. A. Opalosvkii, V. E. Fedorov, Worcester, *Therm. Anal. Proc. 2nd Intern. Conf.* **1968**, 793.
[45] M. A. McGuire, J. Yan, P. Lampen-Kelley, A. F. May, V. R. Cooper, L. Lindsay, A. Puretzky, L. Liang, S. KC, E. Cakmak, S. Calder, B. C. Sales, *Phys. Rev. Mater.* **2017**, *1*, 064001.
[46] F. Beier, H. J. Seifert, *J. Therm. Anal.* **1997**, *50*, 63.
[47] D. V. Drobot, E. A. Sapranova, *Russ. J. Inorg. Chem.* **1974**, *19*, 125.
[48] K. Ikramov, A. Kushakbaev, N. A. Parpiev, L. D. Shevchenko, patent nr.: 356249, U.S.S.R. (Chem. Abs. **1973**).
[49] H. Schäfer, G. Breil, G. Pfeffer, *Z. Anorg. Allg. Chem.* (*ZAAC*) **1954**, *276*, 325.
[50] H. Schäfer, F. Wartenpfuhl, E. Weise, *Z. Anorg. Allg. Chem.* (*ZAAC*) **1958**, *295*, 268.
[51] H. Schäfer, U. Flörke, *Z. Anorg. Allg. Chem.* (*ZAAC*) **1981**, *479*, 89.
[52] F. M. B. Coutinho, M. A. S. Costa, A. L. S. Santos, T. H. S. Costa, L. C. S. Maria, R. A. Pereira, *Fresenius. J. Anal. Chem.* **1992**, *344*, 514.
[53] M. A. S. Costa, A. L. S. S. Silva, F. M. B. Coutinho, L. C. Santa-Maria, R. A. Pereira, *Polymer* **1996**, *37*, 869.
[54] J. Lewis, D. J. Machin, I. E. Newnham, R. S. Nyholm, *J. Chem. Soc.* **1962**, 2036.
[55] T. Higuchi, H. Mori, N. Otsuka, M. Terano, *Macromol. Chem. Phys.* **2000**, *201*, 2789.
[56] H. Miyaoka, K. Hasebe, M. Sawada, H. Sano, H. Mori, G. Mizutani, *Vib. Spectrosc.* **1998**, *17*, 183.
[57] G. Natta, P. Corradini, G. Allegra, *J. Polym. Sci.* **1961**, *51*, 399.
[58] L. A. M. Rodriguez, M. V. A. N. Looy, A. Gabant, *J. Polym. Sci.* **1966**, *4*, 1917.
[59] E. Drent, C. A. Emeis, *Chem. Phys.* **1975**, *10*, 313.
[60] I. Pollini, *Solid State Commun.* **1983**, *47*, 403.
[61] H. Schäfer, R. Laumanns, *Z. Anorg. Allg. Chem.* (*ZAAC*) **1981**, *474*, 136.
[62] K. . Hyde, E. . Hooper, J. Waters, J. . Fletcher, *J. Less Common Met.* **1965**, *8*, 428.
[63] K. Knox, S. Tyree, V. Norman, J. Y. Bassett, University of North Carolina, **1957**, *79*, 3358.
[64] S. Sandoval, E. Pach, B. Ballestreros, G. Tobias, *Carbon* **2017**, *123*, 129.
[65] M. Moaied, J. Hong, *Nanomaterials* **2019**, *9*, 153.

[66] N. Preda, L. Mihut, M. Baibarac, I. Baltog, *Acta Phys. Pol. A* **2009**, *116*, 81.
[67] H. L. Schläfer, *Ber. Bunsenges. Phys. Chem.* **1963**, *67*, 343.
[68] J. J. Zuckerman, *J. Chem. Educ.* **2009**, *43*, 224.
[69] M. A. McGuire, G. Clark, S. KC, W. M. Chance, G. E. Jellison, V. R. Cooper, X. Xu, B. C. Sales, *Phys. Rev. Mater.* **2017**, *1*, 014001.
[70] M. McGuire, *Crystals* **2017**, *7*, 121.
[71] J. Lin, G. J. Miller, *Inorg. Chem.* **1993**, *32*, 1476.
[72] T. Ludwig, PhD thesis, **2001**, Albert-Ludwigs-Universität Freiburg im Breisgau.
[73] J. Köhler, *EIBC* **2014**, John Wiley & Sons, Ltd, UK, ISBN: 9781119951438.
[74] H. Jehn, W. Kurtz, "Gmelin Handbook of Inorg. Chem. - Molybdenum, 8th edition", **1990**, Springer Berlin Heidelberg, *53*.
[75] D. Pohflepp, Master thesis, **2017**, HTW Dresden.
[76] E. Drent, C. A. Emeis, *Solid State Commun.* **1975**, *16*, 1351.
[77] J. Angelkort, PhD thesis, **2009**, Universität Bayreuth.
[78] B. W. P. Griffith, *Platinum Metals Rev.* **1975**, *19*, 60.
[79] W. P. Griffith, "Ruthenium Oxidation Complexes", **2011**, Springer Netherlands, Dordrecht, ISBN: 978-1-4020-9376-0.
[80] G. L. Xia, H. Y. Leng, N. X. Xu, Z. L. Li, Z. Wu, J. L. Du, X. Bin Yu, *Int. J. Hydrogen Energy* **2011**, *36*, 7128.
[81] E. Mannei, F. Ayari, M. Mhamdi, M. Almohalla, A. Guerrero Ruiz, G. Delahay, A. Ghorbel, *Microporous Mesoporous Mater.* **2016**, *219*, 77.
[82] C. Song, T. Ono, M. Nomura, *Bull. Chem. Soc. Jpn.* **1989**, *62*, 630.
[83] L. L. Böhm, *Angew. Chemie - Int. Ed.* **2003**, *42*, 5010.
[84] L. Sementa, M. D'Amore, V. Barone, V. Busico, M. Causa', *Phys. Chem. Chem. Phys.* **2009**, *11*, 11264.
[85] L. Guo, W. Li, W. Feng, Z. Zhang, S. Zhang, *J. Alloys Compd.* **2014**, *602*, 66.
[86] A. Wang, N. P. Balsara, A. T. Bell, *Green Chem.* **2018**, *20*, 2903.
[87] F. Junges, M. C. A. Kuhn, A. H. D. P. dos Santos, C. R. K. Rabello, C. M. Thomas, J.-F. Carpentier, O. L. Casagrande, *Organometallics* **2007**, *26*, 4010.
[88] M. Sun, T. Xu, W. Gao, Y. Liu, Q. Wu, Y. Mu, L. Ye, *Dalt. Trans.* **2011**, *40*, 10184.
[89] H. Jouini, I. Mejri, C. Petitto, J. Martinez-Ortigosa, A. Vidal-Moya, M. Mhamdi, T. Blasco, G. Delahay, *Microporous Mesoporous Mater.* **2018**, *260*, 217.
[90] H. Tao, Y. Gao, N. Talreja, F. Guo, J. Texter, C. Yan, Z. Sun, *J. Mater. Chem. A* **2017**, *5*, 7257.
[91] W. N. Hansen, *J. Appl. Phys.* **1959**, *30*, S304.
[92] Z. Zhang, J. Shang, C. Jiang, A. Rasmita, W. Gao, T. Yu, *arXiv Condens. Matter* **2019**, arXiv:1902.07446v1.
[93] N. Sivadas, S. Okamoto, X. Xu, C. J. Fennie, D. Xiao, *Nano Lett.* **2018**, *18*, 7658.
[94] A. Kitaev, *Ann. Phys.* **2006**, *321*, 2.
[95] F. Zschocke, PhD thesis, **2016**, TU Dresden.
[96] J. Knolle, G. W. Chern, D. L. Kovrizhin, R. Moessner, N. B. Perkins, *Phys. Rev. Lett.* **2014**, *113*, 1.
[97] K. W. Plumb, J. P. Clancy, L. J. Sandilands, V. V. Shankar, Y. F. Hu, K. S. Burch, H. Y. Kee, Y. J. Kim, *Phys. Rev. B - Condens. Matter Mater. Phys.* **2014**, *90*, 1.
[98] A. E. van Arkel, "Reine Metalle", **1939**, Springer Berlin Heidelberg, ISBN: 978-3-642-98880-6.
[99] H. Schäfer, "Chemische Transportreaktionen - Der Transport Anorganischer Stoffe Über Die Gasphase Und Seine Anwendung", **1962**, Wiley VCH, Weinheim, *66*, 885.
[100] M. Binnewies, R. Glaum, M. Schmidt, P. Schmidt, "Chemische Transportreaktionen" **2011**, De Gruyter, Berlin, ISBN: 978-3-11-048350-5.
[101] H. Oppermann, *Solid State Ionics* **1990**, *39*, 17.

[102] M. Binnewies, R. Glaum, M. Schmidt, P. Schmidt, **2012**, De Gruyter, Berlin, ISBN: 978-3-11-025465-5 (english version of reference [100]).
[103] H. Oppermann, M. Schmidt, P. Schmidt, *Z. Anorg. Allg. Chem.* (*ZAAC*) **2005**, *631*, 197.
[104] X. Yu, X. Zhang, Q. Shi, S. Tian, H. Lei, K. Xu, H. Hosono, *Front. Phys.* **2019**, *14*, 6.
[105] D. Weber, L. M. Schoop, V. Duppel, J. M. Lippmann, J. Nuss, B. V. Lotsch, *Nano Lett.* **2016**, *16*, 3578.
[106] F. Poineau, E. V. Johnstone, K. R. Czerwinski, A. P. Sattelberger, *Acc. Chem. Res.* **2014**, *47*, 624.
[107] T. Kong, S. Guo, D. Ni, R. J. Cava, *Phys. Rev. Materials* **2019**, *3*, 084419.
[108] H. Oppermann, *Z. Anorg. Allg. Chem.* (*ZAAC*) **1968**, *359*, 51.
[109] K. Lascelles, H. Schäfer, *Z. Anorg. Allg. Chem.* (*ZAAC*) **1971**, *382*, 249.
[110] T. Standfuß, "Das Ende der Miniaturisierung", **2016**, H.C. Mayr, M. Pinzger, Gesellschaft Für Informatik e.V., Bonn, 2029, ISBN: 978-3-88579-653-4.
[111] Y. Hu, Y. Guo, Y. Wang, Z. Chen, X. Sun, J. Feng, T. M. Lu, E. Wertz, J. Shi, *J. Mater. Res.* **2017**, *32*, 3992.
[112] A. R. West, "Solid State Chemistry and Its Applications", **1984**, John Wiley & Sons, New Dehli, ISBN: 0471903779.
[113] B. Zhou, Y. Wang, G. B. Osterhoudt, P. Lampen-Kelley, D. Mandrus, R. He, K. S. Burch, E. A. Henriksen, *J. Phys. Chem. Solids* **2019**, *128*, 291.
[114] S. M. Winter, A. A. Tsirlin, M. Daghofer, J. van den Brink, Y. Singh, P. Gegenwart, R. Valenti, *J. Phys. Condens. Matter* **2017**, *29*, 493002.
[115] C. Nowka, L. Veyrat, S. Gorantla, U. Steiner, B. Eichler, O. G. Schmidt, H. Funke, J. Dufouleur, B. Büchner, R. Giraud, S. Hampel, *Cryst. Growth Des.* **2015**, *15*, 4272.
[116] C. Huang, J. Zhou, H. Wu, K. Deng, P. Jena, E. Kan, *Phys. Rev. B* **2017**, *95*, 1.
[117] S. Z. Butler, S. M. Hollen, L. Cao, Y. Cui, J. A. Gupta, H. R. Gutie, T. F. Heinz, S. S. Hong, J. Huang, A. F. Ismach, E. Johnston-halperin, M. Kuno, V. V Plashnitsa, R. D. Robinson, R. S. Ruoff, S. Salahuddin, J. Shan, L. Shi, O. M. G. Spencer, M. Terrones, W. Windl, J. E. Goldberger, *ACS Nano* **2013**, *7*, 2898.
[118] G. Guo, G. Bi, C. Cai, *J. Phys. Condens. Matter* **2018**, *30*, 1.
[119] F. Iyikanat, M. Yagmurcukardes, R. T. Senger, H. Sahin, *J. Mater. Chem. C* **2018**, *6*, 2019.
[120] L. Webster, J.-A. Yan, *Phys. Rev. B* **2018**, *98*, 144411.
[121] E. Vatansever, S. Sarikurt, F. Ersan, Y. Kadioglu, O. Üzengi Aktürk, Y. Yüksel, C. Ataca, E. Aktürk, Ü. Aklncl, *J. Appl. Phys.* **2019**, *125*, 083903.
[122] M. Binnewies, R. Glaum, M. Schmidt, P. Schmidt, *Z. Anorg. Allg. Chem.* (*ZAAC*) **2013**, *639*, 219.
[123] M. Grönke, P. Schmidt, M. Valldor, S. Oswald, D. Wolf, A. Lubk, B. Büchner, S. Hampel, *Nanoscale* **2018**, *10*, 19014.
[124] M. Grönke, D. Pohflepp, P. Schmidt, M. Valldor, S. Oswald, D. Wolf, Q. Hao, U. Steiner, B. Büchner, S. Hampel, *Nano-Structures & Nano-Objects* **2019**, *19*, 100324.
[125] M. Binnewies, M. Schmidt, P. Schmidt, *Z. Anorg. Allg. Chem.* (*ZAAC*) **2017**, *643*, 1295.
[126] M. Grönke, B. Buschbeck, P. Schmidt, M. Valldor, S. Oswald, Q. Hao, A. Lubk, D. Wolf, U. Steiner, B. Büchner, S. Hampel, *Adv. Mater. Interfaces* **2019**, *6*, 1901410.
[127] G. Krabbes, W. Bieger, K.-H. Sommer, T. Söhnel, U. Steiner, GMIN version 5.1, package TRAGMIN for calculation of thermodynamic equilibrium, URL: www.tragmin.de, **2014**.
[128] M. Grönke, U. S. F. Arrozi, N. Bronkalla, P. Schmidt, M. Valldor, S. Oswald, T. G. Woodcock, V. Eckert, Q. Hao, L. Plüschke, A. Lederer, K. Nielsch, B. Büchner, S. Kaskel, S. Hampel, *Chem. Mater.* **2019**, *31*, 5305.
[129] R. Wegerhoff, O. Weidlich, M. Kassens, *Imaging Microsc.* **2008**, *Special Ed.*, GIT Verlag, 10.

[130] J. M. Cowley, *Micron* **2004**, *35*, 345.
[131] F. Hammerath, "Magnetism and Superconductivity in Iron-Based Superconductors as Probed by Nuclear Magnetic Resonance", **2012**, Vieweg+Teubner, Wiesbaden, Springer Spektrum, ISBN: 978-3-8348-2422-6.
[132] A. Frisk, L. B. Duffy, S. Zhang, G. van der Laan, T. Hesjedal, *Mater. Lett.* **2018**, *232*, 5.
[133] C. Piamonteze, U. Flechsig, S. Rusponi, J. Dreiser, J. Heidler, M. Schmidt, R. Wetter, M. Calvi, T. Schmidt, H. Pruchova, J. Krempasky, C. Quitmann, H. Brune, F. Nolting, *J. Synchrotron Radiat.* **2012**, *19*, 661.
[134] H. Schäfer, *Z. Anorg. Allg. Chem.* (*ZAAC*) **1980**, *469*, 123.
[135] H. Schäfer, H.-G. V. Schnering, J. Tillack, F. Kuhnen, H. Wöhrle, H. Baumann, *Z. Anorg. Allg. Chem.* (*ZAAC*) **1967**, *353*, 281.
[136] N. Bronkalla, Diploma thesis, **2018**, TU Dresden.
[137] B. Buschbeck, Bachelor thesis, **2019**, HTW Dresden.
[138] J. Nasu, J. Knolle, D. L. Kovrizhin, Y. Motome, R. Moessner, *Nat. Phys.* **2016**, *12*, 1.
[139] J. M. Fletcher, W. E. Gardner, A. C. Fox, G. Topping, *J. Chem. Soc. (A)* **1967**, 1038.
[140] I. Kanesaka, M. Yonesawa, K. Kawai, T. Miyatake, M. Kaguro, *Spectrochim. Acta* **1986**, *42A*, 1415.
[141] Y. Kubota, H. Tanaka, T. Ono, Y. Narumi, K. Kindo, *Phys. Rev. B* **2015**, *91*, 1.
[142] K. Tsutsumi, H. Okamoto, C. Hama, Y. Ishihara, *J. Magn. Magn. Mater.* **1990**, *90* & *91*, 181.
[143] H.-S. Kim, H.-Y. Kee, *Phys. Rev. B* **2016**, *93*, 155143.
[144] A. Narath, H. L. Davis, *Phys. Rev.* **1965**, *137*, A163.
[145] R. D. Johnson, S. C. Williams, A. A. Haghighirad, J. Singleton, V. Zapf, P. Manuel, I. I. Mazin, Y. Li, H. O. Jeschke, R. Valent, R. Coldea, *Phys. Rev. B* **2015**, *92*, 1.
[146] H.-C. Yang, B.-C. Gong, K. Liu, Z.-Y. Lu, *J. Phys. Condens. Matter* **2019**, *31*, 025803.
[147] F. Cavallone, I. Pollini, G. Spinolo, *Phys. Status Solidi* **1971**, *45*, 405.
[148] K. Motizuki, S. Miyata, N. Suzuki, **1980**, *18*, 15.
[149] O. Chauvet, L. Forro, I. Kos, M. Miljak, *Solid State Commun.* **1995**, *93*, 667.
[150] H. L. Schläfer, H. P. Fritz, *Spectrochim. Acta* **1967**, *23*, 1409.
[151] J. F. Moulder, W. F. Stickle, P. E. Sobol, K. D. Bomben, "Handbook of X-Ray Photoelectron Spectroscopy", **2005**, Perkin-Elmer Cooperation, Eden Prairie, Minnesota, ISBN: 0-9627026-2-5.
[152] G. Li, X. Chen, Y. Gan, F. Li, M. Yan, F. Ye, S. Pei, Y. Zhang, L. Wang, H. Su, J. Dai, Y. Chen, Y. Shi, X. Wang, L. Zhang, S. Wang, D. Yu, F. Ye, J. Mei, M. Huang, *Phys. Rev. Mater.* **2019**, *023601*, 51.
[153] L. Liang, V. Meunier, *Nanoscale* **2014**, *6*, 5394.
[154] P. Hajiyev, C. Cong, C. Qiu, T. Yu, *Sci. Rep.* **2013**, *3*, 2593.
[155] A. Borghesi, G. Guizzetti, F. Marabelli, L. Nosenzo, E. Reguzzoni, *Solid State Commun.* **1984**, *52*, 463.
[156] D. Wang, PhD thesis, **2018**, Columbia University.
[157] I. Kanesaka, H. Kawahara, A. Yamazaki, K. Kawai, *J. Mol. Struct.* **1986**, *146*, 41.
[158] K. Manna, H. Huang, W. Li, Y. Ho, W. Chiang, *Chem. Mater.* **2016**, *28*, 7586.
[159] D. Hanlon, C. Backes, E. Doherty, C. S. Cucinotta, N. C. Berner, C. Boland, K. Lee, A. Harvey, P. Lynch, Z. Gholamvand, S. Zhang, K. Wang, G. Moynihan, A. Pokle, Q. M. Ramasse, N. McEvoy, W. J. Blau, J. Wang, G. Abellan, F. Hauke, A. Hirsch, S. Sanvito, D. D. O'Regan, G. S. Duesberg, V. Nicolosi, J. N. Coleman, *Nat. Commun.* **2015**, *6*, 8563.
[160] K. Muthoosamy, S. Manickam, *Ultrason. Sonochem.* **2017**, *39*, 478.

[161] Y. Hernandez, V. Nicolosi, M. Lotya, F. M. Blighe, Z. Sun, S. De, I. T. McGovern, B. Holland, M. Byrne, Y. K. Gun'ko, J. J. Boland, P. Niraj, G. Duesberg, S. Krishnamurthy, R. Goodhue, J. Hutchison, V. Scardaci, A. C. Ferrari, J. N. Coleman, *Nat. Nanotechnol.* **2008**, *3*, 563.
[162] H. Kaur, S. Yadav, A. K. Srivastava, N. Singh, S. Rath, J. J. Schneider, O. P. Sinha, R. Srivastava, *Nano Res.* **2018**, *11*, 343.
[163] J. N. Coleman, M. Lotya, A. O'Neill, S. D. Bergin, P. J. King, U. Khan, K. Young, A. Gaucher, S. De, R. J. Smith, I. V Shvets, S. K. Arora, G. Stanton, H.-Y. Kim, K. Lee, G. T. Kim, G. S. Duesberg, T. Hallam, J. J. Boland, J. J. Wang, J. F. Donegan, J. C. Grunlan, G. Moriarty, A. Shmeliov, R. J. Nicholls, J. M. Perkins, E. M. Grieveson, K. Theuwissen, D. W. McComb, P. D. Nellist, V. Nicolosi, *Science* **2011**, *331*, 568.
[164] A. Jawaid, D. Nepal, K. Park, M. Jespersen, A. Qualley, P. Mirau, L. F. Drummy, R. A. Vaia, *Chem. Mater.* **2016**, *28*, 337.
[165] W. Zhang, Q. Qu, P. Zhu, C. Lam, *J. Mater. Chem. C* **2015**, *3*, 12457.
[166] J. Liu, Q. Sun, Y. Kawazoe, P. Jena, *Phys. Chem. Chem. Phys.* **2016**, *18*, 8777.
[167] H. Wang, V. Eyert, U. Schwingenschlögl, *J. Phys. Condens. Matter* **2011**, *23*, 116003.
[168] H. Wang, F. Fan, S. Zhu, H. Wu, *Europhysics Lett.* **2016**, *114*, 47001.
[169] J. W. Cable, M. K. Wilkinson, E. O. Wollan, *J. Phys. Chem. Solids* **1961**, *19*, 29.
[170] A. Narath, *J. Appl. Phys.* **1964**, *35*, 838.
[171] H. Schäfer, M. Binnewies, W. Domke, J. Karbinski *Z. Anorg. Allg. Chem.* (*ZAAC*) **1974**, *126*, 116.
[172] R. Gruehn, R. Glaum, *Angew. Chemie* **2000**, *112*, 706.
[173] A. W. Struss, J. D. Corbett, *Inorg. Chem.* **1970**, *9*, 1373.
[174] S. Reschke, F. Mayr, S. Widmann, H.-A. K. von Nidda, V. Tsurkan, M. V Eremin, S.-H. Do, K.-Y. Choi, Z. Wang, A. Loidl, *J. Phys. Condens. Matter* **2018**, *30*, 475604.
[175] S. Reschke, F. Mayr, Z. Wang, S.-H. Do, K.-Y. Choi, A. Loidl, *Phys. Rev. B* **2017**, *96*, 165120.
[176] S. H. Do, S. Y. Park, J. Yoshitake, J. Nasu, Y. Motome, Y. S. Kwon, D. T. Adroja, D. J. Voneshen, K. Kim, T. H. Jang, J. H. Park, K. Y. Choi, S. Ji, *Nat. Phys.* **2017**, *13*, 1079.
[177] M. Irmler, G. Meyer, *Z. Anorg. Allg. Chem.* (*ZAAC*) **1987**, *552*, 81.
[178] F. A. Cotton, J. T. Mague, *Inorg. Chem.* **1964**, *3*, 1402.
[179] U. Merten, W. E. Bell, "The High-Temperature Chemistry of Fission-Product Elements. Summary Report", General Atomic Div., General Dynamics Corp., San Diego, California, **1962**.
[180] M. Armbruster, T. Ludwig, H. W. Rotter, G. Thiele, *Z. Anorg. Allg. Chem.* (*ZAAC*) **2000**, *626*, 187.
[181] H. L. Schläfer, H. Skoludek, *Z. Anorg. Allg. Chem.* (*ZAAC*) **1962**, *316*, 15.
[182] K. Brodersen, H.-K. Breitbach, G. Thiele, *Z. Anorg. Allg. Chem.* (*ZAAC*) **1968**, *357*, 162.
[183] H. Hillebrecht, T. Ludwig, G. Thiele, *Z. Anorg. Allg. Chem.* (*ZAAC*) **2004**, *630*, 2199.
[184] J. A. Beekhuizen, PhD thesis, **2006**, Universität Köln.
[185] T. M. Brown, PhD thesis, **1963**, Iowa State University.
[186] V. A. Stenger, *Angew. Chemie* **1966**, *78*, 313.
[187] H. G. von Schnering, J.-H. Chang, M. Freiberg, K. Peters, E.-M. Peters, A. Ormeci, L. Schröder, G. Thiele, C. Röhr, *Z. Anorg. Allg. Chem.* (*ZAAC*) **2004**, *630*, 109.
[188] D. H. Guthrie, PhD thesis, **1981**, Iowa State University.
[189] J. D. Corbett, P. X. Seabaugh, *J. Inorg. Nucl. Chem.* **1958**, *6*, 207.
[190] P. W. Seabaugh, PhD thesis, **1961**, Iowa State University.
[191] M. Ströbele, R. Thalwitzer, H. J. Meyer, *Inorg. Chem.* **2016**, *55*, 12074.
[192] B. Commerscheidt, R. Gruehn, *Z. Anorg. Allg. Chem.* (*ZAAC*) **2001**, *627*, 465.
[193] J. C. Boatman, *Inorg. Chem.* **1965**, *4*, 1486.

[194] A. S. Pronin, A. I. Smolentsev, Y. V. Mironov, *Russ. Chem. Bull.* **2019**, *68*, 777.
[195] G. Thiele, M. Steiert, D. Wagner, H. Wochner, *Z. Anorg. Allg. Chem.* (*ZAAC*) **1984**, *516*, 207.
[196] D. Michael, *ISO/TS 80004-13:2017, URL:* https://www.iso.org/standard/64741.html, **2017**, last accessed on 15th Jan. 2020.
[197] I. Pollini, *Solid State Commun.* **1998**, *106*, 549.
[198] A. Koitzsch, C. Habenicht, E. Müller, M. Knupfer, B. Büchner, H. C. Kandpal, J. van den Brink, D. Nowak, A. Isaeva, T. Doert, *Phys. Rev. Lett.* **2016**, *117*, 126403.
[199] K. S. Burch, D. Mandrus, J. G. Park, *Nature* **2018**, *563*, 47.
[200] T. Pandey, D. S. Parker, *Sci. Rep.* **2018**, *8*, 2.
[201] H. Schäfer, *Z. Anorg. Allg. Chem.* (*ZAAC*) **1986**, *535*, 219.
[202] H. Schäfer, K. -H Huneke, C. Brendel, *Z. Anorg. Allg. Chem.* (*ZAAC*) **1971**, *383*, 49.
[203] J. L. Lado, J. Fernández-Rossier, 2D Mater. **2017**, *4*, 035002.
[204] B. Shabbir, M. Nadeem, Z. Dai, M. S. Fuhrer, Q.-K. Xue, X. Wang, Q. Bao, *Appl. Phys. Rev.* **2018**, 5, 041105.

7 List of Figures

8 List of Tables

9 Appendix

Simulation of vapor transports of transition metal trihalides MX_3

Table A 1: Homogeneous and heterogeneous gas phase equilibria of MCl_3 (M = Ru, Cr).

$RuCl_3$		$CrCl_3$	
Heterogeneous equilibria		***Heterogeneous equilibria***	
$RuCl_3(s) \rightleftharpoons Ru(s) + 1.5\ Cl_2(g)$	(E1)	$CrCl_3(s) \rightleftharpoons CrCl_2(s) + ½\ Cl_2(g)$	(E13)
$RuCl_3(s) \rightleftharpoons RuCl_3(g)$	(E2)	$2\ CrCl_3(s) + 1.5\ O_2(g) \rightleftharpoons Cr_2O_3(s) + 3\ Cl_2(g)$	(E14)
$Ru(s) + O_2(g) \rightleftharpoons RuO_2(s)$	(E3)	$CrCl_3(s) \rightleftharpoons CrCl_3(g)$	(E15)
$RuO_2(s) + O_2(g) \rightleftharpoons RuO_4(g)$	(E4)		
Homogeneous equilibria		***Homogeneous equilibria***	
$Cl_2(g) \rightleftharpoons 2\ Cl(g)$	(E5)	$Cl_2(g) \rightleftharpoons 2\ Cl(g)$	(E16)
$RuCl_3(g) + ½\ Cl_2(g) \rightleftharpoons RuCl_4(g)$	(E6)	$2\ CrCl_3(g) \rightleftharpoons CrCl_2(g) + CrCl_4(g)$	(E17)
$Cl_2(g) + H_2O(g) \rightleftharpoons HCl(g) + HClO(g)$	(E7)	$2\ CrCl_3(g) + 2\ H_2O \rightleftharpoons 4\ HCl(g) + CrO_2Cl_2(g)$	(E18)
$HCl(g) + ½\ O_2 \rightleftharpoons HClO(g)$	(E8)	$CrCl_4(g) + 2\ H_2O \rightleftharpoons 2\ HCl(g) + CrOCl_2(g)$	(E19)
$½\ Cl_2(g) + ½\ O_2 \rightleftharpoons ClO(g)$	(E9)		
$ClO(g) + ½\ O_2 \rightleftharpoons ClO_2(g)$	(E10)		
Vapor transport		***Vapor transport***	
Sublimation: $RuCl_3(s) \rightleftharpoons RuCl_3(g)$	(E11)	*Sublimation*: $CrCl_3(s) \rightleftharpoons CrCl_3(g)$	(E20)
Autotransport:			
$RuCl_3(s) \rightleftharpoons Ru(s) + 1.5\ Cl_2(g)$	(E12.1)		
$RuCl_3(g) + ½\ Cl_2(g) \rightleftharpoons RuCl_4(g)$	(E12.2)		

Table A 2: Homogeneous and heterogeneous gas phase equilibria of MCl_3 (M = Mo, Ti) under consideration of an introduction of transport additions of $MoCl_5$ (with respect $MoCl_3$) and $GaCl_3$ (with respect $TiCl_3$).

$MoCl_3$		$TiCl_3$	
Heterogeneous equilibria		***Heterogeneous equilibria***	
$MoCl_3(s) + MoOCl_4(g) + MoO_2Cl_2(g) \rightleftharpoons 3\ MoOCl_3(g)$	(E21)	$GaCl_3(s) \rightleftharpoons GaCl_3(g)$	(E30)
$2\ MoCl_3(s) \rightleftharpoons MoCl_2(s) + MoCl_4(g)$	(E22)	$TiCl_3(s) \rightleftharpoons TiCl_3(g)$	(E31)
$MoCl_3(s) \rightleftharpoons MoCl_2(g) + Cl_2(g)$	(E23)		
Homogeneous equilibria		***Homogeneous equilibria***	
$MoCl_5(g) + H_2O\ (g) \rightleftharpoons MoOCl_3(g) + 2\ HCl(g)$	(E24)	$2\ GaCl_3(g) \rightleftharpoons Ga_2Cl_6(g)$	(E32)
$2\ MoOCl_3(g) \rightleftharpoons MoO_2Cl_2(g) + MoCl_4(g)$	(E25)	$2\ TiCl_3(g) \rightleftharpoons Ti_2Cl_6(g)$	(E33)
$2\ MoOCl_3(g) + MoCl_5(g) \rightleftharpoons MoOCl_4(g) + MoCl_4(g)$	(E26)	$GaCl_3(g) \rightleftharpoons GaCl_2(g) + ½\ Cl_2(g)$	(E34)
$2\ MoCl_3(g) \rightleftharpoons MoCl_6(g)$	(E27)	$2\ GaCl_2(g) \rightleftharpoons Ga_2Cl_4(g)$	(E35)
$Cl_2(g) \rightleftharpoons 2\ Cl(g)$	(E28)	$2\ GaCl(g) \rightleftharpoons Ga_2Cl_2(g)$	(E36)
		$GaCl(g) \rightleftharpoons Ga(g) + Cl(g)$	(E37)
		$TiCl_4(g) + H_2O\ (g) \rightleftharpoons TiOCl_2(g) + 2\ HCl(g)$	(E38)
		$TiCl_3(g) + H_2O\ (g) \rightleftharpoons TiOCl(g) + 2\ HCl(g)$	(E39)
		$TiCl_4(g) \rightleftharpoons 2\ TiCl_2(g)$	(E40)
		$TiCl_3(g) + O_2\ (g) \rightleftharpoons TiO_2(g) + 1.5\ Cl_2(g)$	(E41)
Vapor transport		***Vapor transport***	
CVT: $MoCl_3(s) + MoCl_5(g) \rightleftharpoons 2\ MoCl_4(g)$	(E29)	*CVT*: $2\ TiCl_3(s) + ½\ Ga_2Cl_6(g) \rightleftharpoons 2\ TiCl_4(g) + GaCl(g)$	(E42)
		CVT: $2\ TiCl_3(s) + GaCl_3(g) \rightleftharpoons 2\ TiCl_4(g) + GaCl(g)$	(E43)

Table A 3: Homogeneous and heterogeneous gas phase equilibria of CrX_3 (X= I, Br) with respect to a slight excess of halide (n_{excess} (X) = 0.05 mol).

CrI_3		**$CrBr_3$**	
Heterogeneous equilibria		***Heterogeneous equilibria***	
$CrI_3(s) \rightleftharpoons CrI_2(s) + ½\ I_2(g)$	(E44)	$CrBr_3(s) \rightleftharpoons CrBr_2(s) + ½\ Br_2(g)$	(E56)
$CrI_3(s) \rightleftharpoons CrI_3(g)$	(E45)	$CrBr_3(s) \rightleftharpoons CrBr_3(g)$	(E57)
$2\ CrI_3(s) + 1.5\ O_2(g) \rightleftharpoons Cr_2O_3(s) + 3\ I_2(g)$	(E46)	$2\ CrBr_3(s) + 1.5\ O_2(g) \rightleftharpoons Cr_2O_3(s) + 3\ Br_2(g$	(E58)
$Cr_2O_3(s) + 2\ HI\ (g) \rightleftharpoons 2\ CrOI_2(g) + H_2O(g)$	(E47)	$CrBr_3(s) + ½\ H_2O\ (g) + ¼\ O_2(g) \rightleftharpoons CrOBr_2(g) + HBr(g)$	(E59)
Homogeneous equilibria		***Homogeneous equilibria***	
$I_2(g) \rightleftharpoons 2\ I(g)$	(E48)	$Br_2(g) \rightleftharpoons 2\ Br(g)$	(E60)
$CrI_3(g)\ ½\ I_2(g) \rightleftharpoons CrI_4(g)$	(E49)	$CrBr_3(g)\ ½\ Br_2(g) \rightleftharpoons CrBr_4(g)$	(E61)
$2\ CrI_3(g) + 2\ H_2O \rightleftharpoons 4\ HI(g) + CrO_2I_2(g)$	(E50)	$2\ CrBr_3(g) + 2\ H_2O \rightleftharpoons 4\ HBr(g) + CrO_2Br_2(g)$	(E62)
$CrI_4(g) + 2\ H_2O \rightleftharpoons 2\ HI(g) + CrOI_2(g)$	(E51)	$CrBr_4(g) + 2\ H_2O \rightleftharpoons 2\ HBr(g) + CrOBr_2(g)$	(E63)
$2\ CrI_3(g) \rightleftharpoons CrI_2(g) + CrI_4(g)$	(E52)	$2\ CrBr_3(g) \rightleftharpoons CrBr_2(g) + CrBr_4(g)$	(E64)
$Cr_2I_4(g) \rightleftharpoons 2\ CrI_2(g)$	(E53)	$Cr_2Br_4(g) \rightleftharpoons 2\ CrBr_2(g)$	(E65)
Vapor transport		***Vapor transport***	
Sublimation: $CrI_3(s) \rightleftharpoons CrI_3(g)$	(E54)	*Sublimation*: $CrBr_3(s) \rightleftharpoons CrBr_3(g)$	(E66)
CVT: $CrI_3(s)\ ½\ I_2(g) \rightleftharpoons CrI_4(g)$	(E55)	*CVT:* $CrBr_3(s)\ ½\ Br_2(g) \rightleftharpoons CrBr_4(g)$	(E67)

Synthesis and characterization of MCl_3 and CrX_3

With respect to the calculated transport rates (TR_{theo}), the determined values refer to a simulation close to experimental conditions. Meaning, that if a slight excess of halide (e.g. I_2) is applied, this is considered in the modeling.

Table A 4: Experimental parameter for the synthesis of $RuCl_3$ bulk flakes.

Temperatures [K]	ΔT [K]	TR_{theo} [mg/h]	TR_{exp} [mg/h]
1073 → 873	200	1.1	0.9
1003 → 933	70	1	0.7
973 → 773	200	0.5	0.3
873 → 773	100	0.02	0.1
773 → 673	100	0.001	0.1

Table A 5: Experimental parameter for the synthesis of $MoCl_3$ bulk flakes (transport agent: $MoCl_5$).

Temperatures [K]	ΔT [K]	TR_{theo} [mg/h]	TR_{exp} [mg/h]
873 → 773	100	-	0.4
823 → 723	100	0.005	0.35
773 → 673	100	0.012	0.26
743 → 673	70	0.006	1
743 → 643	100	0.023	0.14
743 → 593	150	0.049	1.74
653 → 553	100	0.083	0.13

Table A 6: Experimental parameter for the synthesis of $TiCl_3$ bulk flakes (transport agent: $GaCl_3$).

Temperatures [K]	ΔT [K]	TR_{theo} [mg/h]	TR_{exp} [mg/h]
750 → 700	50	23	11.4
750 → 650	100	115	3.7
700 → 550	150	194	0,6
700 → 650	50	78	0.6
700 → 600	100	161	1.1

Table A 7: Experimental parameter for the synthesis of $CrCl_3$ bulk flakes.

Temperatures [K]	ΔT [K]	TR_{theo} [mg/h]	TR_{exp} [mg/h]
1023 → 873	150	19	1.1
1023 → 923	100	18	1.1
973 → 823	150	5	0.9
973 → 873	100	5	1
973 → 923	50	4	0.9
873 → 773	100	-	0.5
873 → 823	50	-	0.7
823 → 723	100	-	0.3
773 → 673	100	-	0.004

Table A 8: Experimental parameter for the synthesis of CrI_3 bulk flakes.

Temperatures [K]	ΔT [K]	TR_{theo} [mg/h]	TR_{exp} [mg/h]
1023 → 823	200	4.63	0.65
923 → 823	100	0.68	0.14
923 → 873	50	0	0.04
923 → 723	200	0.69	0.003

Table A 9: Experimental parameter for the synthesis of $CrBr_3$ bulk flakes.

Temperatures [K]	ΔT [K]	TR_{theo} [mg/h]	TR_{exp} [mg/h]
1023 → 923	100	22.46	0.74
1023 → 823	200	25	7
923 → 823	100	3.6	0.62
873 → 773	100	1.12	7

Table A 10: EDX quantification results of bulk *M*Cl_3 sheets (the red dashed quantification data is indicating the EDX measurement of the running text).

	RuCl₃				***MoCl₃***			
excitation line	Ru Lα		Cl Kα		Mo Lα		Cl Kα	
measuring point	*At %*	*P/B*	*At %*	*P/B*	*At %*	*P/B*	*At %*	*P/B*
1	**26**	238	**74**	553	**25**	29	**75**	66
2	**26**	41	**74**	95	**24**	20	**76**	44
3	**26**	28	**74**	70	**24**	21	**76**	45
4	**26**	27	**74**	63	**24**	24	**76**	57
5	**27**	38	**73**	88	**25**	24	**75**	51
ø	**26**	-	**74**	-	**24**	-	**76**	-

	TiCl₃						***CrCl₃***			
excitation line	Ti Kα		Cl Kα		O Kα		Cr Kα		Cl Kα	
measuring point	*At %*	*P/B*	*At %*	*P/B*	*At %*	*P/B*	*At %*	*P/B*	*At %*	*P/B*
1	**14**	34	**36**	71	**50**	26	**23**	25	**77**	82
2	**18**	35	**47**	79	**35**	35	**20**	26	**80**	75
3	**18**	37	**52**	87	**30**	8	**21**	28	**79**	76
4	**21**	47	**46**	86	**33**	16	**25**	29	**75**	68
5	**22**	37	**44**	104	**33**	21	**20**	26	**80**	74
ø	**19**	-	**45**	-	**36**	-	**22**	-	**78**	-

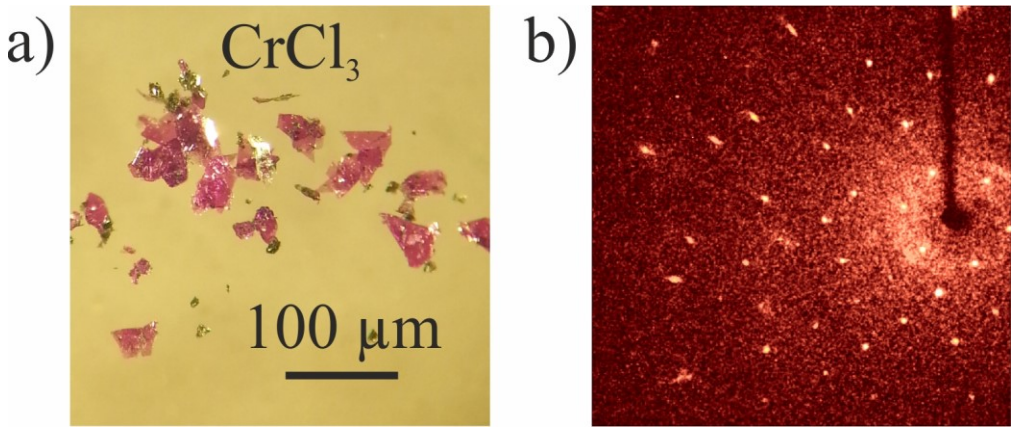

Figure A 1: SCXRD investigation of $CrCl_3$ platelets: **(a)** optical microscopy of representative samples utilized for SCXRD and **(b)** observed *Bragg* reflections of an investigated $CrCl_3$ single crystal.

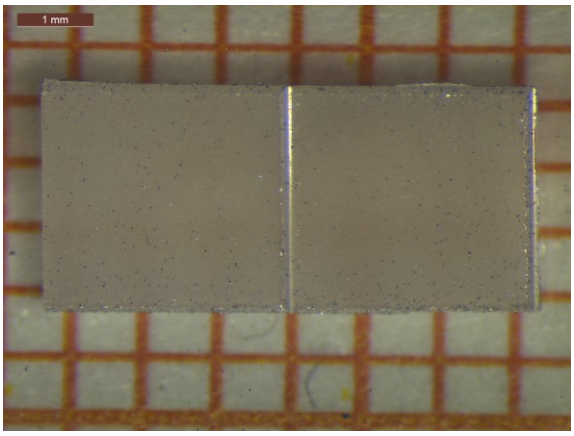

Figure A 2: Optical microscopy of $RuCl_3$ nanoflakes deposited at YSZ using higher temperatures (1373 → 1173 K, ΔT = 200 K) without dwell time (pure heating-up process) proceeding from 1 mg $RuCl_3$ powder.

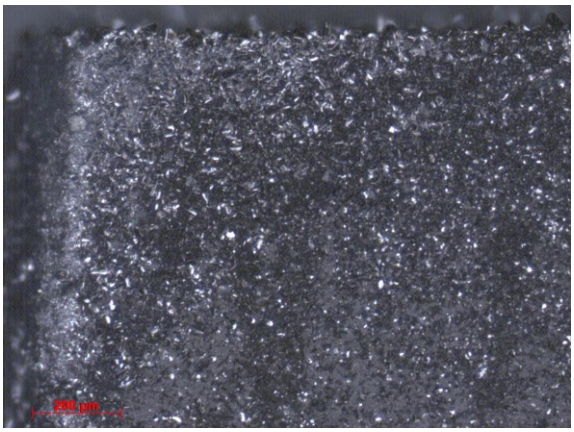

Figure A 3: Optical microscopy of $RuCl_3$ micro- and nanolayers deposited at $SrTiO_3$ using temperatures 973 → 773 K (ΔT = 200 K) for 24 hours proceeding from 30 mg $RuCl_3$ powder.

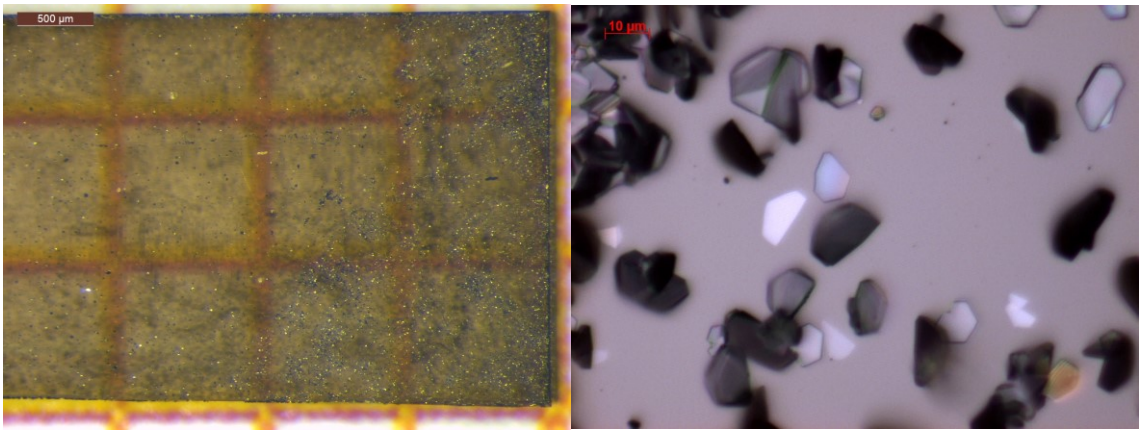

Figure A 4: Optical microscopy of $RuCl_3$ micro- and nanolayers deposited at $LaAlO_3$ using temperatures 973 → 773 K (ΔT = 200 K) without dwell time (pure heating-up process) proceeding from 1 mg $RuCl_3$ powder.

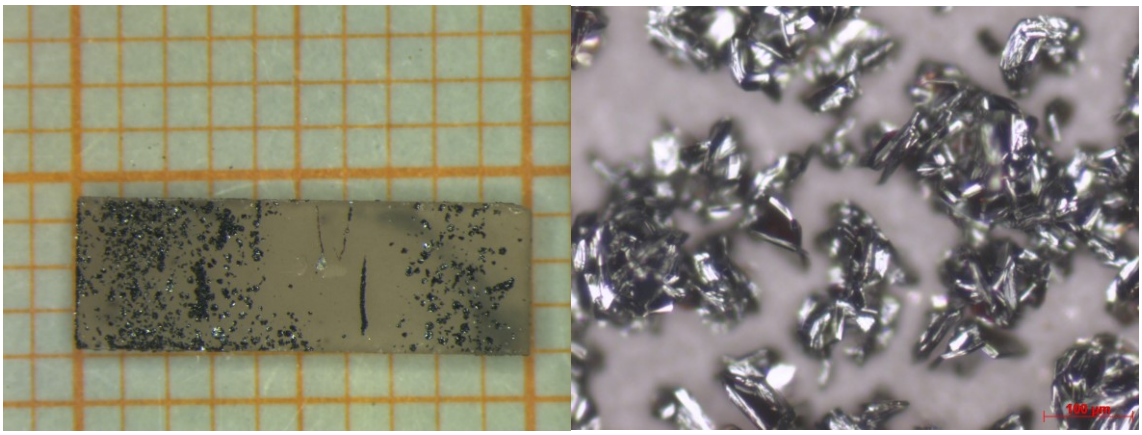

Figure A 5: Optical microscopy of $MoCl_3$ micro platelets deposited at YSZ substrates using temperatures 743 → 643 K (ΔT = 100 K) for 24 hours proceeding from 50 mg $MoCl_3$ and 5 mg $MoCl_5$ powder.

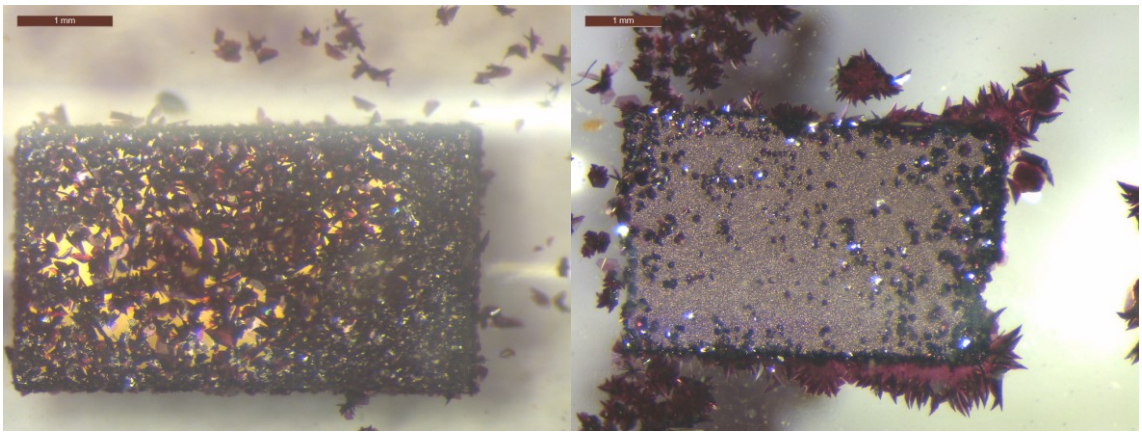

Figure A 6: (left) Optical microscopy of $TiCl_3$ microsheets deposited at Si/SiO_2 (200 nm) using temperatures 700 → 650 K (ΔT = 50 K) for 1 hour proceeding from 24.5 mg $TiCl_3$ and 2 mg $GaCl_3$ powder; **(right)** $TiCl_3$ microsheets deposited at Si/SiO_2 (200 nm) using temperatures 700 → 600 K (ΔT = 100 K) for 1 hour proceeding from 24 mg $TiCl_3$ and 5 mg $GaCl_3$ powder.

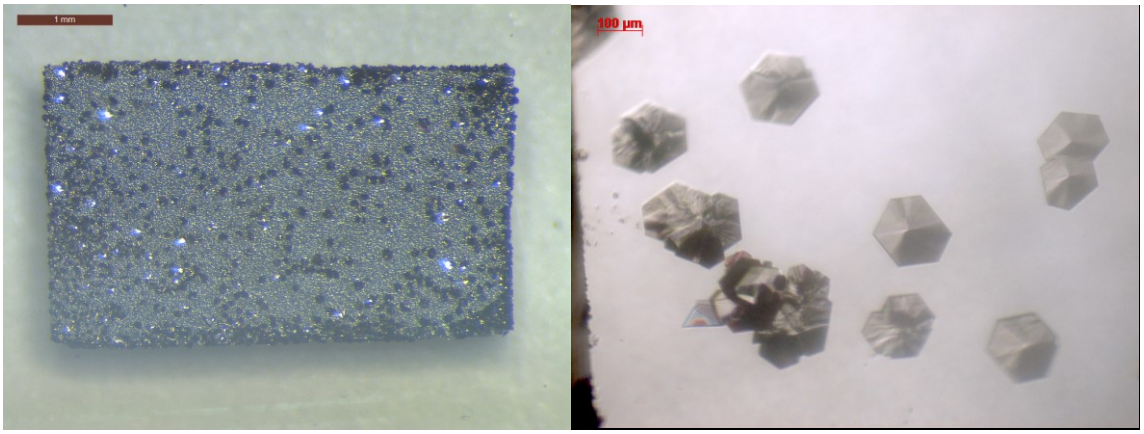

Figure A 7: (left) Optical microscopy of $TiCl_3$ flakes deposited at Si using temperatures 700 → 600 K (ΔT = 100 K) for 1 hour proceeding from 5 mg $TiCl_3$ and 2 mg $GaCl_3$ powder; **(right)** $TiCl_3$ deposited at Si using temperatures 700 → 600 K (ΔT = 100 K) for 0.5 hour proceeding from 25.5 mg $TiCl_3$ and 2 mg $GaCl_3$ powder.

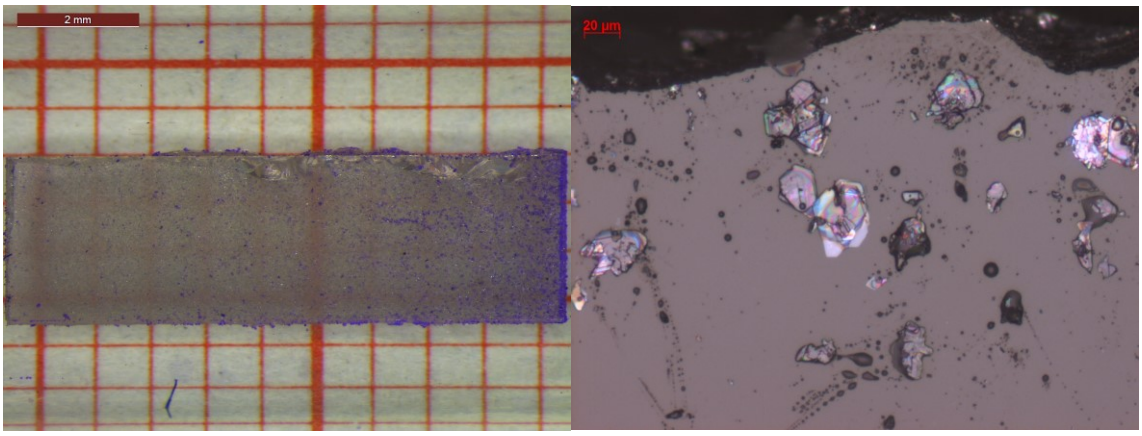

Figure A 8: Optical microscopy of $CrCl_3$ microlayers deposited at Al_2O_3 (sapphire) using temperatures 873 → 773 K (ΔT = 100 K) for 30 minutes proceeding from 1 mg $CrCl_3$.

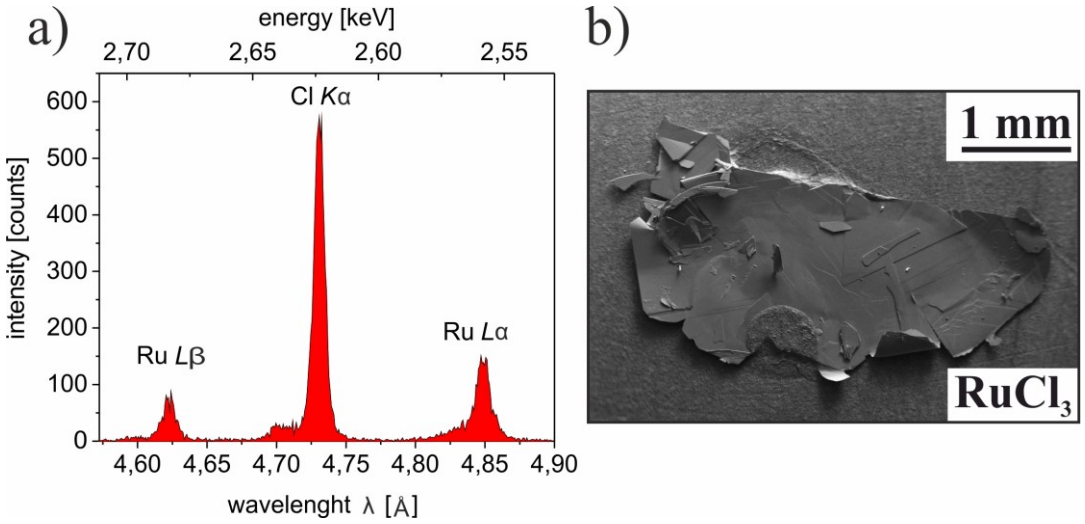

Figure A 9: (a) Obtained WDX spectrum of a $RuCl_3$ bulk flake and **(b)** investigated $RuCl_3$ flake (by WDX).

Table A 11: EDX quantification results of bulk CrX_3 sheets (the red dashed quantification data is indicating the EDX measurement of the running text).

	CrI_3				***$CrBr_3$***			
excitation line	Cr Kα		I Lα		Cr Kα		Br Lα	
measuring point	*At %*	*P/B*	*At %*	*P/B*	*At %*	*P/B*	*At %*	*P/B*
1	**24**	6	**76**	22	**22**	13	**78**	63
2	**23**	5	**77**	22	**22**	12	**78**	61
3	**24**	6	**76**	26	**21**	12	**79**	60
4	**24**	6	**76**	29	**21**	12	**79**	67
5	**24**	6	**76**	25	**21**	12	**79**	69
ø	**24**	-	**76**	-	**21**		**79**	

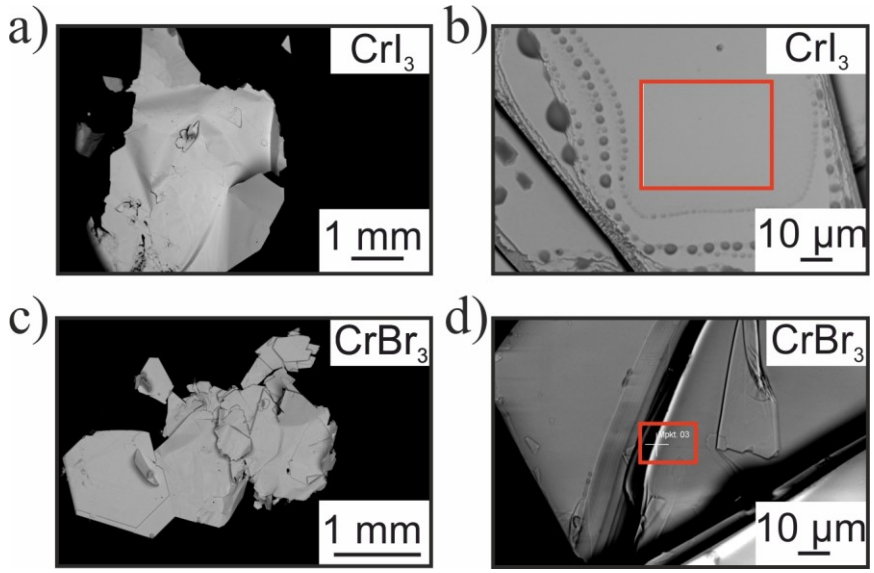

Figure A 10: Investigated CrX_3 (X = I, Br) bulk flakes by wavelength dispersive X-ray analysis (WDX): **(a,b)** CrI_3 and **(c,d)** $CrBr_3$; the red boxes elucidate two exemplary measurement areas.

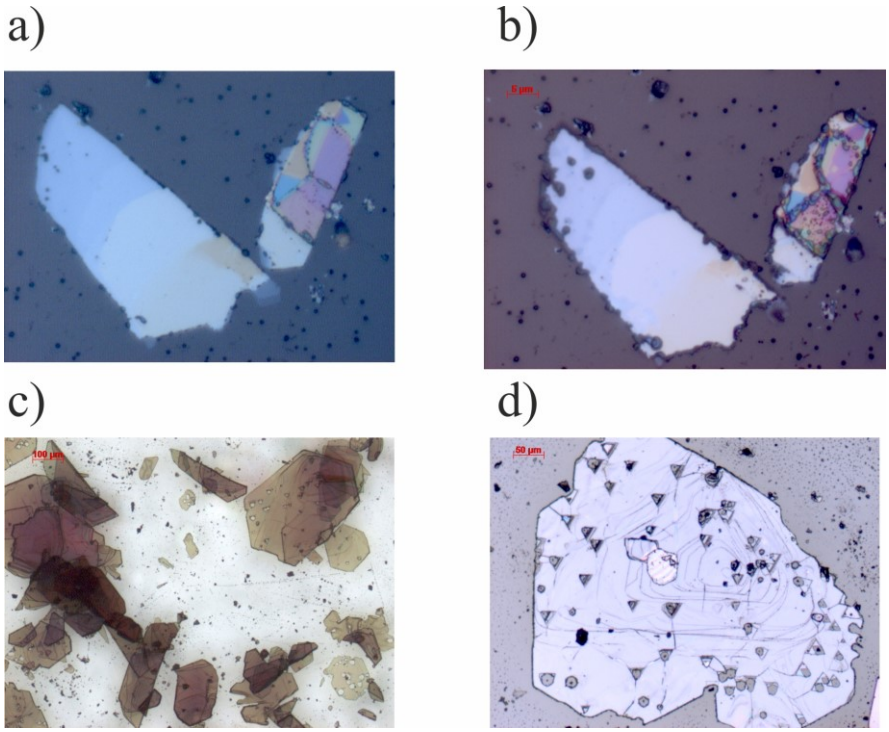

Figure A 11: Optical microscopy of the degradation of $CrBr_3$ micro- and nanosheets due to ambient atmosphere: **(a)** $CrBr_3$ thin sheets after CVT process, **(b)** $CrBr_3$ thin sheets after 24 hours in ambient atmosphere; **(c,d)** various thin $CrBr_3$ crystals after 24 hours in ambient atmosphere.

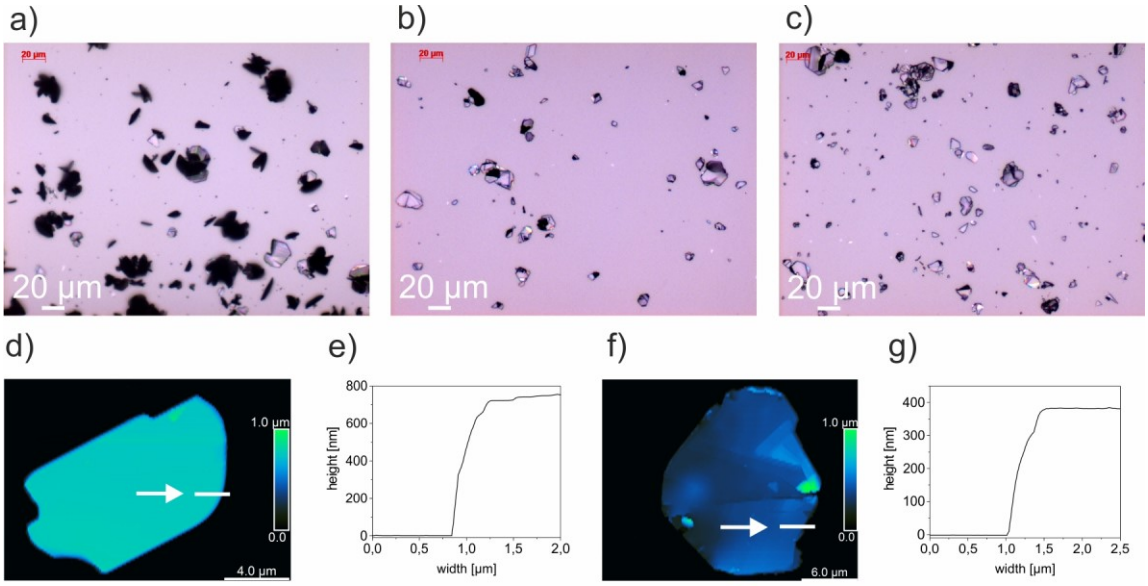

Figure A 12: (a) Optical microscopy of YSZ substrate with deposited α-$RuCl_3$ nanocrystals before sonication; **(b)** after 30 seconds of ultrasonication with ***distilled water***, **(c)** after 3 minutes of ultrasonication with distilled water, **(d)** investigated α-$RuCl_3$ nanocrystal by means of AFM (the white line is indicating the AFM measurement), **(e)** AFM height profile of d), **(f)** investigated α-$RuCl_3$ nanocrystal by means of AFM (the white line is indicating the AFM measurement) and **(g)** AFM height profile of f), taken from [123] (supporting information).

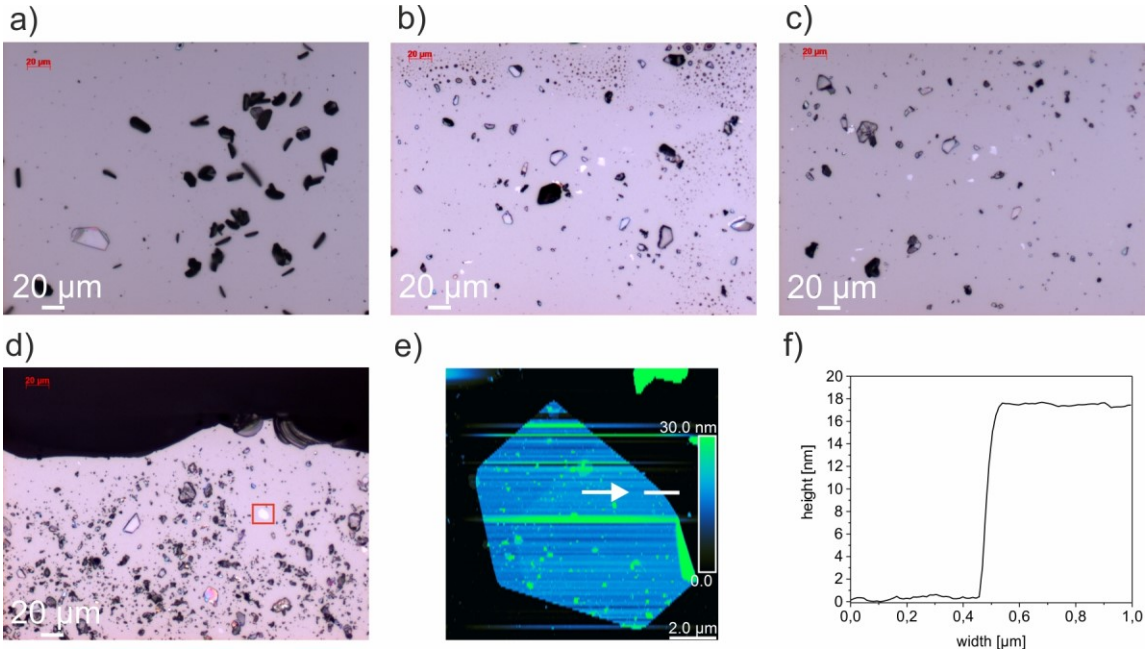

Figure A 13: (a) Optical microscopy of YSZ substrate with deposited α-$RuCl_3$ nanocrystals before ultrasonication; **(b)** after 30 seconds of ultrasonication with ***n-hexane***, **(c)** after 3 minutes of ultrasonication with *n*-hexane, **(d)** investigated α-$RuCl_3$ nanocrystal by means of AFM (the red area is indicating to location of the measurement), **(e)** investigated α-$RuCl_3$ nanocrystal by means of AFM (the white line is indicating the AFM measurement) and **(f)** AFM height profile of e), taken from [123] (supporting information).

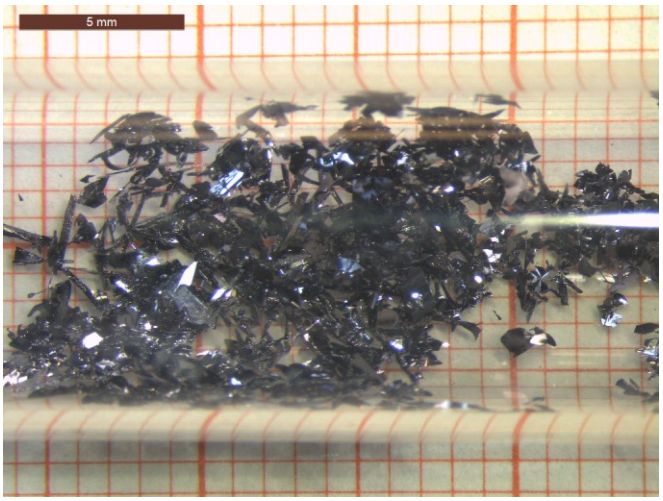

Figure A 14: Optical microscopy of CrI_3 bulk flakes prepared by larger gradient $\Delta T = 200$ K, respectively higher temperatures (1023 K → 823 K).

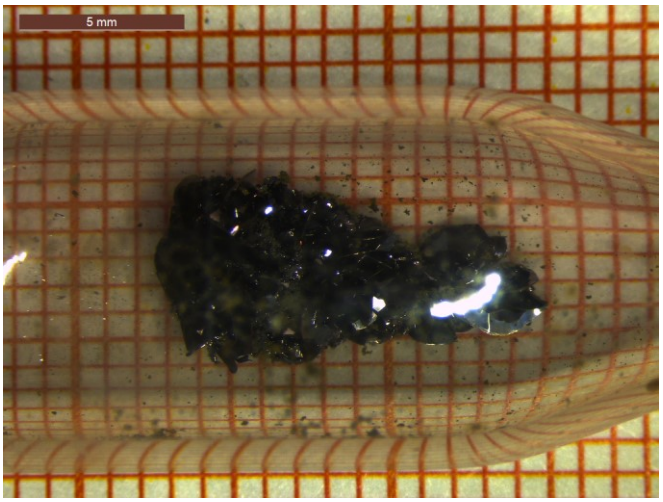

Figure A 15: Optical microscopy of CrI_3 bulk flakes prepared by a temperature gradient $\Delta T = 50$ K, respectively CVT temperatures of 923 K → 873 K.

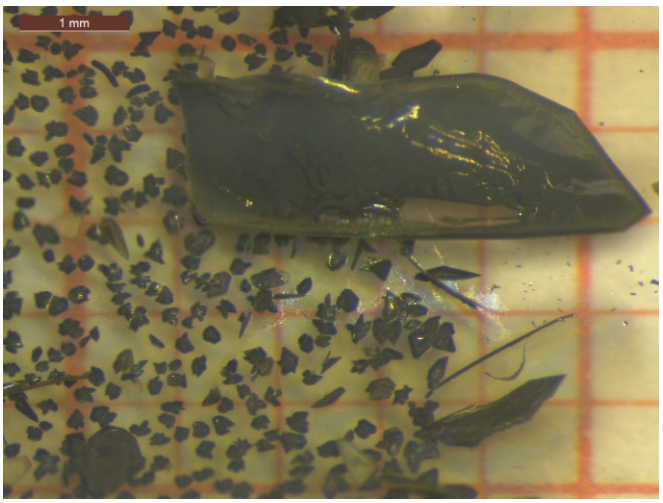

Figure A 16: Optical microscopy of CrI_3 bulk flakes prepared by a temperature gradient $\Delta T = 200$ K, respectively CVT temperatures of 923 K → 723 K.

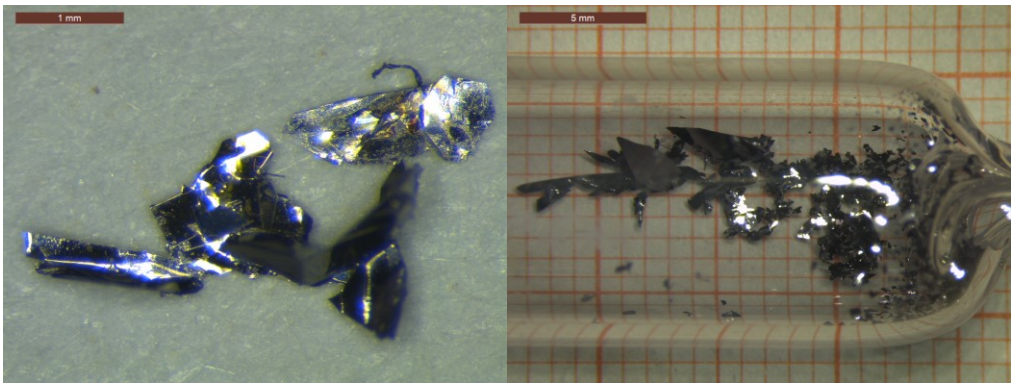

Figure A 17: Optical microscopy of CrI_3 bulk flakes prepared by a temperature gradient ΔT = 100 K, respectively CVT temperatures of 923 K → 823 K after 24 hours **(left)** and 168 hours **(right)**.

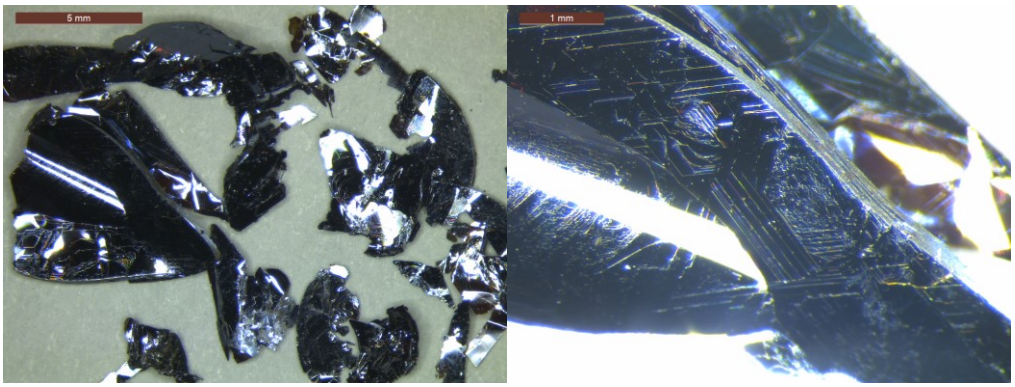

Figure A 18: Optical microscopy of $CrBr_3$ bulk flakes prepared by using a temperature gradient ΔT = 100 K, respectively CVT temperatures of 1023 K → 923 K and duration of 24 hours **(left)** and enlarged image emphasizing the 2D structure **(right)**.

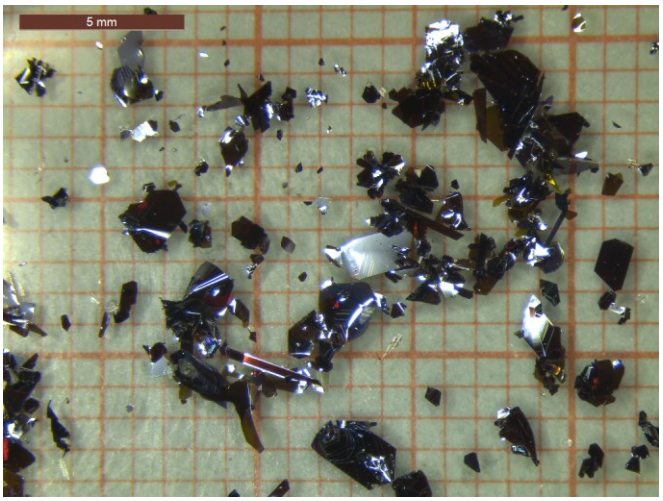

Figure A 19: Optical microscopy of $CrBr_3$ bulk flakes prepared by using a temperature gradient ΔT = 100 K, respectively CVT temperatures of 923 K → 823 K and duration of 24 hours.

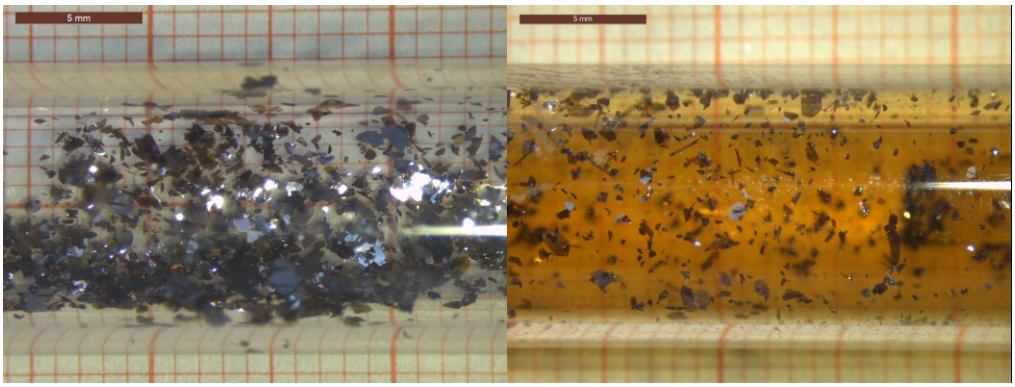

Figure A 20: Optical microscopy of $CrBr_3$ bulk flakes prepared by using a temperature gradient ΔT = 100 K, respectively CVT temperatures of 923 K → 823 K, a slight shortfall of Br_2 (according to $CrBr_3$) and durations of 12 hours **(left)**, or an experiment utilizing 6 hours instead **(right)** and a slight excess of Br_2 (according to $CrBr_3$).

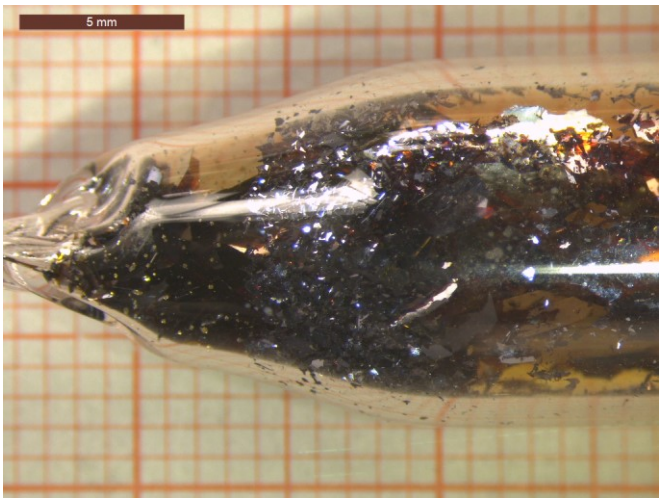

Figure A 21: Optical microscopy of $CrBr_3$ bulk flakes prepared by using a temperature gradient ΔT = 100 K, respectively CVT temperatures of 923 K → 823 K and duration of 174 hours.

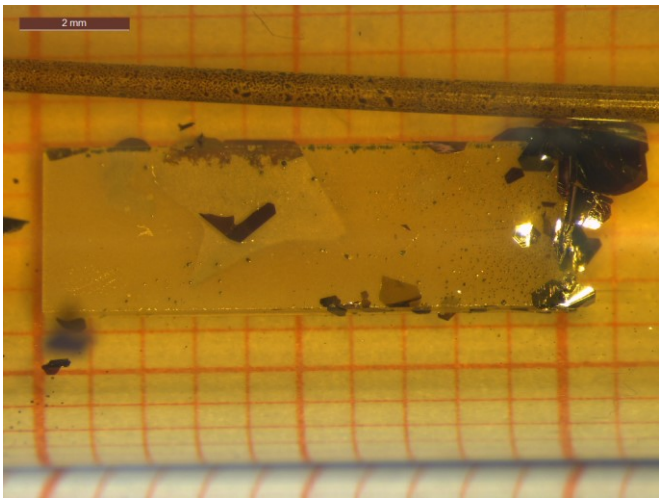

Figure A 22: Optical microscopy of $CrBr_3$ microsheets prepared by proceeding from 10 mg chromium, 50 mg bromine, a temperature gradient ΔT = 100 K, respectively CVT temperatures of 923 K → 823 K and duration of 24 hours.

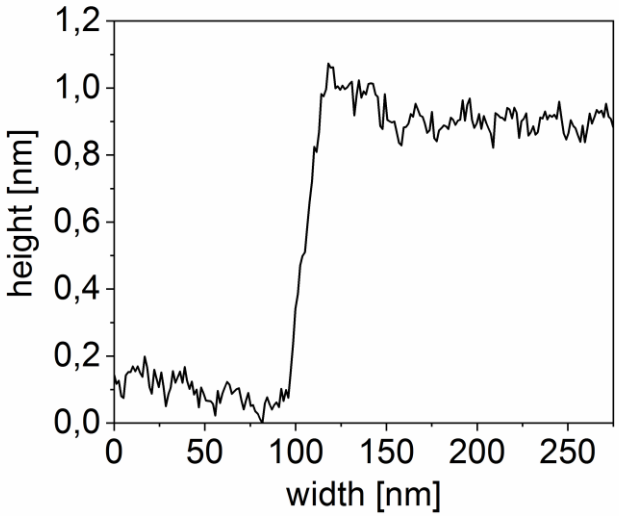

Figure A 23: $CrBr_3$ bilayer on YSZ substrate investigated by AFM, growth conditions: 1023 → 823 K (ΔT = 200 K) for 30 minutes, proceeding from 7.5 mg of chromium and 37 mg of bromine.

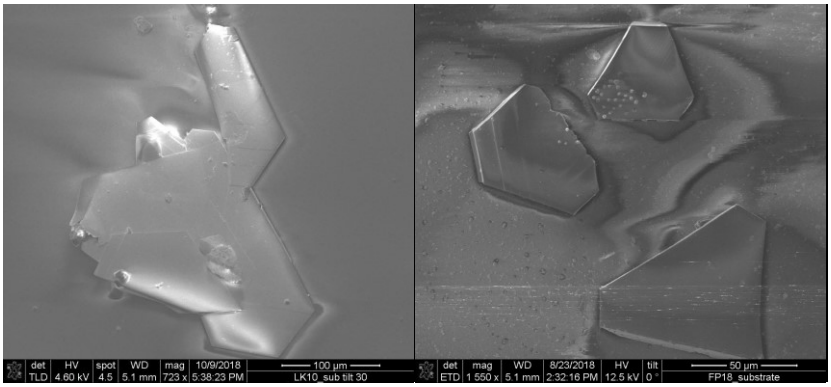

Figure A 24: (left) $CrBr_3$ microsheets on SiO_2 [0001] investigated by SEM, growth conditions: 923 → 823 K (ΔT = 100 K) for 30 minutes, proceeding from 13 mg of chromium and 61 mg of bromine, **(right)** $CrBr_3$ microsheets on SiO_2 [10-10] investigated by SEM, growth conditions: 923 → 823 K (ΔT = 100 K) for 30 minutes, proceeding from 9 mg of chromium and 46 mg of bromine.

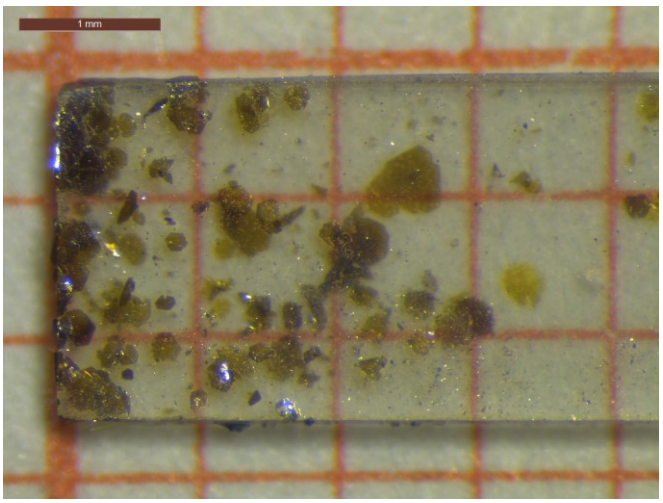

Figure A 25: $CrBr_3$ microsheets on sapphire [0001] investigated by optical microscopy, growth conditions: 923 → 823 K (ΔT = 100 K) for 30 minutes, proceeding from 8 mg of chromium and 39 mg of bromine.

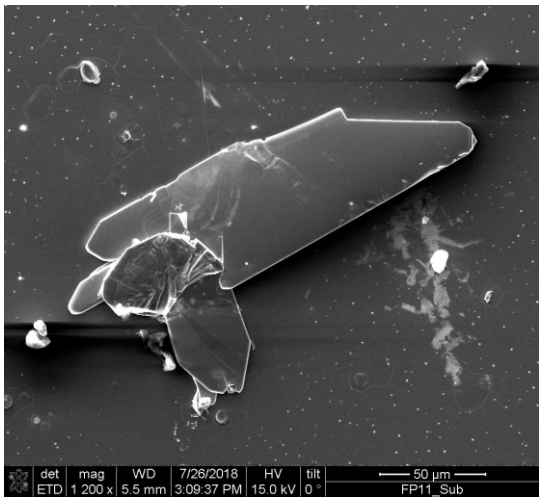

Figure A 26: CrI_3 microsheets on top of $LaAlO_3$ investigated by SEM, growth conditions: 923 → 823 K (ΔT = 100 K) for 30 minutes, proceeding from 2.5 mg of chromium and 20 mg of iodine.

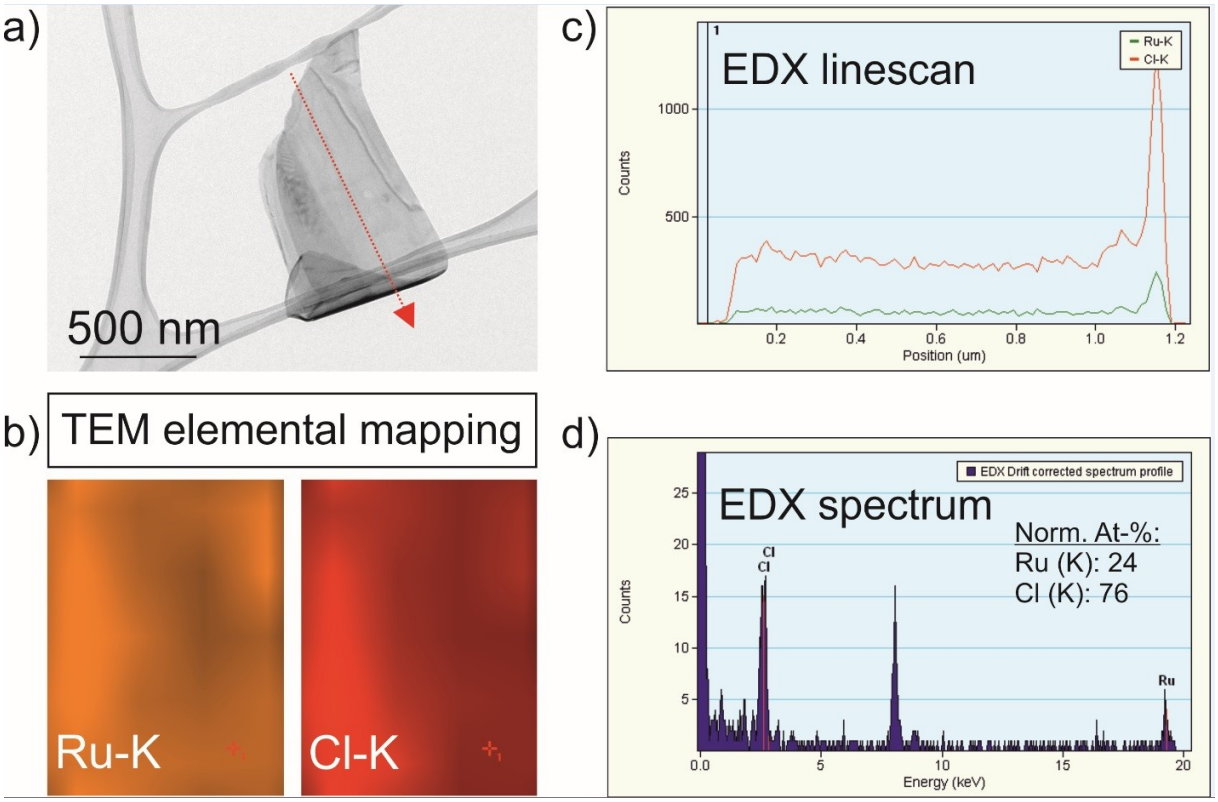

Figure A 27: TEM-EDX investigation of a $RuCl_3$ nanosheet: **(a)** investigated $RuCl_3$ nanosheet with red arrow indicating the linescan of c), **(b)** TEM elemental mapping of Ru and Cl, **(c)** EDX linescan corresponding to the red arrow in a), **(d)** corresponding EDX spectrum taken from [123].

Table A 12: SEM-EDX quantifications of MCl_3 nanosheets (M = Ru, Mo, Ti, Cr; the red dashed quantification data is indicating the EDX measurement of the running text).

	RuCl₃				***MoCl₃***			
excitation line	Ru Lα		Cl Kα		Mo Lα		Cl Kα	
measuring point	*At %*	*P/B*	*At %*	*P/B*	*At %*	*P/B*	*At %*	*P/B*
1	**27**	20	**74**	47	**24**	2	**76**	5
2	**27**	14	**73**	33	**23**	2	**77**	4
3	**24**	15	**76**	40	**23**	7	**77**	17
4	**26**	1	**74**	2	**27**	1	**73**	1
5	**24**	15	**76**	41	**24**	5	**76**	10
ø	**26**	-	**75**	-	**24**	-	**76**	-
	TiCl₃				***CrCl₃***			
excitation line	Ti Kα		Cl Kα		Cr Kα		Cl Kα	
measuring point	*At %*	*P/B*	*At %*	*P/B*	*At %*	*P/B*	*At %*	*P/B*
1	**28**	-	**72**	-	**27**	11	**73**	27
2	**26**	-	**74**	-	**25**	27	**75**	120
3	**28**	-	**72**	-	**28**	12	**72**	27
4	**29**	-	**71**	-	**32**	2	**68**	3
5	**28**	-	**73**	-	**33**	2	**67**	2
ø	**28**	-	**72**	-	**29**	-	**71**	-

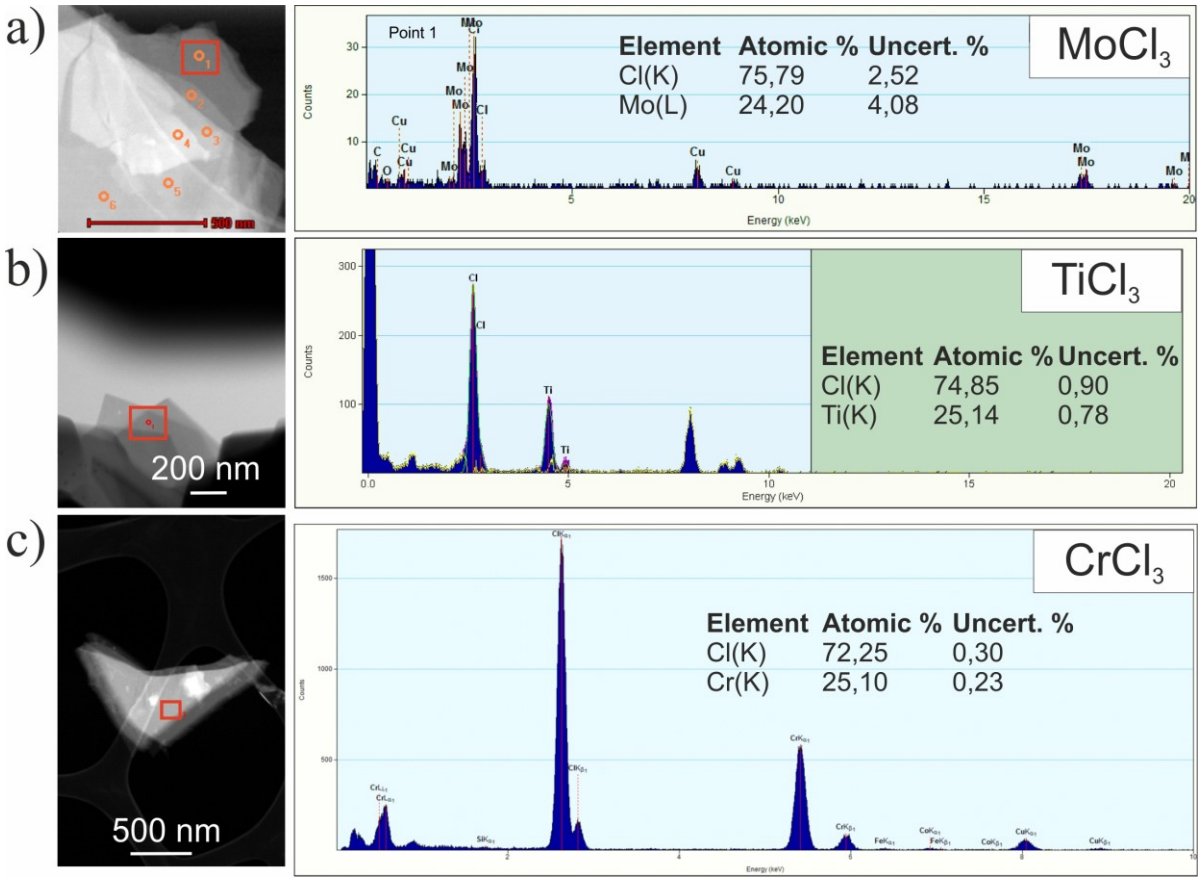

Figure A 28: TEM-EDX investigations of MCl_3 nanosheets: **(a)** $MoCl_3$, **(b)** $TiCl_3$ and **(c)** $CrCl_3$

Table A 13: SEM-EDX quantifications of CrX_3 nanosheets (X= I, Br; the red dashed quantification data is indicating the EDX measurement of the running text).

	CrI_3					
excitation line	Cr Kα		I Lα		O Kα	
measuring point	*At %*	*P/B*	*At %*	*P/B*	*At %*	*P/B*
1	**23**	3	**66**	11	**11**	2
2	**24**	5	**76**	22	**-**	-
3	**25**	6	**75**	23	**-**	-
4	**23**	4	**68**	14	**10**	1
5	**24**	4	**76**	17	**-**	-
ø	**24**	-	**72**	-	**(10)**	-
	$CrBr_3$					
excitation line	Cr Kα		Br Lα		O Kα	
measuring point	*At %*	*P/B*	*At %*	*P/B*	*At %*	*P/B*
1	**18**	10	**81**	61	**1**	1
2	**20**	11	**79**	62	**1**	1
3	**13**	8	**86**	50	**1**	1
4	**14**	8	**81**	51	**5**	1
5	**15**	10	**84**	51	**2**	1
ø	**18**	-	**82**	-	**2**	-

Table A 14: Gas-phase ethylene polymerization catalyzed by α-$TiCl_3$ microsheets [128].

Entries	Catalyst	Catalytic activity ($m_{polymer}$ / m_{TiCl3})
1	α-$TiCl_3$ (bulk)	5.0
2	α-$TiCl_3$ at YSZ (microsheets)	5.8
3	α-$TiCl_3$ at YSZ (microsheets, exfoliated)	6.2

Table A 15: Literature survey of previously executed CVT of MCl_3 structures

Ti	V	Cr	Mn	Fe	Co	Ni
[61,100,128]	[100,103]	[72,100,103,109,171]	-	[157,172]	-	-
Zr	**Nb**	**Mo**	**Tc**	**Ru**	**Rh**	**Pd**
[173]	[100]	[100,103,135,171]	[106]	[72,100,103,174–176]	[100]	-
Hf	**Ta**	**W**	**Re**	**Os**	**Ir**	**Pt**
[173]	[100]	-	[177,178]	[100,179] **14**	[179]	[100]

Table A 16: Literature survey of previously executed CVT of MBr_3 structures

Ti	V	Cr	Mn	Fe	Co	Ni
[61,100]	[107]	[72,100,104]	-	[172,180]	-	-
Zr	**Nb**	**Mo**	**Tc**	**Ru**	**Rh**	**Pd**
[181]	[100]	[72,100,102]	[106]	[72,100,182,183]	-	-
Hf	**Ta**	**W**	**Re**	**Os**	**Ir**	**Pt**
[184]	[100]	[185]	[186]	- **15**	[100]	[187]

Table A 17: Literature survey of previously executed CVT of MI_3 structures

Ti	V	Cr	Mn	Fe	Co	Ni
[77]	[100,103]	[31,34]	-	-	-	-
Zr	**Nb**	**Mo**	**Tc**	**Ru**	**Rh**	**Pd**
[188]	[189,190]	[191]	[106]	-	[192]	-
Hf	**Ta**	**W**	**Re**	**Os**	**Ir**	**Pt**
[184]**16**	[193]	[100]	[194]	- **17**	[100]	[195]

14 The observations indicate that "$OsCl_3$" has a wide homogeneity range, from $OsCl_{3.1}$ to $OsCl_{3.9}$, but no clear indicators for $OsCl_3$ are mentioned.
15 In reference [201] *Schäfer* described investigations of "$OsBr_3$" and observed that actually $OsO_{0.5}Br_3$ exists and demonstrated further similarities to "$OsCl_3$" samples.
16 Extensive work by *Beekhuizen* on hafnium iodides revealed a phase width of "HfI_3" samples with HfI_{3+x} ($x = 0.2 – 0.5$), similar to investigations of "$OsCl_3$" samples.
17 Basic information on the synthesis of OsI_3 can be found at reference [202].